Image intensifier studies of low intensity triboluminescence, electroluminescence and photoluminescence of solids

Thesis

THE OPEN UNIVERSITY

PHYSICS DISCIPLINE

IMAGE INTENSIFIER STUDIES OF LOW INTENSITY TRIBOLUMINESCENCE, ELECTROLUMINESCENCE AND PHOTOLUMINESCENCE OF SOLIDS

by

GEOFFREY N CHAPMAN BA (OXON)

Thesis submitted as partial fulfilment of the requirements for the degree of Doctor of Philosophy

February 1981

Date of Submission: 4.3.81

Date of award: 7.7.81

No part of this thesis has previously been submitted for a degree, or other qualification, to this or any other university or institution.

CONTENTS

LIST OF FIGURES

ACKNOWLEDGEMENTS

I wish to thank Dr. J.C. Ramage and Dr. A.J. Walton for supervising this work, and for spending what must have been many tedious hours reading the manuscript of this thesis.

I am grateful to: Dr. Aitken, Department of Archaeology, University of Oxford, for the loan of the thermoluminescence oven; Dr. I. Austin, University of Sheffield, for the amorphous silicon samples; Dr. D.B. Darby, Department of Metallurgy and Science of Materials, University of Oxford, for the CL and SEC pictures and for the GaP samples; Professor E. Davis, University of Leicester, for the amorphous phosphorus samples; Dr. J. Field and Dr. G. Swallowe, Cavendish Laboratory, Cambridge, for samples of glasses and polymers; G. Botley and Sons Ltd., Old Church Street, Chelsea, for supplying many samples of minerals; Dr. R. Harley, Clarendon Laboratory, Oxford for doped fluorite samples; Dr. R. Nicholas, Clarendon Laboratory, Oxford, for $Ga_{1-x}Al_xAs$ samples; and Dr. D.R. Wight, RSRE, for a $Ga_{1-x}Al_xAs$ sample .

I wish to thank The Open University for funding a Research Studentship.

I have had helpful discussions with G. Fasol, D. Roberts, S. Swithenby and others too numerous to mention.

I am grateful to Roger, Bill, Nobby, Ted and others for helping construct some of the equipment described in this thesis. I also wish to thank, my parents, E.B., C.C., M.C., G.F., C.G., G.G., P.G., J.H., C.P.H., E.K., R.S., A.W., J.W., and M.W., who all in one way or another, helped the completion of this thesis. Last but not least I wish to thank especially Sue Craig for her most accurate typing.

PUBLICATIONS

G.N. Chapman, J.C. Ramage and A.J. Walton

"High-gain image intensifier studies of electroluminescence in III-V semiconductors"

J. Appl. Phys (1980); 51, 1; pp 616-618

G.N. Chapman, A.J. Walton

"Spectral Studies of The Light Emitted on Cutting Minerals with a Diamond Saw"

Proceedings of the Archaeological Conference on Thermoluminescence (P.A.C.T.) Oxford (1980); in the press.

Image Intensifier Studies of Low Intensity Triboluminescence, Electroluminescence and Photoluminescence of Solids

G. N. CHAPMAN

Abstract

A four-stage magnetically focused image intensifier tube (IIT) with an optical power gain of about 10^6 was used in both spatial and spectral investigations of solids.

The spectral studies involved the design and construction of a spectrograph to disperse light across the input photocathode of the IIT. Spectra were then amplified by the IIT and displayed on the output phospher where they were photographically recorded. The system was intensity corrected and used to measure the triboluminescence (TL) spectra from small quantities ($\simeq$ 10 grams) of material. The TL spectra of minerals including amethyst, zircon, and various calcites and fluorites were recorded for the first time with high spectral resolution. Origins of these TL spectra were investigated, and many were correlated with appropriate term diagrams. The results are discussed following a detailed and critical review of the literature. Light emission from cutting a number of glasses and polymers on a diamond saw was also recorded and the (continuum like) spectra

obtained were compared with black body radiation (at the temperature estimated to occur at a crack tip due to release of plastic deformation energy). Differences were noted in some cases between the TL which occurred at fracture and the light emission of the same samples when cut on the diamond saw. These differences are discussed with reference to the photoluminescence spectra of the samples. Thermoluminescence spectra were also recorded, again using an IIT spectrograph, and the results were compared with TL of similar specimens.

A spatial study of semiconductors was made by projecting the image of a small area (typically 50 μm^2) of the specimen, using a microscope, onto the input photocathode of the IIT. The high optical power gain of the system was utilized in a spatial investigation of semiconductor electroluminescence (EL) and photoluminescence (PL). The EL of GaP and $Ga_{1-x}Al_xAs$ ($x = 0.35$ and 0.52) was recorded and the EL of the latter was compared with cathodoluminescence of the same specimen to highlight the complementary nature of the techniques. The homogeneity of the PL of a sample of amorphous silicon was studied at 77K in a specially constructed cryostat. The application of the method to other homogeneity measurements is discussed.

INTRODUCTION

This thesis describes an experimental study of low light level phenomena. A spatial study was made of semiconductor luminescence (mainly photoluminescence (PL) and electroluminescence (EL)) and a spectral study of triboluminescence (TL) was undertaken. TL is the light emission which accompanies the fracture of some solid materials. The semiconductor study required faint PL and EL images to be recorded, while the TL study needed a record of faint transient spectra.

For many years photomultipliers (PMs) have been used in the study of low light level phenomena. Single photons can be detected with PMs but their use is limited because they are single channel instruments. To record spatial images with a PM would require a scanning system. To record TL spectra with a PM would likewise require a scanning instrument such as a monochromator to move the required wavelength range over the PM tube. In any scanning system much signal information is wasted because only part of the signal is detected at any one time.

IITs have been used in astronomy and biology but there have been few applications in solid state physics. They can have the same gain as a PM, and in addition any image projected onto the input photocathode is reproduced on the output phospher, where the image can then be photographed. Any image projected onto a PM photocathode simply produces an output proportional to average intensity. An IIT facilitates the recording of faint semiconductor luminescence images because the image formed on the IIT input photocathode can be directly photographed on the IIT output phospher with a short (of order seconds) time exposure. Direct photography of the luminescence images, if possible at all, would require very long time exposures.

Faint TL emission can be recorded by dispersing the spectra across the IIT photocathode and photographing the output phospher. The advantage of this method of recording TL spectra is that all wavelengths are recorded continuously and simultaneously. This is particularly important since TL emission can be of a shorter duration than the time taken to scan a monochromator through the required wavelength range.

CHAPTER 1

IMAGE INTENSIFIER TUBE EQUIPMENT

1.1 Image Intensifier Tubes

An image intensifier tube (IIT) may be treated as a "black box" with an input plane and an output plane. An image projected and focused onto the input plane is reproduced essentially undistorted in the output plane, but with increased brightness. All IITs have in common a photocathode which converts the incoming light into an electron image, and which imposes its own spectral response. The output image is formed on a phospher screen which glows under electron bombardment. There can be a wavelength shift depending on the input photocathode wavelength sensitivity and the output phospher emission spectrum. What happens between photocathode and phospher varies from tube to tube.

In a simple one-stage electrostatic tube, electrons are accelerated from the photocathode to the phospher by an electric field and are focused by an arrangement of electrodes (see figure 1.1) built into the tube. All one stage tubes of this type suffer from bad off-axial aberrations, but have the advantage of being small and light. One of the reasons for the low off-axial resolution is that electrons emitted at an angle θ from the photocathode normal, where $\theta \neq 90^{o}$, may not be brought to focus in the same position as those emitted at $\theta = 90^{o}$. Magnetic focusing overcomes this problem. A magnetic field is applied along the tube axis, perpendicular to both phospher and photocathode, so that electrons accelerated by a potential difference between photocathode and phospher will move around the axial magnetic field.

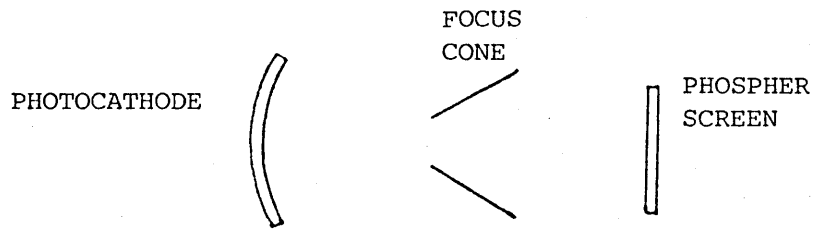

a) SPHERICAL ELECTROSTATIC

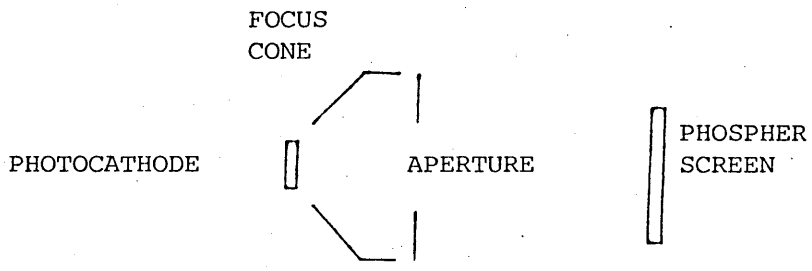

b) PLANAR ELECTROSTATIC

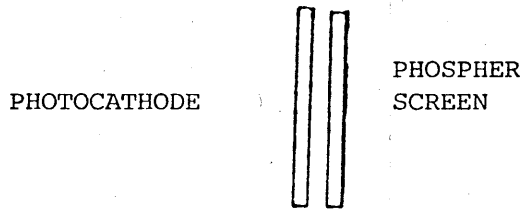

c) PLANAR PROXIMITY

FIGURE 1.1 TYPICAL ELECTRODE ARRANGEMENTS FOR ONE STAGE IMAGE TUBES.

Consider an electron with initial velocity components of V_L along the tube axis and V_T parallel to the photocathode. In a tube of length d with an electric field E applied

$$d = \frac{eET^2}{2m} \qquad 1$$

where e and m are the electrons charge and mass respectively and T is the time taken by the electron to travel the distance d. Equation 1 assumes that

$$V_L T << \frac{eET^2}{2m} \qquad 2$$

which is normally the case.

In a plane parallel to the photocathode, from the equations for circular motion in a magnetic field

$$eV_T B = \frac{mV_T^2}{r} \quad \text{and} \quad V_T = \frac{2\pi r}{T}$$

so that

$$\frac{eB}{2\pi m} = \frac{1}{T} \qquad 3$$

If equations 1 and 3 are both satisfied then

$$d = \frac{eE}{2m}\left(\frac{2\pi mn}{eB}\right)^2 \qquad 4$$

When equation 4 is satisfied an electron, no matter what its initial velocity components (provided equation 2 is satisfied), will complete exactly n circular orbits in the time taken to travel the length of the tube. Thus for the combinations of E, B, n and d which satisfy equation 4 there is a one to one correspondence between the points at which electrons leave the photocathode and those points at which they strike the phospher. A tube which uses magnetic focusing

should produce an image with fewer aberrations than an electrostatically focused tube.

Another type of IIT is the so called "Channel Plate Intensifier" in which one to one correspondence between phospher and photocathode positions is maintained by channelling the electrons along a fine array of glass tubes. Electron gain is achieved by secondary emission from the tube walls, and is lower than in magnetically focused IITs.

The overall optical gain of a system employing a one stage tube, whether electrostatically or magnetically focused, after allowing for coupling optics, is little better than directing the image straight onto a photographic film. However an IIT with several closely coupled stages can achieve a gain greater than 10^6. This enables single photoelectrons emitted from the first photocathode, to give a developable spot on a film which records the output phospher. In the tubes used in these experiments four stages were coupled by three intermediate phospher-mica-photocathode sandwiches (see figure 1.2). An electron from the input photocathode will hit the phospher of the first phospher-mica-photocathode sandwich with a typical energy of 10 keV. If there is a 20% efficiency for conversion of photoelectrons into photons of a wavelength to which the photocathode is sensitive (the spectral responses are closely matched), then each photoelectron will excite about 1000 photons. Substantially all of these are directed by the aluminium backing (figure 1.2) to the 10% quantum efficient photocathode so that about 100 photoelectrons are liberated from the intermediate sandwich by each incident photoelectron. In a four-stage tube (three intermediate sandwiches plus the input photocathode and output phospher) of commercial quality like the IIT used in this research (see figure 1.3) a photoelectron from the input

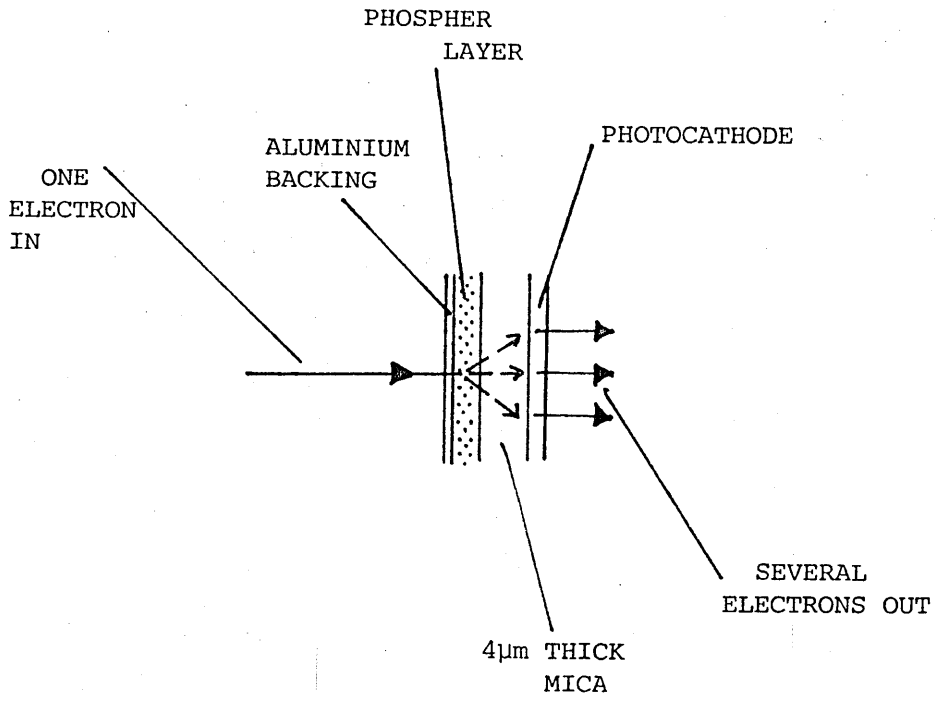

FIGURE 1.2 AN INTERMEDIATE PHOSPHER-PHOTOCATHODE SANDWICH (After Coleman and Boksenberg, 1976).

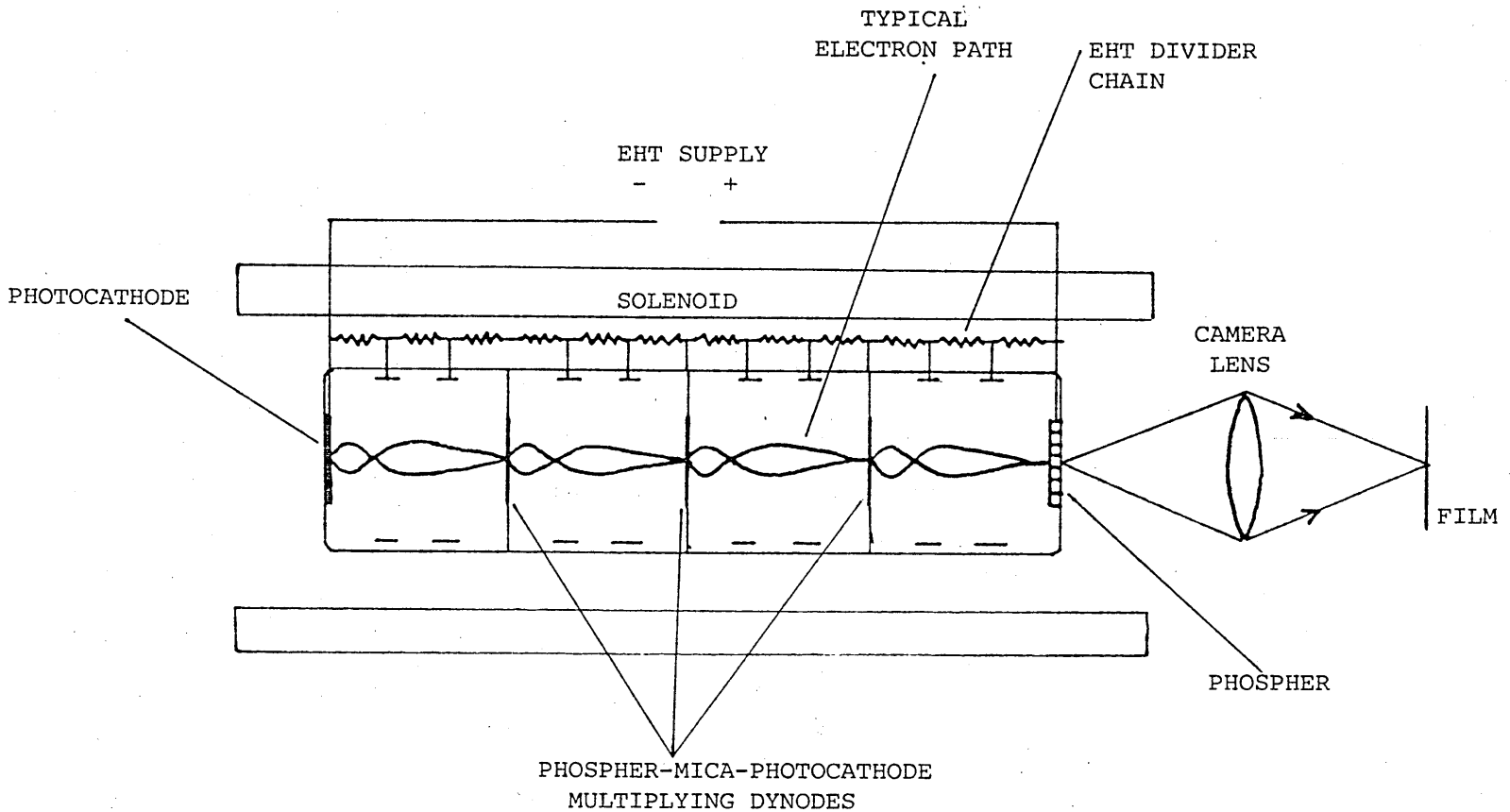

FIGURE 1.3 SCHEMATIC DIAGRAM OF AN IMAGE INTENSIFIER TUBE (EMI TYPE 9912).

photocathode can give rise to 10^7 photons at the output phospher. This is a light gain of 10^6 in the blue part of the spectrum where the input photocathode quantum efficiency is about 10%. An f2.8 camera lens (the f number of a lens is, of course, its focal length divided by its diameter) viewing the phospher will accept ≃ 0.5% of the light from the phospher and can focus onto the photographic film with a magnification of unity. A scintillation of 10^7 photons from a four stage IIT thus leads to about 5×10^4 photons focused on the photographic emulsion. If there is a photographic detective quantum efficiency (see appendix one) of only 0.1% this will result in 50 photographic grains; easily sufficient to record on a densitometer. Thus a single photoelectron from the IITs first photocathode can be recorded.

Another possible device which was considered for low light level detection was a silicon intensifier vidicon, however these are not ideally suited for single photon detection because they are affected by electrical noise in the silicon diode target array (Reynolds, 1980). For an extensive review of IITs and their properties see Coleman and Boksenberg (1976).

The IITs used in this research are four-stage high gain EMI type 9912 with axial magnetic focusing (.03 to .05 tesla) and forced air cooling of the focusing coil, (see figure 1.3). Both a "setting-up" quality and full specification tube were used at appropriate times. The tubes were interchangeable within the same focusing coil. Data for each IIT is given in table 1.1. The photocathode quantum efficiency is plotted in figure 1.4. The spatial resolution of a tube is described by its modulation transfer function (MTF). A typical MTF is shown in figure 1.5. The spatial resolution is limited to about 0.05 mm across most of the 40 mm diameter phospher

TABLE 1.1 DATA ON EMI TYPE 9912 IMAGE INTENSIFIER TUBES

	SETTING-UP TUBE	FULL SPECIFICATION TUBE
Photocathode sensitivity	112 μA per lumen	115 μA per lumen
Gain	10^6 at 34 kV	10^6 at 34 kV
Dark Current	5×10^{-9} Lux EBI[a]	5×10^{-10} Lux EBI[a]
Spatial Resolution	25 line pairs per mm[b]	35 line pairs per mm[b]
Photocathode type	Extended S20[c]	Extended S20[c]
Useful Diameter	40 mm	40 mm
Quantum Efficiency		
at 800 nm	.54%	.36 %
655 nm	2.9 %	2.8 %
550 nm	6.4 %	7.2 %
440 nm	11.5 %	15 %

a "EBI" means equivalent brightness input. For the extended S20 photocathode 5×10^{-10} Lux $\simeq$ 50 electrons cm^{-2} s^{-1} and 5×10^{-9} Lux $\simeq$500 electrons cm^{-2} s^{-1}.

b Quoted for 5% output contrast with 100% input contrast.

c Quantum efficiency is shown as a function of wavelength in Figure 1.4

USEFUL CONVERSION DATA

1 Lux $\simeq$ .1 lumen per square foot = .1 foot candles (fc) illuminance

Starlight $\simeq 10^6$ "blue" photons cm^{-2} s^{-1} $\simeq 10^{-6}$ fc

Moonlight $\simeq 10^{-4}$ fc

Twilight $\simeq 10^{-2}$ fc

Room light $\simeq$ 1 fc

Sunlight $\simeq 10^2$ fc

At 555 nm there are 655 lumens per watt

1 lumen $\simeq 4 \times 10^{15}$ "green" photons per second

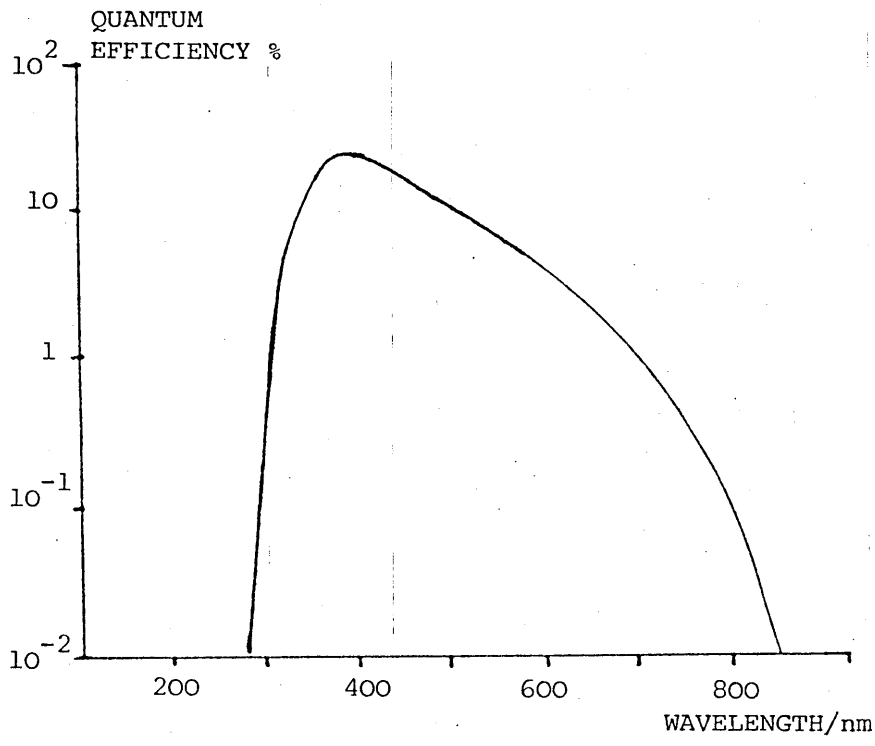

FIGURE 1.4 QUANTUM EFFICIENCY AS A FUNCTION OF WAVELENGTH FOR A TYPICAL EMI 9912 IIT WITH S20 PHOTOCATHODE (After EMI Ltd., 1975)

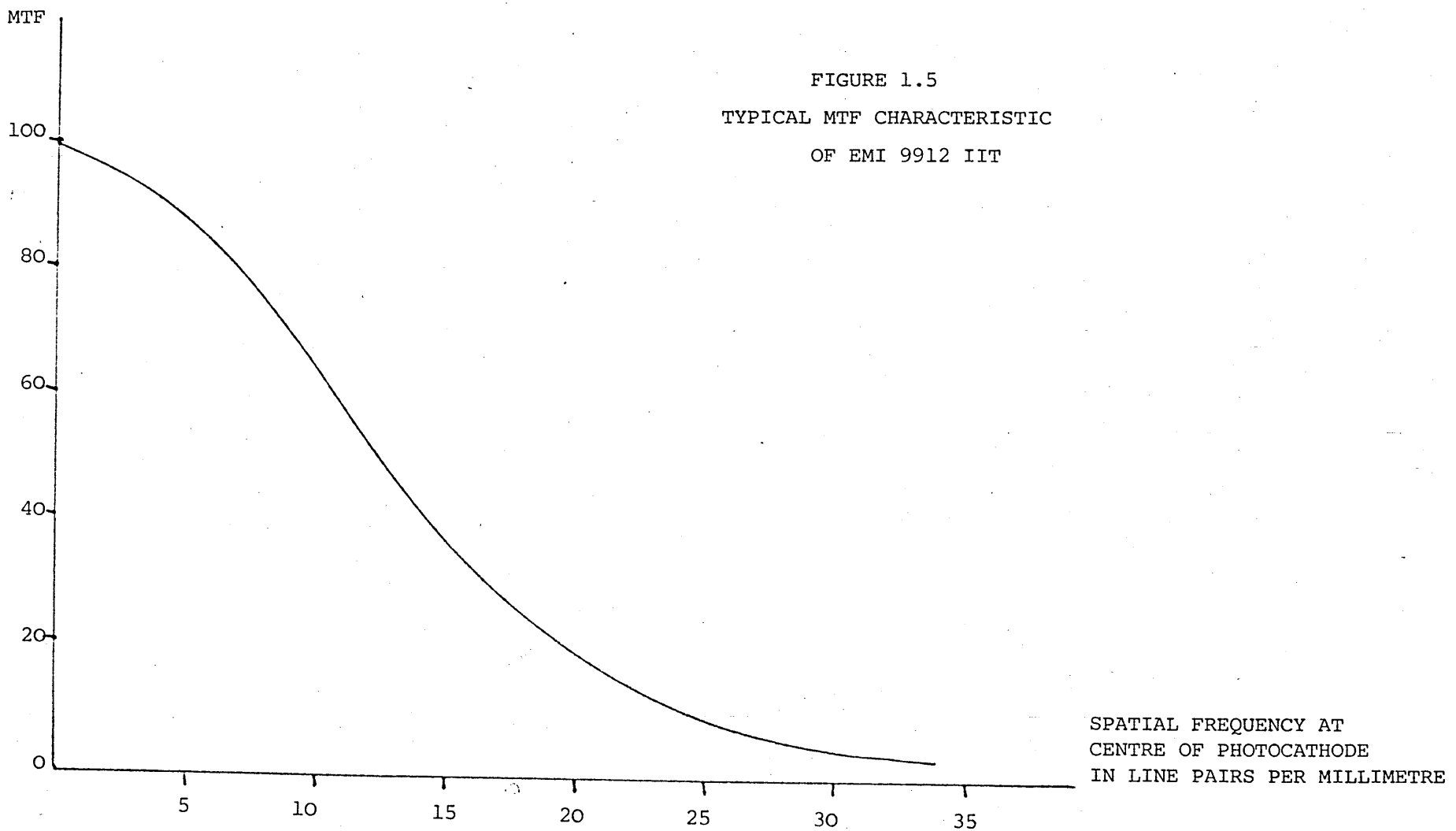

FIGURE 1.5

TYPICAL MTF CHARACTERISTIC

OF EMI 9912 IIT

because of transverse light spread in the intermediate phospher-photocathode sandwiches. At low light levels, as has been discussed by Rose (1973), the resolution of an IIT system is governed by photon statistics rather than by imperfections in the tube itself. To take a simple example, if a low contrast scene yields a total of 10^4 photoelectrons from the IIT photocathode within the integration time of the recording medium, and the photocathode has a diameter of 40 mm, then the mean separation between photoelectrons will be about 0.3 mm. This means that the maximum attainable resolution under these conditions is less than 0.3 mm.

Noise, which is visible as random light spots on the IIT phospher (figure 1.6) is of two types, thermal electrons from the first and second photocathodes, and bright scintillations sometimes called ion spots. The latter are probably due to ions bombarding the photocathode and releasing a large number of photoelectrons as a group.

The IIT is only one component in an optical system which includes input and output optics and a recording medium. An efficient input optical system is necessary to direct as many photons as possible onto the IIT photocathode, and an efficient output optical system must image the phospher onto the recording film without unacceptable light scatter or aberrations. The design of an IIT spectrograph to couple efficiently to the IIT input is described in section 1.3.3 and photography of the IIT output phospher† is considered in section 1.2.2. The coupling of a microscope to the IIT for the purposes of spatial imaging is described in chapter 5.

† For alternative spellings refer to The Oxford English Dictionary.

FIGURE 1.6 IIT NOISE

Both photoelectron noise, and ion spots are visible. Scale bar equals 5 mm on the IIT phospher.

1.2.1 Installation of the Image Intensifier Tube

This section describes the initial installation of the EMI IIT system and its calibration in readiness for connection to the spectrograph and microscope systems. The tube and housing, with its power supply and controls, were mounted on a two level trolley. The electronics and cooling fan were on the lower level and the focusing coil housing, into which the tube was placed, was on the upper level. Adjustable height flaps were fixed at either end of the trolley on which to stand equipment that would be used with the IIT, such as the camera box, microscope and spectrograph. Preliminary experiments with the setting-up grade tube in the focus coil housing, and using a photon gain of about 10^6 indicated the sensitivity of the tube. A glowing cigarette at 3 metres could produce a significant output. This showed that care would be needed to shield stray light when the tube was operating. Hence all experiments were performed in a blacked-out room with the minimum necessary illumination provided by careful use of dense red filter covered torches, that were never pointed directly at the photocathode.

Focusing of the IIT was performed by eye, while adjusting the focus coil current, for each electron acceleration voltage applied to the tube (EHT), and hence each gain, in integer multiples of 1 kV from 20 kV to 38 kV (the maximum specified EHT voltage for this type of tube). Coarse focusing was performed with an EMI resolution chart, faintly illuminated by a microscope lamp connected to a variable voltage power supply. An image of the chart was projected onto the photocathode with a photographic enlarger lens. Fine focusing was performed by observing the noise spots on the output phospher with a 20 x magnification microscope. For example a focus current of 7.7A was required at an EHT setting of 20 kV, and a current of 9.8A was

required at 33 kV. I found that there were long term drifts in the required focusing current, so the focus was always checked before an important experiment and the system was recalibrated if necessary. A plot of tube EHT voltage against the square of focusing current was found to be a straight line as expected for a magnetically focused tube (see equation 4 above).

The optical gain of IITs of this type plotted as a function of voltage is shown in figure 1.7. Unless otherwise stated, in all that follows the IIT was set to give an optical gain of about 10^6, so allowing single photon events to be recorded photographically.

After the IIT was switched on it was always allowed to stabilize for 10 to 15 minutes before any experiments were performed. Noise on the phospher was found to be reduced by occasional rotation of the tube electric field divider chain potentiometers. This probably reduced a static electric charge build up in parts of the tube.

1.2.2 Photography of the Image Intensifier Tube Phospher

Various ways of photographing the output phospher were considered. A direct fibre optic coupling between the output phospher and a film is commercially available, but this makes observation of the IIT output during a photographic exposure impossible, and it was thought too restricting to be used in these experiments. The best combination of camera, camera lens, auxillary close up lens if needed, photographic film, preflash if needed, and developer had to be found. A camera box was also needed so that exact and reproducible positioning of the camera could be achieved.

Account had to be taken of the two types of IIT output that would need recording

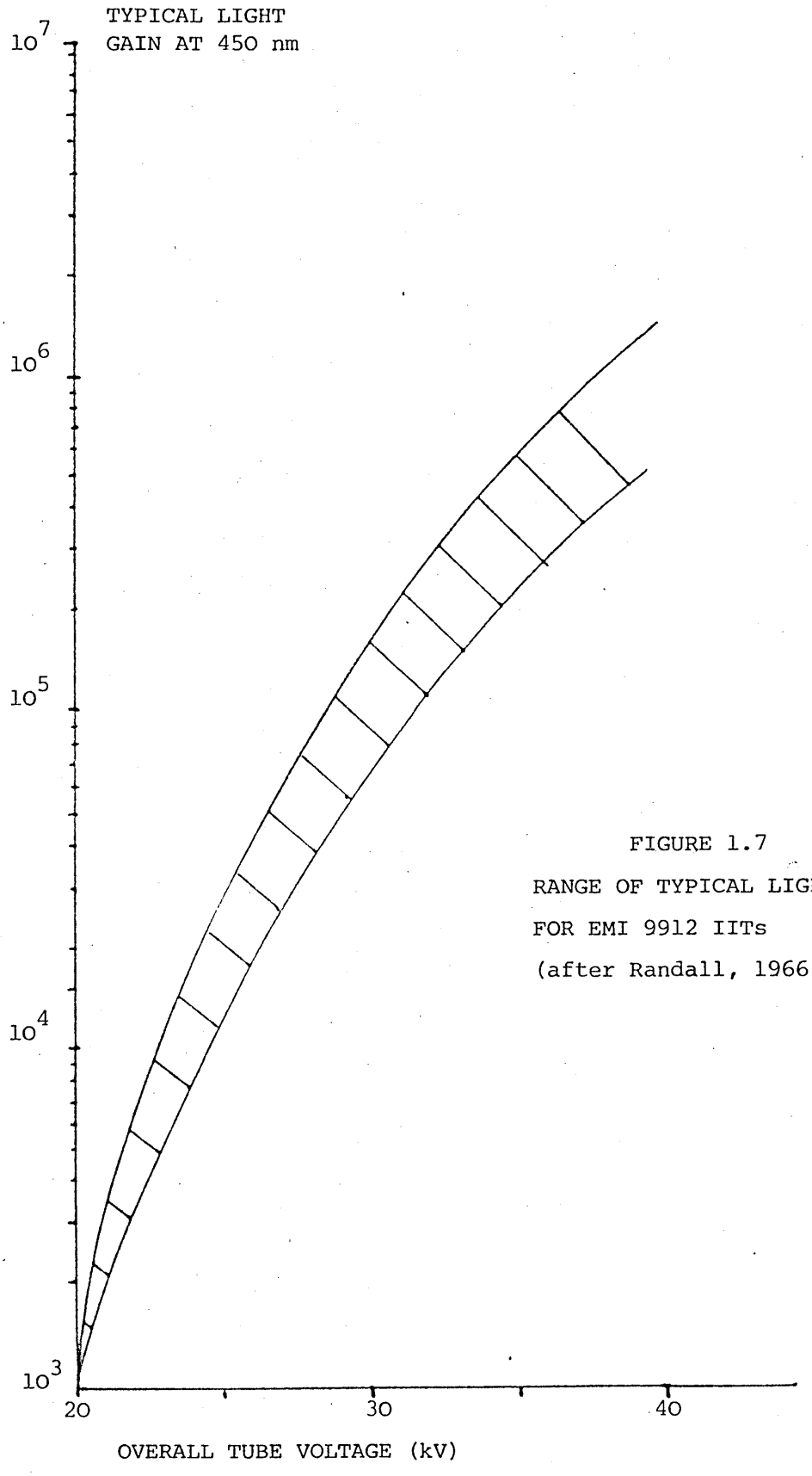

FIGURE 1.7
RANGE OF TYPICAL LIGHT GAINS
FOR EMI 9912 IITs
(after Randall, 1966)

a) Brief flashes of light corresponding to triboluminescent spectra as materials fractured.

b) Continuous outputs such as photoluminescence images, where long exposure times are possible.

Case "a)" was the more critical. Ideally all light spots on the phospher, originating from single photoelectron emission at the first photocathode would be recorded. Inevitably this would record photoelectron noise as well as signal since the individual spots are indistinguishable. This corresponds to what is sometimes called "class one detection" (Kodak Ltd., 1973). The input noise applied to the film is very low and the signal, which consists of all light spots on the phospher, controls the exposure conditions. A film must be selected with sufficient sensitivity to record these spots. The typical characteristic curve of a film is shown in figure 1.8, and optical density (D) is discussed in Appendix 1 at the end of this chapter.

Preliminary experiments using a trial camera system showed that short exposures of faint phospher images were often not recorded or were recorded in the "toe" of the characteristic curve. To improve signal detection I decided to adopt the technique of exposure preflashing (Kodak Ltd., 1973). Preflashing is accomplished by providing a uniform low level exposure of the film to light prior to the signal exposure. This raises the background fog but also elevates the signal exposure to a steeper part of the characteristic curve, so that D(signal) - D(base) is increased more rapidly than the film granularity, see figure 1.9. In microscopic terms preflashing provides photons that produce sensitivity specks on the film, some developable (to produce an overall fogging), others with too few silver atoms to be developable, but requiring fewer additional

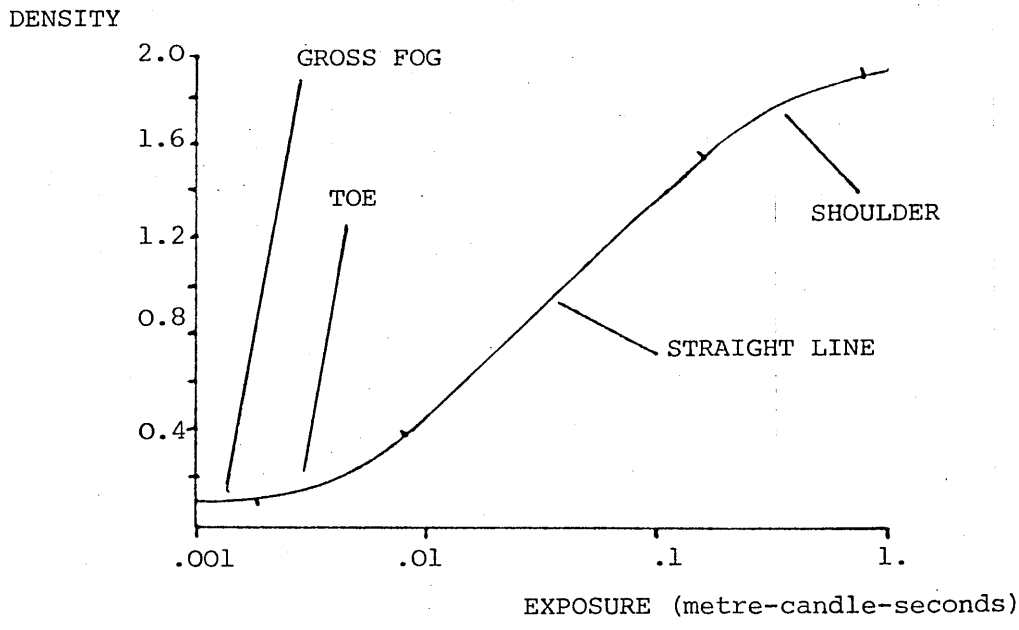

FIGURE 1.8 TYPICAL CHARACTERISTIC CURVE OF A PHOTOGRAPHIC EMULSION. Toe, straight line portion and shoulder are delineated.

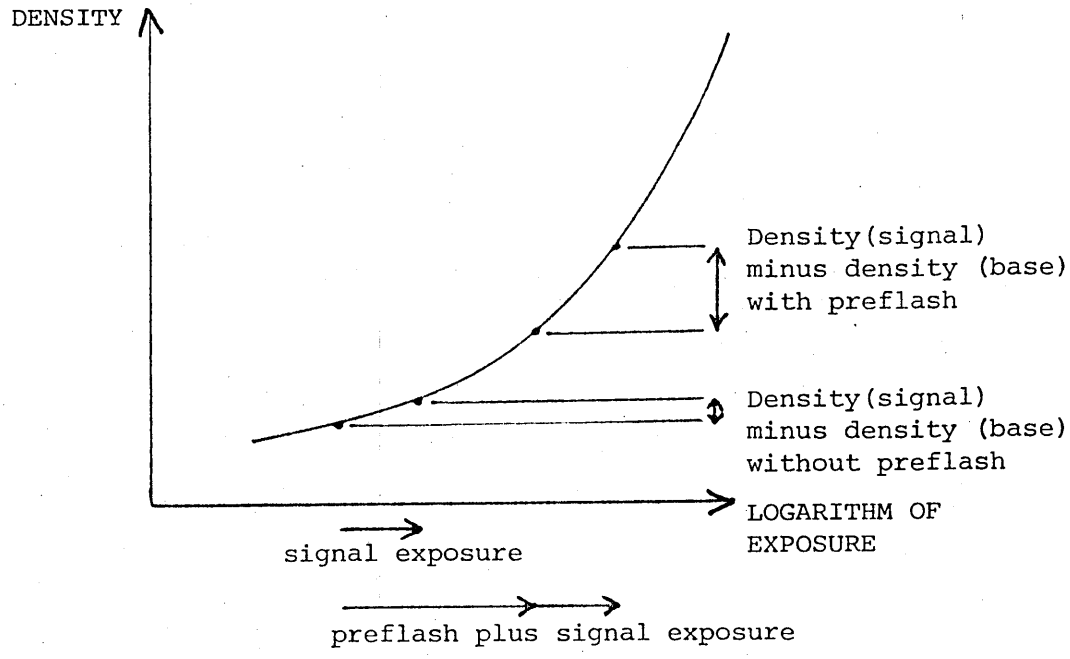

FIGURE 1.9 THE EFFECT OF PREFLASHING A PHOTOGRAPHIC EMULSION

photons to render them developable than if there had been no pre-flashing. Thus by adding signal photons some of the subdevelopable grains are rendered developable and so signal photons are absorbed in a more useful manner. A typical photograph (on a preflashed film) of part of the phospher is shown in figure 1.6, where photoelectron noise, and ion spot noise are both visible. A series of negatives with differing preflash were taken, and a preflash that raised the base fog by about 0.15 in density for Tri-X (Kodak) film developed in HC-110 (so that the total film density was the original base density of 0.4, plus 0.15) was found to record most phospher light spots. The exposure to achieve this preflash depended on developing procedure.†

In the case of continuous IIT outputs preflashing was found unnecessary since long time exposures to record weak signals were possible. Also the camera lens could be stopped down and exposure time increased to improve definition.

1.2.3 Selection of Camera Lens, Close-up Lens and Camera Position

Various cameras, lenses and close-up lenses were tested to determine the most suitable arrangement. There were a number of requirements which had to be fulfilled. The horizontal diameter of the output phospher (40 mm) had to be reproduced on the film with adequate resolution and with as large a lens aperture (small f number) as possible. A large magnification between phospher and film would

---

†On Tri-X, (Kodak), film developed in HC-110 for the manufacturers recommended time plus 50%, and with the camera placed directly over a neutral density filter covered slide illuminator box, 1/60th second at f8 exposure was given. This was when using a Nikon f1•4, 50 mm focal length lens on a Nikon F2 camera, with the focus set to infinity. Further details in section 1.2.3.

ensure that no information was lost due to film granularity but conversely a small magnification would mean that only the central part of the film was used and so losses due to lens aberration would be minimized. Inevitably a compromise had to be reached. A Nikon F2 camera was tested with various combinations of the following, Vivitar f2.5 macro lens, Nikon f3.5 macro lens, Nikon f1.4 lens; Nikon extension ring set K; Nikon lens reversing ring; "Proxizoom" close up lens, achromatic close up lens (H.W. English and Co.), close up lens (Hoya) and a close up lens (Canon). A Canon f0.95 fixed lens camera was also tested. The most convenient test was to photograph IIT phospher noise. The Nikon f1.4 lens with a "Hoya 3+" close up lens (a converging lens of 330 mm focal length) to give a total magnification of 0.32 times was found to be the best compromise. The 40 mm phospher was recorded as a 13 mm diameter disc on the film. This camera system had acceptable resolution but with the lens stopped down to f2.8 resolution was further improved, principally by reduction of light scatter around high contrast highlights. The camera was focused photographically by recording a series of negatives each with slightly differing camera focus. Focusing by eye in the viewfinder was too inaccurate, and also with some focusing screens (e.g. Nikon F2 M type, calibrated scale screen) there was an error between film focus and screen focus. Sometimes a different magnification from the 0.32 times quoted above was used, by varying the camera position. IIT photography was considered by Becker (1972) but none of the lenses that he found suitable were still available.

1.2.4 Selection of Film and Developer

With the chosen lens and camera system various film and developer combinations were tested. The camera magnification meant that only films which could record details of at least $\simeq$ 0.02 mm would be suitable. The optimum preflash for each film was determined and

the following film and developer combinations were tested, each with its optimum preflash, but were rejected on the grounds stated:-

Film	Developer	Comment
2475[a]	DK-50[b] or Acuspeed[c]	Excessive background fog and granularity
HP5[d]	Acuspeed	
Tri-X[a]	Acuspeed	
HP5	Aculux[c] or Promicrol[e]	Fine to medium granularity but too few light spots rendered developable
Tri-X	Aculux	

a Eastman Kodak Co. U.S.A.

b Eastman Kodak Co. U.S.A. - Diluted 1 + 1 with water

c Paterson Products Ltd.

d Ilford Ltd.

e May and Baker Ltd.

Kodak, DK-50, HC-110, Tri-X, Promicrol, Acuspeed and Aculux are trademarks.

Unfortunately Kodak 2485 film is not available in small quantities in the U.K. and so could not be tested. Neither could Ilford XP1-400 (Maude, 1980).

The finest granularity (measured on the Joyce Loebl microdensitometer, see appendix 1) and the most visible record of IIT phospher light spots, was obtained with Tri-X developed in HC-110 at a dilution of 1 to 31 parts of water. Development was for the manufacturers standard time plus 50%; this is the maximum forced development recommended by Kodak.

The film was preflashed to a density of 0.15 above base fog. HP5 developed in HC-110 and Tri-X in Promicrol produced almost indistinguishable results from the chosen combination of Tri-X developed in HC-110. Suitable film developer combinations for IIT photography were also considered by Reynolds (1966).

The overall sensitivity of the system was estimated using the following technique which is similar to that used by Waters and Reynolds et al. (1962). A Beta-light† source was placed a known distance from the IIT photocathode with neutral density filters in the light path so that about 50 photons cm^{-2} s^{-1} hit the photocathode. Photographs were taken of the IIT phospher with the IIT gain set at 10^6. The Nikon F2 camera fitted with a f1.4 lens of focal length 50 mm and a +3 Hoya close-up lens as described in section 1.2.3 was used with the chosen film developer combination of Tri-X developed in HC110. The IIT phospher was photographed both with and without the Beta-light illumination. These photographs indicated, by counting developed silver grains, that about 55% of photoelectrons leaving the first photocathode were being detected on the film.

1.3.1 Introduction to the Image Intensifier Tube Spectrograph

This instrument was designed and built for the purpose of recording triboluminescent (TL) spectra††. These spectra are transient and of low intensity so a spectrograph for recording them must have a high optical gain, as well as the ability to record a range of wavelengths simultaneously. These criteria are satisfied by an IIT spectrograph.

---

†A "Beta-light" source (Saunders-Roe Developments Ltd.) glows with an approximately constant light intensity due to tritium decay.

††Throughout this thesis the abbreviation TL will be used for both triboluminescence and triboluminescent, THL for thermoluminescence and thermoluminescent and PL for photoluminescence and photoluminescent. Which is intended should be clear from the context.

In this type of system the photocathode of the IIT is located in the plane that would be occupied by a plate in a conventional spectrograph, and the output phospher of the IIT is photographed to obtain a record of the spectrum. The spectral sensitivity of such a system is usually limited by the spectral response of the IIT, and the spectral resolution is limited by the spatial resolution of the IIT.

The IIT spectrograph is a multichannel recording instrument and as such has two distinct advantages over monochromator or filter, and photomultiplier type spectrometers, which have been used in the past to measure a number of TL spectra, see for example Walton (1977). The advantages are that less energy is absorbed within the system, and that the whole spectral range is recorded at once so that correct relative intensities of transient sources can be easily displayed. The spectrograph was optimally designed for low light level sources, with a high aperture, and has substantially better gain and resolution than other non-astronomical spectrographs. Previous work on IIT spectrographs is described in section 1.3.8.

1.3.2 Preliminary Work

Initially I tried converting a commercial monochromator into an IIT spectrograph. A Czerny-Turner type monochromator (A "Spex- Minimate" imported by Glen Creston) with an optical speed of f4 and with a 1200 lines per mm (1 mm^{-1}) grating blazed at 500 nm, was adapted. Normally the monochromator is used with both input and output slits in position and with a photomultiplier or other non-spatially discriminating detector positioned beyond the output slit. With the input slit still in position but the output slit removed a series of spectral lines (depending on the light source) can be seen in the output focal plane, and their images can be formed on a piece of ground glass placed in that position. The observed spectral

range with 540 nm at the centre of the field of view is about 80 nm, and a resolution of better than 1 nm can be obtained with a 0.25 mm input slit.

The output plane of the monochromator was positioned to correspond with the input photocathode of the IIT. This created some geometrical problems because, with the concave mirror (focal length 300 mm) fitted to the monochromator (see figure 1.10), the focal plane could not be made to coincide with that of the IIT photocathode due to the large ($\simeq$ 70 mm) distance between the end wall of the IIT case and the photocathode. An additional concave lens was mounted into the monochromator, on a moveable base, to take the focal plane the necessary extra distance away from the monochromator. Focusing adjustment was obtained by changing the position of this lens. An example of the performance of this instrument, with the converted monochromator connected to the IIT, is given in figure 1.11. The IIT gain is set at 10^6 and part of the spectrum of a krypton test lamp can be seen.

I found that only the brightest TL spectra could be recorded on this instrument. A densitometer trace of the TL spectrum of crushed terbium doped fluorite is shown in figure 1.12. The apparatus used for generating TL is discussed fully in chapter 3.

Overall the adapted monochromator spectrograph had a resolution of about 1 nm. There were two main difficulties associated with the instrument.

a) With available gratings the whole visible spectrum of 400 to 750 nm could not be simultaneously dispersed across the IIT photocathode.

b) It had a low aperture (f4), and the TL spectrum mentioned above

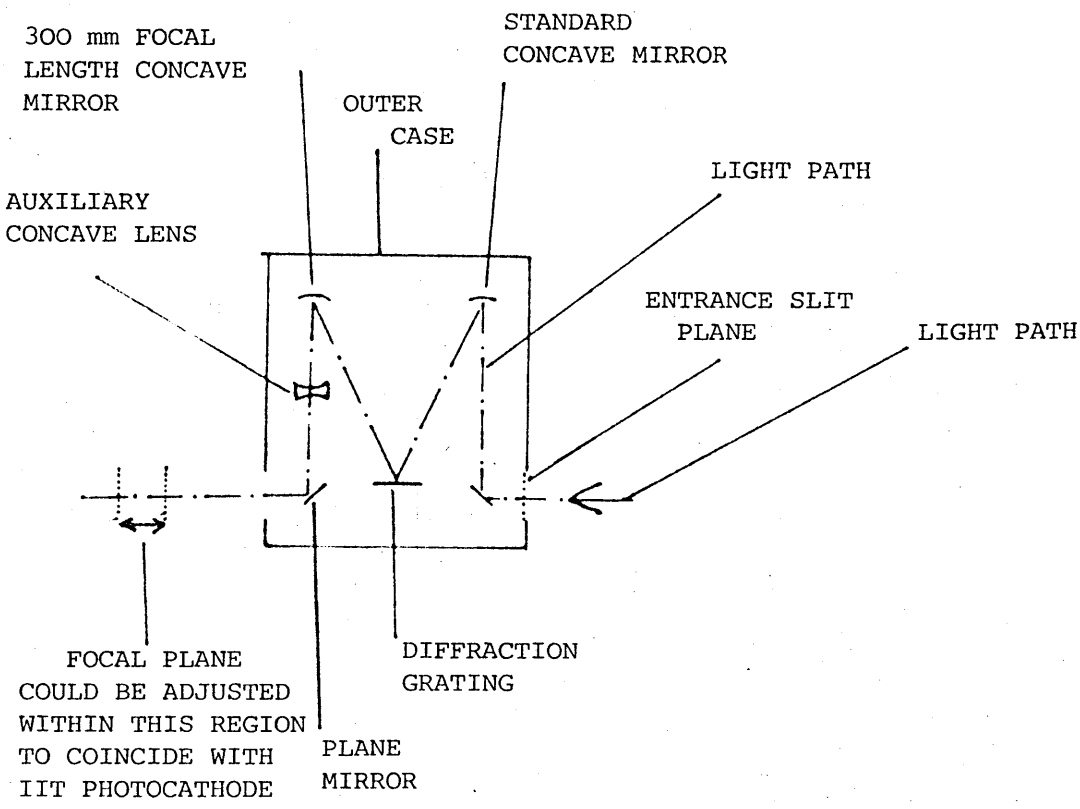

FIGURE 1.10 THE "SPEX MINIMATE" MONOCHROMATOR

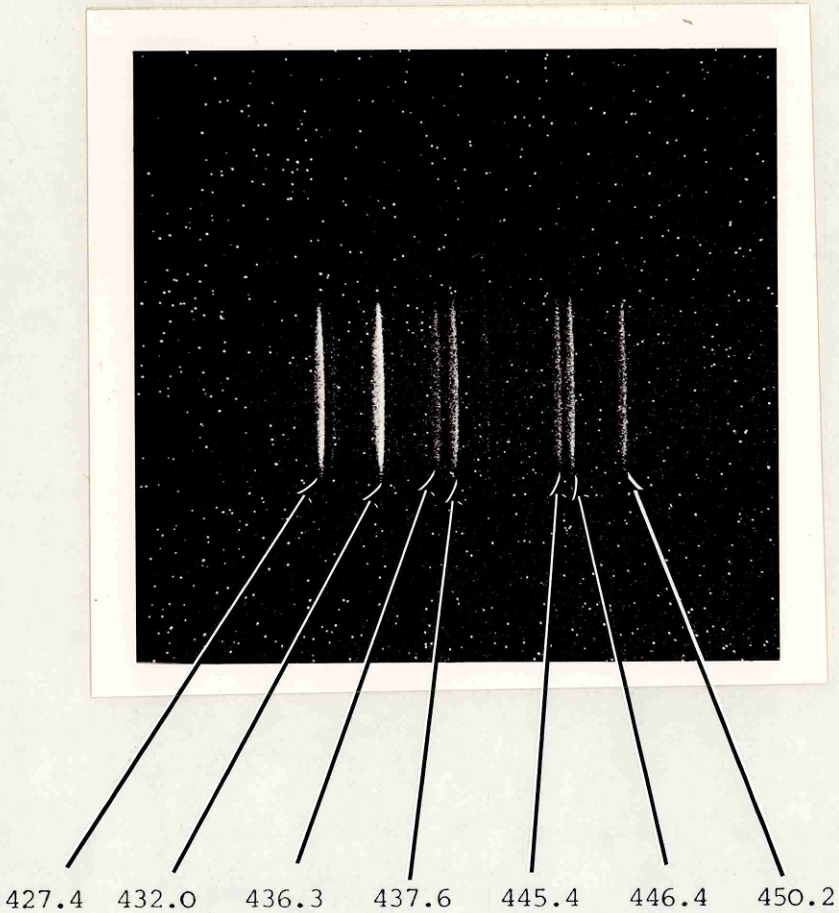

FIGURE 1.11 PART OF THE KRYPTON SPECTRUM RECORDED ON THE "SPEX MINIMATE" SPECTROGRAPH

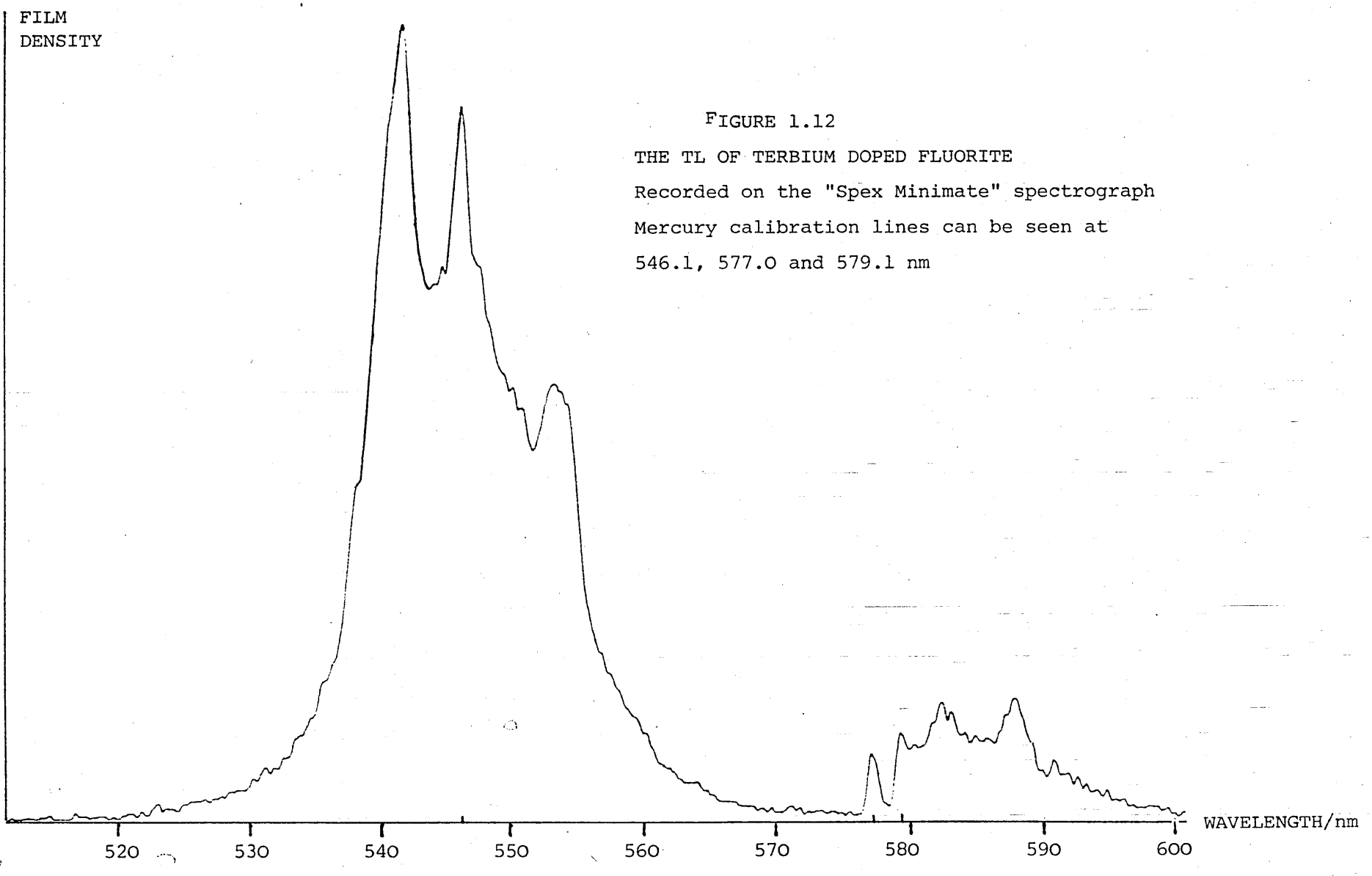

FIGURE 1.12

THE TL OF TERBIUM DOPED FLUORITE

Recorded on the "Spex Minimate" spectrograph

Mercury calibration lines can be seen at

546.1, 577.0 and 579.1 nm

was the only one that could be recorded.

It was to overcome these problems that a specially designed spectrograph was built.

1.3.3 Optimum Design of the Image Intensifier Tube Spectrograph

The basis of the instrument is shown in figure 1.13. In the usual way light is first collimated by lens C, dispersed by grating G and then brought to a focus on the photocathode by telescope lens T. Due to the spectral response of the IIT a spectrograph wavelength range of about 400 to 750 nm was required. These limits correspond respectively to the cut off wavelength of the standard zinc crown window at the input end of the IIT, and to the wavelength at which the quantum efficiency of the photocathode drops to less than 1%. It was decided that the instrument should have two gratings, one to disperse the range 400 to 750 nm over the whole photocathode, and one to disperse this range in three sections with a corresponding increase in overall resolution. Requirements following directly from these, and other subsidiary requirements which were considered in the design of the IIT spectrograph are now listed:-

a) With each diffraction grating the correct spectral range (400 to 750 nm with one grating and with the other grating 400 to 520, 520 to 630 and 630 to 750 nm) should be projected onto the IIT photocathode by an appropriate rotation of the grating. The full photocathode diameter should be utilised, and the spectral lines should be as bright as possible.

b) Any limit on resolution (e.g. grating spacing or telescope lens resolution) should always be less than the limit imposed by the IIT spatial resolution.

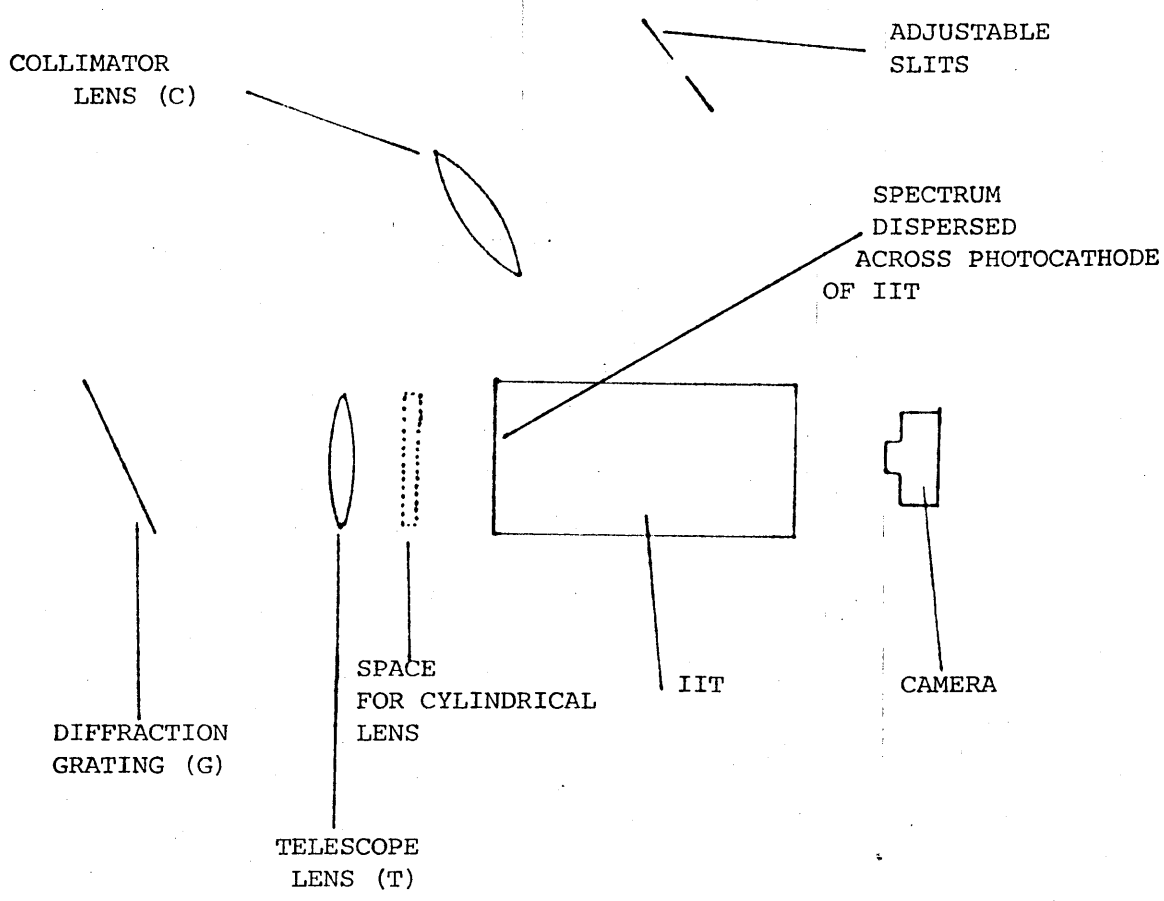

FIGURE 1.13 ARRANGEMENT OF COMPONENTS IN THE IIT SPECTROGRAPH (not to scale). See the photographs in Figures 1.19 and 1.20

c) Blazed gratings should be used at the optimum angles for maximum efficiency.

d) The telescope lens should be as nearly normal to the grating as possible, to give approximately linear dispersion.

e) Any vignetting which may occur for certain wavelength ranges should be reduced to a minimum.

f) The facility for inserting a cylindrical lens to reduce spectral line height but increase energy per unit area (Glazunov, 1963) should be included.

g) The spectrograph had to be designed so that it could be filled with light using an appropriate condenser lens or fibre optic system

h) On changing diffraction gratings their position must be reproducible, and it should be possible to mount both gratings in the same position, since this greatly facilitates construction and means that the collimator and telescope lenses can be in fixed positions.

i) The telescope lens if so required by its focal length must be physically small enough to fit into the end of the IIT case (diameter 80 mm).

j) All angles and distances must conform to the physical limitations of the IIT and its housing size.

Inevitably some of the requirements were mutually exclusive and a compromise between the various criteria had to be reached. That the spectral lines should be as bright as possible, requires a consideration of how the energy per unit area in a spectral line varies with parameters internal and external to the spectrograph. I will first consider internal parameters on the assumption that non-overlapping line spectra are being observed. It is assumed in the

analysis which follows that the whole area of the collimator is filled with light and that the slit is fully and uniformly illuminated with an image of brightness B. Brightness is optical energy per second per unit area per unit solid angle from a source. The energy per second passing down the spectrograph shown in figure 1.14 is E where

$$E = \frac{BAa_1}{f_1^2} \qquad 5$$

Neglecting losses, the energy per second per unit area in the image is given by

$$\frac{E}{a_2} = \frac{BAa_1}{f_1^2 a_2} \qquad 6$$

By geometric optics

$$\frac{a_2}{a_1} = \frac{f_2^2}{f_1^2} \qquad 7$$

The energy per unit area per second in the image is thus given by

$$\frac{BA}{f_2^2} \qquad 8$$

The energy per unit area per second in the image is thus proportional to the area of the collimator divided by the telescope focal length squared. If the telescope diameter is equal to the collimator diameter then the energy per unit area per second in the image is proportional to the inverse of the square of the f number of the telescope lens. The IIT spectrograph was thus designed with as small a telescope lens f number as possible, within the limiting condition that the telescope in conjunction with the diffraction grating must give the required linear dispersion at the photocathode. Since lenses with short focal lengths are generally available with smaller f numbers than long focal length lenses it was necessary to operate

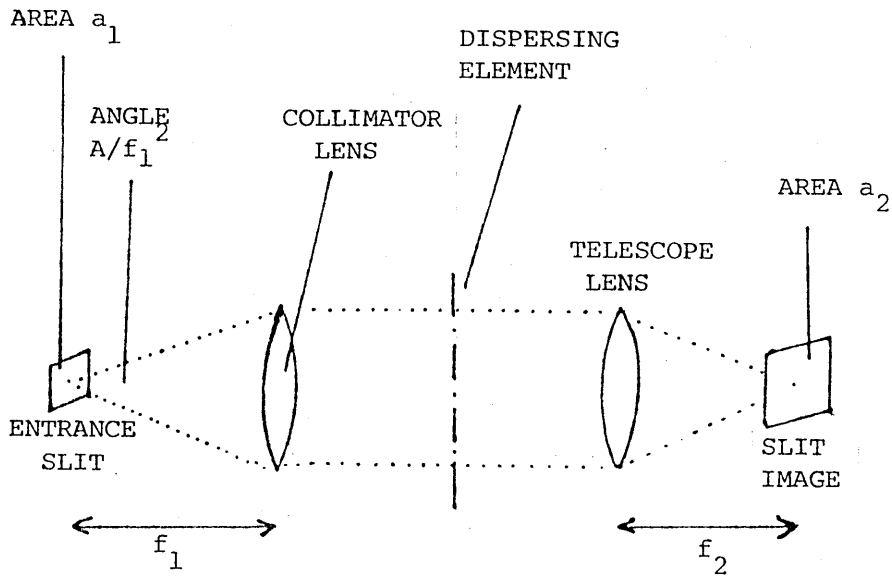

FIGURE 1.14 SPECTROGRAPH OPTICS USED IN CALCULATION OF SPECTRAL LINE BRIGHTNESS

with as short a focal length as possible so that bright spectral lines would be obtained. A short telescope lens focal length meant using a grating with as high an angular dispersion as possible to enable the required linear dispersion to be achieved. An 1800 l mm^{-1} grating (the closest ruled grating that I could obtain) has an approximate angular dispersion of 1800 microradians per nanometre, and with a 135 mm focal length lens gives a linear dispersion of about 4 nm mm^{-1}. To spread 400 to 750 nm into three regions over the 40 mm photocathode requires a linear dispersion of about 3 nm mm^{-1}. The 4 nm mm^{-1} provided by the 135 mm focal length telescope lens and 1800 lmm^{-1} grating combination can be made to approach 3 nm mm^{-1} by operating away from normal grating incidence.

The best compromise was thought to be a 1800 l mm^{-1} grating blazed at 500 nm, with a 135 mm focal length f2 telescope lens†. This combination would disperse the whole spectral range onto the photocathode in three overlapping regions by rotation of the grating. A 600 l mm^{-1} grating blazed at 500 nm was chosen to disperse the whole spectral range simultaneously across the photocathode in combination with the 135 mm focal length telescope lens. The modulation transfer function (MTF) of the telescope lens was chosen to be compatible with the IIT spatial MTF. A 600 mm focal length f8 telephoto lens (Vivitar) was used as the collimator.

In arriving at equation 8 (above) for the energy per second per unit area in a spectral line it was assumed that the collimator was completely filled by light coming from the slits and that the whole area of the slits was filled with light. The condenser lens system must be designed to realize both these criteria. Once the slits

---

†Footnote, manufactured by Soligor and with ferrous iris blades removed to avoid distorting the IIT magnetic focusing.

and collimator are both filled with light from a given source no further increase in the energy per unit area in the image is possible.

Below I will consider how to maximize the sample volume, that is the region from which light is directed by a condenser lens, into the spectrograph. With a large sample volume the positioning of TL fracturing equipment (described in chapter 3) is facilitated. I initially decided to design for a condenser lens input optics system, although an appropriately sized fibre optic light guide would be used on occasions to transmit light to the spectrograph slits.

Nielsen (1930 and 1947) has discussed the problem of how best to fill a spectrograph with light. Firstly he considered a uniform light emitting volume as shown in figure 1.15 of height 2h, length ℓ and width 2g with a condenser lens of focal length F and diameter 2D placed a distance z from the slits. The slits were of height 2s, the collimator was of diameter 2b, and its focal length was f. The source to condenser lens distance was u and the distance from condenser lens to the slits was z. The telescope focal length was f_1 the height of the slit image was $2s_1$. By purely geometrical optics, ignoring diffraction, he derived a number of relations between these quantities for maximizing the useful source volume. One practical limiting factor in any chosen system was the availability of a particular focal length and diameter combination for the condenser and collimator lenses. To maximize the source volume the following conditions were found, with the assumption that $2h < 2s$;

$$F = \frac{hf}{b - s} \qquad \text{I}$$

$$z = \frac{(h+s)f}{b - s} \qquad \text{II}$$

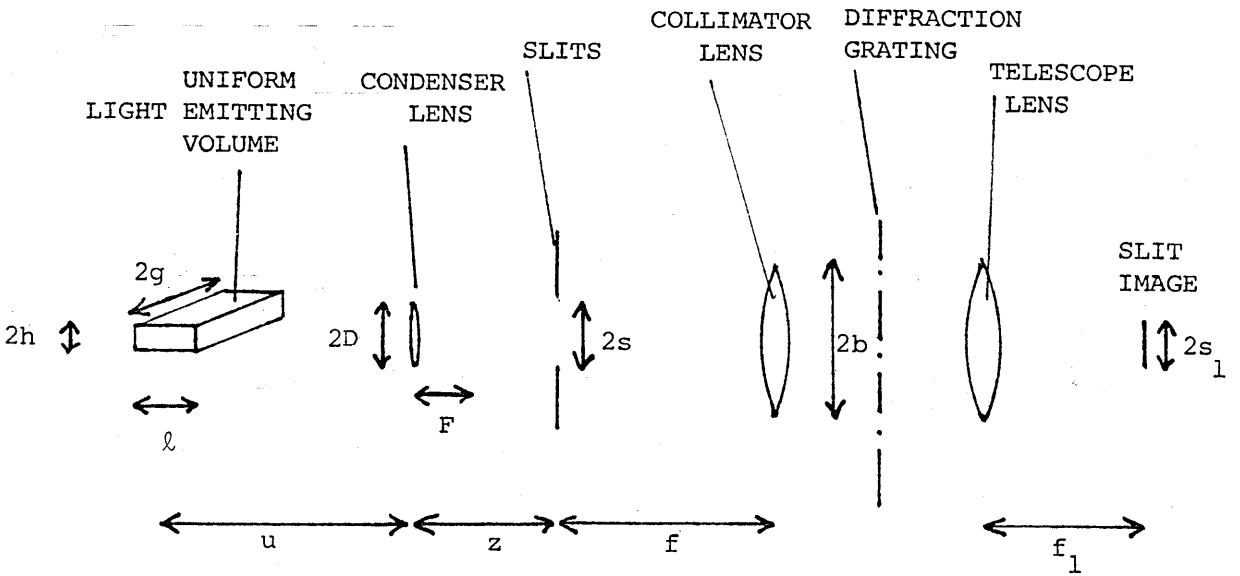

FIGURE 1.15 THE IIT SPECTROGRAPH AND CONDENSER LENS SYSTEM

$$\frac{2s}{2s_1} = \frac{f}{f_1} \qquad \text{III}$$

$$\frac{2D}{z} > \frac{2b}{f} \qquad \text{IV}$$

"I" and "II" lead to a maximum source length of

$$\ell = \frac{h^2 f}{bs} \qquad \text{V}$$

$$\frac{1}{F} = \frac{1}{u} + \frac{1}{z} \qquad \text{VI}$$

Other requirements and those that have been previously mentioned are;

$f + z + u < 2$ metres — VII

Collimator diameter should not be less than telescope diameter — VIII

Telescope f number should be as small as possible — IX

f_1 must be large enough to give the required linear dispersion in conjunction with the grating — X

Making use of these criteria and, for example, adopting h = 1 mm

with

$f_1 = 135$ mm

$2b = 45$ mm

$f = 600$ mm

$F = 34$ mm

$2D = 20$ mm

leads to

$s = 4.9$ mm

$z = 199$ mm

$s_1 = 1$ mm

$\ell = 5.5$ mm

This arrangement agrees with all the spectrograph criteria except that the whole area of the collimator is not filled with light. With the 600 mm f8 collimator lens 2b can be 75 mm, although the telescope lens reduces this to 67 mm diameter, whereas above 2b = 45 mm. The arrangement which I adopted, and which was used with the IIT spectrograph, is given below.

$f_1 = 135$ mm

$2b = 67$ mm

$f = 600$ mm

$F = 140$ mm

$2D = 95$ mm

$2h = 12.8$ mm

leading to

$s = 10$ mm

$z = 418$ mm

$s_1 = 2.2$ mm

$\ell = 73$ mm

The arrangement was realised with commercially available lenses. A 95 mm diameter, 140 mm focal length photographic enlarger condenser lens was used.

1.3.4 Geometry of the Spectrograph

In the previous section I explained the reasons for my choice of condenser lens, diffraction grating, collimator lens and telescope lens. In this section I discuss the spatial arrangement within the spectrograph of these optical components, and in particular the positioning of the diffraction gratings. The design was developed bearing in mind the criteria listed in the previous section, and in particular the spectral ranges required and the blaze of the gratings. Blazed gratings are discussed in appendix 2.

Since the wavelengths projected onto the photocathode are required to vary with rotation of the grating it was found useful to express the diffraction grating equation in an unfamiliar form so that the wavelength positioned at the centre of the photocathode for any grating rotation could be easily found. From figure 1.16 the grating equation can be expressed as

$$\sin (i + \theta_T) - \sin(r - \theta_T) = \frac{n\lambda}{d} \qquad 9$$

where angles as shown in the figure are positive. With the IIT positioned relative to the grating such that $r = 0^o$ for the wavelength that will have a spectral line in the centre of the IIT photocathode, and with $i = 45^o$, equation 9 reduces to

$$\sin (45 + \theta_T) + \sin \theta_T = \frac{n\lambda_c}{d} \qquad 10$$

where λ_c, which is the wavelength at the photocathode centre, varies with grating rotation (θ_T).

After a particular grating position had been found, with the help of equation 10, it was important to check for vignetting. This was done using scale diagrams and led to the arrangement shown in figure

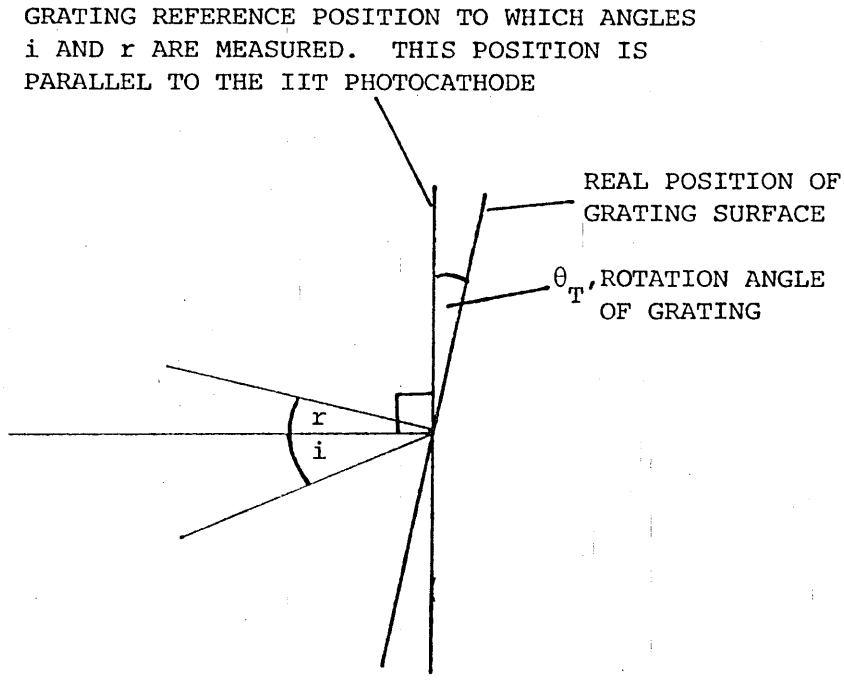

FIGURE 1.16 GRATING ORIENTATION WITH RESPECT TO "REFERENCE POSITION"

1.17 for the 600 l mm^{-1} grating. The IIT spectral response acted as a filter removing problems of diffracted second orders occurring. I found that the 1800 l mm^{-1} grating could be used in two orientations, either alignment A or alignment B of figure 1.18. Zero order is on opposite sides of the telescope lens for each alignment so to utilize the blazing, the grating needed to be inverted (top and bottom) when changing alignments. Alignment A had the advantages of the range 400-750 nm being covered in three regions as originally required, and of almost linear dispersion. Alignment B covers the range 400-750 nm in eight regions by grating rotation, and collects the whole width of the collimator beam. All my measurements with the 1800 l mm^{-1} grating used alignment B because it gave brighter spectral lines. Although higher than originally required the dispersion was found useful in the measurement of TL line spectra.

The theoretical resolution for the IIT spectrograph system, assuming an IIT resolution of only 15 lines per mm, and no loss of resolution in the camera, is 0.75 nm with the 600 l mm^{-1} grating, and 0.1 nm with the 1800 l mm^{-1} grating.

1.3.5 Construction and Testing of the Spectrograph

The spectrograph was constructed in a light tight aluminium box (figure 1.19) which bolted onto the photocathode end of the IIT (figure 1.20). The gratings were mounted on the rotatable table with aluminium brackets using "Bostick-2" rubber solution. By means of screws the exact position and angle of the grating could be adjusted. Micrometer slits of length 20 mm, whose width could be adjusted up to 5 mm by means of a micrometer, were fixed in the focal plane of the collimator using an adapted camera lens mounting ring. Light tight doors were fitted to the aluminium spectrometer box to

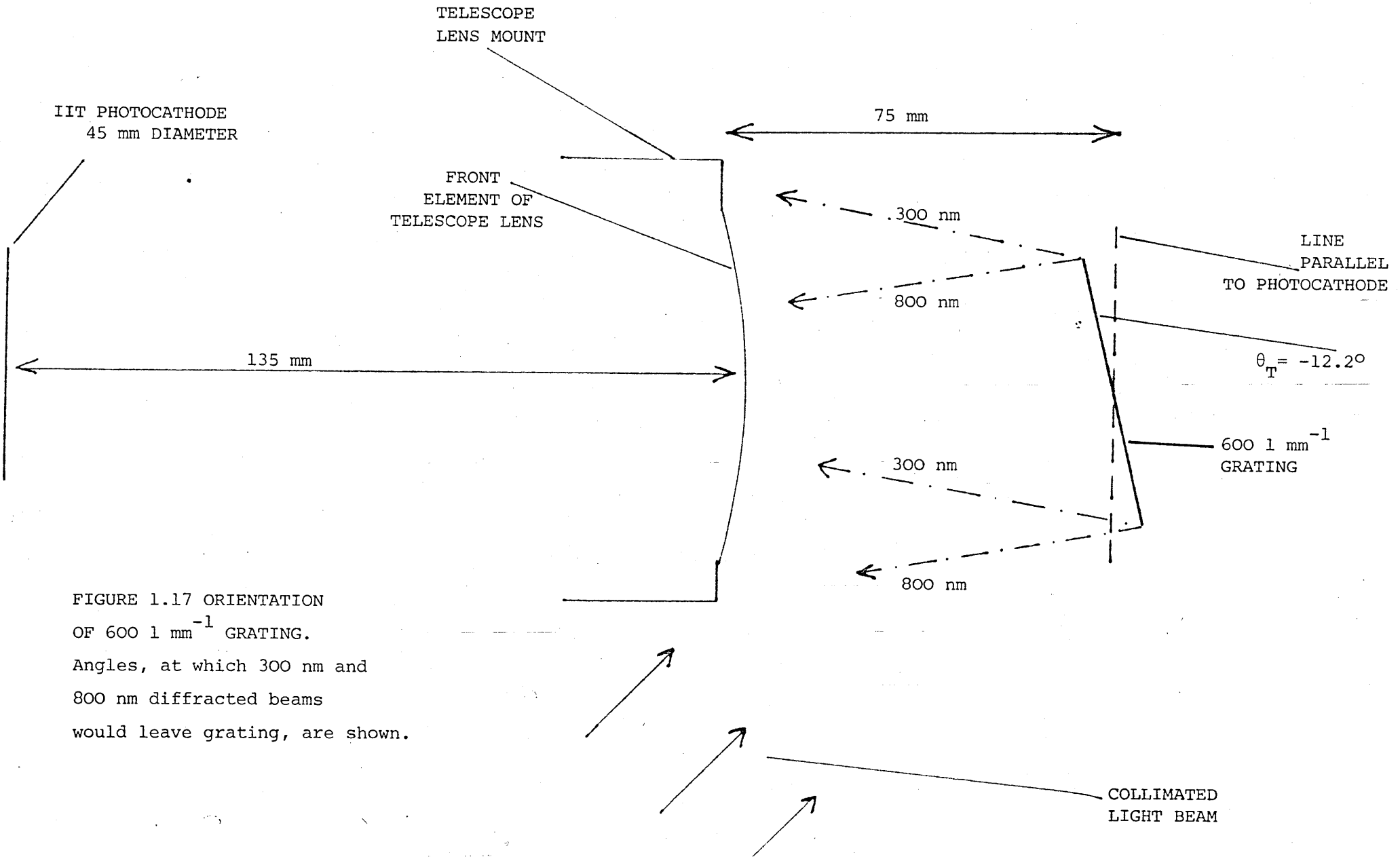

FIGURE 1.17 ORIENTATION OF 600 l mm^{-1} GRATING. Angles, at which 300 nm and 800 nm diffracted beams would leave grating, are shown.

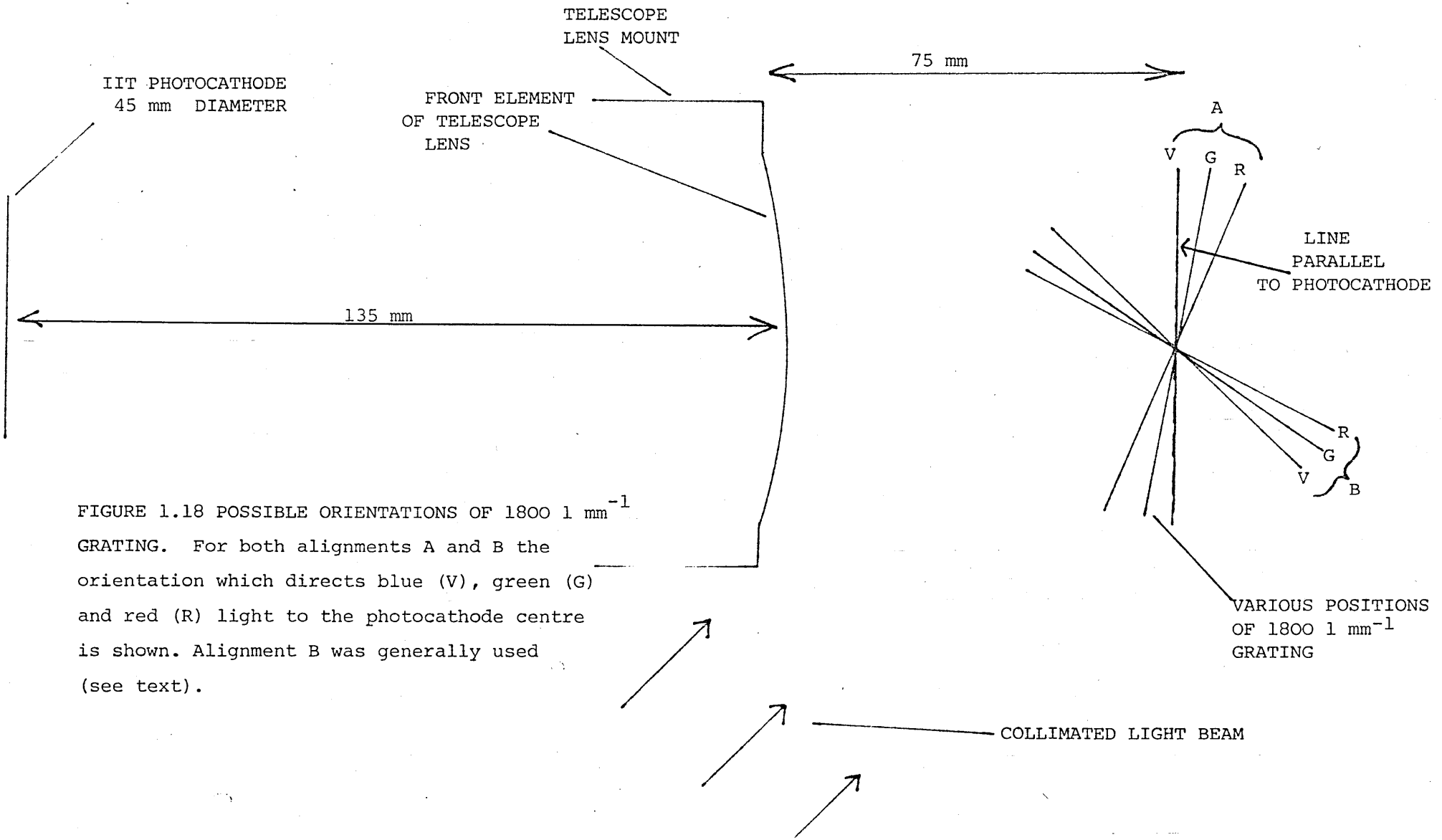

FIGURE 1.18 POSSIBLE ORIENTATIONS OF 1800 l mm^{-1} GRATING. For both alignments A and B the orientation which directs blue (V), green (G) and red (R) light to the photocathode centre is shown. Alignment B was generally used (see text).

TELESCOPE LENS
135 mm FOCAL LENGTH
f2 APERTURE

600 l mm^{-1} or 1800 l mm^{-1}
DIFFRACTION GRATING

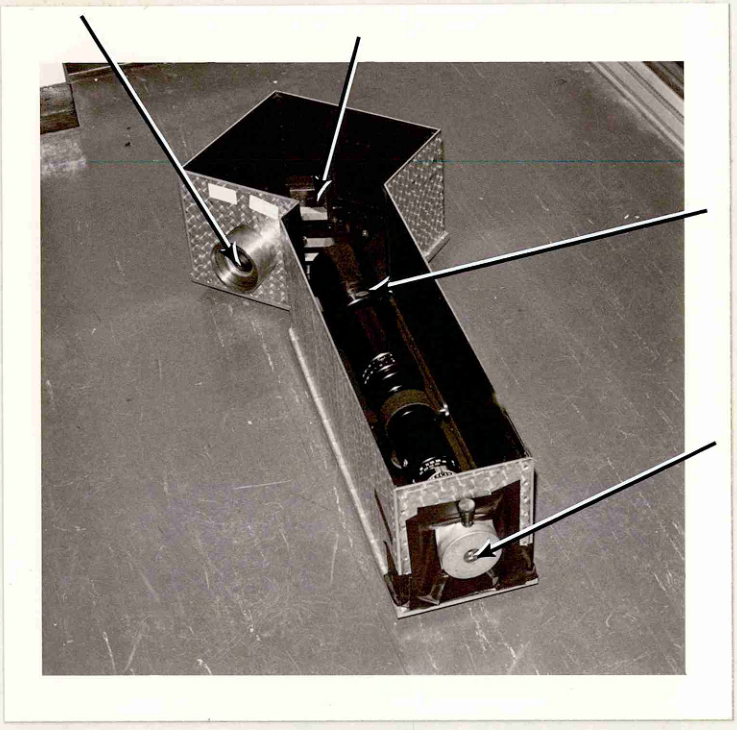

COLLIMATOR LENS
600 mm FOCAL
LENGTH, f8
APERTURE

SLITS
20 mm IN LENGTH

FIGURE 1.19 THE IIT SPECTROGRAPH WITH THE IIT REMOVED.
Spectrograph lid taken away.

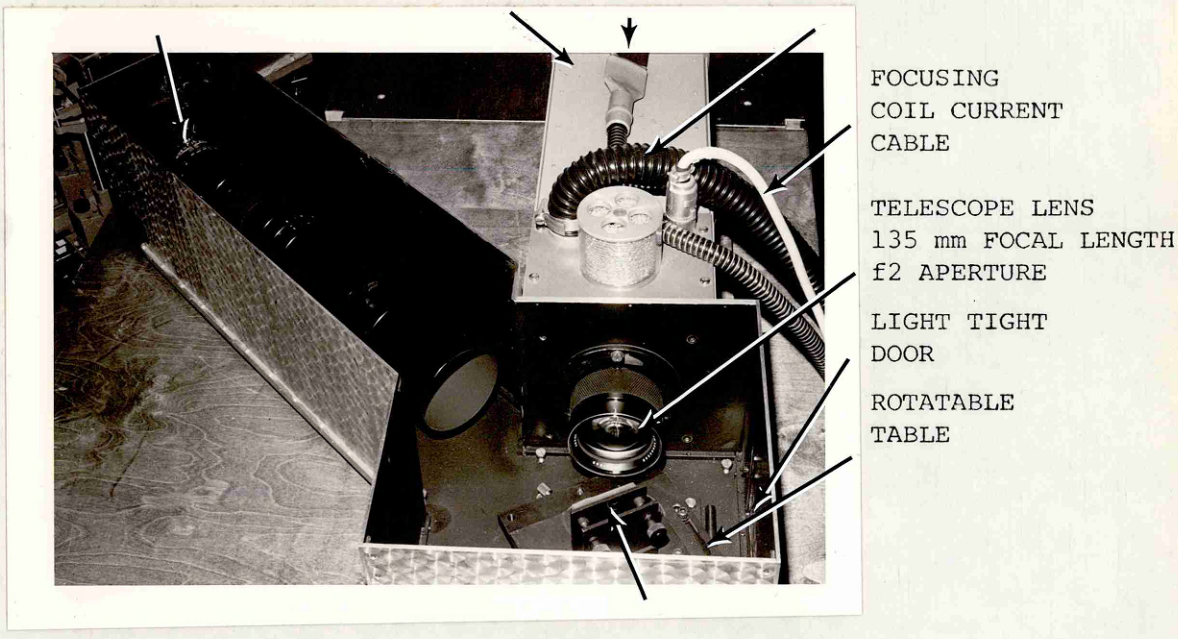

FIGURE 1.20 THE IIT SPECTROGRAPH

Spectrograph lid removed

enable the collimator and telescope lenses to be adjusted, and to enable the grating to be rotated. The condenser lens system was located on an optical bench (Ealing Beck Ltd.).

Before it was attached to the IIT the spectrograph was tested, with a ground glass screen placed in the position that would be occupied by the IIT photocathode. The ground glass screen was observed with a microscope. There was no noticeable vignetting within the required spectral range. With mercury, neon and krypton spectral lamps the spectrograph resolution was checked across the whole spectrum, with both gratings. The spectrograph resolution was always much greater than the IIT spatial resolution. For example with the 600 l mm^{-1} grating and suitably adjusted slits the neon lines at 534.11 and 534.33 nm could be clearly distinguished on the ground glass screen. They were spaced by about 0.025 mm, and could not be distinguished on the IIT when the IIT spectrograph was used.
In normal use the spectrograph slits were set to about 0.29 mm so that resolution was just limited by the IIT, rather than by slit width.

To check the efficiency of the condenser system a photomultiplier was placed in the spectrograph telescope lens focal plane so that the spectrograph output intensity could be measured. The photomultiplier current was monitored with an electrometer (Keighley model 602). The 600 l mm^{-1} grating zero order was centred on the photomultiplier and a small constant light source (a "Beta-light") was positioned at various points inside the sample volume. The "Beta-light" was masked except for a 1 mm diameter light emitting hole. No "blind spots" were found in the sample volume, which was calculated (see above) as 12.8 x 13 x 73 mm^3. I found that when the "Beta-light" was anywhere

in the calculated sample volume the photomultiplier output was always greater than 60% of its maximum value. The maximum photomultiplier output occurred when the "Beta-light" was approximately centrally placed within the calculated sample volume.

A similar test was conducted for the fibre optic light guide. This showed that the source should be as close to the light guide as possible and within a $\simeq 20^{o}$ half-angle cone, whose apex is at the end of the light guide.

After these tests the spectrograph was bolted to the end of the IIT and the whole was rigidly fixed to the IIT table. The camera box was attached to the output end of the IIT and the condenser system was aligned with the spectrograph. The condenser system was on a separate table to the spectrograph to avoid vibration transmission from crystal crushers, but this did mean that from time to time the alignment had to be rechecked. Provision was also made for securely clamping the fibre optic light guide in the position of the collimator focal plane.

After all the components were securely mounted the whole system required focusing and fine adjustments to the alignment. Coarse focusing was carried out by eye but fine focusing was performed photographically. Firstly the camera focus was set exactly by photography of IIT phospher noise spots; this also provided a check on the IIT focus. The collimator was then focused to give parallel light by placing a pin in the approximate position of its focal plane, and a mirror at the front of the lens. The reflected image of the pin was observed from behind the lens. The object pin was moved along the lens axis until a position of no parallax between the pin and its image was found. The pin was then in the focal plane

of the lens, and by careful measurement the slits were placed in this position. The correctly focused collimator then remained fixed while a series of photographs were made of spectral lines dispersed by the whole IIT spectrograph system, as the telescope lens focus was adjusted. For the purpose of this alignment the slits (0.29 mm width) were uniformly illuminated with a mercury lamp. This procedure completed the focusing of the IIT spectrograph.

1.3.6 Spectral Calibration

It was necessary to include a spectral calibration exposure on every experimental data negative so that wavelengths could be accurately determined. If a condenser system was in use the calibration lamp was made to illuminate the slits via a semisilvered mirror which was placed in the light path (but removed for TL exposures). If a fibre optic light guide was in use the calibration lamp (reduced in intensity by suitable neutral density filters) was positioned in front of the light guide. A typical mercury calibration spectrum, taken with the light guide and 600 l mm^{-1} grating, is shown in figure 1.21. A densitometered record of this negative is shown in figure 1.22, and the record of a calibration spectrum taken with the 1800 l mm^{-1} grating is shown in figure 1.23. In practise, after photography and densitometry, the resolution obtainable with the 1800 l mm^{-1} grating is about 0.2 nm, and with the 600 l mm^{-1} grating about 1 nm. Computer polynomial fits were made to the calibration wavelengths obtained from these and other negatives. The polynomial

$$\lambda = ax + bx^2 + cx^3 + dx^4 + e$$

was used where λ is wavelength, x is position on the negative as read by the densitometer and a,b,c,d and e are constants. The polynomial enabled all calibration wavelengths in the range 400 to 750 nm to be fitted within better than 1nm (600 l mm^{-1} grating) or

435.8 nm 546.1 nm

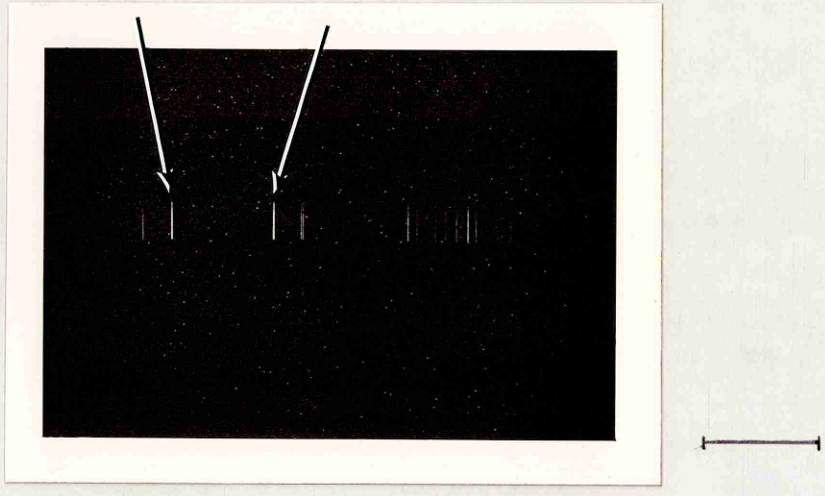

FIGURE 1.21 MERCURY CALIBRATION SPECTRUM
RECORDED ON THE IIT SPECTROGRAPH
Some argon lines are also visible. Scale bar equals 10 mm.

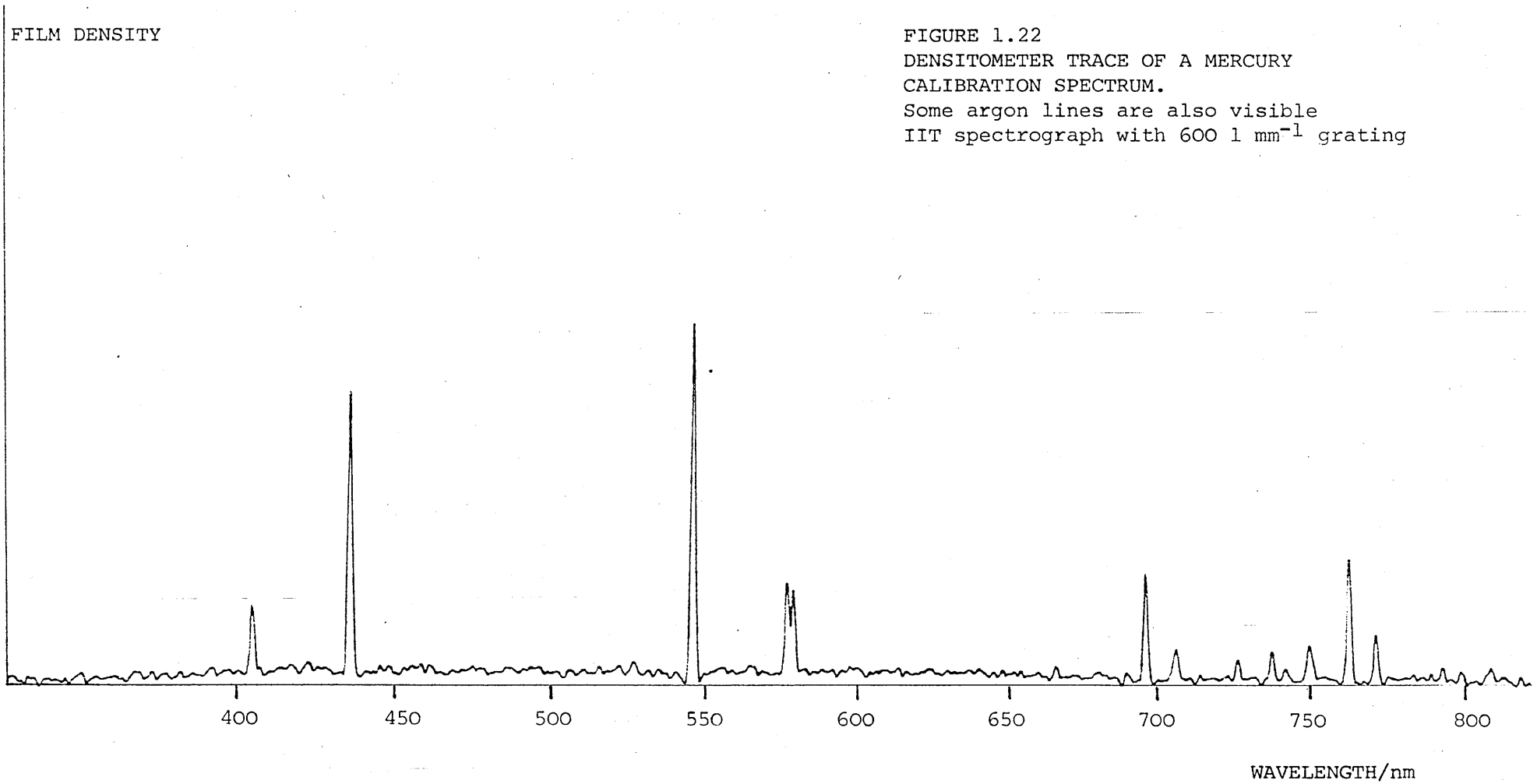

FIGURE 1.22
DENSITOMETER TRACE OF A MERCURY CALIBRATION SPECTRUM.
Some argon lines are also visible
IIT spectrograph with 600 l mm^{-1} grating

FIGURE 1.23

DENSITOMETER TRACE
OF A MERCURY CALIBRATION SPECTRUM
IIT spectrograph with 1800 l mm^{-1} grating

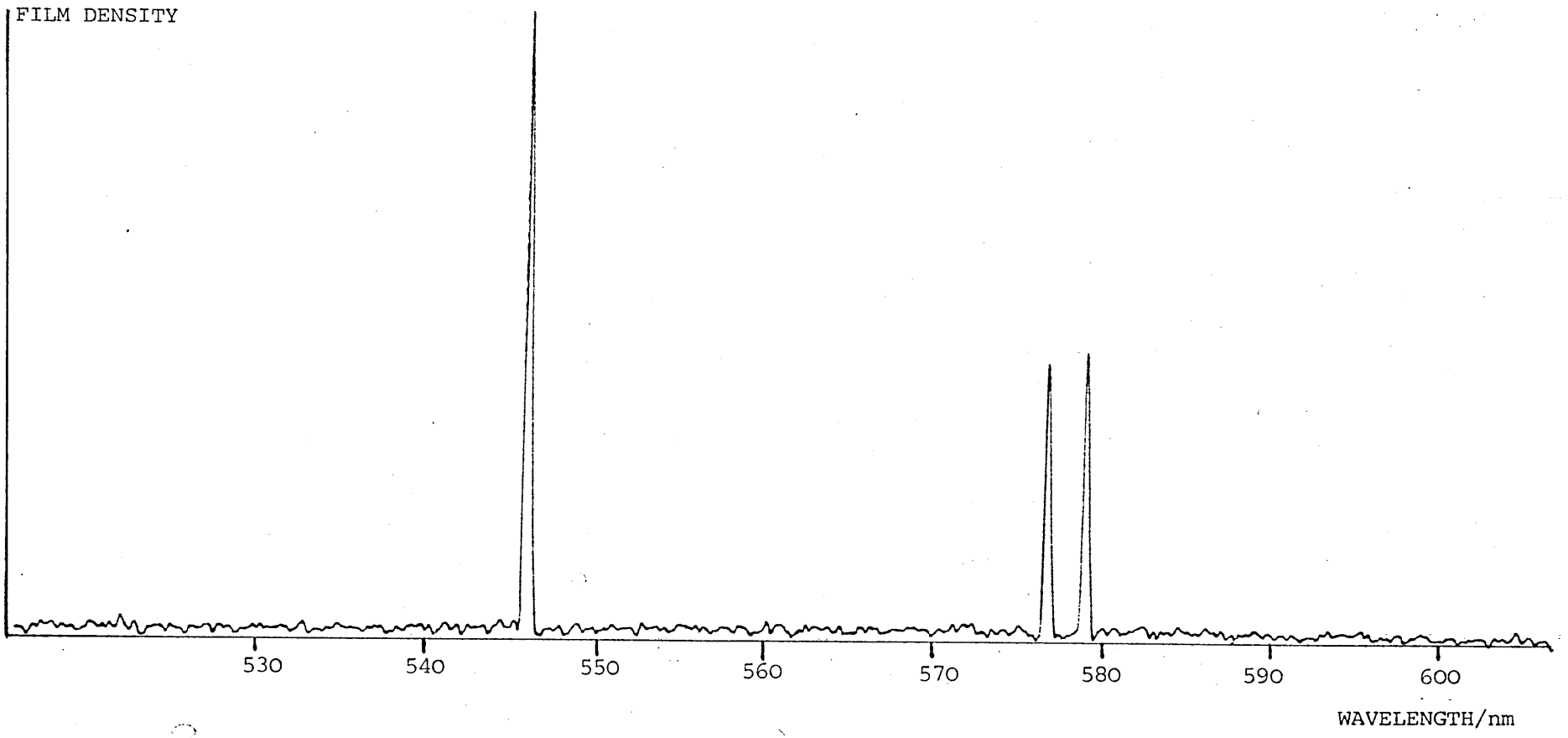

0.2 nm (1800 l mm^{-1} grating). A typical example is given in table 1.2 where the predicted wavelengths from such a polynomial fit (600 l mm^{-1} grating) are compared with the calibration wavelengths of each line. This particular calibration extended about 70 nm beyond the nominal 750 nm near infra-red cut off. The appropriate polynomial was computed for every data negative and was used to apply a wavelength scale to the recorded data. Calibration lines were normally put across only half of the data on a negative so that they would not obscure experimental results. Sometimes calibration lines were put across the whole negative in which case the experiment would be repeated without calibration lines, to check that no data had been obscured.

1.3.7 Intensity Calibration

In addition to the wavelength calibration some experimental data films included standard lamp (see appendix 3) exposures for the purpose of intensity calibration. These exposures were made for each grating position and every arrangement of spectrograph input optics. The intensity calibration relates film density at each position on a negative, and hence in each small wavelength range, to the light intensity entering the spectrograph slits within that wavelength range. An intensity calibration is necessary when (as in chapter 4) the shape and peak wavelength of a broad continuous spectrum are of importance. An intensity calibration does not affect the peak position of narrow spectral lines so the line TL spectra of chapter 3 were not intensity corrected. It should be noted that almost all the TL spectra presented in the literature (see chapter 2) are not intensity corrected.

The IIT spectrograph system's output is in the form of a densitometer record such as figure 3.12 in which film density versus wavelength

Calibration Wavelength Nanometres	Wavelength from polynomical fit Nanometres
404.7	404.47
435.8	436.20
546.1	546.05
577.0	576.64
579.1	579.08
696.5	696.90
706.7	706.99
727.2	727.15
738.4	738.52
751.5	751.37
763.5	763.34
772.4	772.21
794.8	794.53
801.5	801.47
811.5	811.47
826.4	826.72

TABLE 1.2 A Polynomical Fit to Calibration Wavelengths, with the IIT Spectrograph and 600 l mm^{-1} grating.

is recorded for a particular spectrum. The density within a small area of the film, say the area occupied by one spectral line, is related to the exposure received within that area of film by the Hurter-Driffield (H-D) curve. Exposure is often measured in Joules per square metre or in metre-candle-seconds. The H-D curve is a plot of film density against the logarithm of film exposure and is sometimes called a "D : log E" curve. Standard H-D curves at low light levels relate to ambient light exposures where single silver halide grains in the film are struck by individual photons and not as here, by sudden bursts of hundreds of photons from the IIT phospher. It was therefore necessary to measure the H-D curves through the IIT. Most of my spectra were taken with exposures of 10 to 30s and so an H-D curve was used which was measured under these conditions, through the IIT camera system, with the IIT at 33 kV EHT, a gain of $\simeq 10^6$. See figure 1.24. Application of the appropriate H-D curve to a densitometered spectrum enables a graph of the logarithm of exposure at the film surface to be plotted against wavelength for a particular spectrum. This is shown as step A of figure 1.25.

A correction curve obtained with a standard lamp is the ratio of light intensity at the slits (or end of the light guide), to the logarithm of exposure at the film surface; plotted against wavelength for a given exposure time. The correction curve is multiplied by the plot of logarithm of exposure at the film surface against wavelength (step B of figure 1.25) to give a graph of light intensity at the slits against wavelength, which of course is the corrected spectrum.

The standard lamp correction curve is obtained by recording the

FIGURE 1.24 THE H-D CURVE OF TRI-X DEVELOPED IN HC-110

The IIT was set at 33 kV and the preflashed film was developed at 20°C for the Kodak recommended time plus 50%. The IIT photocathode was uniformly illuminated with a "Beta-light" placed about one metre from the photocathode. Exposure was varied by placing different neutral density filters in the light path between Beta-light and photocathode. Exposure time was 20 seconds.

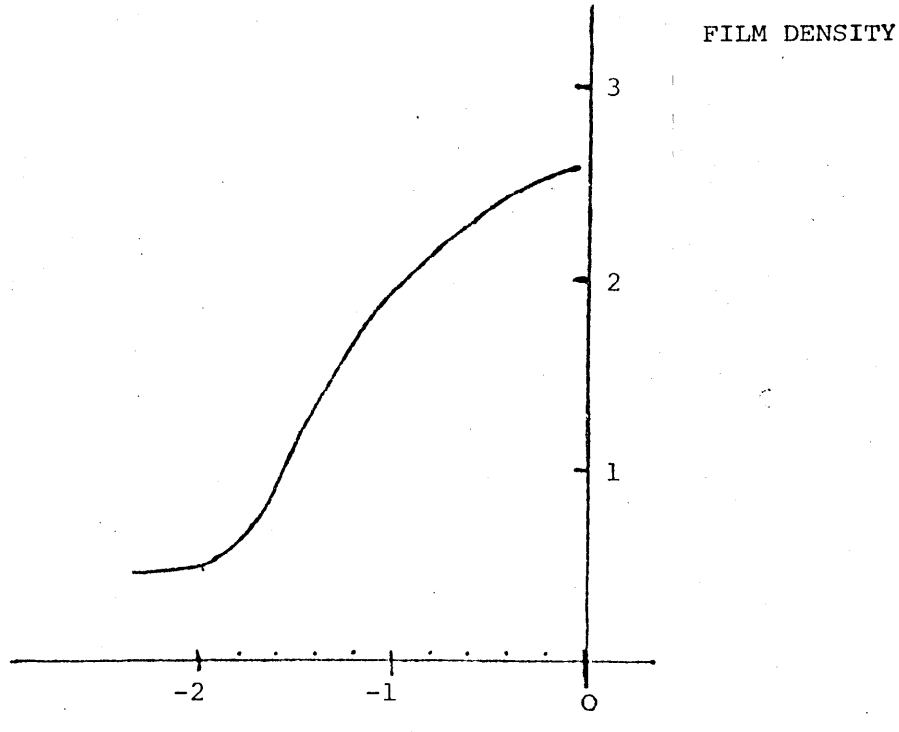

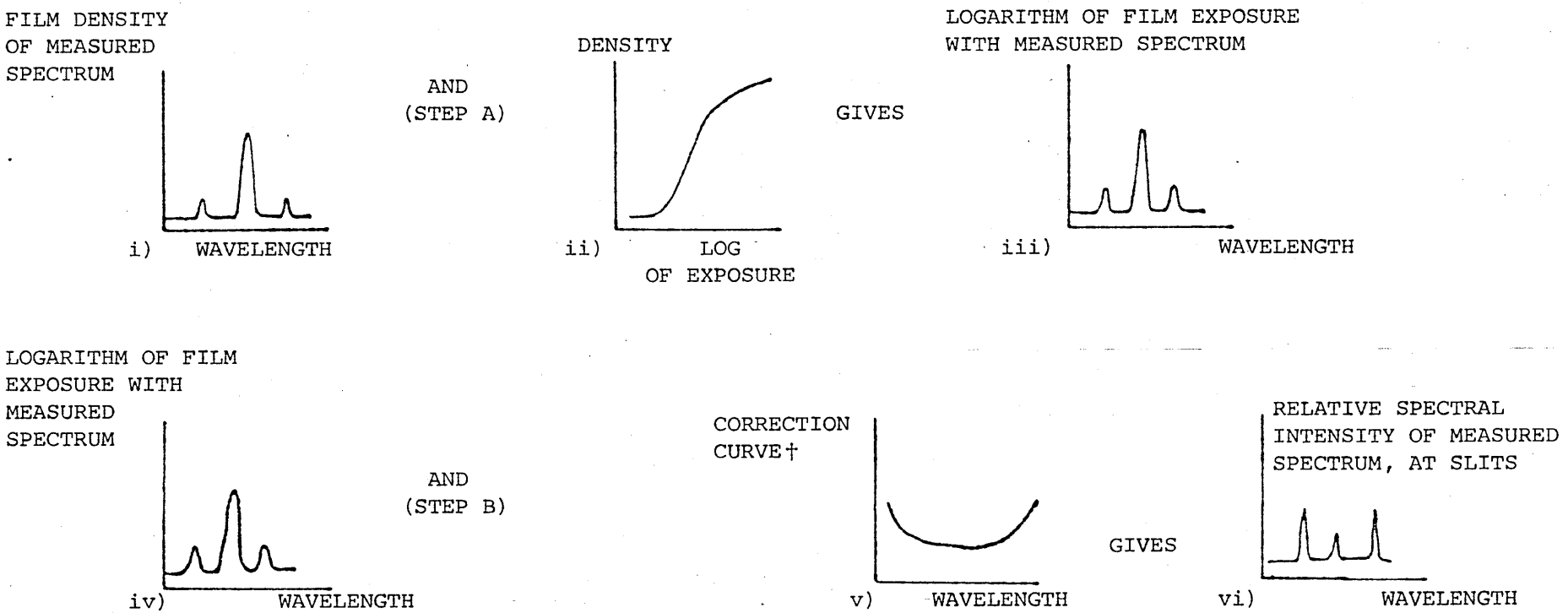

†see Figure 1.26

vi) is, of course, the corrected spectrum

FIGURE 1.25 DIAGRAMMATIC REPRESENTATION OF INTENSITY CORRECTION PROCEDURE

standard lamp spectrum through the IIT spectrograph (step 1 of figure 1.26). This spectrum is converted via the known H-D curve to a graph of logarithm of film exposure versus wavelength . The latter is compared (step 2 of figure 1.26) with the spectral power distribution of the lamp (Jones, 1970) to give the correction factor which, as a function of wavelength, is the correction curve.

The procedure outlined above makes the assumption that at every given wavelength the IIT and lens system is linear with respect to intensity changes so that twice the exposure at the film surface in a given spectral line requires twice the light energy to enter the slits in the appropriate wavelength range. This assumption is reasonable provided the light is not bright enough to cause saturation of the IIT phospher.

In practise the procedure shown in figure 1.25 can be simplified because all useful spectral information is recorded on a linear (to within 10%) part of the H-D curve.Spectral correction, due to variations in film and processing, is rarely achieved to better than 10% (Reynolds, 1980). That the information is recorded on a linear part of the H-D curve is ensured by preflashing (see section 1.2.2) the film which has the effect of making exposures of weak spectral lines occur above the toe of the curve (see figure 1.8). With this simplification the only information needed to correct spectra is a graph of the ratio of relative spectral intensity of the standard lamp at the spectrograph input (slits or light guide), to film density, plotted against wavelength. Such correction curves were made with the same film preflashes, as the measured spectra. The correction curves were stored as an array in a computer and multiplied by measured spectral densities as required, to produce

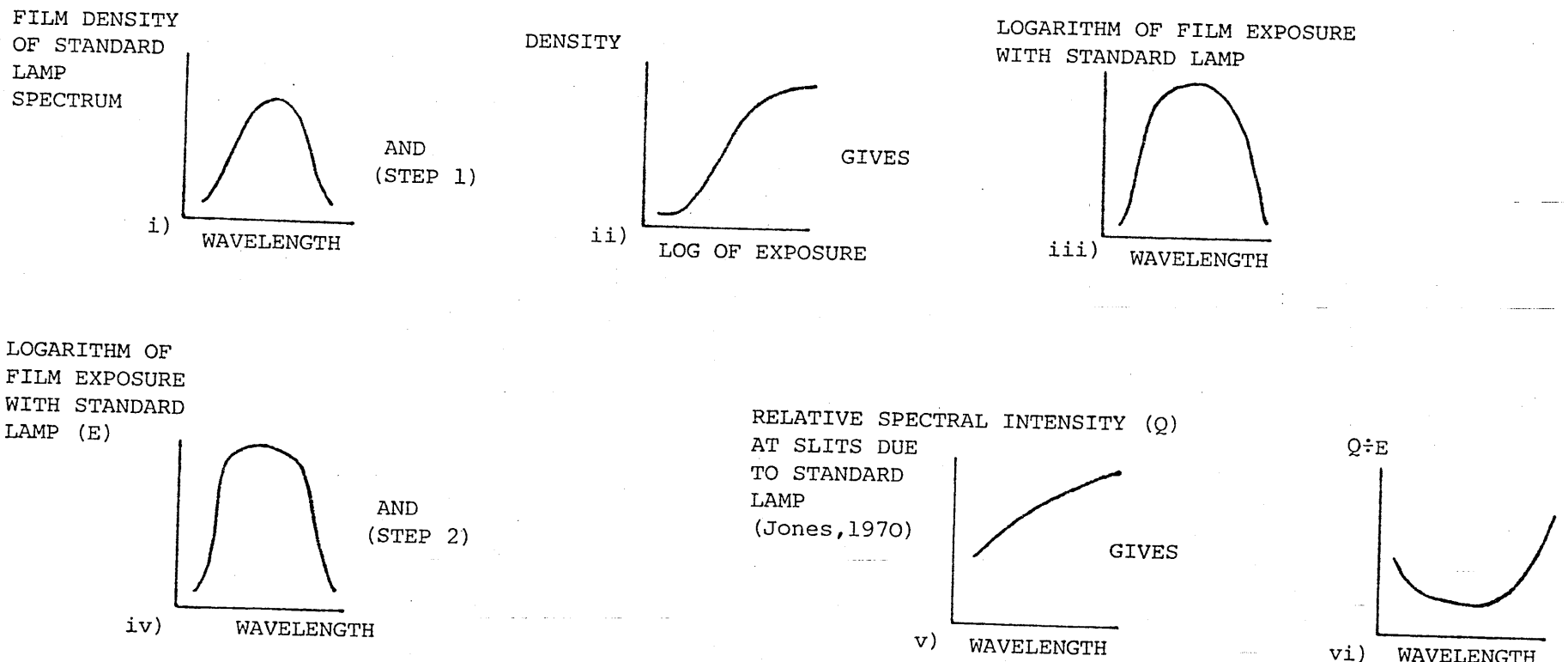

FIGURE 1.26 DIAGRAMMATIC REPRESENTATION OF METHOD USED TO PLOT A CORRECTION CURVE

corrected spectra. The correction curve applicable to a typical photographic film is plotted in figure 1.27. The curve was plotted for a light guide spectrograph input, and with the 600 l mm^{-1} grating.

1.3.8 Previous Image Intensifier Tube Spectrographs

IIT Spectrographs have been reported in the literature but none have been optimally designed. Gruner (1973) built an IIT spectrograph but this had lower gain than the one reported in this chapter. It was fitted with an f2.8 telescope lens and had a maximum resolution of 0.4 nm. In addition it suffered from severe vignetting at the ends of the spectral range. The same instrument was mentioned by Walton and Botos (1978), who reported (wrongly) that it had an f2.7 telescope lens.

An IIT spectrograph is mentioned by Kafalas (1968) but it is simply an adaptation of a commercial Czerny-Turner type spectrometer with an aperture of f6.3. It was not specially designed and in his paper Kafalas mentions the need for an improved spectrograph.

Another method for measuring very low light level transient spectra is described by Bailiff, Morris and Aitken (1977). Essentially they describe an instrument which quickly scans a series of interference filters over a photomultiplier. They show that the instrument can be used to measure weak thermoluminescent (THL) spectra. It is not a multichannel system and light passed by only one particular filter goes through the instrument at any one time. A test of the sensitivity of this system compared to an IIT spectrograph (Walton, 1980) has shown that the latter is more sensitive and versatile.

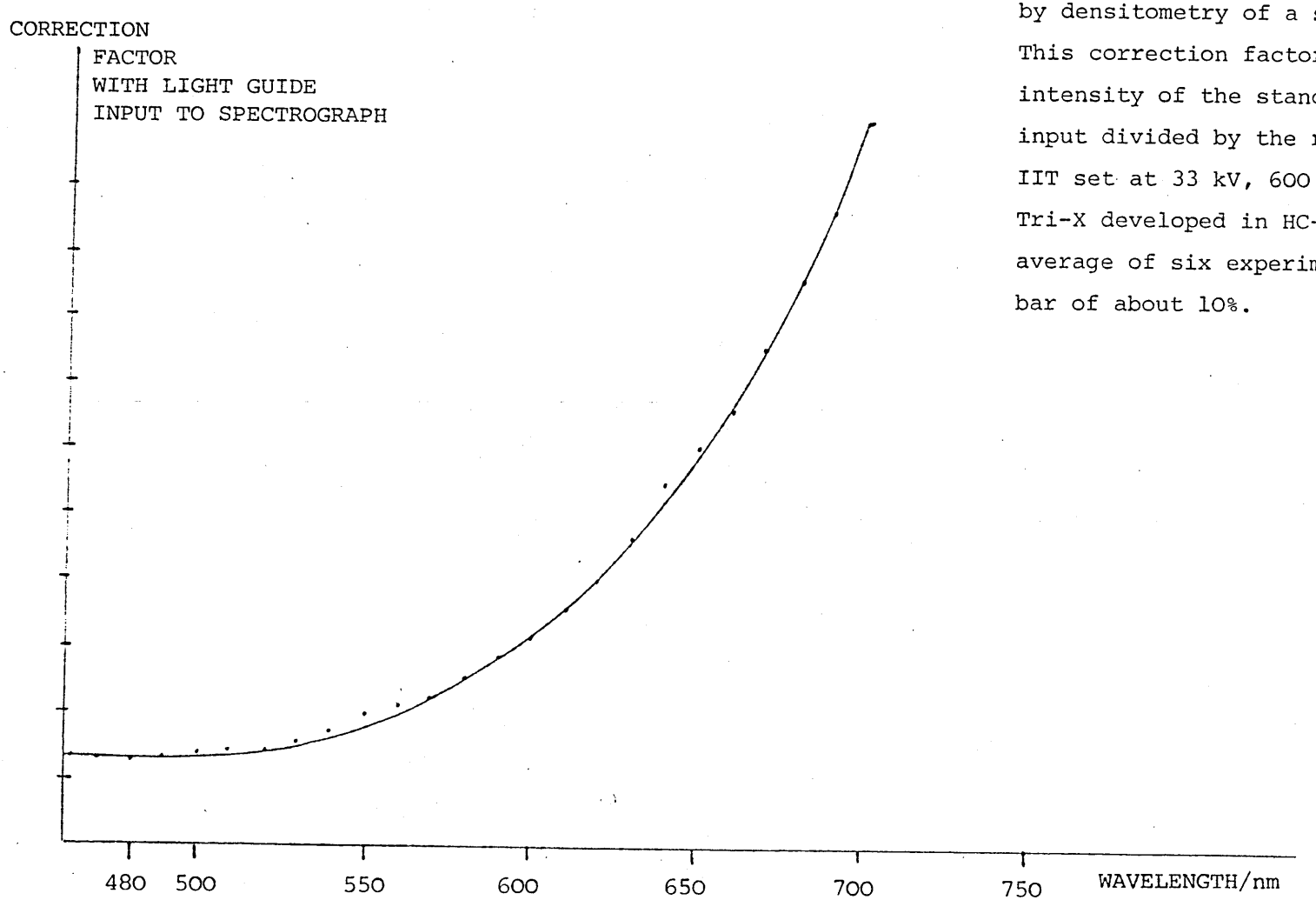

FIGURE 1.27 A TYPICAL CORRECTION CURVE FOR THE IIT SPECTROGRAPH SYSTEM

The correction factor was obtained by densitometry of a standard lamp spectrum. This correction factor is the relative spectral intensity of the standard lamp at the light guide input divided by the recorded film density. IIT set at 33 kV, 600 l mm^{-1} grating used, with Tri-X developed in HC-110. The curve is an average of six experiments with a vertical error bar of about 10%.

Some interesting comments on digitizing the IIT output are contained in a report by Iredale and Ryden (1967), but are not relevant here since densitometry of the output and computer assisted intensity correction were found to be sufficient for small quantities of data. Digitizing the IIT output is only worthwhile when quick handling of large volumes of data is required.

1.4 A Beam Divison Spectrometer

A beam division spectrometer is shown in figure 1.28. The ratio of the charge integrator outputs equals the ratio of light intensity at the wavelength of the signal filter; to the total light intensity, as recorded on photomultiplier A. The instrument was built to give a simple demonstration of TL, and to show how TL spectra can be measured without a spectrograph. A study of TL in the infra-red could be made with this instrument if photomultiplier B had a suitable spectral response e.g. S1 type photocathode.

1.5 Thermoluminescence Apparatus

When a THL material is heated it emits light in particular temperature regions, giving glow peaks. This arises from a process where the recombination of a charge carrier with a luminescent centre, occurs after its thermal release from a trapping site (Curie, 1963). I studied THL in a comparison with TL. A spatial study of THL was not undertaken (see Walton and Debenham, 1980), but THL spectra were recorded from small ($\simeq$ 5 mm^2) specimens. The samples were cleaned by chemical etching and were then placed on a heated stage. The stage could be electrically heated so that its temperature rose linearly with time, typically at 2.5^{o}C per second. The stage was continually flushed with argon to surpress spurious luminescence

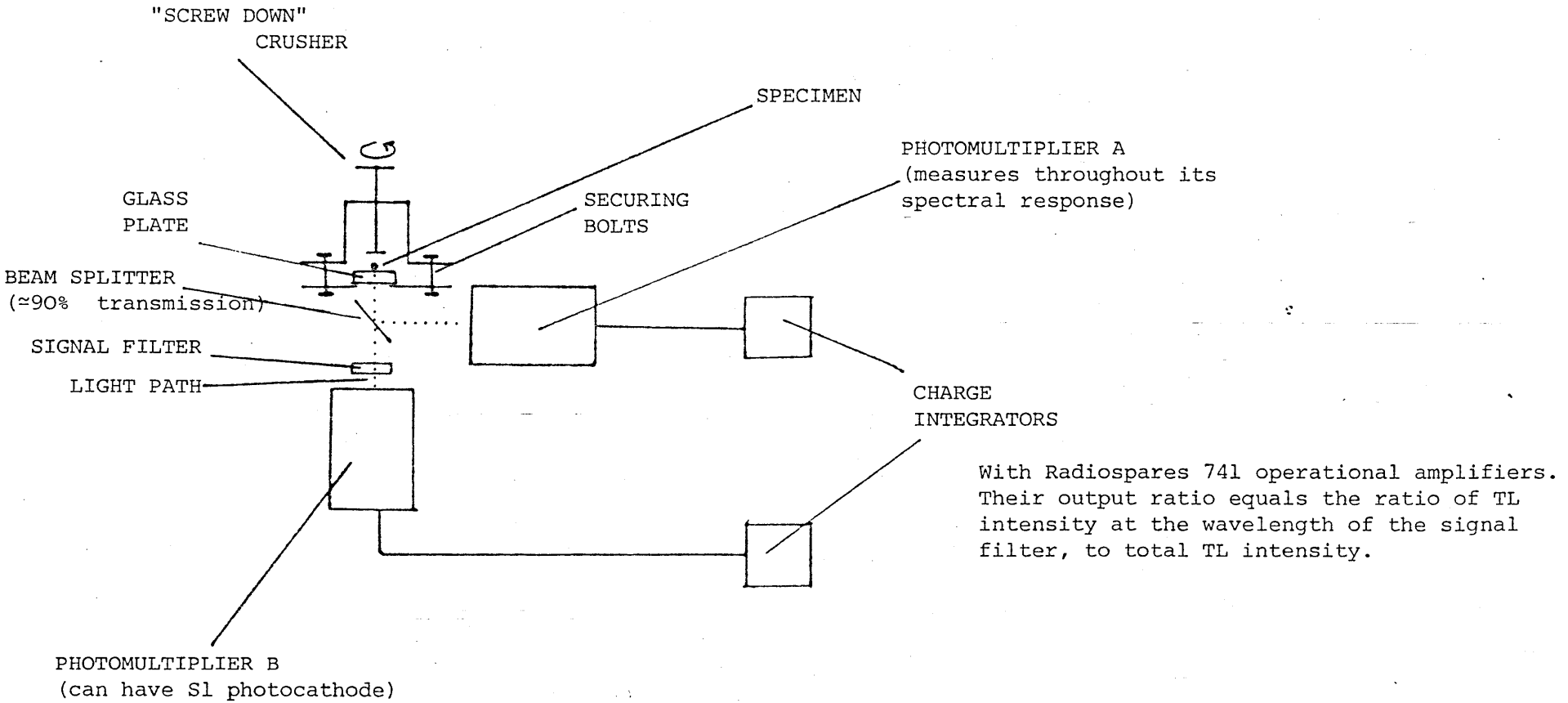

FIGURE 1.28 A BEAM DIVISION SPECTROMETER

emissions. The oven† consisted of an electrically heated nichrome plate whose temperature was recorded by means of a NiCr-NiAl thermocouple. The apparatus is shown in figure 1.29. A mirror and condenser lenses enable the image of the specimen to be focused onto the IIT spectrograph†† input slit. THL spectra can be recorded for any interval of temperature by opening and closing the camera shutter at the required time. Glow curves are plots of, total THL light intensity within the spectral sensitivity of the instrument, against temperature. They could be recorded at the same time as spectra were photographed, by measuring the total IIT phospher light output through a light guide leading to a photomultiplier (PM). The PM current was plotted against temperature on a chart recorder synchronized with the oven. Provision was also made for insertion of spectral calibration lamps into the optical path so that THL spectra could be calibrated.

1.6 Photoluminescence Apparatus

PL spectra for comparison with TL spectra, were measured in one of two ways:

a) PL spectra extending into the infra-red, from only a small (typically 50 micrometres diameter) area of material, were measured with a monochromator as shown in figure 1.30. The specimen was excited with a 632·8 nm He-Ne laser filtered (Ealing Beck Ltd., 31-6703) to remove faint unwanted lines. The resulting PL was focused onto the slits of a Czerny-Turner type monochromator. The monochromator was fitted with a 600 l mm^{-1} grating blazed at 1 μm. The monochromator output

---

†Kindly loaned by Dr. Aitken of The Department of Archaeology, University of Oxford.

††In obtaining the THL spectra a duplicate of the spectrograph described in section 1.3.5 (built in 1980 by A.J. Walton) was employed.

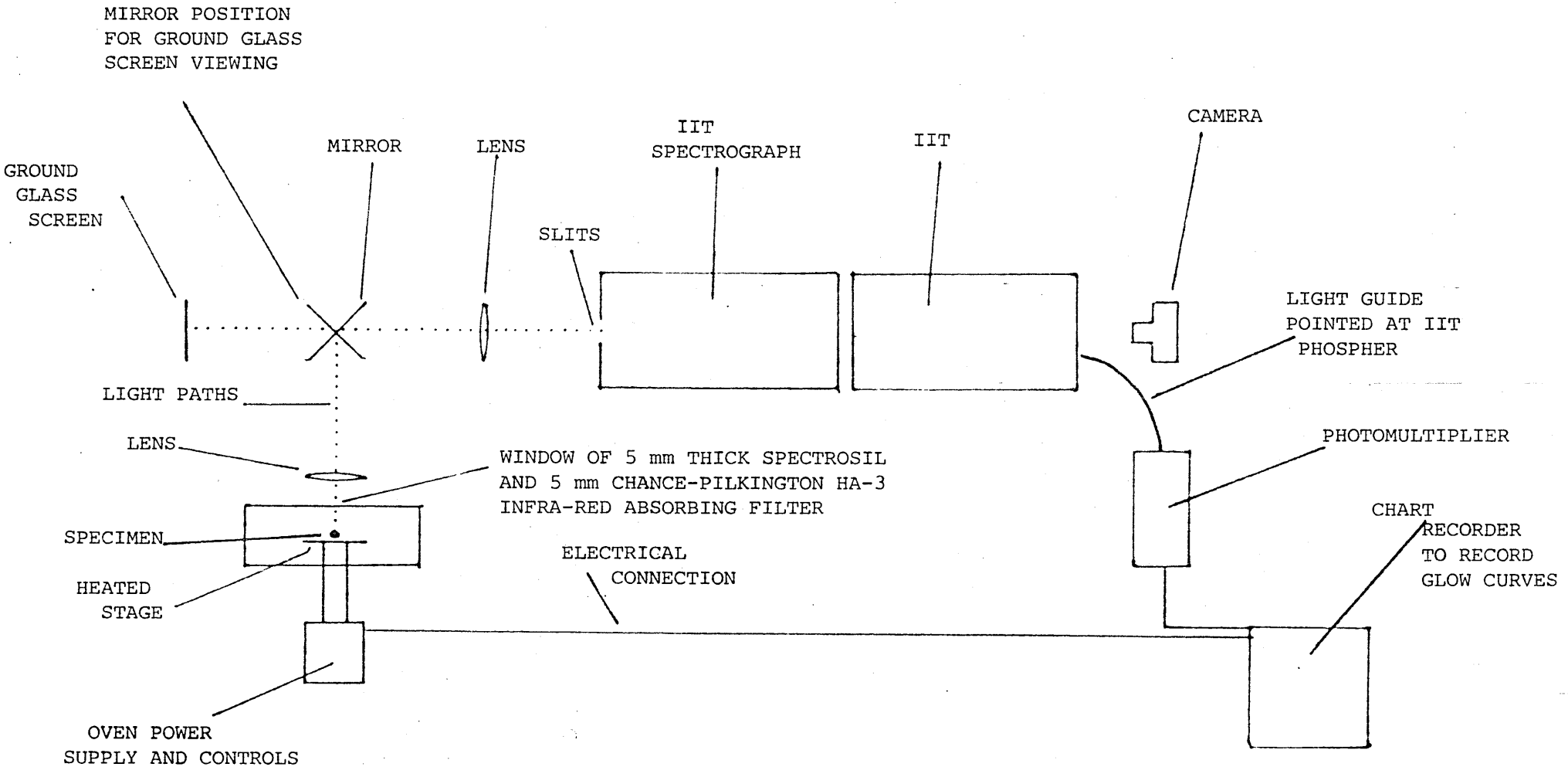

FIGURE 1.29 THERMOLUMINESCENCE APPARATUS

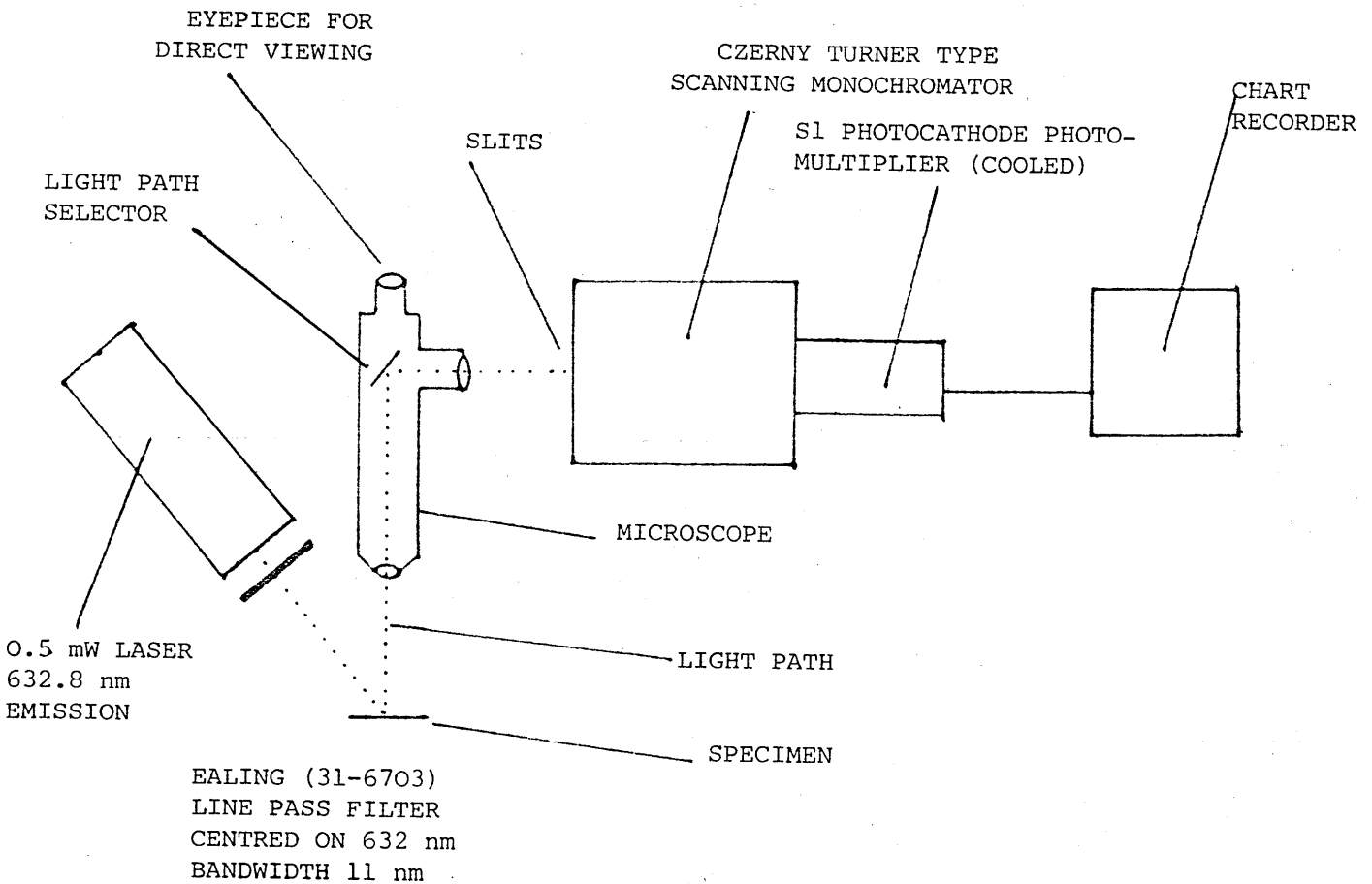

FIGURE 1.30 APPARATUS FOR RECORDING PHOTOLUMINESCENCE SPECTRA WITH He-Ne LASER EXCITATION

was measured with a cooled S1 photocathode photomultiplier tube (EMI type 9684 B) and recorded on a chart recorder as a function of wavelength. The coupling optics were normally a Gillet and Sibert "University Lynx" microscope fitted with a projection eyepiece. The microscope is described in detail in chapter 6.

b) PL spectra that required an excitation source other than the He-Ne laser were measured with a spectrofluorimeter (manufactured by Applied Photophysics Ltd., London W1.). The instrument had a 250 W xenon lamp excitation source, input and output monochromators with 1 nm resolution, and a cooled S20 photomultiplier detector. There was an angle of 90° between input and output beams in the specimen box. The instrument is drawn diagrammatically in figure 1.31. Care was taken that direct reflection of the input beam into the output monochromator did not occur. The PL of an area $\simeq$ 1 cm diameter was sampled with this apparatus. It was found to be of most use for measuring the PL spectra of samples prior to measuring their triboluminescence spectra.

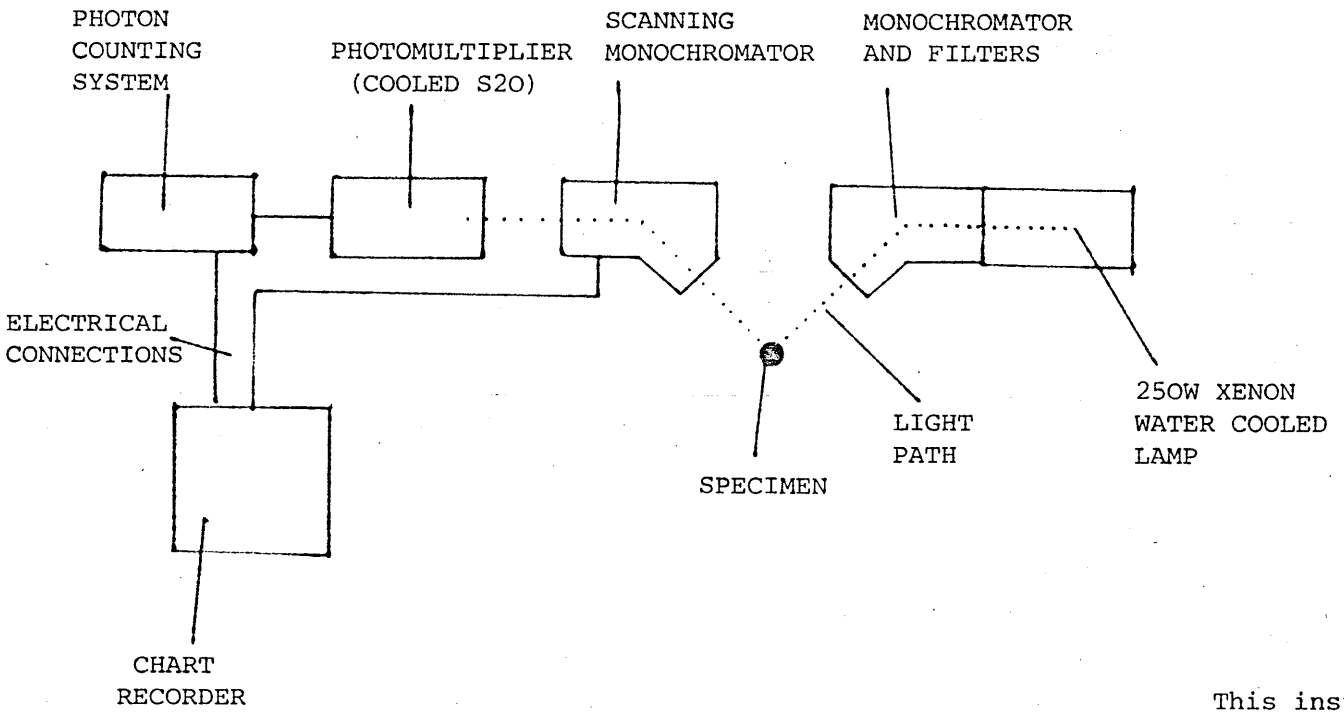

This instrument was manufactured by Applied Photophysics Ltd., London, W.1.

FIGURE 1.31 MAIN FEATURES OF THE SPECTROFLUORIMETER

CHAPTER 1

APPENDIX 1

Optical Density

Transmission density (D) is defined as the logarithm of the ratio of the radiant flux I_o incident on the developed image, to the radiant flux T_o transmitted by the developed image.

$$D = \log_{10} \frac{I_o}{T_o}$$

$$= \log_{10} \frac{1}{T}$$

T is the transmittance of the developed image. Density is a useful quantity because the eye judges brightness differences on an approximately logarithmic scale. Two types of density may be measured, diffuse and specular. Diffuse density is a measurement taken with an angle of collection of 180°. Specular density however is measured with an angle of collection approaching 0° (in practise 5° to 10°), see figure 1.32.

All experimental results were densitometered on a commercial double beam recording microdensitometer (Joyce Loebl and Co. Ltd., mark IIIC, number 985). This instrument measures specular density, it operates on a nulling principle and was found to give exactly reproducible results. Before the commercial machine was available a "home made" densitometer was built using a microscope, photomultiplier and stabilized current powered tungsten-halogen light source, to measure specular density. This densitometer gave an output current proportional to 10^{D}. An antilogarithm amplifier (Intersil 804) was used to convert this to a current proportional to D. The system was limited by the stability of the antilogarithm amplifier, of the

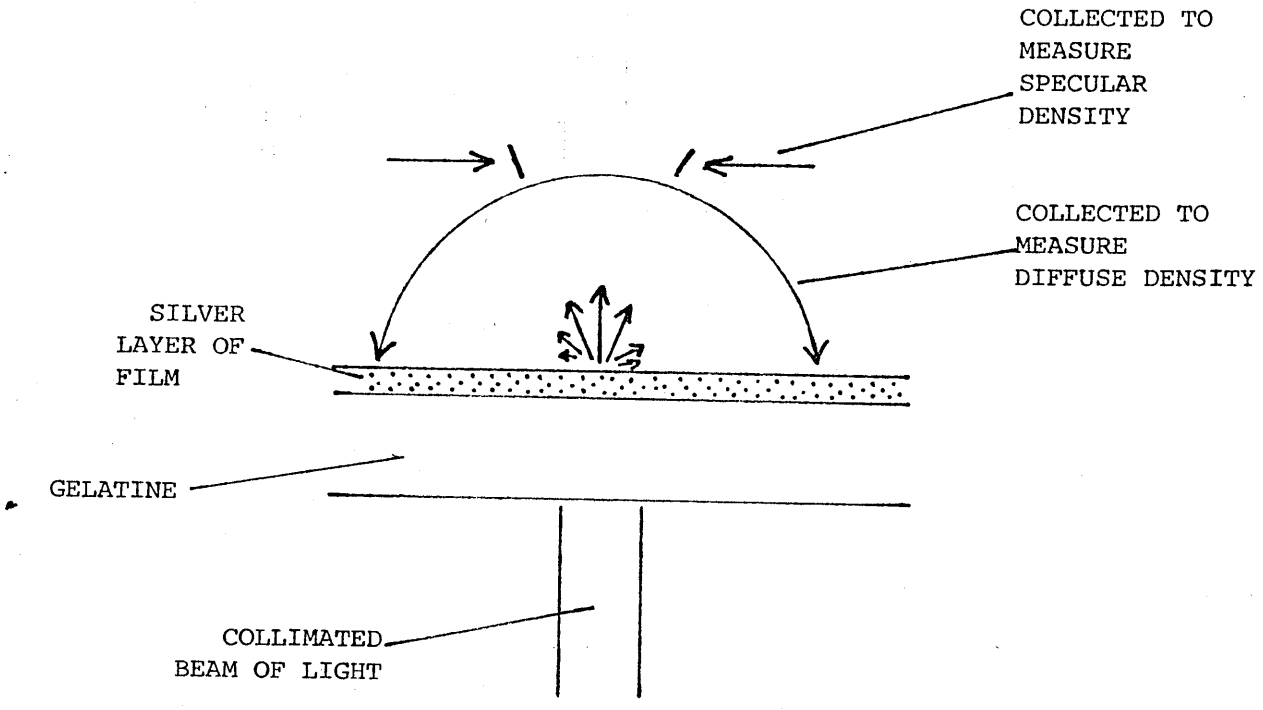

FIGURE 1.32 SPECULAR AND DIFFUSE DENSITY

photomultiplier power supply and of the light source, resulting in an unacceptable noise signal on the densitometered trace.

Film density (D) may be related to the number of developed silver grains in a negative emulsion by using the Nutting formula (Dainty and Shaw, 1974)

$$D = \frac{na}{A} \log_{10} e$$

where e is the base of natural logarithms, n is the number of silver grains in area A, and a is the area of one grain.

The quality of an image recorded on photographic film can be measured by detective quantum efficiency (DQE), which is defined as

$$DQE = \frac{\left(\frac{\text{Signal}}{\text{noise}}\right)^2_{OUT}}{\left(\frac{\text{Signal}}{\text{noise}}\right)^2_{IN}}$$

(Bird, Jones and Ames 1969). The signal to noise ratio of a photographic image is defined by

$$\left(\frac{\text{Signal}}{\text{noise}}\right)_{OUT} = \frac{\text{Density above base fog of recorded signal } (D_R)}{\text{Film Granularity at } D_R}$$

Film granularity is an objective measure of the spatial variation of density with distance. Numerically, diffuse root-mean-square granularity is 1000 times the standard deviation of density produced by the granular structure of the material, when a uniformly exposed and developed sample is scanned by a microdensitometer having a circular measuring aperture of specified diameter (normally 48 μm).

Typical detective quantum efficiency curves of a film emulsion and of some photocathodes are plotted in figure 1.33 as a function of wavelength.

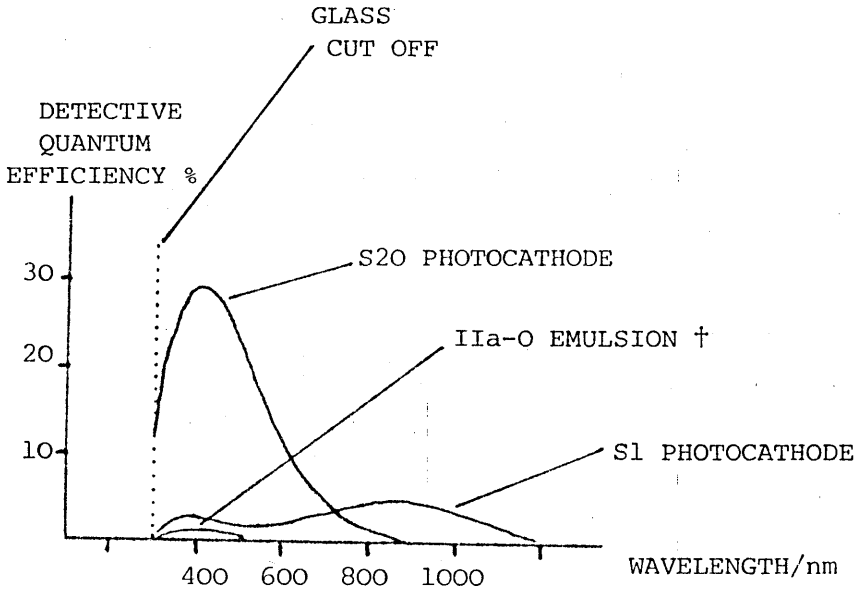

†IIa-O is a Kodak spectroscopic plate emulsion (see Kodak Ltd.,1973) and is approximately "equivalent" to a 160 ASA film.

FIGURE 1.33 COMPARISON OF DETECTIVE QUANTUM EFFICIENCIES OF FILM AND PHOTOCATHODE

CHAPTER 1

APPENDIX 2

Blazed Gratings

A blazed grating has flat smooth groove faces inclined to the surface by a constant groove angle θ. The purpose of blazing is to increase the grating efficiency i.e. the proportion of optical power leaving the grating in the required order and in the required wavelength region, to the total incident optical power. The grating equation may be written as

$$m\lambda = a (\sin \alpha \pm \sin \beta) \qquad 1$$

see figure 1.34. The plus sign signifies that β is on the same side of the grating normal as α. The gratings used in the IIT spectrograph were 600 l mm^{-1} blazed at 500 nm (a blaze angle (θ) of 8.63^{o}) and 1800 l mm^{-1} blazed at 500 nm ($\theta = 26.75^{o}$). The blaze angle equals the angle of the facet normal to the grating normal. By definition the first order blaze wavelength is the wavelength of light for which the direction of reflection from the groove face is the same as the angle of diffraction in the first order for a given angle of incidence. The blaze wavelength is usually quoted in first order although a grating is also blazed in the n^{th} order for one n^{th} of this wavelength. Gratings are often used in the so called littrow configuration where $\alpha = \beta$ so that the groove face is normal to the ray path. Then $m\lambda = 2 a \sin \beta$, and reflection and diffraction coincide. In this configuration β equals the blaze angle θ and the first order littrow blaze wavelength is defined by

$$\lambda_L = 2 a \sin \theta \qquad 2$$

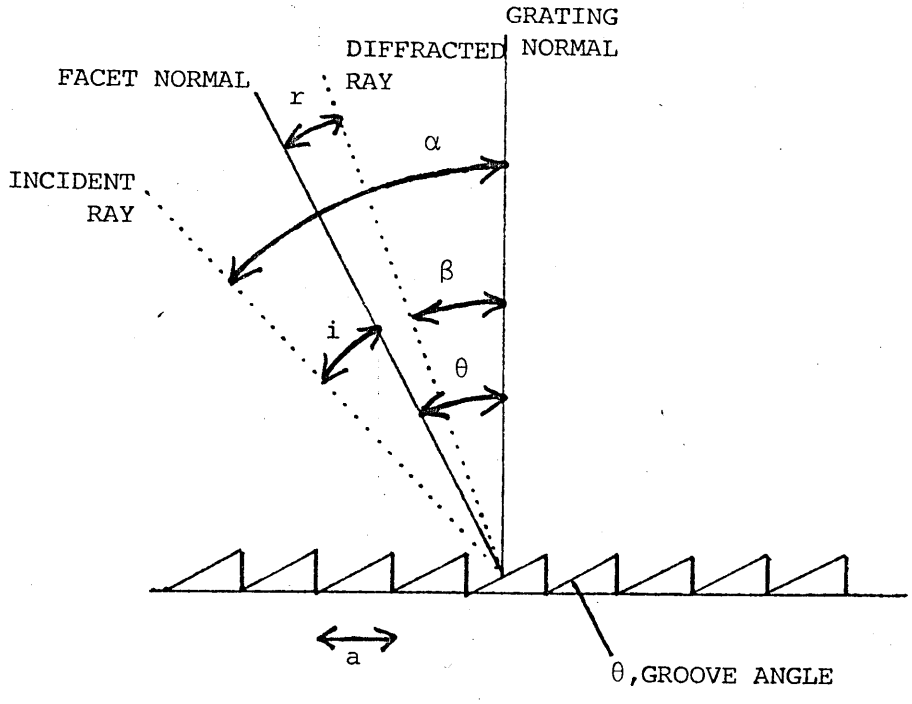

β is positive when it is on the same side of the grating normal as α, negative if on the opposite side.

FIGURE 1.34 DIFFRACTION GRATING NOMENCLATURE

This equation relates the normally quoted blaze wavelength (λ_L) to the groove angle. The importance of this equation is that the blaze wavelength varies little from λ_L for non-littrow configurations.

The blaze wavelength for any given grating configuration can be calculated. When the gratings used in this experiment had been positioned to give the required wavelength range and dispersion across the photocathode I checked that the blaze wavelength for that configuration lay between 400 and 750 nm. From figure 1.34.

$$i = \alpha - \theta \qquad 3$$

$$r = \theta - \beta \qquad 4$$

From the laws of reflection

$$i = r \qquad 5$$

When reflection coincides with diffraction

$$\alpha - \theta = \theta - \beta \qquad 6$$

$$2\theta = \alpha + \beta \qquad 7$$

The diffraction equation 1 becomes

$$m\lambda = 2a \sin\left(\frac{\alpha+\beta}{2}\right) \cos\left(\frac{\alpha-\beta}{2}\right) \qquad 8$$

by using the standard relationship

$$\sin\alpha + \sin\beta = 2 \sin\left(\frac{\alpha+\beta}{2}\right) \cos\left(\frac{\alpha-\beta}{2}\right) \qquad 9$$

Using (7), equation (8) becomes

$$m\lambda_B = 2a \sin\theta \cos\left(\frac{\alpha-\beta}{2}\right) \qquad 10$$

This is the blaze wavelength for m^{th} order, where α and β are defined in figure 1.34 and 2a sin θ is a constant of the grating. But

$$2a \sin \theta \qquad 11$$

is the littrow blazed wavelength in first order (λ_L) so

$$m \lambda_B = \lambda_L \cos\left(\frac{\alpha-\beta}{2}\right) \qquad 12$$

This is the relationship that I sought, it relates the littrow blazed wavelength as quoted in many manufacturers catalogues, to the actual blazed wavelength for a given grating configuration.

From (12) it follows (because cos 26^o = 0.9) that with $\alpha - \beta < 52^o$ then the blaze wavelength will not be less than 90% of the littrow quoted value. Thus the blaze wavelength of the gratings in the IIT spectrograph is always in the range 400 to 750 nm.

The useful range of wavelengths either side of the blazing peak is approximately 0.7 times to 1.5 times the blaze wavelength before efficiency drops to less than 50% of its peak value. For the gratings used in the IIT spectrograph this corresponds to a useful range covering most of the visible spectrum, but depending on the exact grating configuration.

Each blazed grating is marked with an arrow. This points towards the side of zero order for the brightest first order.

CHAPTER 1

APPENDIX 3

The Standard Lamp

The standard lamp was a minature bipin tungsten-halogen projection lamp type A1/215. The filament temperature was measured by N.P.L. (calibration 08109P/CT2/86-87) as 2856K for particular operating conditions. These included vertical mounting, a 10 minute warm-up period and operation at 7.48 volts and 6.880 amps. The operating conditions were strictly reproduced whenever I used the lamp. The current was set using a standard resistor and high impedance digital voltmeter. In practise it was necessary to reduce the intensity of the lamp with neutral density filters (manufactured by Oriel). Their density as a function of wavelength was recorded on a spectrophotometer and was applied as a correction factor to the spectral power distribution of the lamp. The spectral power distribution of the lamp was obtained from tables published by NPL (Jones, 1970). These tables include the absolute spectral radiant intensity per candela, $Q(\lambda)$, for tungsten sources at 2856 K with 10 nm wavelength intervals. A "De Vos" type tungsten surface is assumed, viewed through a window with a constant transmission factor of 0.91. Only relative intensities were of importance to this research so it was not necessary to know the absolute intensity of the lamp.

CHAPTER 2

TRIBOLUMINESCENCE, AN INTRODUCTION AND REVIEW

2.1 Introduction

Triboluminescence from the Greek *tribo* (to rub) should refer to any light which results from rubbing a material, and piezoluminescence to any luminescence resulting from pressing a material. In practise TL is defined as light whose origin is the mechanical deformation or fracture of a solid, i.e. light resulting from the application of mechanical energy to a solid. Synonymous are piezoluminescence, mechanoluminescence and trennungslicht - from the German *trennung* meaning to shear or separate. This definition embraces a wide range of luminescent processes including the light emission when "sellotape" is unrolled (gas discharge produced by static electricity), when mercury flows over glass, and when an assortment of solids are fractured, for example sugar, ice, glass and rock salt. The glowing fragments produced when hard objects are struck or frictionally heated is also called TL. A simple demonstration of TL is to crush a sugar cube in a pair of pliers while observing it with dark adapted eyes. A blue-white flash of light will be seen.

Chemiluminescence is the light originating from the products of a chemical reaction and not from the original material. It can be included within the definition of TL, if the reaction is a direct result of mechanical deformation or fracture. An example of chemi-luminescence is the emission of light from crushed peanuts. The term tribo-induced chemiluminescence to describe TL arising from new reaction products and not from the original material, is sometimes found in the literature. If the mechanical energy applied to a solid results in a local increase in temperature and consequently in

thermoluminescence, the effect is called tribothermoluminescence. (This differs from tribo-induced thermoluminescence which will be mentioned in Chapter 3, where a heated sample, which as a result of this heating exhibits no subsequent thermoluminescence, is crushed and then found to be thermoluminescent again).

Although embracing such a wide range of phenomena, TL effects may be classified under a number of subheadings. Classification can be according to material, excited state origin, or the mechanism of population of the excited state. Classification by excited state origin or class of material, is most frequently found in the literature.

The main origins of TL are:

1) Luminescence resulting from a gas discharge - nitrogen for TL in air.

2) Crystal fluorescence and phosphorescence, including the fluorescence and phosphorescence of metal centres.

3) Excited states which occur in only a small number of materials. These include luminescence from charge transfer complexes, from free radicals, from conduction band to valence band transitions, thermal radiation from small hot regions within a sample, and luminescence that resembles the sample electroluminescence.

Crystal fluorescence and crystal phosphorescence may be referred to together as crystal photoluminescence. One substance may exhibit TL of more than one origin.

The literature on TL is very widely spread, sometimes neither TL nor one of its synonyms is mentioned in a particular account, and the same

work has on several occasions been reported separately by new workers in the field with no knowledge of its previous publication.

The interest and importance of TL lies in its link between the structural, mechanical, electrical and luminescent properties of solids. The purpose of all TL research, in general terms, is to determine the excited state origins of the luminescence and the mechanism of population of these states. In this chapter I will review all the important literature that relates to triboluminescence. As the field has recently been reviewed by Walton (1977) I have placed more emphasis on post - 1977 work.

2.2 Fracturing Procedures Employed in Producing Triboluminescence

Depending upon the material and the light detection system, different methods of producing TL may be used. For detection by eye, crushing a crystal in pliers or a pestle and mortar is often sufficient. Crystals can be dropped into liquid nitrogen, where the thermal shock causes TL by cracking. A crystal can also be held against a milling tool, grinding wheel (but not a silicon carbide wheel because this material is TL), rotating diamond saw or similar. For spectroscopic work crystals may be ground or crushed against an optical window. Much early TL work, which involved the direct exposure of photographic plates, required the development of machines which could quickly grind or crush large volumes ($\simeq$ 20 kg) of material (Longchambon, 1925; Nelson, 1926). The fracturing procedures that were tested during this research are discussed in section 3.2.

2.3 Early Work on Triboluminescence

TL was almost certainly observed in ancient times. Anyone chipping or cutting cane sugar or one of many natural minerals after dark would

have observed TL. The faint glow of frozen seas or rivers at night may have been observed - it is due to the TL of ice. The earliest written record of TL is contained in Francis Bacon's "The Advancement of Learning" (1605), in which he mentions the TL of sugar. Wedgwood's paper of 1792 entitled "Experiments and Observations on Production of light from different Bodies by Heat and by Attrition" mentions TL of diamond, fluorite, quartz, glass, agate, ruby, topaz, pottery, enamel and mica. He was the first to have recorded the observation of TL upon applying samples to the circumference of a revolving grit wheel. He notes that bodies give out light the instant they are rubbed together, and cease when attrition is discontinued. He also notes that "bodies are not luminous by simple pressure, but only when they are at all broken by the pressure". He did not observe deformation luminescence. Wedgwood interpreted TL as a heating of the surfaces of materials. In 1820 Heinrich, after a number of experiments, suggested several TL mechanisms including "electricity resulting from friction" and "chemical decomposition produced by friction". Much of the other early TL work is of use for its extensive listing of TL materials and their colours. It is reviewed by Trautz (1905, 1910), Gernez (1908), Imhof (1917), Weiser (1918a and 1918b), Longchambon (1925) and Lenard and Schmidt et al. (1928). Harvey's "History of Luminescence" (1957) gives an interesting early history of TL and other types of luminescence.

All the early experimental work was done by eye or using direct vision spectroscopes. Due to the low intensity of TL it was not until Longchambon (1922) that any TL spectra were successfully photographed. A system using narrow strips of filter sandwiched between photographic film and a glass plate, onto which crystals were directly crushed, was first used by Weiser (1918a and 1918b). It allowed a photographic

record of TL to be made but had low spectral resolution and failed to reveal the nitrogen gas discharge emitted by Weiser's samples.

2.4.1 Tribo-induced Gas Discharge Luminescence

A very common origin of TL is gas discharge luminescence. The first report of TL, Bacon (1605), mentions the light emitted when sugar is scraped. Early photographic spectra of TL (Longchambon 1925) recorded a well defined vibronic band structure. This structure was compared with gas discharge spectra and revealed the origin of TL from sugar and a number of other materials as the $^3\Pi u \rightarrow {}^3\Pi g$ fluorescence of the second positive system of nitrogen (see appendix 1). It is of note that to excite the $^3\Pi u$ state, and hence the observed TL, requires a minimum energy of 8.9×10^4 cm^{-1} ($\simeq$ 11 eV). The observation of a nitrogen discharge led Longchambon to suggest an electrical origin of TL. As will be reported later (chapters 3 and 4) I have measured many TL spectra that contain the nitrogen gas discharge. An example is shown in figure 2.1; it was recorded on the IIT spectrograph and is shown without intensity correction. The nitrogen gas discharge band head wavelengths have been photographically recorded and measured by Pankhurst and Gaydon (reported in Pearse and Gaydon 1963). Using higher resolution than that of the IIT spectrograph, and a discharge tube as source, they found that the bands were degraded toward shorter wavelengths. Part of a table of band head wavelengths from Pearse and Gaydon (1963) is reproduced in table 2.1. My TL spectrum in figure 2.1 clearly shows the bands at 426.9, 420.0, 414.2, 409.5, 405.9, 399.8 and 394.3 nm. Longchambon (1925) made a detailed study of nitrogen gas discharge TL and recorded some lines from the nitrogen first negative system (due to N_2^+) at 391.4, 388.3,

FIGURE 2.1 TL OF SUGAR Mercury calibration lines can be seen at 404.7, 435.8, 546.1, 577.0 and 579.1 nm. The wavelengths of seven TL lines are marked.

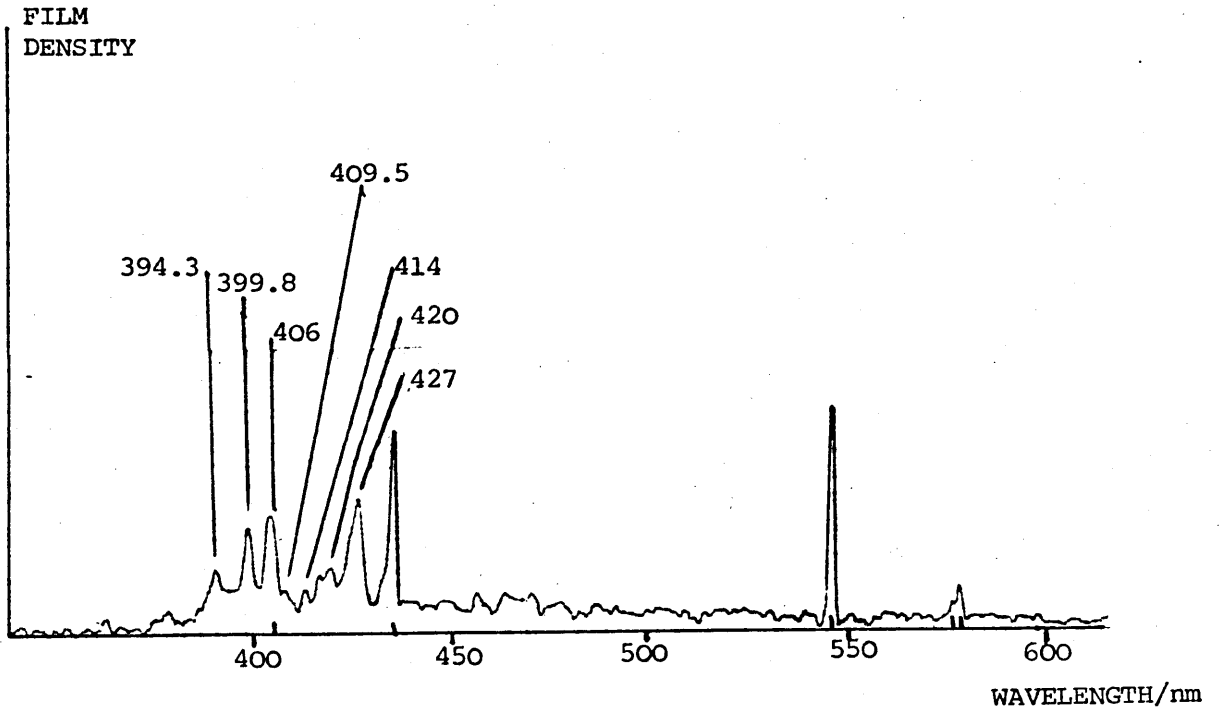

λ	I	v', v"	λ	I	v', v"
4976.4	o	4, 11	4059.4	8	o, 3
4916.8	o	1, 7	3998.4	9	1, 4
4814.7	1	2, 8	3943.o	8	2, 5
4723.5	1	3, 9	3894.6	7	3, 6
4667.3	o	o, 5	3857.9	5	4, 7
4649.4	1	4, 1o	3804.9	1o	o, 2
4574.3	2	1, 6	3755.4	1o	1, 3
449o.2	3	2, 7	371o.5	8	2, 4
4416.7	3	3, 8	3671.9	6	3, 5
4355.o	3	4, 9	3641.7	3	4, 6
4343.6	4	o, 4	3576.9	1o	o, 1
4269.7	5	1, 5	3536.7	8	1, 2
42oo.5	6	2, 6	35oo.5	4	2, 3
4141.8	5	3, 7	3469	o	3, 4
4o94.8	4	4, 8	3446	o	4, 5

TABLE 2.1 VIBRATIONAL LEVELS OF THE UPPER (v') AND LOWER (v") ELECTRONIC STATES OF THE SECOND POSITIVE SYSTEM OF NITROGEN.

The electronic states are $^3\Pi_u$ (upper) and $^3\Pi_g$ (lower). After R.C. Pankhurst and A.G. Gaydon (Pearse and Gaydon, 1963). Approximate relative intensities are given in the columns labelled "I". Wavelengths are in angstroms.

358.1, 356.3 354.8 and 329.2 nm. These were too far into the ultra-violet to record on the IIT spectrograph but may be compared with the more intense lines recorded by Pearse and Gaydon (1963) at 391.4, 388.4, 358.2, 356.4, 354.9 and 329.3 nm in the first negative system of nitrogen. As well as by spectral comparison, many workers have inferred the presence of nitrogen discharge emission by studying the TL of crystals under a neon atmosphere, and observing by eye the characteristic red discharge emission of neon.

2.4.2 Detailed Review of Tribo-induced Gas Discharge Luminescence Literature

The literature in the area of tribo-induced gas discharge luminescence relates mainly to sugar, but other materials investigated include rock salt and various other minerals. Gas discharge luminescence often occurs with other luminescences, such as photoluminescence. Early work noted the existence of TL from sugar and a number of other materials particularly crystals with noncentrosymmetric structure. The first attempt to measure the TL spectrum of sugar was by Burke (1898). He was unable to obtain a photographic record because of "the rapid rate at which the samples of sugar wore out", but viewing a direct vision spectroscope he saw that the spectrum was "confined to the more refrangible end of the spectrum commencing somewhere about F", that is in the region of less than 486 nm wavelength.

Burke interpreted this as showing that the TL is not due to particles of sugar becoming red or white hot.

Experiments by Tschugaeff (1901) found that a high proportion of crystalline materials which are TL lack a centre of symmetry in their structure, and as a result of these observations Vernadsky (1910) proposed that TL has a piezoelectric origin. In 1913 Langevin

proposed that TL arose in *piezoelectric* crystals through breakdown of the gas, a breakdown brought about by the electric field (existing between the two oppositely charged fracture planes) produced by piezoelectric charging. Voigt (1913) reported that in sugar crystals no TL was produced when a single crystal was cleaved in a plane parallel to the piezoelectric axis, although TL was produced from all other cleavage planes. This experiment was repeated by Longchambon (1925) with tartaric acid, which belongs to the same crystal class as sugar, and which was found to behave in the same way.

Longchambon investigated the pressure dependence of sugar TL and found that the intensity increased with decreasing air pressure, passing through a maximum between 40 torr and 1 torr. This pressure dependence was also investigated by Meyer and Polly (1965a and 1965b) and found to be what one would expect for a gas discharge emission.

Grinding TL crystals in a variety of vessels with a variety of materials reveals no systematic differences in the TL (Cotton and Goodgame et al. 1962) when compared with fracture by thermal shock. It was thus thought that frictional electrification is not of major importance in TL excitation. However when cutting some polymers with a rotating diamond saw (see chapter 4) the nitrogen discharge which was sometimes observed could have had a static electrification origin.

A qualitative estimate of the magnitude of the electric field that produces the gas discharge can be made on the basis of Langevin's (1913) model of the creation of oppositely charged surfaces during the movement of a crack in a piezoelectric crystal. As an example I shall use triglycine sulphate ($C_6H_{17}N_3O_{10}S$) but the

calculation can be repeated for sugar (Walton, 1977) and other crystals. When a stress is applied to a piezoelectric crystal one surface along the direction of stress becomes positively charged, the other surface negatively charged. When a crack moves across the crystal it separates into two parts. The newly created surface near the positively charged end of the unbroken crystal is negatively charged, and visa versa. An intense electric field is generated between the two newly created and oppositely charged surfaces. I shall assume that the piezoelectric constant "d" remains unchanged up to the fracture stress "σ_f" of the crystal, and that the stress near the crack tip is not relaxed before gas discharge occurs. I will also assume that the stress near the tip of the mobile crack acts along the crystal's polar direction. The charge density ρ of the new surfaces near the tip of the crack will be $d\sigma_f$. For triglycine sulphate crystals d_{22} at $300^{o}C$ is 16.7×10^{-12} CN^{-1} (Ikeda, 1962) and the fracture stress is 3.8×10^{8} Nm^{-2}. Therefore the charge density of the newly created surfaces will be 6.3×10^{-3} $C\ m^{-2}$ and the electric field (E) between the surfaces will be

$$E = \frac{\rho}{\varepsilon_o} = 7.1 \times 10^{8}\ Vm^{-1} \quad \dagger$$

To initiate gas discharge in air at atmospheric pressure requires 3×10^{6} Vm^{-1} (Harnwell, 1949). This rough estimate supports Langevin's explanation of TL excitation, by piezoelectrification of newly created surfaces.

Chandra and Shrivastava (1979) considered the TL (at $27^{o}C$) of triglycine sulphate, guanidine aluminium sulphate, rochelle salt, diglycine manganous chloride dihydrate, lithium ammonium tartrate monohydrate and potassium dihydrogen phosphate crystals. Only nitrogen gas discharge TL was observed. All these materials are

† This is an underestimate because the applied stress will be less than the crack tip stress.

piezoelectric (at 27°C) with non-centrosymmetric space groups†. Chandra and Shrivastava observed no TL from the centrosymmetric (and hence non piezoelectric) materials glycine silver nitrate, thiourea, ammonium sulphate and azobenzene. As a conclusion they evoked the piezoelectric model (Vernadsky, 1910 and Langevin, 1913) with the requirement that since lithium ammonium tartrate monohydrate, potassium dihydrogen phosphate and rochelle salt are piezoelectric only in torsion, there must be sufficient torsion near mobile crack tips in these materials to produce the necessary charge. Unfortunately Chandra and Shrivastava did not consider NaCl or a number of other materials that were found early this century (Tschugaeff, 1901 and Longchambon, 1925) to be TL *and* centrosymmetric - hence not piezoelectric.

Chandra and Elyas (1979) report experiments on some crystals of the disphenoidal and pyramidal classes which are piezoelectric and exhibit TL. They also report experiments on crystals of the dipyramidal class which are non-piezoelectric and do not exhibit TL. From this they suggest the piezoelectric origin of TL.

Chandra and Verma (1980) have reported the TL of sodium bromate and sodium chlorate. They measured a nitrogen gas discharge spectrum and suggested either piezoelectrification or the separation of charged fracture planes as the most likely TL mechanism.

Longchambon (1925) recorded nitrogen discharge lines from crystals with a centre of symmetry including NaCl, $CuSO_4$, $CdSO_4$ and $BaClO_3$. He concluded that although the symmetry is incompatible with a

---

†Note that a non-centrosymmetric crystal *may* be piezoelectric, while a centrosymmetric crystal cannot be piezoelectric.

piezoelectric origin, the phenomena is still of an electrical nature. He suggested that the crystal does not break into two neutrally charged halves, but fractures with slight irregularities on both surfaces leading to charged fracture planes.

The (III) planes in NaCl are alternately positively and negatively charged, and their separation would result in a charge transfer. The surface energy of these planes is high. Hikata and Elbaum et al. (1963) give the surface free energy of a (III) plane in NaCl as 0.872 Jm^{-2}, compared to 0.150 Jm^{-2} for a (IOO) plane and 0.375 Jm^{-2} for a (IIO) plane. As was noted by Meyer and Obrikat et al. (1970a and 1970b) a charge density of $1/5000^{th}$ of that of a (III) plane would suffice to cause a gas discharge. This low percentage may have escaped detection in experiments designed to study the morphology of fracture planes (Meyer and Gragert, 1963). Meyer and Obrikat et al. (1970a and 1970b) concluded that the TL of NaCl is a result of charged fracture planes.

Wawner and Krukonis (1976) reported the TL of boron† filaments and suggested charged fracture plane induced gas discharge as the mechanism.

Wedgwood was the first of many to repeat TL experiments under water and oil. More recently experiments have been done under vacuum. The most informative of these experiments was performed by Zink (1978) who showed that sucrose crystals (vacuum degassed at 350 K to remove

---

†This is TL of an element. In the early days of TL it was thought - for no particular reason other than negative experimental results - that elements were not TL, see Imhof (1917).

nitrogen adsorbed in the crystal) emit no light when broken in nitrogen-free benzene. Zink also showed that atmospheric nitrogen is not necessary for the TL, but only absorbed or adsorbed nitrogen, because he saw nitrogen bands *in vacuo* from sucrose crystals that had not been outgassed. Chandra (1978) also attempted to eliminate the discharge part of TL by crushing sugar, and other materials, under liquid anhydrous diethyl ether. He still obtained weak TL, for which absorbed or adsorbed nitrogen may have been responsible. He concluded that part of the TL is due to gas discharge and part to an inherent excitation of the material. This conclusion was also reached by Wick (1937).

Hardy and Zink (1976) investigated the TL of the tetrahedral manganese (II) complex $Mn(Ph_3PO)_2\ Br_2$[†]. When crushed in air a nitrogen discharge emission as well as a manganese centred luminescence are seen, but when vacuum degassed and fractured under argon only the manganese centred TL is seen. In this case the metal centred luminescence is clearly not all due to photoluminescent excitation by the nitrogen discharge although a small part of it may be. A possible excitation mechanism is that of radiationless transition (Lin and Wutz et al., 1980). This mechanism proposes that the high pressures and temperatures near a crack tip perturb energy levels resulting in a population shift which occurs on or before relaxation of the pressure. Repopulation later takes place to restore equilibrium with an emission of photons. This mechanism is discussed in section 2.5.

[†]Ph represents the phenyl group C_6H_5

2.4.3 Review of Literature related to Nitrogen Gas Discharge Fracture Kinetics

Work has been reported on the kinetics of gas discharge TL, in particular from sugar crystals. Chandra (1976) has studied the time variation of TL intensity (wavelength integrated over the detector response) after the application of stress to a crystal. He found that the TL did not appear at the instant of impact of the stress, but after a certain time that depended on the magnitude of the stress. The decay time of TL from sugar crystals was found to be 4.2×10^{-3}s. The most recent summary of his work (Chandra and Zink, 1980) considers a) the relationship between TL and small sudden decreases in the fracture region of the force - compression curve; and b) the intensity versus time dependence of the TL, measured as a function of velocity of impact of a piston onto single crystals of tartaric acid, sugar, ammonium tartrate, lithium sulphate monohydrate or citric acid monohydrate. All these materials exhibit TL from the second positive system of molecular nitrogen.

To summarize sections 2.4.1 to 2.4.3; the appearance of the nitrogen gas discharge in a TL spectrum may be explained by electrical mechanisms. Mechanically generated free electrons lead to photon emission by electron impact on nitrogen molecules. The electrons could be generated by piezoelectric effects caused by compression of non-centrosymmetric crystals, by frictional electrification caused by rubbing two dissimilar materials together, or by electrification within a crystal caused by shear, cleavage, or rupture resulting in charged fracture planes. Piezoelectrification of a crystal by pressure requires the crystal to be noncentrosymmetric, but not all non-centrosymmetric crystals are TL, and some TL crystals are centrosymmetric.

2.5.1 Tribo-induced Crystal Photoluminescence

Longchambon (1925) first noticed that when a TL spectrum contained nitrogen gas discharge luminescence, and was accompanied by other luminescence, then the other luminescence often resembled crystal photoluminescence. He studied uranium nitrate, natural fluorite, uranium acetate and barium, calcium and magnesium platinocyanates, and noticed no differences between the TL that was not due to the gas discharge itself and the samples' own photoluminescence (PL) spectra. Nelson (1926) reached the same conclusion from a study of minerals. Wick (1940) studied the TL of sugar and noted that the addition of fluorescent oils or dyes to the sugar caused an increase in the intensity of the TL due to "fluorescence excited by the spark emitted when the crystals are broken". Since then many workers have concluded that a very likely outcome of a measurement of TL is that it will be similar to the sample PL at the same temperature. If the only effect of the mechanical energy applied during TL was to populate excited electronic states one would expect TL and PL to be identical. However differences have recently been observed and give evidence of perturbations to the emitting centres (Hardy and Baldwin et al., 1977).

2.5.2 Triboluminescence from Molecular Crystals

TL which may be associated with crystal PL can be divided into two groups:

a) Tribophosphorescence involves emission from an excited electronic state with a different spin from the ground state. This luminescence is spin forbidden.

Tribophosphorescence is excited in only a small number of organic crystals such as hexaphenylcarbodiphosphorane and phthalic anhydride,

and was formally classed as a phosphorescence on account of its lifetime (Zink, 1978). In these two compounds TL occurs at room temperature while PL occurs only at lower temperatures (≃ 77 K). This phenomena is discussed later.

The room temperature PL and TL spectra of N-acetylanthranilic acid are similar and were recorded by Hardy and Baldwin et al. (1977). The PL was classed as a phosphorescence on account of its lifetime. The structure of this material has been studied in detail recently (Mascarenhas, Almeida and Lechat, 1980). The material is highly TL and the crystal structure has interesting features relating to the possible TL excitation mechanism. It crystallizes in a polar noncentrosymmetric space group and its symmetry and crystal structure are appropriate for the building of large dipole moments due to mechanical stress.

b) Tribofluorescence involves emission from an excited electronic state with the same spin as the ground state. Tribofluorescence is exhibited by for example, phenanthrene, courmarin and methyl salicylate. The latter is a flavouring agent in confectionery and is in part responsible for the TL of a number of sugar based sweets (Angelos, Zink and Hardy, 1979).

Hardy and Baldwin et al. (1977) studied the TL of a number of molecular crystals. They found that the TL corresponds closely to crystal fluorescence in the case of courmarin. With this material the PL peak occurs at 389 nm, while the TL maxima is at 415 nm; both measured at room temperature. Structure on the fluorescence peak, with a 1630 cm^{-1} spacing that corresponds to the C = C stretch, was readily resolved. The PL peak shows no such structure. This appearance of detailed structure and the changes in relative intensities of emission bands in TL relative to PL appear to be

related to changes in the Franck-Condon factors (and hence the vibronic emission intensities) caused by the application of mechanical energy to the crystal, resulting in localised increases in temperature and pressure.

The observation of TL, but not PL at the same sample temperature, in for example phthalic anhydride, Zink (1978), may be the result of an enhancement of the luminescence intensity that occurs when the material is perturbed by high pressures or temperatures as a result of mechanical excitation. It is known that pressure can change both fluorescent and phosphorescent lifetimes and quantum yields, and it is possible that the emitting centres have a larger cross section for excitation by the TL process than by absorption of a photon.

2.5.3 Metal Centred Triboluminescence

TL may also be associated with the excited states of metal complexes and metal ions, or with traces of metal ion in an otherwise non TL matrix. Such TL is usually a localized transition involving d or f orbitals of the metal, and is often closely related to the PL of the material.

Hardy and Zink (1976) studied the TL of discrete metal complexes, in particular of tetrahedral manganese (II) complexes $Mn(Ph_3PO)_2Cl_2$, $Mn(Ph_3PO)_2Br_2$, $(MePh_3P)_2MnCl_4$ and $(Et_4N)_2MnBr_4$[†]. The TL is a superposition of $^4T_1 \rightarrow {}^6A_1$ manganese metal centred phosphorescence and a weak $^3\Pi u \rightarrow {}^3\Pi g$ nitrogen emission. The energy of the manganese-centred PL decreases linearly with pressure up to 42 k bar. Hardy and

---

[†] Ph represents the phenyl group C_6H_5-; Me represents the methyl group CH_3-; Et represents the ethyl group CH_3-CH_2-

Zink found that the TL and *atmospheric pressure* PL spectra were superimposable, and concluded that the emitting manganese centres in the TL experiment were at atmospheric pressure. Superimposable TL and PL spectra are common when the emissions are, as with these compounds, long lived spin forbidden phosphorescences. When the emitting state is short lived then significant differences between TL and PL spectra can be found. The differences (e.g. in courmarin as mentioned above) take the form of enhanced intensities on the sides of main peaks, and are accounted for by considering the effect of pressure on the emitting molecule.

A more critical test for determining the pressures of the emitting sites was made by Zink, Hardy and Gliemann (1980). They considered $((CH_3)_3NH)_3\ Mn_2Cl_2$, a linear chain Mn(II) compound containing both 6 and 4 fold coordinated Mn sites. Both TL and PL spectra exhibit simultaneous emissions from both sites. The TL is due to a $^4E \rightarrow {}^6A$ transition from the 6-fold coordinated Mn ion and $^4T \rightarrow {}^6A$ from the 4-fold coordinated Mn ion. A comparison of relative PL emission intensities as a function of pressure was made. This gives a more sensitive pressure measurement than previous methods (Hardy and Zink, 1976; discussed above) which looked at frequency (and hence energy) shifts with pressure. The TL spectrum was found to have within experimental error, the same intensity ratio as observed for PL at atmospheric pressure. This result argues strongly against a mechanism involving thermal population of excited states under high pressure *in this compound*. (Also to bring the ground and first excited state of this compound to an energy spacing of kT would require very high pressures of several hundreds of kilobars).

Zink (1974) reports the TL of uranyl nitrate hexahydrate as a

phosphorescence centred on the uranyl ion. A vibronic structure is observed in both TL and PL, where it has the same relative intensities and spacings. This is expected no matter whether excitation is nitrogen discharge induced or by high pressure radiationless repopulations, or by another method; because the lifetime of the TL is long compared to that of the mechanical relaxation in the crystal. The spectrum peaks at 540 nm and has a weak vibrational structure superimposed upon it, with a spacing of 840 cm^{-1}. This structure arises from the symmetric O-U-O stretch. The PL spectra of powder (large surface area per unit volume) and large crystals (small surface area per unit volume) show that for powders self absorption of the highest energy vibronic bands is less than the corresponding self absorption in large crystals. A comparison of the TL, with the PL spectra (Zink, 1974) for large crystals and powders of this material suggests that the TL originates primarily either from small crystals or from near the surface of large crystals.

TL also occurs in substances containing only a trace of metal ion impurity. An example is a rare earth metal in a calcium fluoride matrix. Energy transfer from the crystal bulk to the emitting metal impurities either by way of photoexcitation from nitrogen gas discharge luminescence, or by radiationless repopulation of levels due to high temperatures or pressures, precedes the localized metal centred emission. The luminescence is normally either from the d shell of a transition metal or the f shell of a lanthanide (rare earth). Early accounts note the TL of fluorite and one of the first attempts to measure the spectrum was made by Nelson (1926). He excited the luminescence with a wire brush held against a rotating wheel of the material. He found a single broad band at 570 to 590 nm with a maximum at 577 nm. With the benefit of hindsight this can certainly be said to have been due to a rare earth (RE) impurity.

The structure of fluorites is discussed in appendix 2. Wick (1937) studied the TL of fluorites produced by grinding the samples with a pestle and mortar. She used a direct-vision spectroscope and reported the difficulties caused by the dimness of the TL. She studied TL both before and after exposure to radium and tried to relate TL to thermoluminescence (THL). From a large collection of natural fluorites she found all to be TL, and that the TL was much brighter after exposure to radium for 18 to 24 hours. Most of the TL spectra that she *observed* resulted from experiments with artificially irradiated samples. With the IIT spectrograph I could *record* the fainter TL spectra of natural unirradiated fluorites, see chapter 3. The spectra that Wick observed were "well defined narrow bands, such as are characteristic of the fluorescence, phosphorescence and thermoluminescence spectra of the fluorites". To the limit of her resolution the TL spectra were the same as the PL and THL. Since Wick's (1937) work no detailed study has been made of the TL of fluorite crystals containing traces of metal ion.

TL of a rare-earth origin was reported by Hurt and McAvoy et al., (1966) but no detailed spectra were recorded. They found that the TL of europium tetrakis (dibenzoylmethide)-triethylammonium was so strong as to be visible in "broad daylight", at room temperature when crystals were broken with a glass rod or spatula in a test-tube. TL was detected with a monochromator and photomultiplier, at wavelengths characteristic of europium (III) fluorescence. Green TL characteristic of 4f-shell fluorescence in terbium was observed on breaking crystals of terbium tetrakis (dibenzoylmethide)-triethylammonium.

A number of studies of the alkali halides have been made (Meyer, Obrikat and Rossberg 1970a, 1970b; and Walton, 1977). The first detailed study by Longchambon (1925) was made by crushing 25 kg of

NaCl during an 8 hour photographic exposure. He recorded a nitrogen discharge spectrum but the sodium atom fluorescence (notably the D-lines at 589.0 and 589.6 nm) was not recorded. The most recent study using a monochromator and beam division apparatus (Krutyakova and Smirnov 1979) has resolved the sodium D-lines in the TL of sodium fluoride; but has failed to find the black body radiation reported by other workers (Walton, 1977 and Meyer, Obrikat and Rossberg, 1970). Krutyakova and Smirnov consider that nitrogen bands are caused by gas discharge luminescence in cracks filled with air, while the sodium lines are caused by the development of discharge processes in cracks isolated from the atmosphere. They also observed the 670.8 nm Li (I) line in the TL of lithium fluoride, together with some nitrogen bands. Their work highlights the need for good resolution when studying TL and they specifically note the problem of recording low intensity spectra with high resolution.

The TL of quartz was first observed by Beals (1923) and it may in part have a PL origin, due to impurities such as manganese that are often present in natural samples. Beals observed quartz TL by rubbing rotating quartz tubes together. He saw a continuous spectrum covering the visible and extending into the ultra-violet with no sign of any lines. He could "not excite the luminescence by friction with steel or any substance less hard than the quartz". Longchambon (1925) studied quartz TL due to fracture (not rubbing) and noted by eye a continuum, intense from 480 to 430 nm, weak below 430 nm, and with nitrogen discharge lines at 435.7 and 424 nm.

2.6 Triboluminescence of Other Origins

2.6.1 Organic Charge Transfer Complexes and Free Radicals

The spectroscopy of these complexes has been studied in detail by

Griegleb (1961). The only known example of charge transfer TL is from 1.1 phenanthrene/tetrachlorophthalic anhydride (Zink, 1978). Other photoluminescent charge-transfer complexes studied by Zink were found not to be TL.

The TL seen during the rupture of human bony tissue (Kranya, Knebs and Laizau, 1977) has been associated with the recombination of the free radicals which appear upon bond breaking, and also with the gas discharge produced during formation of new surfaces (microcracks).

2.6.2 Conduction Band to Valence Band Transitions

Jenny (1957) detected infra-red TL as GaAs, InP, Si and Ge were sand blasted, and noted that the smaller their energy gap the further into the infra-red was their TL emission.

Takada (1977) studied the TL of silver halide powder that was mechanically abraded at liquid nitrogen temperature. He found a green peak at 550 nm and a red peak at 610 nm, from silver iodobromide and silver bromide respectively. These peak positions were the same in PL and thus gave direct evidence that electrons could be excited to the conduction bands in these silver halides by mechanical abrasion. These observations led Takada to propose a mechanism for photographic pressure effects. Electrons generated by pressure cause developable silver specks in the same way as electrons generated by light.

2.6.3 Thermal Radiation

Continuous TL emission across the whole spectrum is sometimes explained as thermal radiation from a small hot region within the sample (Walton, 1977). The hot region could occur at the tip of a

growing crack as a result of the release of plastic deformation energy, it could occur as a result of frictional heating or it could result from burning. For example burning iron flakes are produced when an iron rod is touched against a grinding wheel. The spectra so produced have been studied by Ohman (1978, 1979) who claims to have found various molecular and radical (CH, Fe, C_2 and CN) lines as well as a high temperature continuum. He had difficulty in recording the low intensity spectra. I recorded the light emission from cut steel and have discussed the emission in more detail in chapter 4.

A broad featureless emission has been observed by some workers (Meyer, Obrikat and Rossberg, 1970 and Walton, 1977) in the TL of alkali halides. It has been attributed to both black body radiation and conduction band to surface band transitions. However, as mentioned above, Krutyakova and Smirnov (1979) observed the TL of sodium fluoride and saw some lines characteristic of sodium emission, but recorded no continuous emission at all.

The validity of the thermal radiation explanation of TL is examined in more detail in chapter 4.

2.6.4 Tribo-induced Electroluminescence

Wick (1937) noted that the mineral sphalerite (ZnS with Mn and other impurities) gave TL which was fundamentally different from that of the fluorites. The TL intensity was not increased by radium exposure and samples did not exhibit tribo-induced thermoluminescence. Wick found that the TL bore no relation to THL and did not depend upon previous excitation. She concluded that the emission was characteristic of the material itself and was not dependent on any other excitation than mechanical breaking or cutting. Meyer and Obrikat (1969), and Thiessen and Meyer (1970) studied the TL spectra of ZnS doped with

Cu, Ag and Mn. The spectra were found to correspond to the PL spectra with small shifts in the energies of the main peak. All these shifts in the TL maxima were in the same direction as those observed in PL when a hydrostatic pressure of 2.5 to 3.7 kilobars is applied to a crystal of the material. However the TL spectra very closely match the (room temperature and atmospheric pressure) EL spectra which suggests that the TL has an electrical origin, rather than one of high pressure PL. No gas discharge has been observed on fracturing ZnS except by Chudacek (1966) who recorded a nitrogen discharge of about 2% of the total ZnS TL intensity - and this probably had a static electricity origin due to discharge from a plastic window in his crushing apparatus. Experiments by Scarmozzino (1971) have shown that large hydrostatic pressures, capable (by piezoelectric coefficient calculations) of giving a piezoelectric polarisation large enough to excite TL, do not in practise have this effect. He concluded that ZnS TL is not due to a piezoelectrically induced field across the bulk of a crystal.

The literature on ZnS TL is reviewed by Walton (1977) who concludes that the TL which occurs on crushing ZnS crystals is due to excitation of EL centres by moving charged dislocations. Under hydrostatic pressure the dislocations do not move.

CHAPTER 2

APPENDIX 1

The Nitrogen Gas Discharge Spectrum

A large number of band systems are attributed to the neutral nitrogen molecule. In nitrogen discharge tubes the first, second and third positive systems are the most readily seen. The second positive system is the most easily obtained in a discharge through air, and is the system most often observed in TL. The positive systems of the nitrogen discharge are so called because they are most readily observed in the positive column of a discharge tube. The first negative system is seen in the negative glow region of such a tube.

Electrons in a nitrogen molecule move about a field which is cylindrically symmetric with respect to the internuclear axis. The component of orbital angular momentum of the electrons about the internuclear line is $\frac{\Lambda h}{2\pi}$ and the component of spin angular momentum is $\frac{Sh}{2\pi}$. The values Λ = 0, 1, 2 or 3 are represented by Σ, Π, Δ or Φ respectively. An electronic state of the molecule is designated by $^{2S+1}\Lambda$ for example $^{3}\Pi$. Orbital wavefunctions can either be symmetric or antisymmetric with respect to the centre of symmetry of the molecule, and this property is indicated by a "g" or "u" respectively (from the German *gerade* or *ungerade*) added to the state designation e.g. $^{3}\Pi u$. In addition a "+" or "-" is sometimes added (e.g. $^{3}\Sigma_{g}^{+}$) to indicate symmetry or antisymmetry with respect to reflection in any plane through the intermolecular axis.

Part of the energy level diagram for molecular nitrogen is reproduced in figure 2.2, where energies of electronic states of the

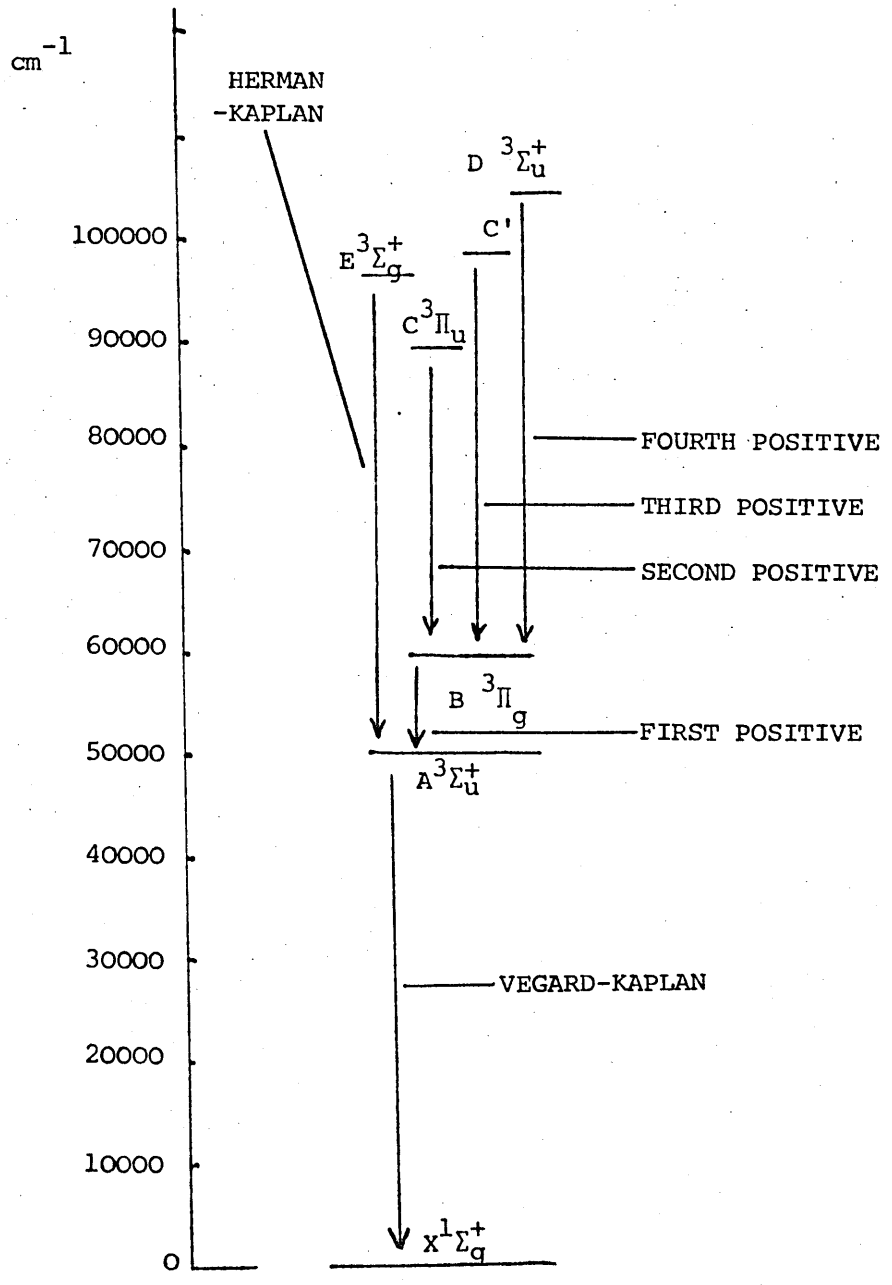

FIGURE 2.2 PART OF THE ENERGY LEVEL DIAGRAM OF MOLECULAR NITROGEN (after Pearse and Gaydon, 1963). Electronic states are shown. Vibrational levels superimposed on each electronic state are not shown, for clarity. The second positive system is normally seen in TL. Further details are in chapter 2, appendix 1.
Letters A, B, C, C', D, E and X are conventional labelling.

molecule are shown. Onto these are superimposed vibrational and rotational structure of typical spacing 1000 cm^{-1} and 10 cm^{-1} respectively.

In the nitrogen gas discharge spectrum shown in figure 2.1 each line corresponds to different initial or final vibrational levels within the same electronic transition $^3\Pi u \rightarrow {}^3\Pi g$. The vibrational quantum numbers are included in table 2.1. In addition every observed line has rotational structure which is not resolved in figure 2.1. Further details are given by Herzberg (1950 and 1971).

CHAPTER 2

APPENDIX 2

Fluorites

CaF_2 in its naturally occurring form is known as fluorite. Each Ca^{2+} ion is surrounded by 8 equivalent nearest neighbour F^- ions, forming the corners of a cube, of which Ca^{2+} is at the centre.† The structure has a face centred cubic translational group and a space lattice of symmetry O_h^5. Fluorite is not piezoelectric. The lattice is stable and strongly bound with a melting point of 1360°C (Hayes, 1974). The forbidden band gap is 12 eV.

Artificial crystals may be grown by crystallization from the molten salt, and the crystal readily accepts rare earth (RE) dopants. This is important because early work into the fluorescent properties of natural fluorite revealed the source of the luminescence as traces of rare earth metal ions (Haller, Lippmann and Bouty, 1909). CaF_2 is a convenient anhydrous host for these ions. The rare earths normally exist in the RE^{3+} configuration substituting for a Ca^{2+} ion - with the exception of europium which is normally found as Eu^{2+}. With the RE^{3+} configuration an extra F^- ion in a nearby interstitial site retains charge neutrality. In general form the rare earth inner shell configuration is

$$1s^2\ 2s^2\ 2p^6\ 3s^2\ 3p^6\ 3d^{10}\ 4s^2\ 4p^6\ 4d^{10}.$$

The outer shell configuration for each atom and ion is shown in table 2.2. Part of an energy level diagram for triply ionized rare earths is reproduced in figure 2.3. The ground states are found by application of Hund's rules. The divalent ions' level spacings are

† Each F^- ion has about it a tetrahedron of Ca^{2+} ions.

Element	Atomic number	RE^{o}	RE^{2+}	RE^{3+}
Ce	58	$4f^{1}\ \{5s^{2}5p^{6}\}\ 5d^{1}\ \{6s^{2}\}$	$4f^{1}\ \{5s^{2}5p^{6}\}\ 5d^{1}$	$4f^{1}\ \{5s^{2}5p^{6}\}$
Pr	59	$4f^{3}\ \{5s^{2}5p^{6}\}\text{-}\{6s^{2}\}$	$4f^{3}\ \{5s^{2}5p^{6}\}$	$4f^{2}\ \{5s^{2}5p^{6}\}$
Nd	60	$4f^{4}\ \{5d^{2}5p^{6}\}\text{-}\{6s^{2}\}$	$4f^{4}\ \{5s^{2}5p^{6}\}$	$4f^{3}\ \{5s^{2}5p^{6}\}$
Pm	61	$4f^{5}\ \{5s^{2}5p^{6}\}\text{-}\{6s^{2}\}$	$4f^{5}\ \{5s^{2}5p^{6}\}$	$4f^{4}\ \{5s^{2}5p^{6}\}$
Sm	62	$4f^{6}\ \{5s^{2}5p^{6}\}\text{-}\{6s^{2}\}$	$4f^{6}\ \{5s^{2}5p^{6}\}$	$4f^{5}\ \{5s^{2}5p^{6}\}$
Eu	63	$4f^{7}\ \{5s^{2}5p^{6}\}\text{-}\{6s^{2}\}$	$4f^{7}\ \{5s^{2}5p^{6}\}$	$4f^{6}\ \{5s^{2}5p^{6}\}$
Gd	64	$4f^{7}\ \{5s^{2}5p^{6}\}5d^{1}\ \{6s^{2}\}$	$4f^{7}\ \{5s^{2}5p^{6}\}\ 5d^{1}$	$4f^{7}\ \{5s^{2}5p^{6}\}$
Tb	65	$4f^{8}\ \{5s^{2}5p^{6}\}5d^{1}\ \{6s^{2}\}$	$4f^{8}\ \{5s^{2}5p^{6}\}\ 5d^{1}$	$4f^{8}\ \{5s^{2}5p^{6}\}$
Dy	66	$4f^{10}\{5s^{2}5p^{6}\}\text{-}\{6s^{2}\}$	$4f^{10}\{5s^{2}5p^{6}\}$	$4f^{9}\ \{5s^{2}5p^{6}\}$
Ho	67	$4f^{11}\{5s^{2}5p^{6}\}\text{-}\{6s^{2}\}$	$4f^{11}\{5s^{2}5p^{6}\}$	$4f^{10}\{5s^{2}5p^{6}\}$
Er	68	$4f^{12}\{5s^{2}5p^{6}\}\text{-}\{6s^{2}\}$	$4f^{12}\{5s^{2}5p^{6}\}$	$4f^{11}\{5s^{2}5p^{6}\}$
Tm	69	$4f^{13}\{5s^{2}5p^{6}\}\text{-}\{6s^{2}\}$	$4f^{13}\{5s^{2}5p^{6}\}$	$4f^{12}\{5s^{2}5p^{6}\}$
Yb	70	$4f^{14}\{5s^{2}5p^{6}\}\text{-}\{6s^{2}\}$	$4f^{14}\{5s^{2}5p^{6}\}$	$4f^{13}\{5s^{2}5p^{6}\}$
Lu	71	$4f^{14}\{5s^{2}5p^{6}\}5d^{1}\ \{6s^{2}\}$	$4f^{14}\{5s^{2}5p^{6}5d^{1}\}$	$4f^{14}\{5s^{2}5p^{6}\}$

TABLE 2.2 ELECTRONIC CONFIGURATION OF RARE EARTH ATOMS AND IONS

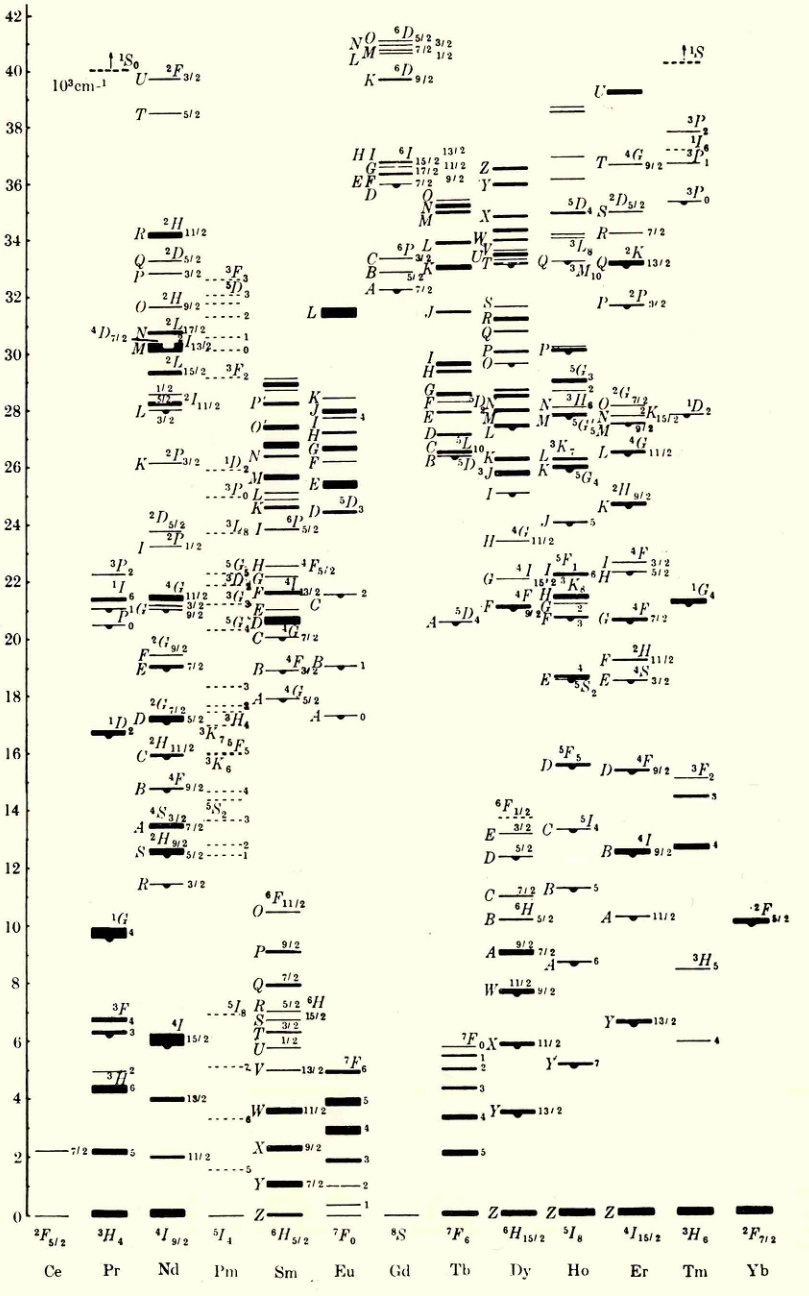

FIGURE 2.3 ENERGY LEVEL DIAGRAM FOR TRIPLY IONIZED RARE EARTHS IN CUBIC SITES.

Fluorescing levels are indicated by pendant half-circles.

After Dieke, 1968.

similar to those of the trivalent ions but with a 15% energy scale reduction. Figure 2.3 shows levels for the RE^{3+} configurations given in table 2.2. Other configurations like $4f^{K-1}$ 5d, $4f^{K-1}$ 6s and $4f^{K-1}$ 6p have energy level differences which are in the ultra-violet. RE^{2+} energy levels of $4f^{K}$ and $4f^{K-1}$ 5d configurations have energies in the same order as the isoelectronic RE^{3+} ion and energy level differences that are in the visible.

In summary visible emission can occur from a $4f^{K} \rightarrow 4f^{K}$ level in RE^{3+} and RE^{2+} ions; and from a $4f^{K-1}$ 5d $\rightarrow 4f^{K}$ level in RE^{2+} ions. Electric dipole transitions between states of the same configuration are parity forbidden (e.g. $4f^{K} \rightarrow 4f^{K}$) but this is strictly true only for free ions and is not obeyed in crystals due to interactions (crystal field and impurity) mixing different parity states.

Perturbation of the energy levels of an ion due to the field of the surrounding ions is a crystal field perturbation. An energy level diagram can be characterized by L, S and J. The last mentioned is a good quantum number provided that crystal field energies are small (less than spin-orbit interaction). Crystal field perturbations are weak for f electrons in incomplete 4f shells. This is because the f electrons are beneath the $5s^2$ and $5p^6$ outer shells and have a range which means little overlap with neighbouring ions.

For $4f^{K} \rightarrow 4f^{K}$ transitions crystal field splittings lead to a fine structure (of order 100 cm^{-1}; see chapter 3, appendix 1), narrow lines and a slight shift from one crystal to another. This small displacement of narrow crystal field lines makes assignment of transitions between levels easy; however matching the fine structure due to crystal field splitting of levels is more complicated. Different crystal field

splittings result from the same ion in non-equivalent positions e.g. in cubic and tetragonal sites.

The $4f^{K-1}$ 5d → 4f transitions are broad bands (≃ 1500 cm^{-1}), they are parity allowed, and involve d electrons with a crystal field perturbation which is much greater than that of f electrons. The d electron crystal field splitting (≃ 1500 cm^{-1}) can be greater than the spin orbit interaction. As a result of this large crystal field perturbation to $4f^{K-1}$ 5d energy levels there is a greater energy difference between equivalent atoms in different crystal sites than for $4f^{K}$ levels. Highly coloured crystals normally contain RE^{2+} ions with their broad parity allowed absorption while crystals containing only RE^{3+} ions appear clear because only weak parity forbidden absorption occurs.

In summary, transitions between energy levels of a $4f^{K}$ configuration will give line spectra that vary by a few nm from crystal to crystal dependent on the exact crystal field perturbation. Transitions from levels of a $4f^{K-1}$ 5d configuration to levels of a $4f^{K}$ configuration (which are in the visible for RE^{2+} ions only) are broad and can mask the weaker $4f^{K} \rightarrow 4f^{K}$ parity forbidden emission.

CHAPTER 3

TRIBOLUMINESCENCE LINE SPECTRA

3.1 Introduction

The purpose of recording TL spectra was to analyse the emission in terms of known structural and optical properties of the samples concerned, and to determine the excited state origins and/or mechanisms of population of these states. I have investigated the effect of different fracturing techniques on the recorded spectra (where more than one technique gives sufficient TL intensity for a record to be made) and have made some comparisons with thermoluminescent (THL) and photoluminescent (PL) spectra.

The TL spectra that were recorded on the IIT spectroscope can be divided into two groups

a) Continuous TL that extends over all or most of the range 400 to 700 nm; the subject of chapter 4.

b) Line Spectra; the subject of this chapter. Different types of excited state origin may be attributed to the two groups.

A summarizing list of all the materials which I found to exhibit TL is given below, after a description of the TL fracturing equipment, and then the line spectra are considered in detail.

3.2 Triboluminescence Fracturing Equipment

Ideally a study of TL would include a record of any variation in the TL of a particular material as it was fractured along a number of different crystallographic planes. Voigt (1913) showed for sucrose crystals that no TL occurred for fracture along the piezoelectric axis,

but TL occurred for all other planes. Unfortunately I have found that a *spectral* study requires a greater light intensity than can be produced by fracturing one crystal along a known plane so all my TL, both line spectra and continua, have been produced by either a) cutting, or b) crushing a number of crystals at once. A good review of early TL crushers is given by Walton (1977). The only published work that has appeared since then on this subject is by Chandra and Elyas (1977) who describe a method of dropping weights with almost zero velocity onto crystals. I have investigated a number of fracturing techniques, listed below under a) to d).

a) A domestic food blender with a light guide placed in the top of the blending jar, and leading to the spectrograph slits. This was successful in producing bright TL if a large volume of crystals was available. One difficulty with this apparatus was that the end of the light guide soon became covered in an opaque layer of powder. Another difficulty was the high rate of crystal consumption compared with other techniques. For these two reasons the blender was not used for any of the main TL experiments.

b) Crushing a crystal in the jaws of a pair of high ratio plier type cutters was a method used for materials that are highly TL, such as sugar and some of the doped fluorites. The crystal could be crushed either in the sample volume of the condenser system, in front of the spectrograph slits (if care was taken not to damage the slits), or in front of the end of a fibre optic light guide that led to the slits.

c) For the beam division system a "screw down" crusher was built (see figure 3.1). This crushed the sample onto a glass plate, either positioned over the beam division system described in chapter 1, or directly over a photomultiplier. The photomultiplier signal could be

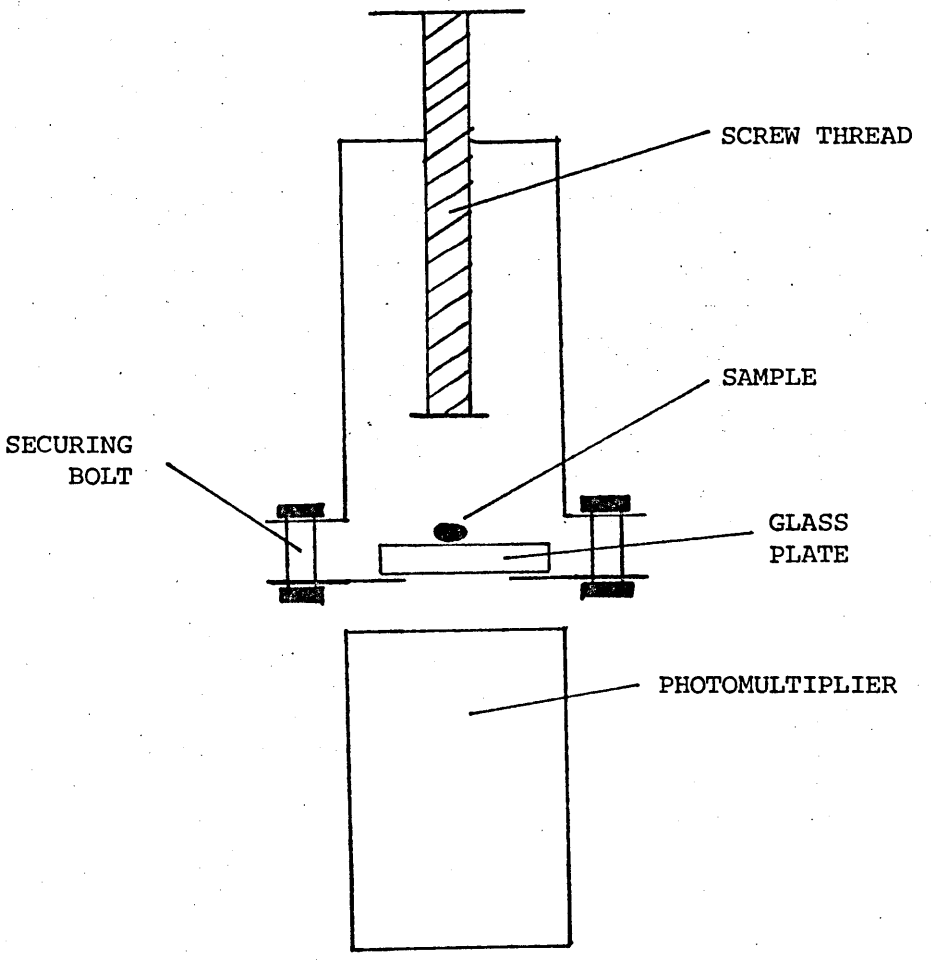

FIGURE 3.1 "SCREW DOWN" CRYSTAL CRUSHER

See also figure 1.28

taken directly to a storage oscilloscope and records of TL intensity versus time could be made. The technique is similar to that used by Chandra and Zink (1980). This system was sometimes used in assessing whether materials were or were not TL before subjecting them to a full IIT spectrographic analysis.

d) The brightest TL spectra could be recorded if samples were slowly powdered by pressing them against a rotating diamond saw blade† with a normal force of between 30 and 90 grams weight. I found that the spectral information was unaffected by variations in this force.

The cutting technique had the advantage of consuming much less material than other fracturing methods. The saw rotated at 1440 rpm (described below as high speed) or at 480 rpm (low speed). One end of a light guide of circular cross section was positioned to one side of the cutting blade adjacent to the cutting surface, so that it collected any light emitted near the cutting surface. The other end of the light guide (one metre long, 10 mm diameter,with a slit end of 20 x 3.9 mm, manufactured by TBL, 200 Harehills Lane, Leeds) which fanned out into a slit shape, illuminated the IIT spectrograph slits. The spectrograph was described in detail in chapter 1. When a sample (such as glass or calcite) was cut on the saw the (undispersed) emission was usually just visible to a fully dark adapted eye. The radiation collected by the light guide and directed into the IIT spectroscope would normally produce a photographic negative that was suitable for densitometry with between 10 and 30s duration of camera exposure.

---

†The blade was manufactured by Felker Rimlock Inc. U.S.A. It was 0.6 mm thick and 152 mm diameter. The blade was mounted in a "Robilt" saw, model M6, imported by Hirsh Jacobson Merchandising Co. Ltd., 91 Marylebone High Street, London, W.1.

Most of my TL results, as stated above, were recorded while cutting a sample with the diamond saw because of the high light output per given mass of crystal. Particularly bright specimens were also positioned in the centre of the sample volume of the condenser system (described in chapter 1) and crushed with the high ratio pliers.

3.3.1 Introduction to Triboluminescence Results

A number of the materials examined gave no TL as judged either by a dark adapted eye, or recorded on the IIT spectrograph. These materials, all cut and crushed at room temperature, were gallium phosphide (band gap 2.24 eV), silver chloride (as the mineral cerargyrite, from Chile), and the minerals dolomite ($CaMg(CO_3)_2$) and thenardite (Na_2SO_4). With some materials a very faint TL could be recorded on the IIT spectrograph without dispersion (grating set to diffract zero order) but not when the emission was dispersed. These materials were polypropylene, high density polythene, barite ($BaSO_4$), calcite ($CaCO_3$), calamine ($Zn_4Si_2O_7(OH)_2.H_2O$), celestite ($SrSO_4$), fluorite (CaF_2) containing traces of holmium, erbium and lutetium but not other rare earth impurities, selenite ($CaSO_4 \cdot 2H_2O$ a transparent, well crystallized gypsum), magnesite ($MgCO_3$) and sylvite (KCl). Materials that exhibited TL which could be recorded with sufficient intensity to enable a useful densitometer trace to be obtained are listed in table 3.1. Of these materials the TL of yellow calcite, sugar, fluorite doped with terbium, and quartz (SiO_2) were all recorded with both crystal crushing and diamond saw cutting. The TL of the other materials was only bright enough or of a long enough duration to record when samples were cut on the diamond saw.

Of the materials whose TL was recorded with both crushing and cutting, only quartz gave a different spectrum in each case. These differences in the quartz TL are discussed in chapter 4. The main TL line spectra

Amethyst (quartz with manganese impurities)

Armour plate Glass

Calcite (Yellow, Derbyshire)

Fluorite (Artificially doped with dysprosium, europium, samarium or terbium†)

Fluorite (Natural from Cumbria and Co. Durham)

High Density Lead Glass

Polycarbonate

Polysulphone

Pyrex Glass

Quartz

Soda-lime Glass

Steel

Sugar

Zircon ($ZrSiO_4$)

†TL was also observed from a gadolinium doped sample, but was found to be due to impurities rather than the gadolinium itself.

TABLE 3.1 MATERIALS WHOSE TL SPECTRA WERE RECORDED.

that will be discussed in this chapter are listed in table 3.2. The fluorites were studied in particular detail because of their availability and bright TL, and because they have been well characterized in other ways (cathodoluminescence and photoluminescence; see for example El'yashevich, 1953 and Hayes, 1974).

3.3.2 Sugar

Whether cut or crushed sugar crystals give the TL spectrum shown in figure 3.2. The spectrum, which has been reported by many people, is a nitrogen gas discharge as discussed in chapter 2.

3.3.3 Polymers

A number of polymers were cut with the diamond saw to see if any continuous radiation was present, although this was thought to be unlikely since previous experiments (Fox and Fuller, 1971) have indicated polymer crack tip temperatures of 700 to 800 K. There would be no significant radiation in the visible region of the spectrum for temperatures of this magnitude. I found no evidence of any continuous emission but polycarbonate and polysulphone gave the familiar nitrogen gas discharge spectrum (see figures 3.3 and 3.4). It is possible that the discharge is due to a build up of static electric charges on the samples, which are good insulators. Light emission from polypropylene and high density polythene was very weak and no nitrogen gas discharge nor continuum was recorded.

3.3.4 Calcite (Yellow, Derbyshire)

The TL of yellow calcite has not been studied before. It is visible to the dark adapted eye, and the same TL spectrum is recorded whether the material is cut or fractured, see figure 3.5. There are three broad peaks centred around 562, 602 and 645 nm. The three peaks are

MATERIAL	GRATING USED AND TL WAVELENGTH RANGE RECORDED†	COMMENTS
Sugar	600 l mm^{-1}	
Polycarbonate	600 l mm^{-1}	
Polysulphone	600 l mm^{-1}	
Calcite (Yellow, Derbyshire)	600 l mm^{-1}	Natural THL and PL spectra also recorded
≃ 1%†† Terbium doped fluorite	"Spex Minimate" 520-610 nm	PL spectra also recorded
	"Spex Minimate" 430-520 nm	
	600 l mm^{-1}	TL spectra recorded at room temperature
	600 l mm^{-1}	and ≃ 80 K
≃ 1% Europium doped fluorite	600 l mm^{-1}	PL spectra also recorded
≃ .01% Gadolinium doped fluorite	600 l mm^{-1}	
≃ 1% Dysprosium doped fluorite	1800 l mm^{-1} 430-520 nm	
	1800 l mm^{-1} 520-600 nm	
	600 l mm^{-1}	PL spectra also recorded
≃ 1% Samarium doped fluorite	600 l mm^{-1}	PL spectra also recorded
Purple fluorite, Weardale, Cumbria	600 l mm^{-1}	
Yellow fluorite, Scoredale, Co.Durham	600 l mm^{-1}	
Green Fluorite, Heights Quarry, Cumbria	600 l mm^{-1}	TL of a natural sample
	1800 l mm^{-1} 530-600 nm	TL of a natural sample
	600 l mm^{-1}	TL of a heated (thermally drained) sample
	600 l mm^{-1}	TL of an irradiated sample
		THL of a natural samples was also recorded
Faint Purple fluorite, Weardale, Cumbria	600 l mm^{-1}	
Blue fluorite, Cumbria	600 l mm^{-1}	

† The 600 l mm^{-1} grating has a wavelength range of about 400 nm to 750 nm

††Atomic concentration

TABLE 3.2 LIST OF THOSE TL LINE SPECTRA WHICH ARE DESCRIBED IN CHAPTER 3

Samples were cut on the rotating diamond saw with a light guide directing the TL to the IIT spectrograph. The IIT EHT was set at 33 kV. Spectral correction was not applied.

This is a copy of figure 2.1

FIGURE 3.2 TL OF SUGAR

Mercury calibration lines can be seen at 404.7, 435.8, 546.1, 577.0 and 579.1 nm.
The wavelengths of seven TL lines are marked

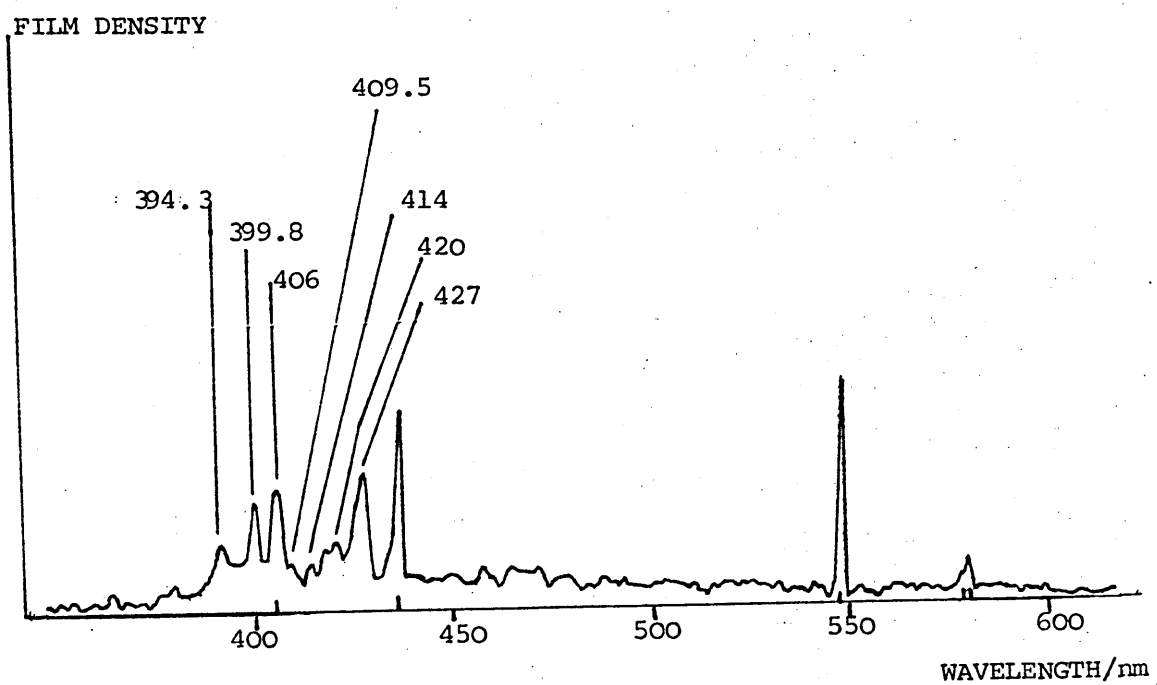

FIGURE 3.3 TL OF CUT POLYCARBONATE

Mercury calibration lines can be seen at 404.7, 435.8, 546.1, 577.0 and 579.1 nm

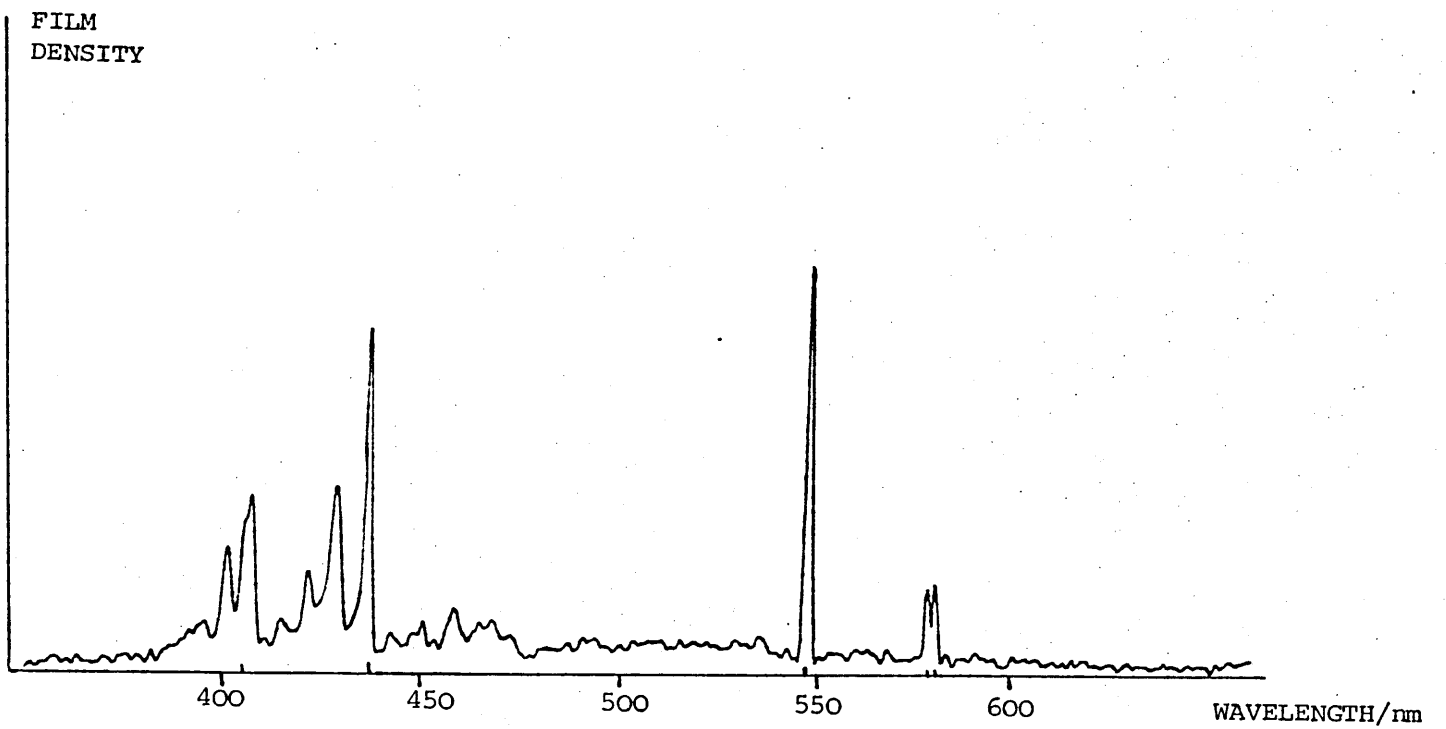

FIGURE 3.4 TL OF CUT POLYSULPHONE

Mercury calibration lines can be seen at 404.7, 435.8, 546.1, 577.0 and 579.1 nm

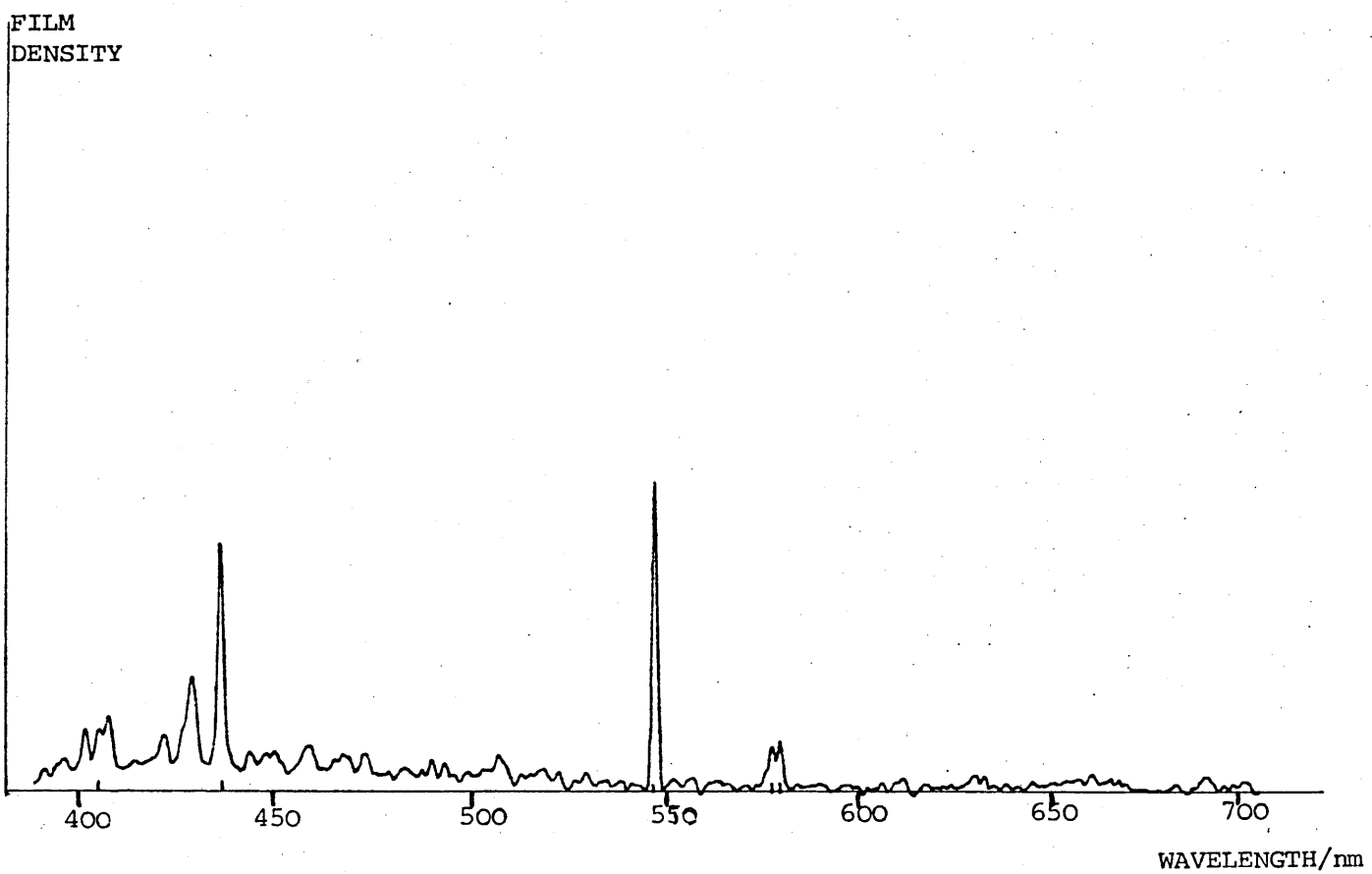

FIGURE 3.5 TL OF YELLOW CALCITE

Mercury calibration lines can be seen at 404.7, 435.8, 546.1, 577.0 and 579.1 nm

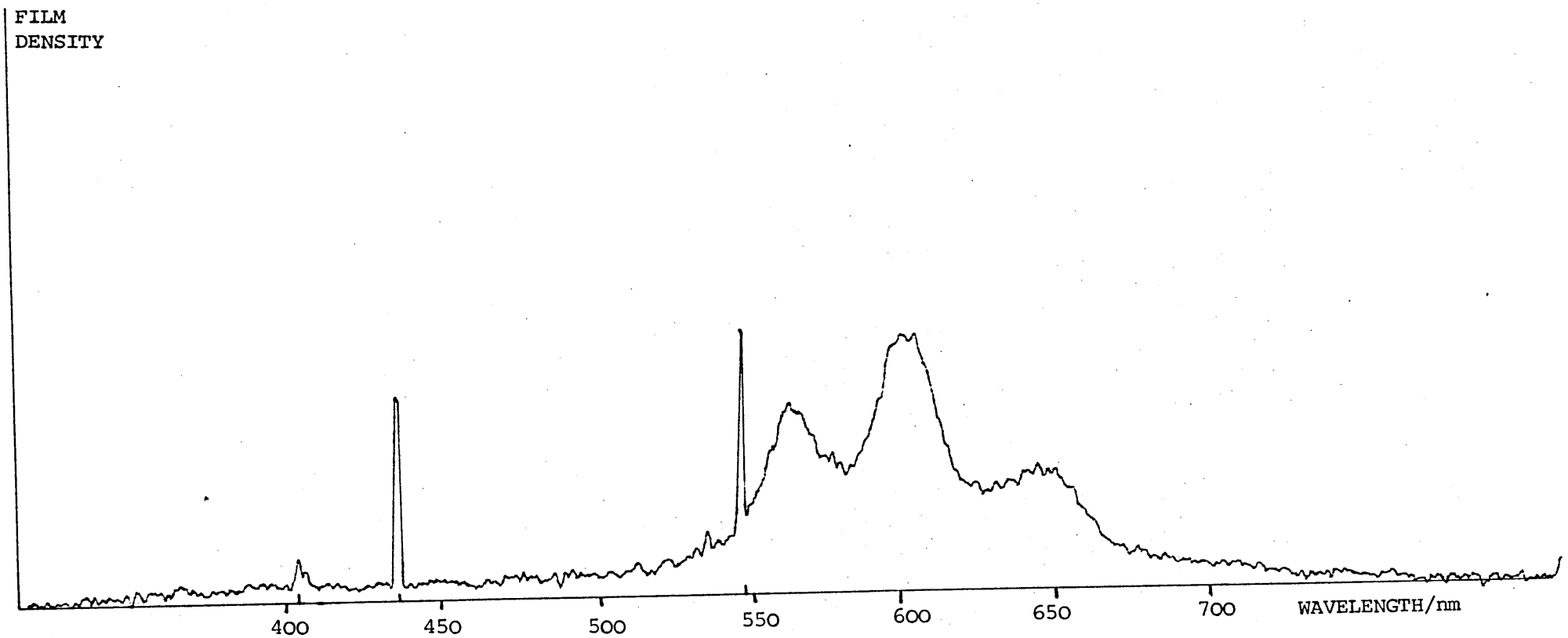

visible in PL with 400 nm excitation, see figure 3.6. A sample of calcite that had been thermally drained by heating to 500°C for 30 minutes, produced faint TL compared with the unheated material. Only the 645 nm peak could be faintly recorded. The PL of this heated sample, although much weaker than before, still included all three peaks at 562, 602 and 645 nm. After subsequent irradiation† a thermally drained sample gave almost as much TL as a sample that had not been thermally drained.

The natural THL†† of this material is a continuum when heated between 90°C and 180°C above room temperature, see figure 3.7. From 180°C to 350°C above room temperature the THL (see figure 3.8) contains two (at 562 and 602 nm) of the three peaks that were seen in TL.

That thermally drained samples show much fainter TL than undrained samples implies that the TL of this sample could be associated with THL. Perhaps the TL is just THL induced by high temperatures at the cutting surface, but in that case the two spectra would be expected to be identical. Observed THL wavelengths depend on the nature of the centres with which the electrons recombine after thermal release from storage traps. That three peaks are visible in the TL spectrum of the material may be due to an additional mechanism which operates under TL excitation such as radiationless repopulation (Lin and Wutz et al., 1980) and is responsible for the appearance of the 645 nm line, whereas electrons released from traps in THL may only excite the emission centres at 562 and 602 nm. The three peaks at 562, 602 and 645 nm could be associated

---

†Irradiation with a thermoluminescence saturation x-ray dose was kindly carried out by Dr. N. Debenham, Department of Archaeology, University of Oxford.

††"Natural" refers to a sample which has not been artificially heated or irradiated.

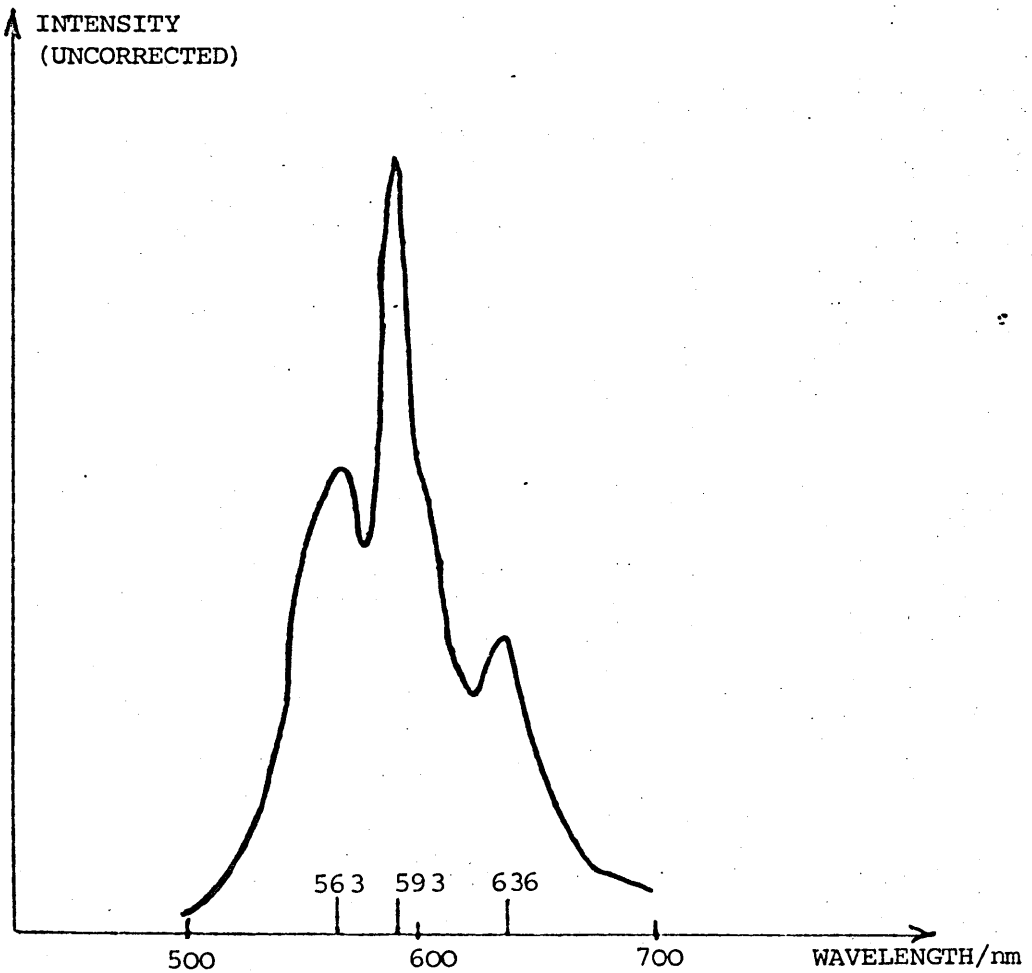

FIGURE 3.6 PL OF YELLOW CALCITE

400 nm excitation.
Recorded on S20 photomultiplier

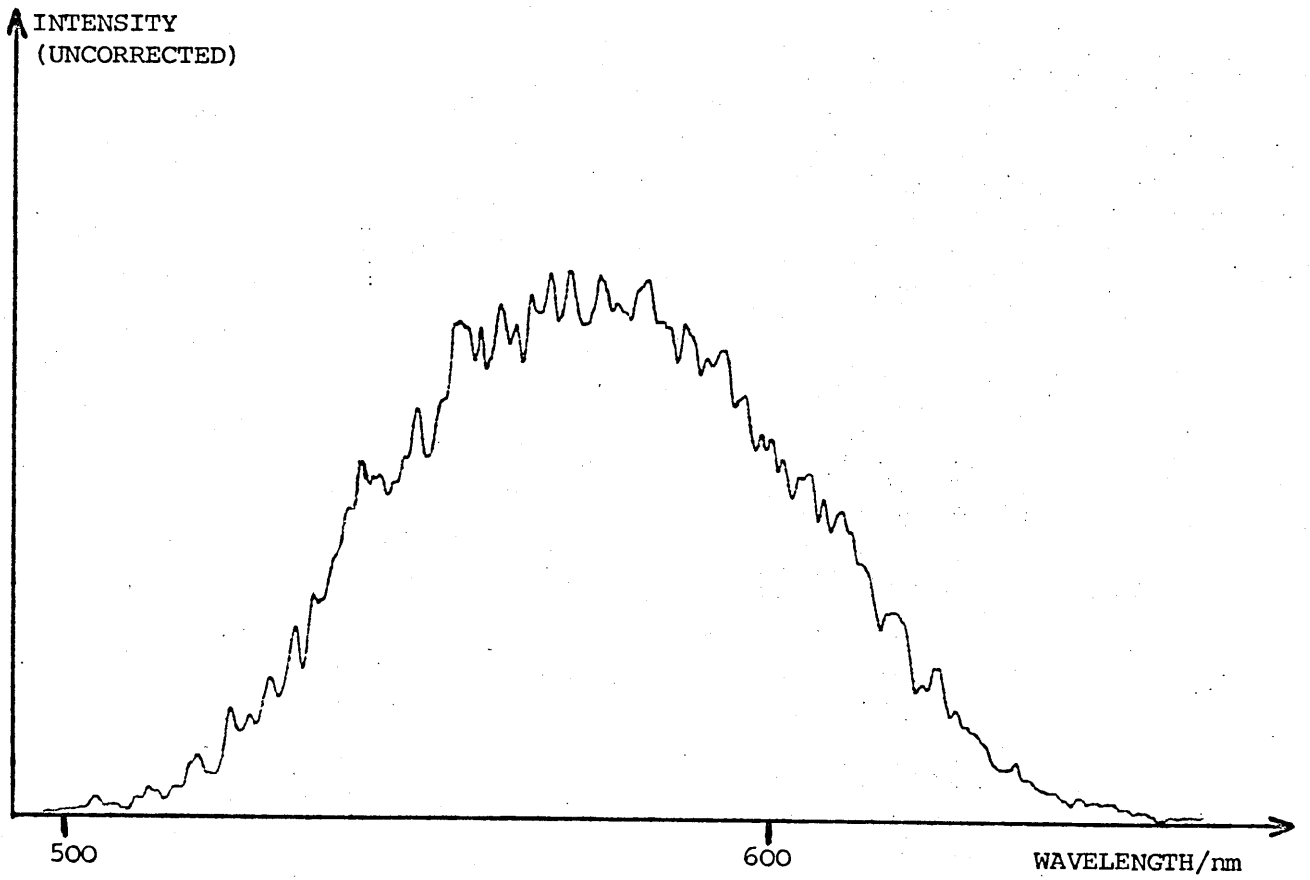

FIGURE 3.7 THL OF YELLOW CALCITE 90° to 180° ABOVE ROOM TEMPERATURE.
This is THL of a natural (unirradiated) sample.

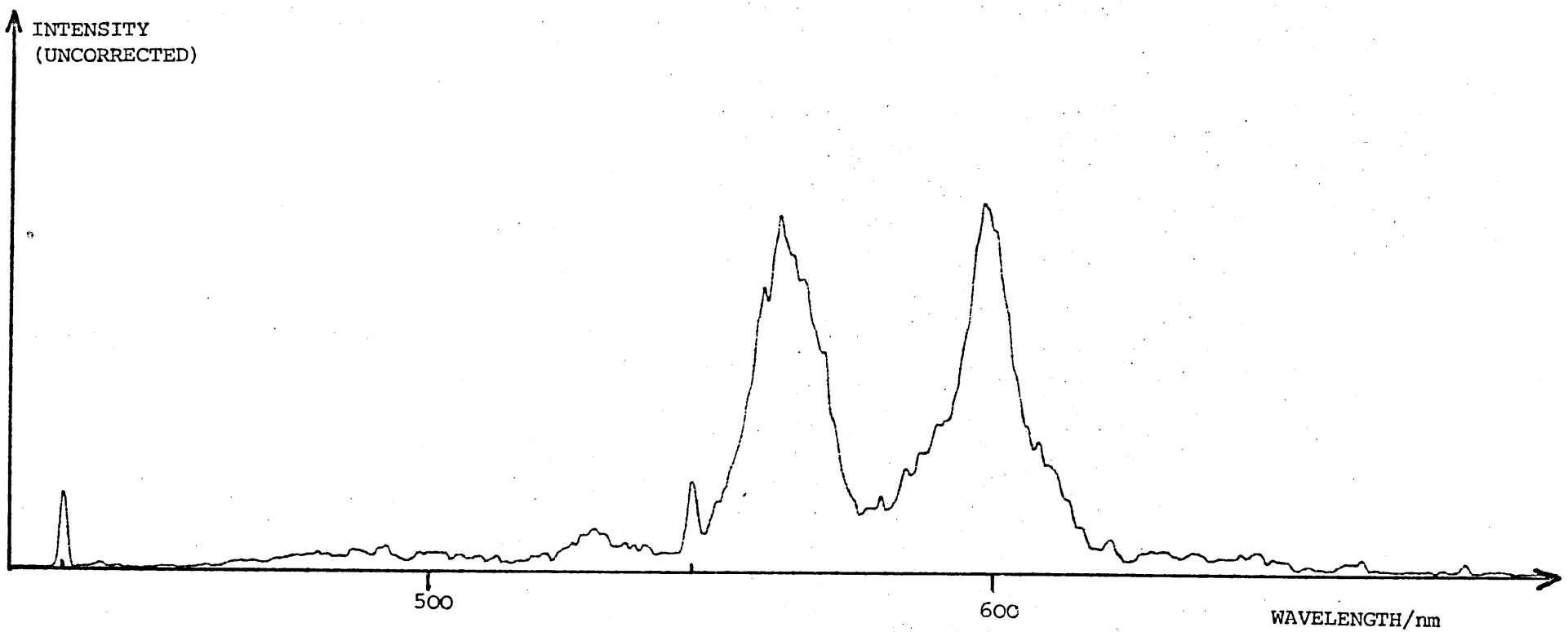

FIGURE 3.8 THL OF YELLOW CALCITE 180° to 350°C ABOVE ROOM TEMPERATURE.

This is THL of a natural sample. Mercury calibration lines are visible at 435.8 and 546.1 nm.

with the rare earth samarium (Sm) (see figure 3.26 which is discussed in section 3.3.9). The TL may be a combination of emission from Sm^{3+} levels populated by radiationless excitation as a result of high temperatures and pressures near the cutting surface as well as emission from some THL populated levels.

That the TL of a thermally drained sample can be almost completely restored by irradiating the sample suggests that the electron traps in the material which are emptied by heating (THL) can be refilled by irradiating the material

RE^{2+} ions, which have a strong absorption in the visible, could account for the yellow colouring of this calcite sample.

This calcite also exhibits tribo-induced thermoluminescence (first studied in detail by Nyswander and Cohn, 1930). A thermally drained specimen (which, of course, will give no THL) when crushed and reheated again, does then emit THL radiation. This THL, which was induced by crushing the sample, is called tribo-induced THL.

It is known that THL can be drained by ultra-violet light so it is possible that cutting a material, and producing an ultra-violet nitrogen gas discharge during this process, drains the THL in the surrounding areas of the sample. Specimens for THL are often prepared by cutting slices of material with a diamond saw. The above work emphasizes that it may be important to etch away the surface regions of the sample which could have been thermally drained during cutting. A knowledge of TL spectra may enable a prediction to be made of whether tribo-induced THL is likely to occur in cut (or finely ground) specimens, or whether any THL will be drained by the cutting process.

In yellow calcite I have shown that some similarities exist between TL and THL spectra. Differences arise because TL is not just THL excited by high temperatures near a cutting surface. Neither do TL excitation techniques necessarily result in all the emission visible in a THL spectrum.

3.3.5 Fluorite doped with Terbium

The TL spectrum is shown as recorded on the IIT spectrograph with a 600 l mm^{-1} grating in figure 3.9 and as recorded on the "Spex Minimate" spectrograph in figures 3.10 and 3.11. Although all the more intense peaks were recorded on both spectrographs some of the weaker peaks were below the threshold sensitivity of the "Spex Minimate" system. The effect of temperature on the TL spectrum was investigated by keeping one sample cool in liquid nitrogen (77 K) until immediately before cutting it. A comparison of figures 3.9 and 3.12 shows that apart from a slight change in relative intensity, cooling the sample to liquid nitrogen temperature immediately before cutting has no effect on the TL spectrum. Perhaps this is because the part of the sample from which TL emission occurs is frictionally heated by the cutting blade.

I have found that the TL lines observed with the fluorites can be associated with traces of the rare earths. A detailed energy level diagram is shown in figure 3.13 for the triply ionized rare earth terbium (Tb), with which this sample is doped. This figure should be compared with figure 2.3. The principle term to term transitions are superimposed on the spectrum in figure 3.14. Most of the TL lines in this sample occur by transitions from $^5D_3$ and $^5D_4$ levels to $^7F_{6,5,4}$ and $^7F_3$. The PL spectrum at 350 nm excitation (figure 3.15, with the highest spectrofluorimeter resolution of 1 nm) shows the same term to term transitions as the TL spectrum, but there appears to be more

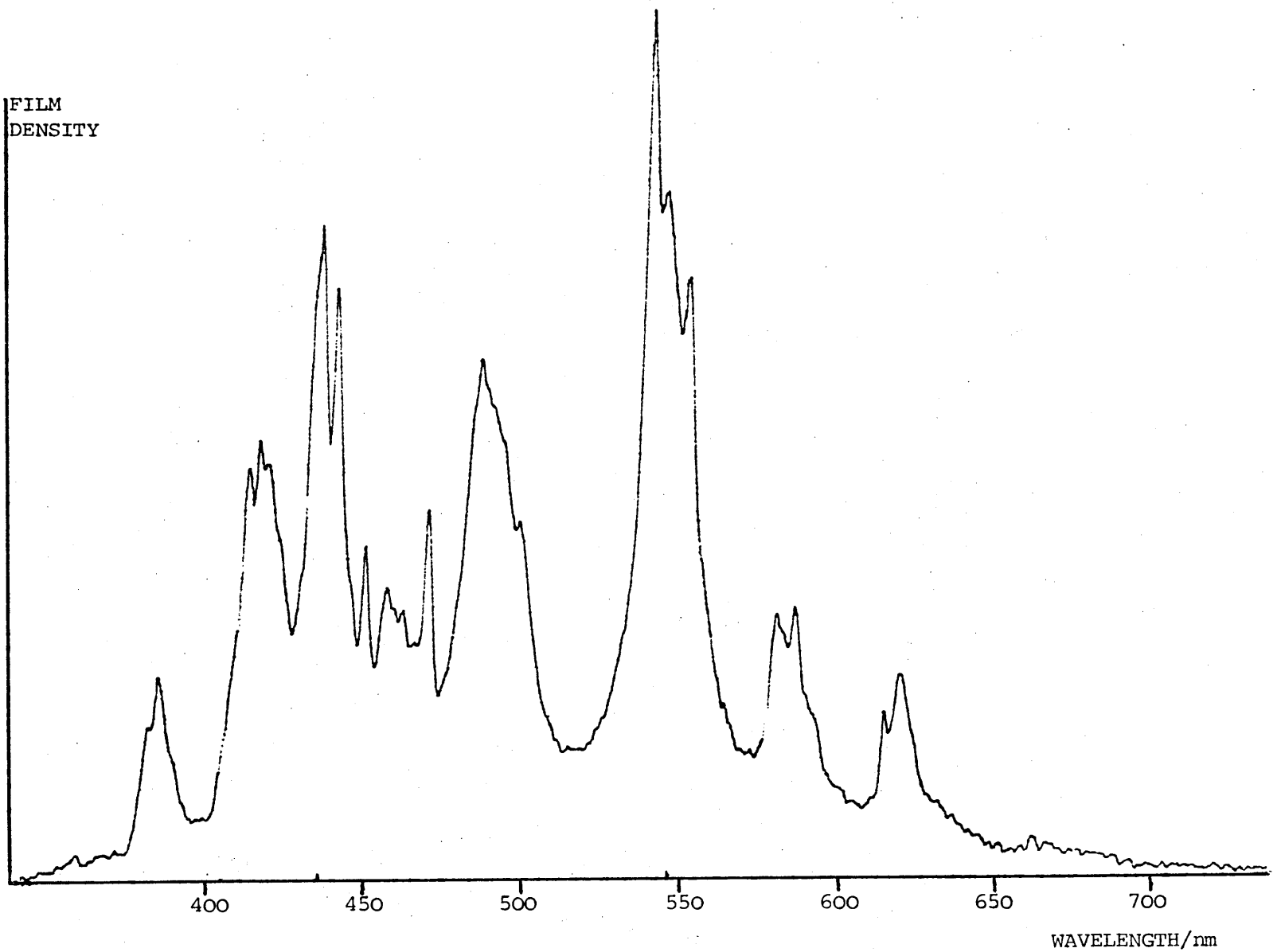

FIGURE 3.9 TL OF TERBIUM DOPED FLUORITE

Mercury calibration lines can be seen at 435.8 and 546.1 nm

FIGURE 3.10 TL OF TERBIUM DOPED FLUORITE.

Recorded on the "Spex Minimate" spectrograph.

A Mercury calibration line can be seen at 435.8 nm.

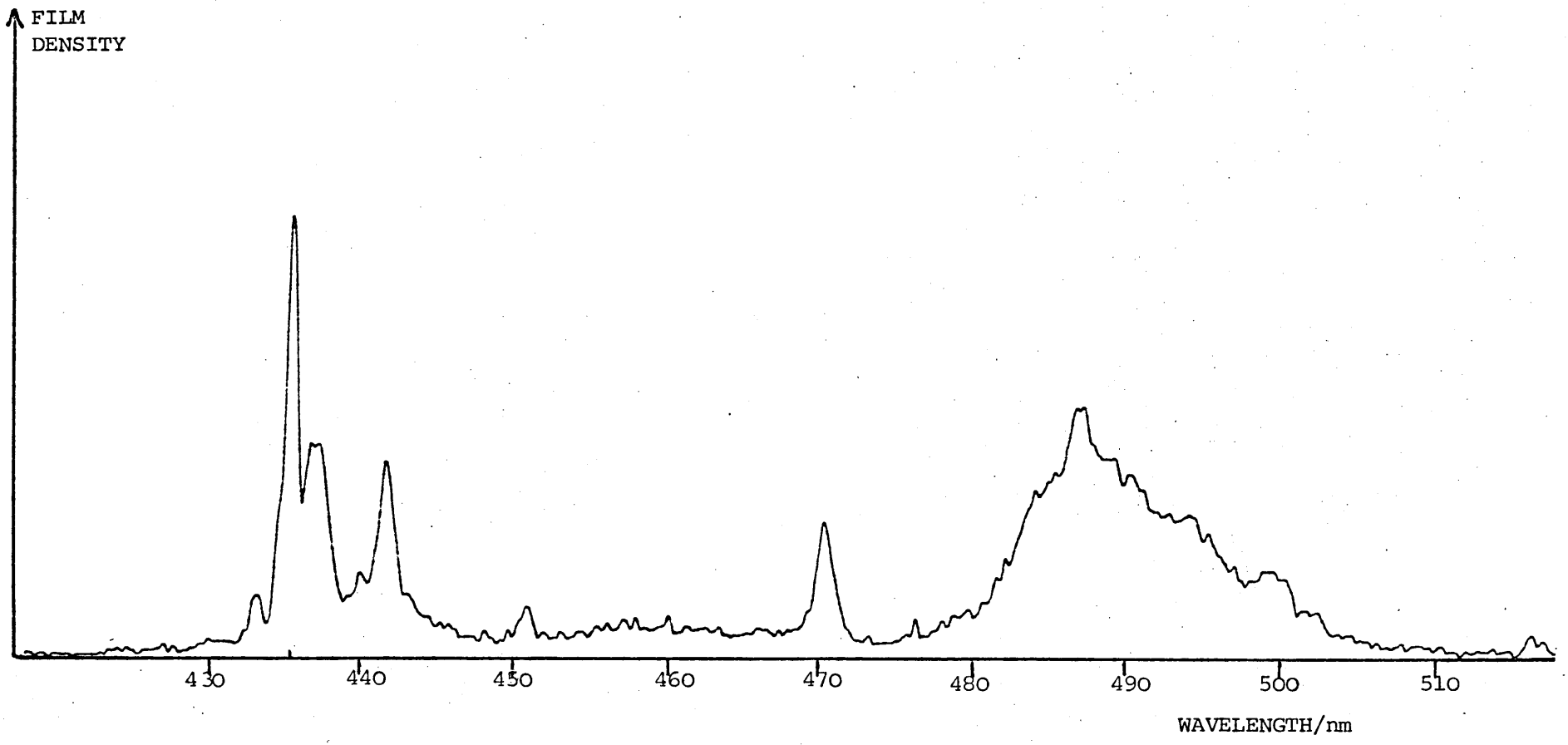

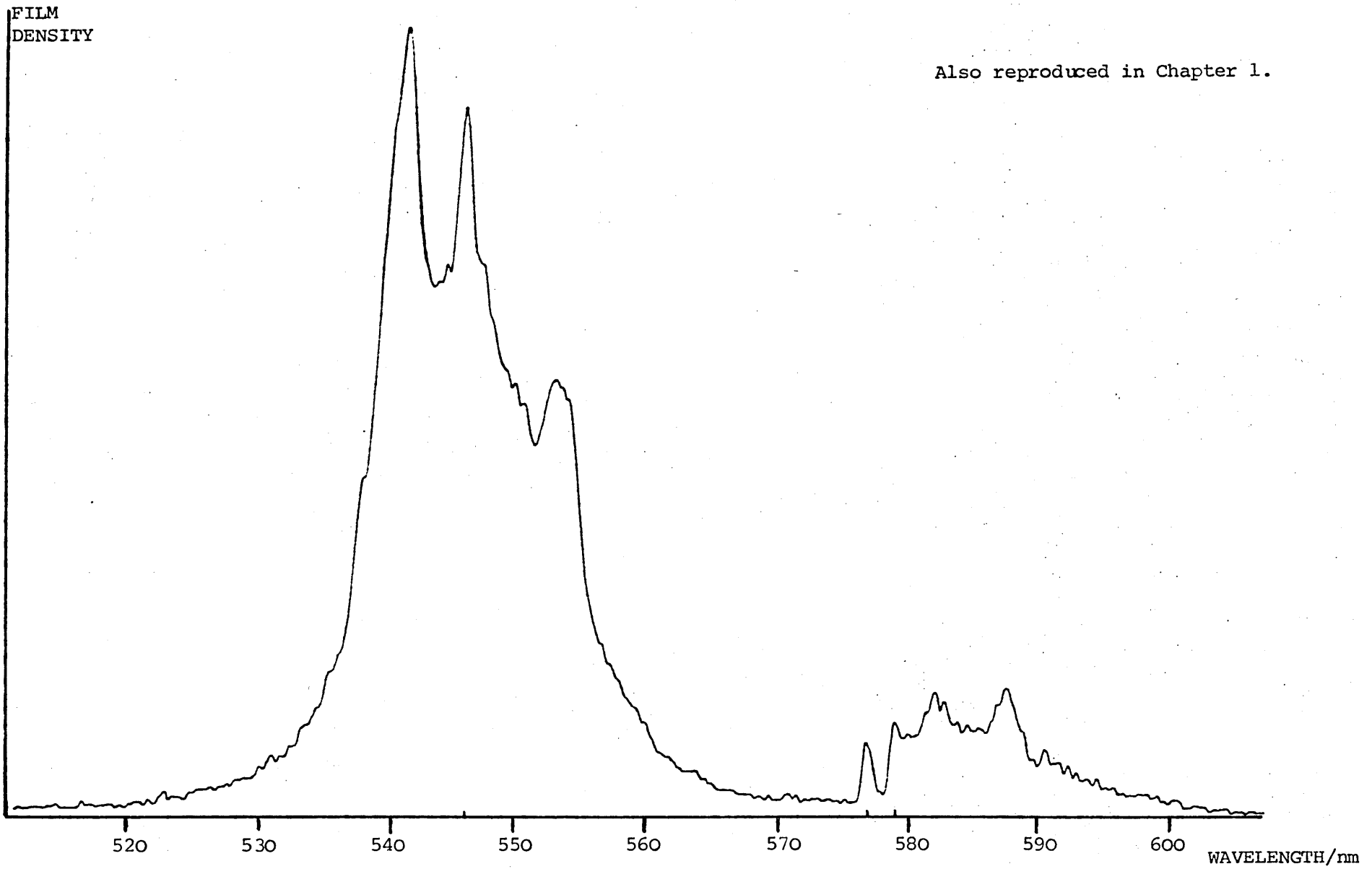

Also reproduced in Chapter 1.

FIGURE 3.11 TL OF TERBIUM DOPED FLUORITE

Recorded on the "Spex Minimate" spectrograph. Mercury calibration lines can be seen at 546.1, 577.0 and 579.1 nm

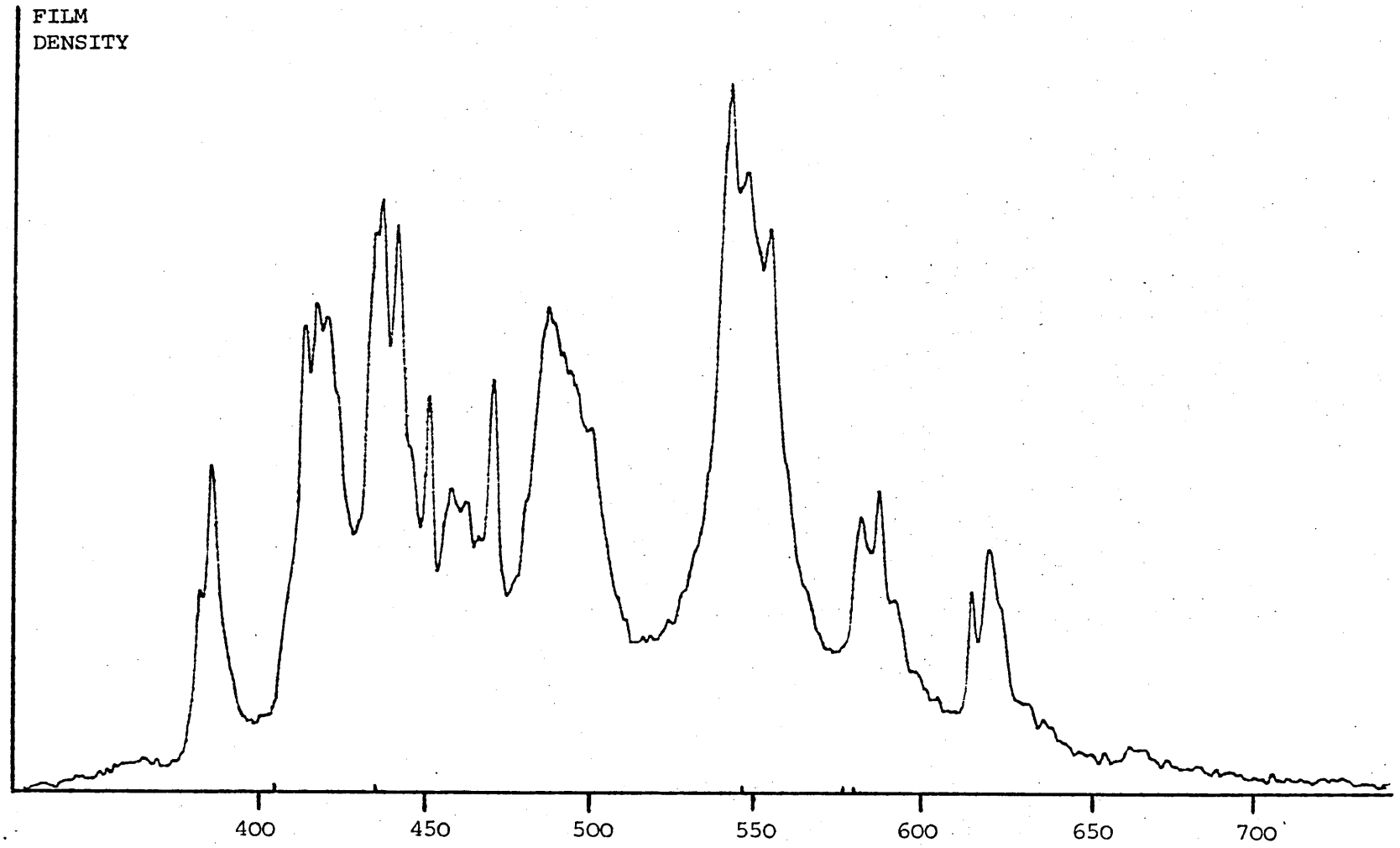

FIGURE 3.12 TL OF TERBIUM DOPED FLUORITE AT ≃ 77 K

Mercury calibration lines can be seen at 435.8 and 546.1 nm

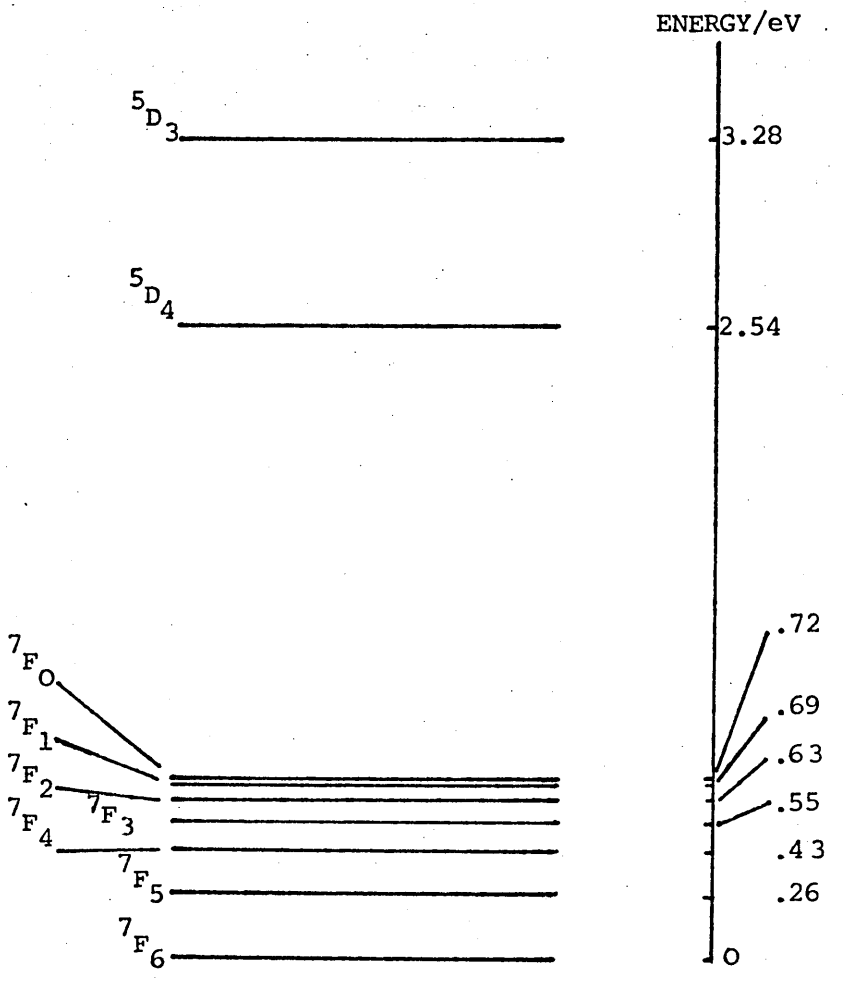

FIGURE 3.13 ELECTRONIC LEVELS OF TRIPLY IONIZED TERBIUM after El'yashevich (1953)

FIGURE 3.14 TL OF TERBIUM DOPED FLUORITE, WITH TERM TO TERM TRANSITIONS SUPERIMPOSED

Mercury calibration lines can be seen at 435.8 and 546.1 nm.

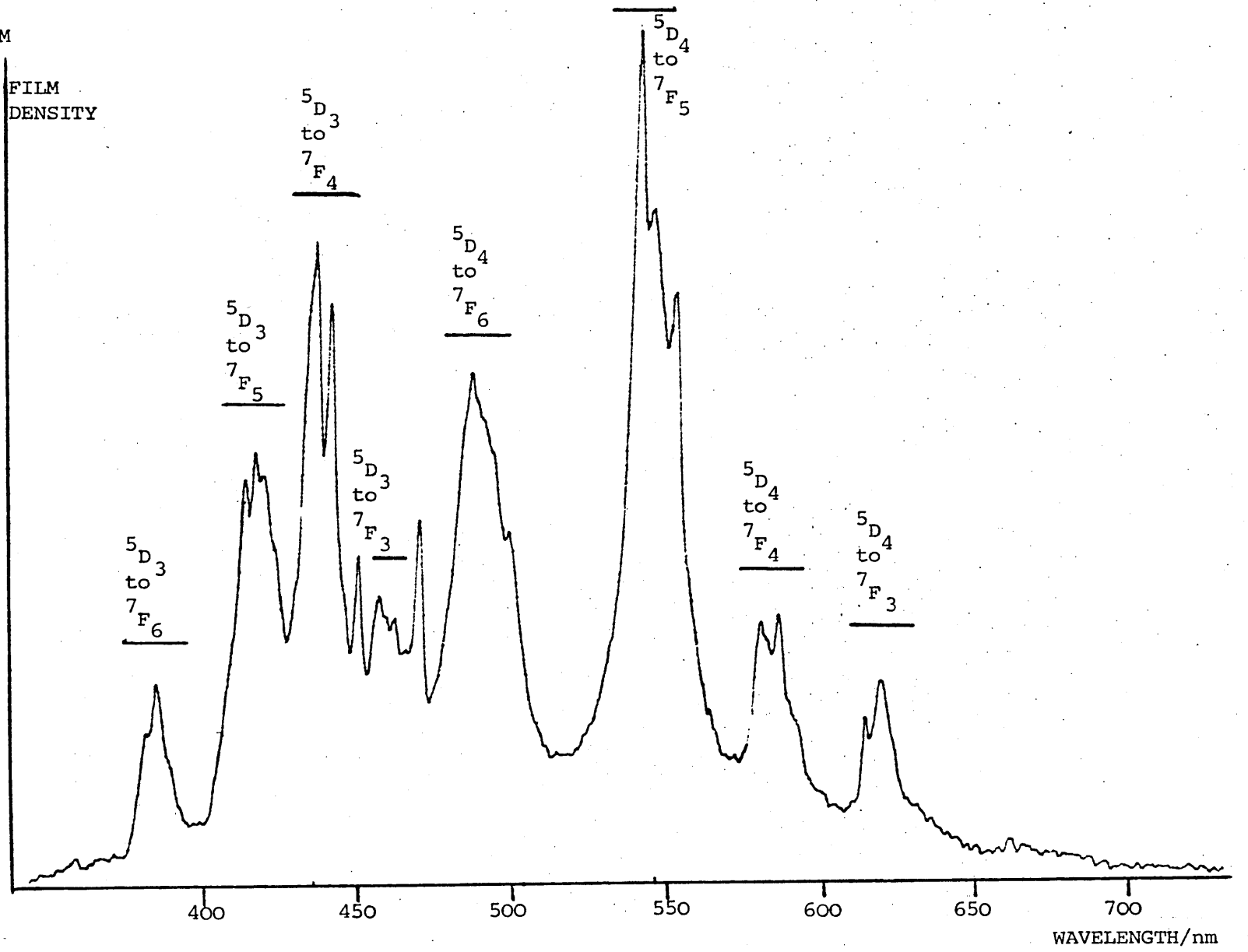

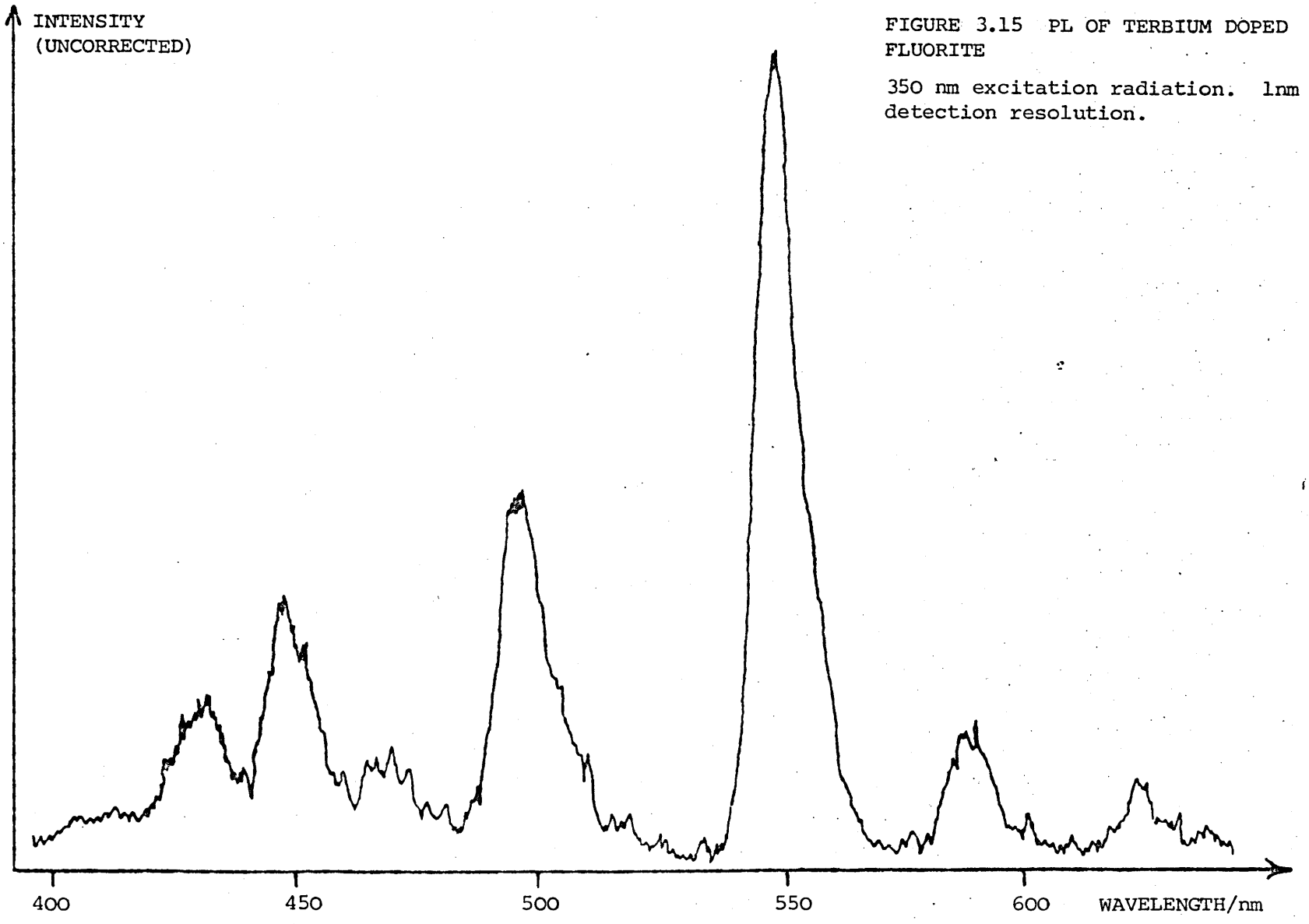

FIGURE 3.15 PL OF TERBIUM DOPED FLUORITE

350 nm excitation radiation. 1nm detection resolution.

detail in the TL spectrum. Both TL and PL spectra were, of course, reproducible. Neither the PL nor TL spectra depended on which part of a sample was under test.

One possible explanation for the appearance of greater detail in the TL spectrum is that some lattice vibrational structure is superimposed onto the TL spectrum giving the appearance of greater detail.

3.3.6 Fluorite doped with Europium

The TL spectrum of cut europium (Eu) doped fluorite is shown in figure 3.16[†]. There is a broad band centred around 430 nm and a line at 588 nm. The PL spectrum (figure 3.17) contains only one peak at around 430 nm. The energy level diagram for Eu^{3+} is shown in figure 3.18. The line at 588 nm could result from a $^5D_0 \rightarrow {}^7F_0$ transition. The broad peak visible in PL and TL is due to an Eu^{2+} transition ($4f^6 5d \rightarrow 4f^7$). Europium is the only rare earth dopant which readily occurs in the Eu^{2+} configuration (see chapter 2, appendix 2) and its presence has been reported elsewhere (Marfunin, 1979) as leading to a "blue violet glow". The width of the peak at 430 nm is consistent with that of a 4f5d → 4f transition.

3.3.7 Fluorite doped with Gadolinium

The TL spectrum of cut gadolinium (Gd) doped fluorite is shown in figure 3.19. From the energy level diagram of Gd^{3+} (figure 3.20) the lowest ground state to first excited state energy is seen to be in the near ultra-violet at 310 nm. The peaks which I have recorded cannot be due to transitions to the Gd^{3+} ground state. I would expect any TL due to Gd^{3+} to be weaker than the comparable TL observed from the

[†]The TL of Tetrakis (dibenzoylmethide) Europate (III) has been published as a crude spectrum containing six points (Hardy and Baldwin et al., 1977). These points delineate a peak at ≃ 620 nm which corresponds to $^5D_0 \rightarrow {}^7F_2$ on the energy level diagram of Eu^{3+}. A peak at ≃ 588 nm was not recorded.

FIGURE 3.16 TL OF EUROPIUM DOPED FLUORITE

Mercury calibration lines can be seen at 404.7, 435.8, 546.1, 577.0 and 579.1 nm

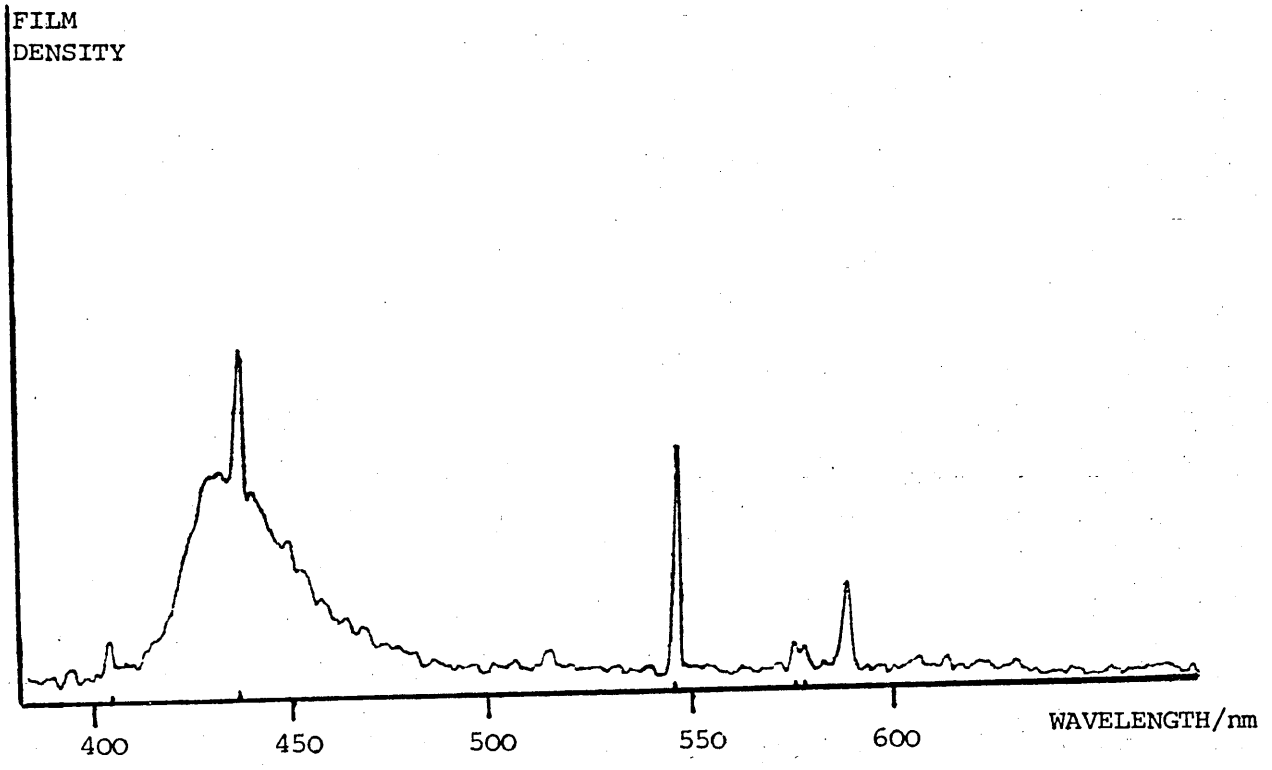

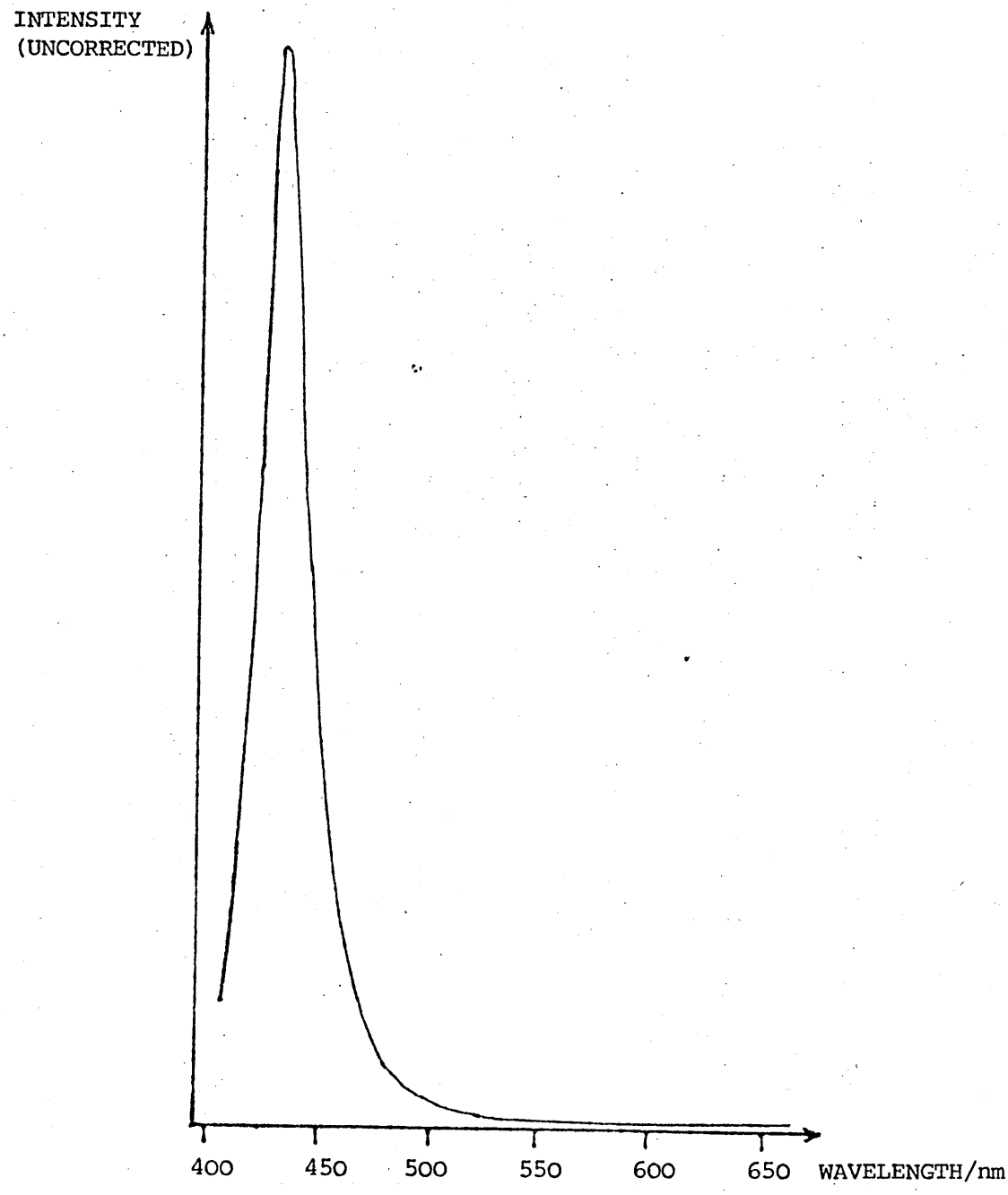

FIGURE 3.17 PL OF EUROPIUM DOPED FLUORITE
400 nm excitation radiation

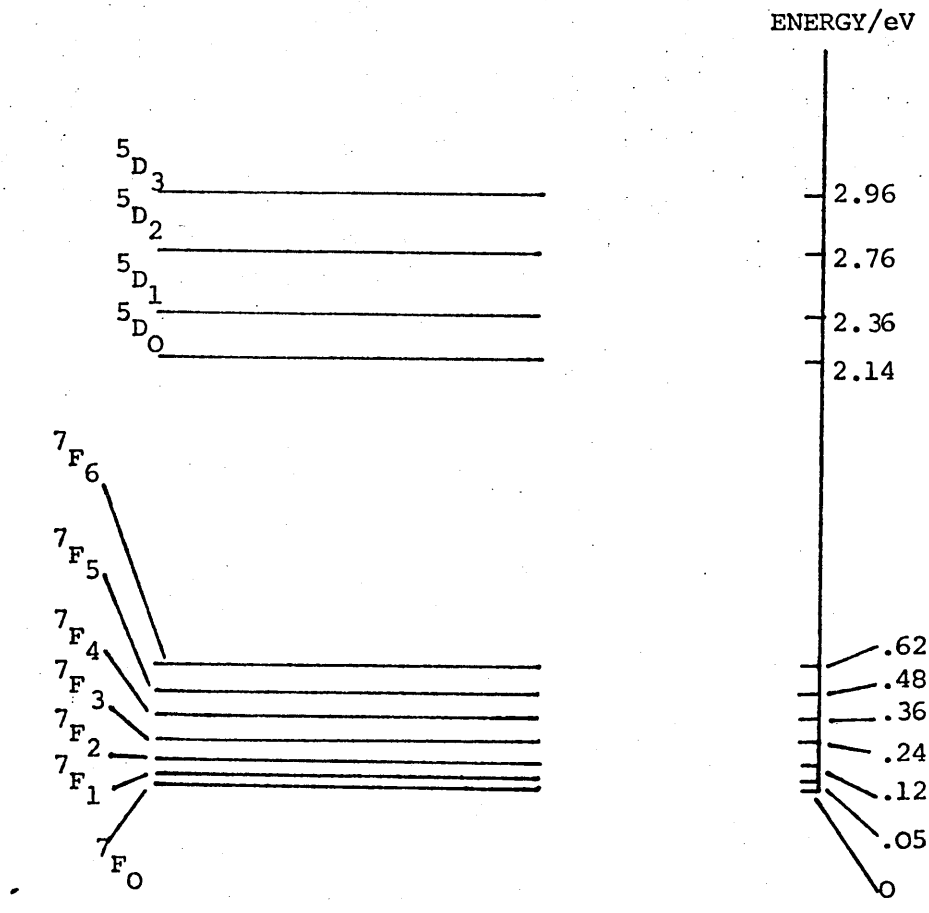

FIGURE 3.18 ELECTRONIC LEVELS OF TRIPLY IONIZED EUROPIUM after El'yashevich (1953)

FIGURE 3.19 TL OF GADOLINIUM DOPED FLUORITE

Mercury calibration lines can be seen at 404.7, 435.8, 546.1, 577.0 and 579.1 nm.

The structure seen here is due to impurities - see text section 3.3.7.

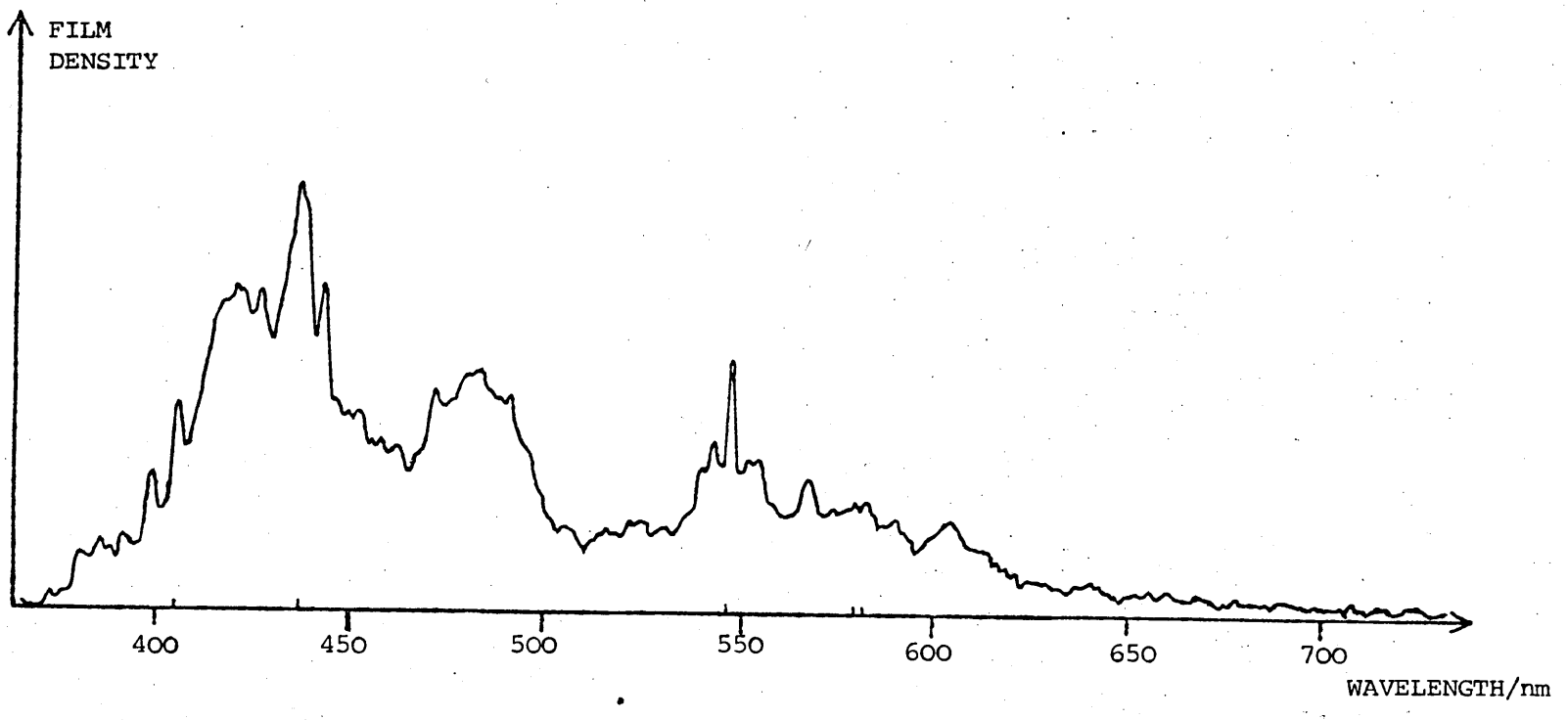

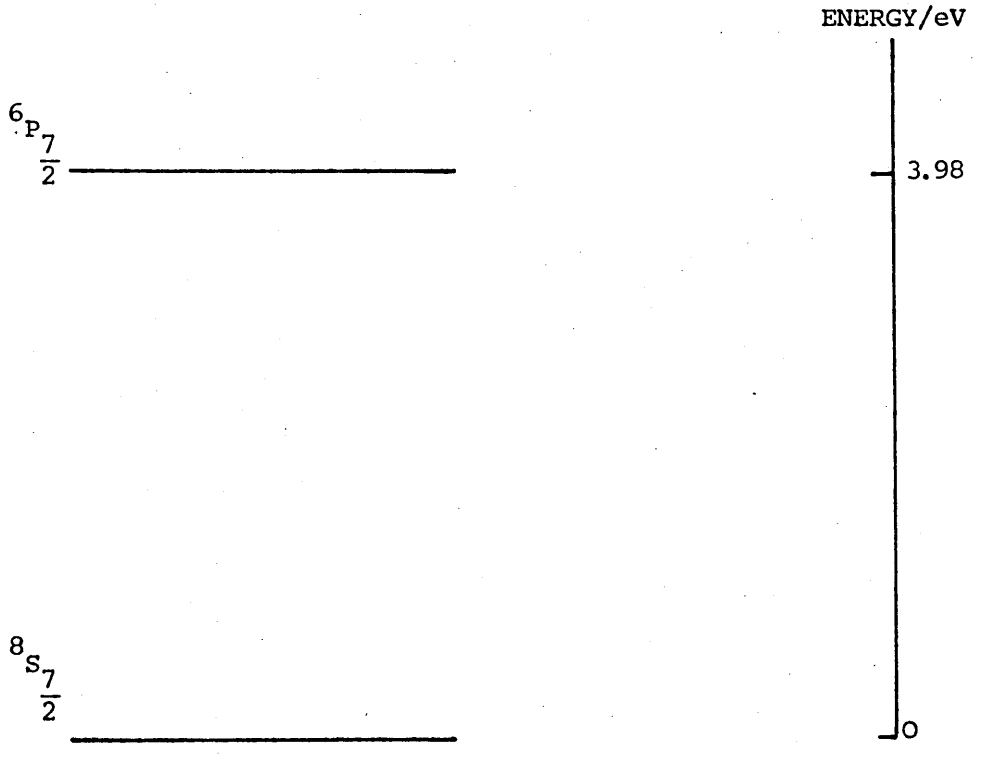

FIGURE 3.20 ELECTRONIC LEVELS OF TRIPLY IONIZED GADOLINIUM
after El'yashevich (1953)

other doped fluorites because the Gd sample was doped to .01% whereas the other samples were doped to 1% atomic concentration. Close examination shows that the TL of this sample can be attributed to terbium (Tb^{3+}) (see figure 3.9), dysprosium (Dy^{3+}) (see figure 3.21) and perhaps europium (Eu^{2+}) impurities, and that no gadolinium emission has in fact been recorded.

3.3.8 Fluorite doped with Dysprosium

The TL spectrum of cut dysprosium (Dy) doped fluorite was recorded with the 600 lmm^{-1} grating (figure 3.21), and also with the 1800 $l\ mm^{-1}$ grating (figures 3.22 and 3.23). The two bands observed in TL at $\simeq$ 480 nm and $\simeq$ 580 nm fit into the energy level diagram (figure 3.24) as $^4F_{9/2} \rightarrow {}^6H_{15/2}$ and as $^4F_{9/2} \rightarrow {}^6H_{13/2}$ respectively. The structure of each band may be determined by the sites and crystal field splittings of the ions, see appendix 1. The PL spectrum of this sample contains two broad bands centred around 480 and 578 nm (figure 3.25). They correspond to the bands seen in TL.

3.3.9 Fluorite doped with Samarium

Three groups of lines can be seen in the TL spectrum of cut fluorite doped with samarium (Sm), at $\simeq$ 570, $\simeq$ 600 and $\simeq$ 650 nm (figure 3.26). These groups are also visible in the PL spectrum (figure 3.27) but there appears to be greater detail in the TL spectrum perhaps because of the superposition of some lattice vibrational structure. The energy level diagram for Sm^{3+} is shown in figure 3.28 and the TL could arise from $^4G_{5/2} \rightarrow {}^6H_{9/2}$, $^4G_{5/2} \rightarrow {}^6H_{7/2}$ and $^4G_{5/2} \rightarrow {}^6H_{5/2}$. Differences in wavelength between the observed spectrum and that predicted by the energy level diagram may be due to crystal field perturbations to the emitting centres, see appendix 1; and to some vibrational structure.

FIGURE 3.21 TL OF DYSPROSIUM DOPED FLUORITE

Mercury calibration lines can be seen at 404.7, 435.8, 546.1, 577.0 and 579.1 nm

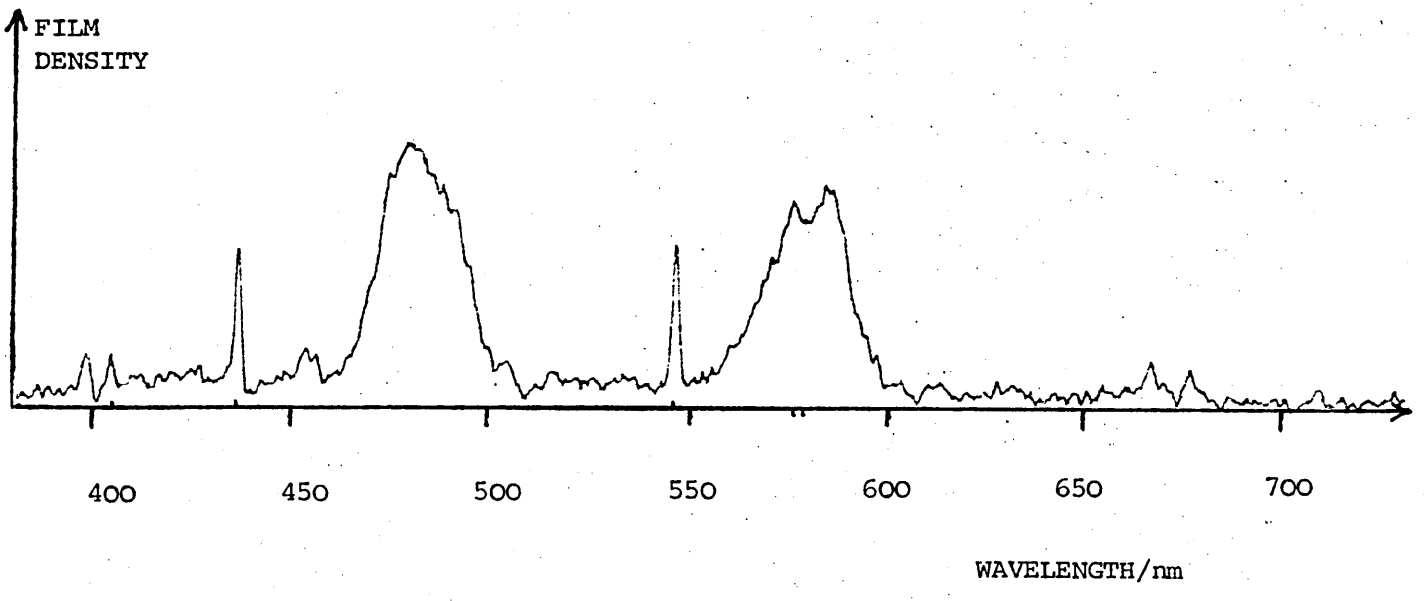

FIGURE 3.22 TL OF DYSPROSIUM DOPED FLUORITE

A mercury calibration line is visible at 435.8 nm

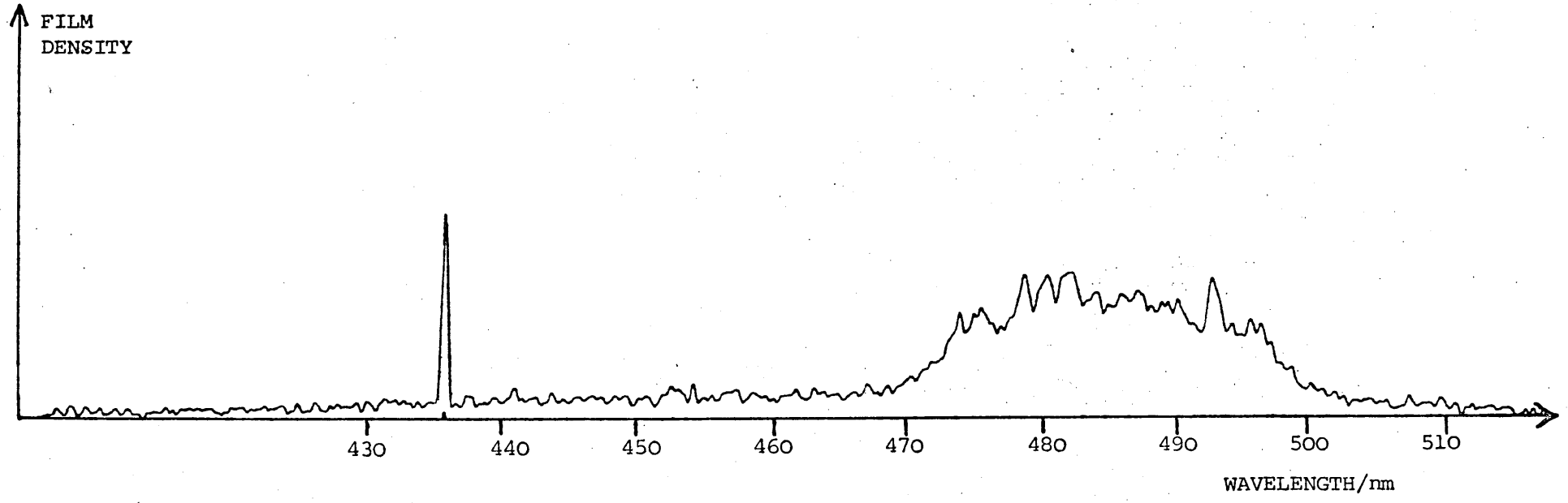

FIGURE 3.23 TL OF DYSPROSIUM DOPED FLUORITE

Mercury calibration lines can be seen at 546.1, 577.0 and 579.1 nm

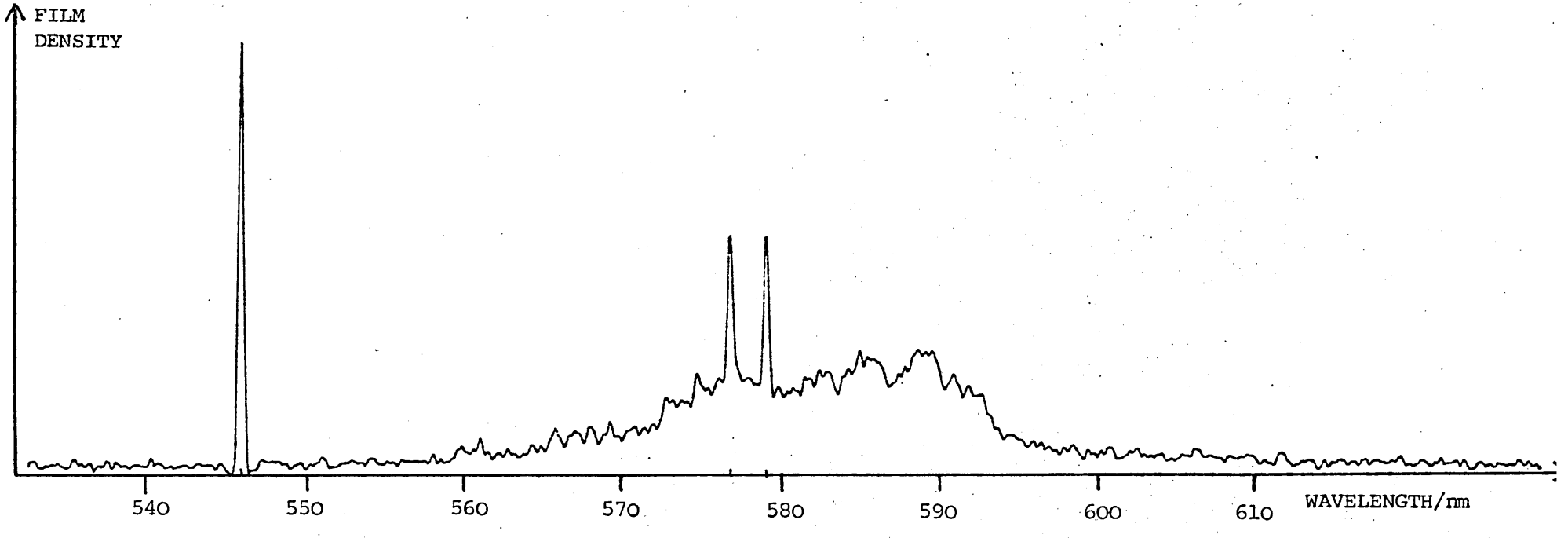

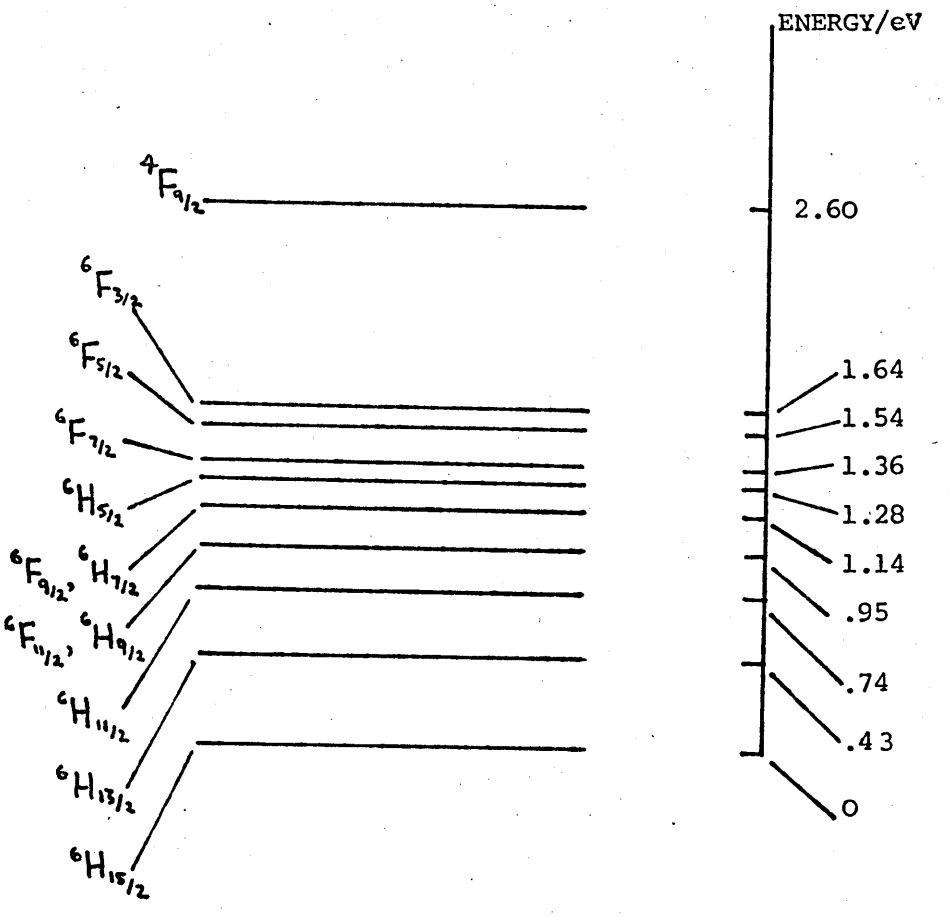

FIGURE 3.24 ELECTRONIC LEVELS OF TRIPLY IONIZED DYSPROSIUM after El'yashevich (1953)

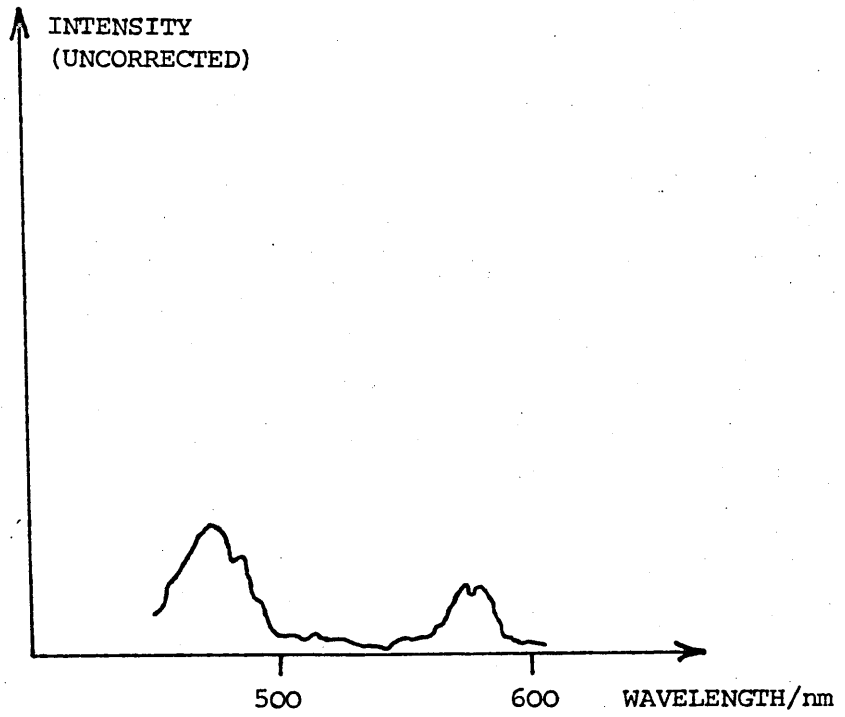

FIGURE 3.25 PL OF DYSPROSIUM DOPED FLUORITE

400 nm excitation; signal recorded on S20 photocathode photomultiplier

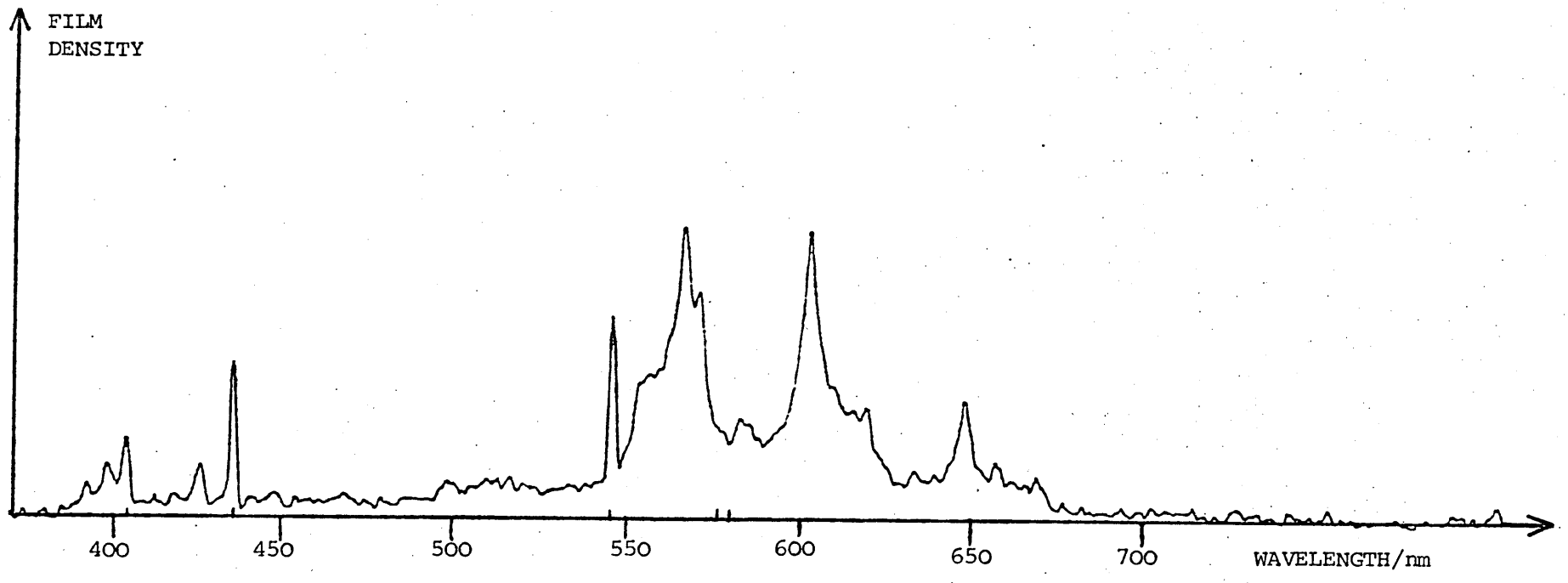

FIGURE 3.26 TL OF SAMARIUM DOPED FLUORITE.

Mercury calibration lines can be seen at 404.7, 435.8, 546.1, 577.0 and 579.1 nm

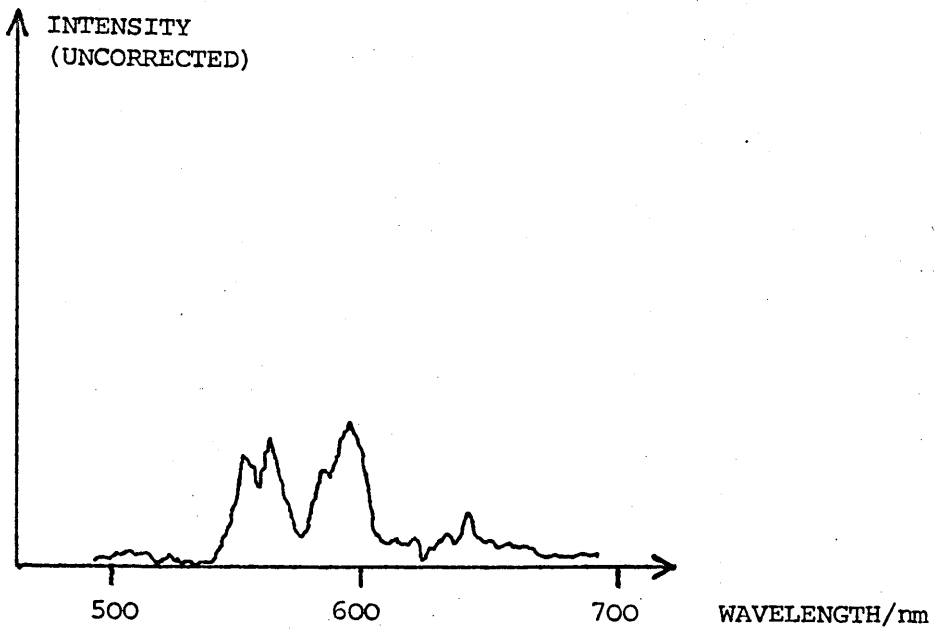

FIGURE 3.27 PL OF SAMARIUM DOPED FLUORITE

400 nm excitation. Recorded on S20 photocathode photomultiplier

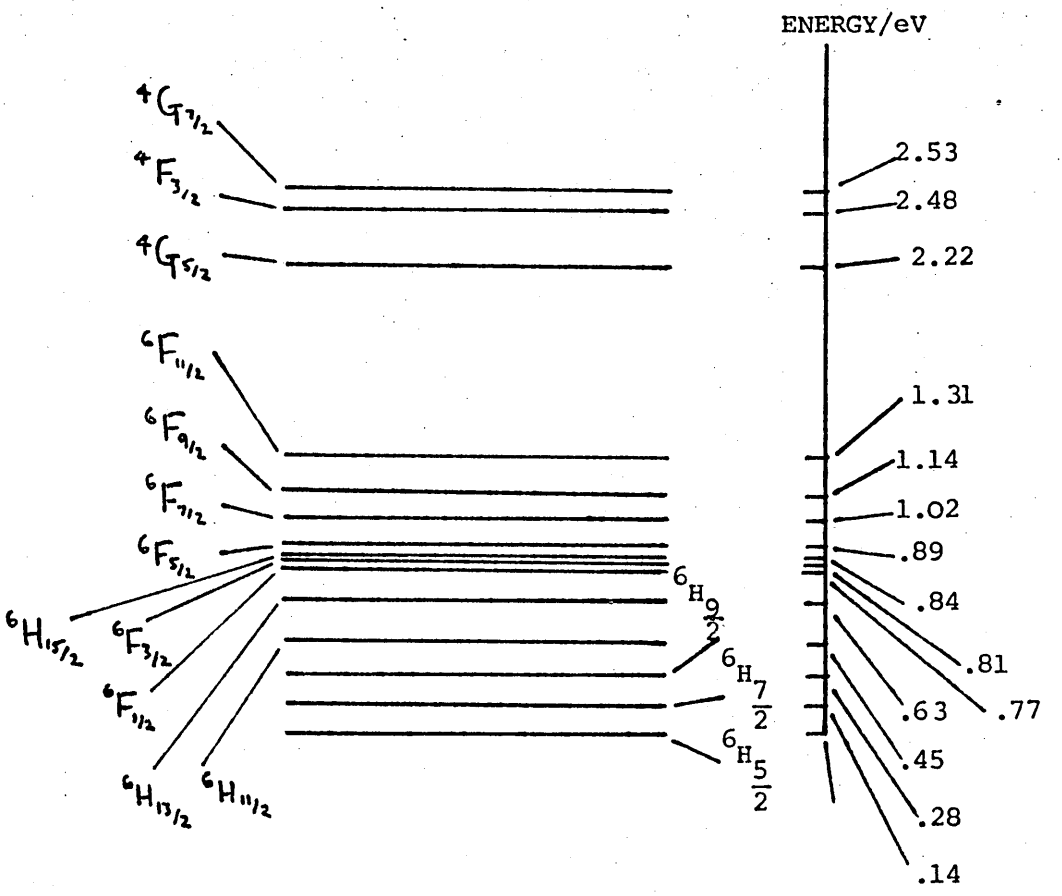

FIGURE 3.28 ELECTRONIC LEVELS OF TRIPLY IONIZED SAMARIUM
after El'yashevich (1953)

Nitrogen gas discharge lines are visible in this sample's TL spectrum (figure 3.26). Neither Nelson (1926) nor Wick (1937) could detect any nitrogen gas discharge accompanying the TL of crushed fluorites.

3.3.10 Natural Fluorites

Generally speaking the natural fluorites show TL which is a combination of a number of the spectra of the singly doped fluorites.

Purple fluorite from Weardale, Cumbria was faintly TL with a broad peak at 425 nm and a nitrogen gas discharge spectrum visible, see figure 3.29. This resembled the TL of the europium doped sample (but without the 588 nm line) and the broad peak is probably due to Eu^{2+} emission.

Yellow fluorite from Scoredale Co. Durham was only weakly TL (see figure 3.30). The TL spectrum resembles that of fluorite 1 and nitrogen gas discharge lines can again be seen.

Green fluorite from Heights Quarry, Cumbria was strongly TL. The TL of the natural specimen (figure 3.31) shows a broad peak at ≃ 420 nm (probably due to Eu^{2+}) and a number of lines which could be due to terbium, in particular a line near 541 nm. The TL of this sample, around 550 nm, was recorded with the 1800 l mm^{-1} grating fitted into the IIT spectrograph (figure 3.32).

The sample was heated overnight to 500°C to drain all THL, and then the TL spectrum was measured. It contained only the broad peak at ≃ 420 nm (figure 3.33). That some TL is visible after heating to a sufficiently high temperature to exhaust all THL is evidence that TL is not just THL released by virtue of local hot spots induced by grinding. On irradiation (see footnote in section 3.3.4) the TL was restored almost to its original total intensity (figure 3.34); although the spectral

FIGURE 3.29 TL OF PURPLE FLUORITE, WEARDALE, CUMBRIA

Mercury calibration lines can be seen at 404.7, 435.8, 546.1, 577.0 and 579.1 nm

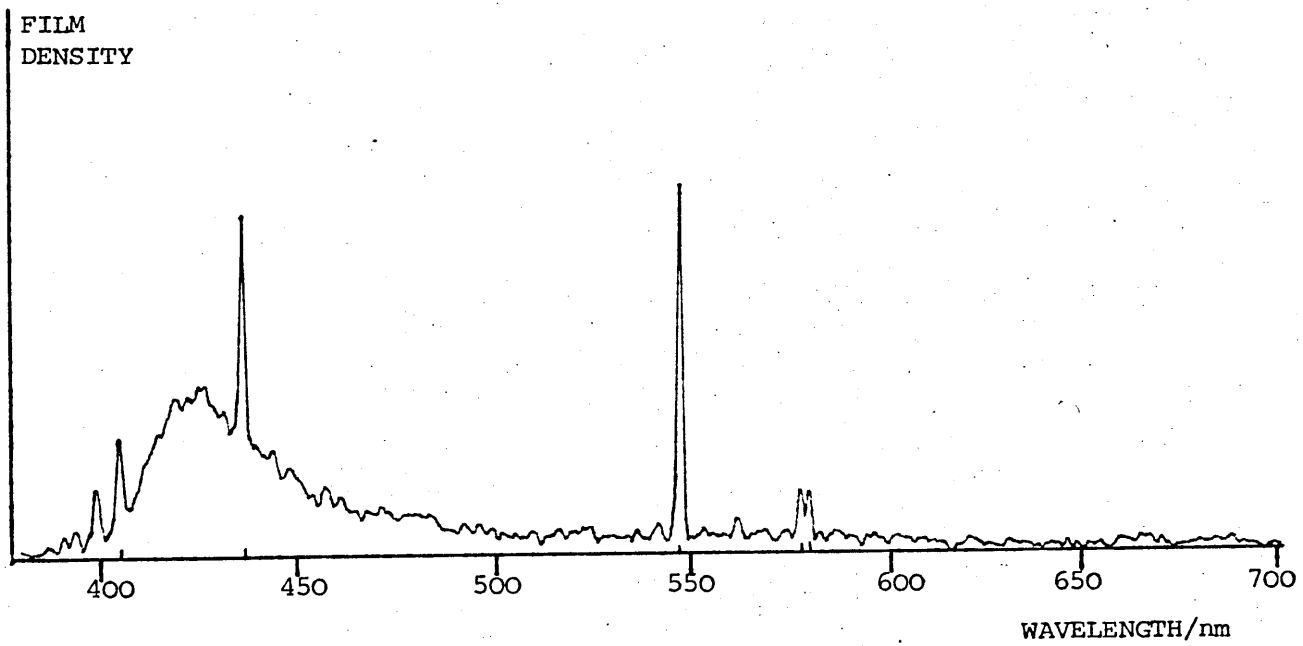

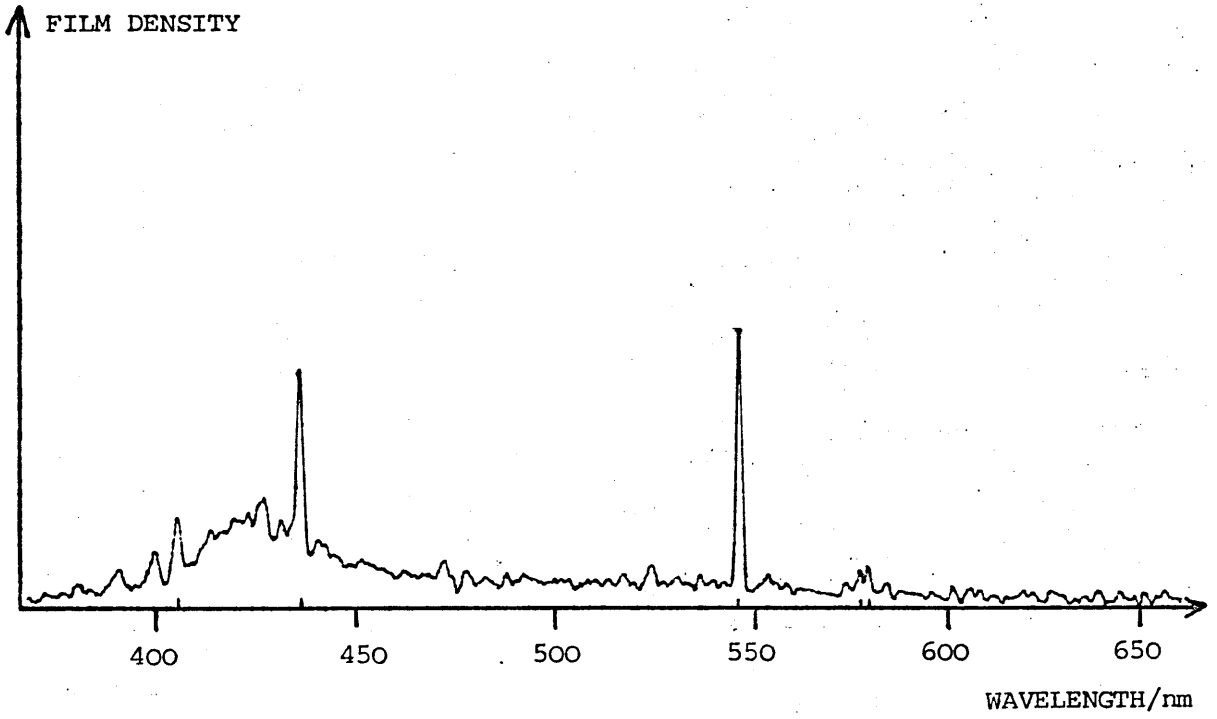

FIGURE 3.30 TL OF YELLOW FLUORITE, SCOREDALE, CO. DURHAM

Mercury calibration lines can be seen at 404.7, 435.8, 546.1 577.0 and 579.1 nm

FIGURE 3.31 TL OF GREEN FLUORITE, HEIGHTS QUARRY, CUMBRIA

Mercury calibration lines can be seen at 404.7, 435.8, 546.1, 577.0 and 579.1 nm

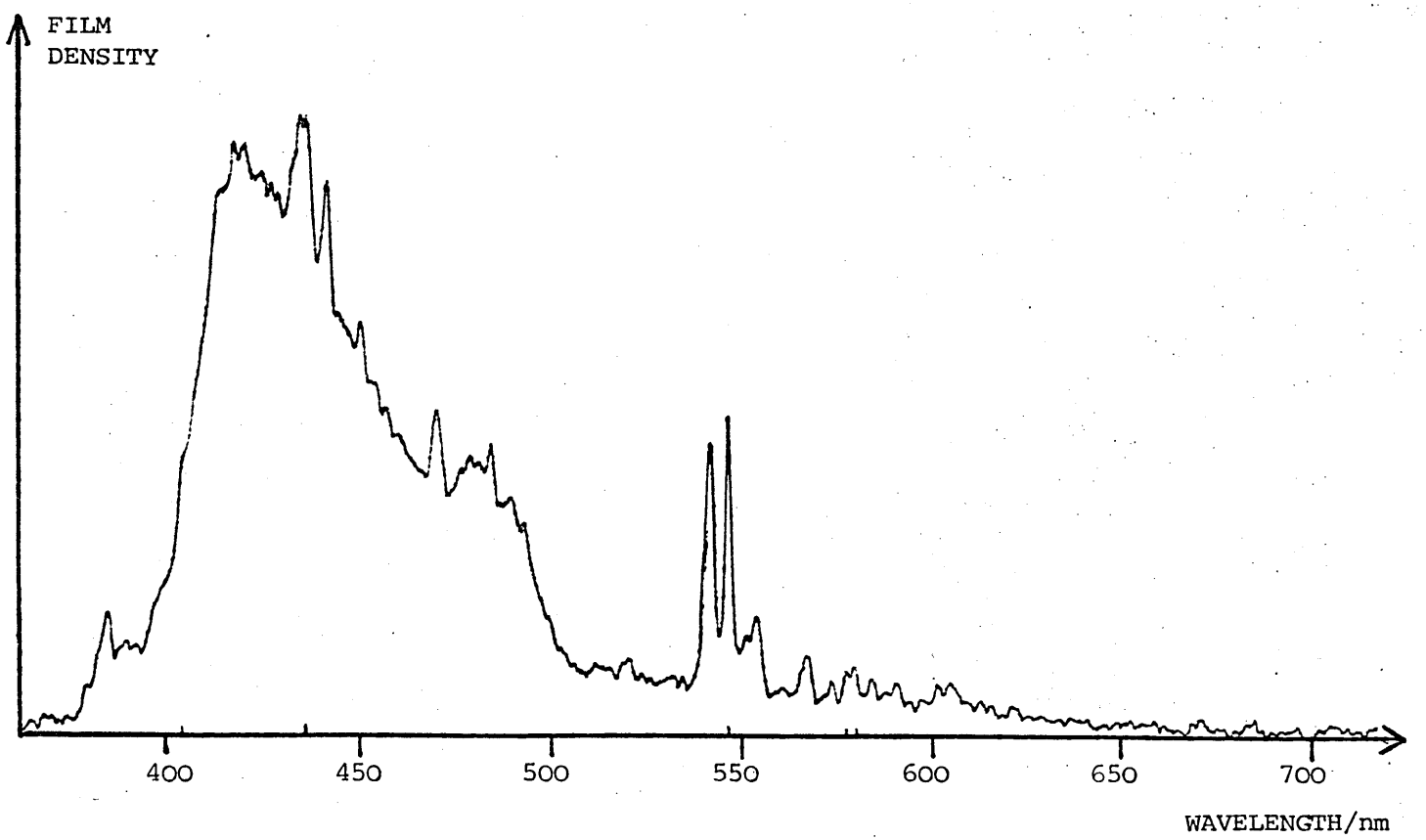

FIGURE 3.32 TL OF GREEN FLUORITE, HEIGHTS QUARRY, CUMBRIA.
Mercury calibration lines can be seen at 546.1, 577.0 and 579.1 nm

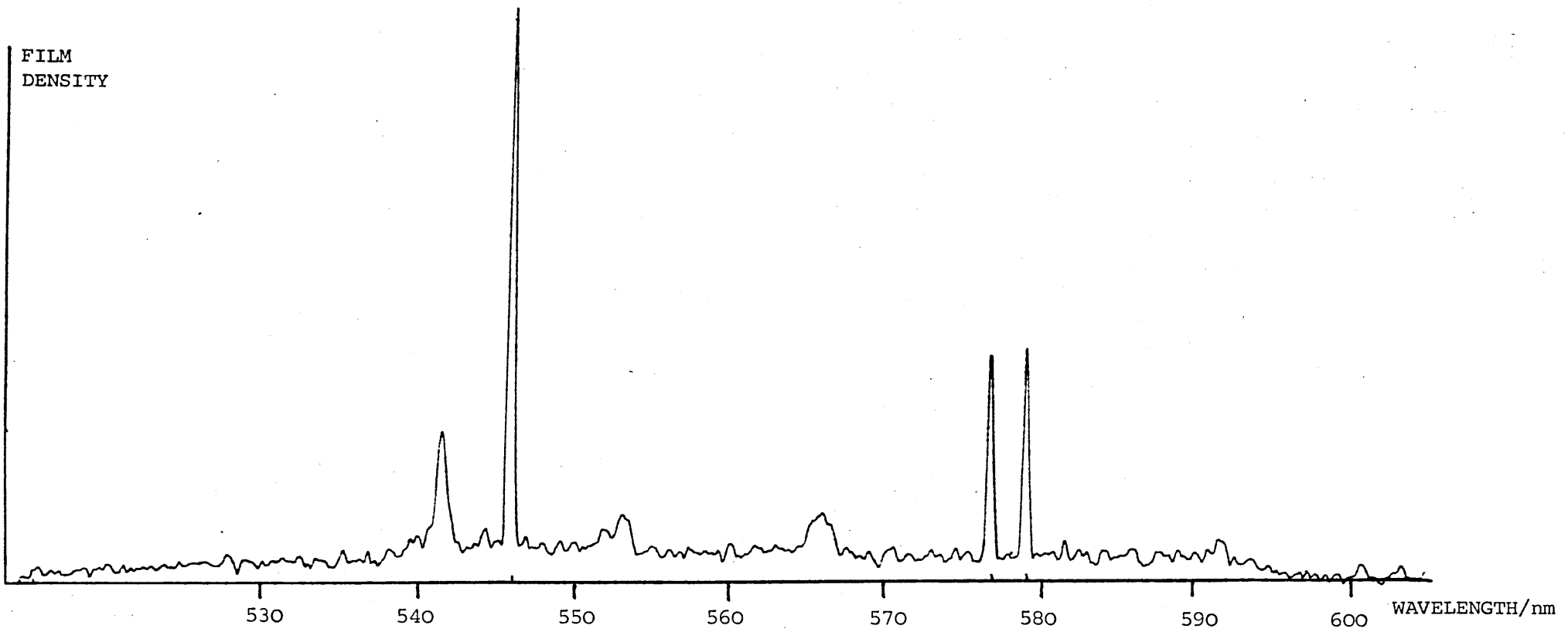

FIGURE 3.33 TL OF GREEN FLUORITE, HEIGHTS QUARRY, CUMBRIA; (HEAT TREATED SAMPLE)

Mercury calibration lines can be seen at 404.7, 435.8, 546.1, 577.0 and 579.1 nm. Before TL the sample was heated to 500° C to exhaust all THL.

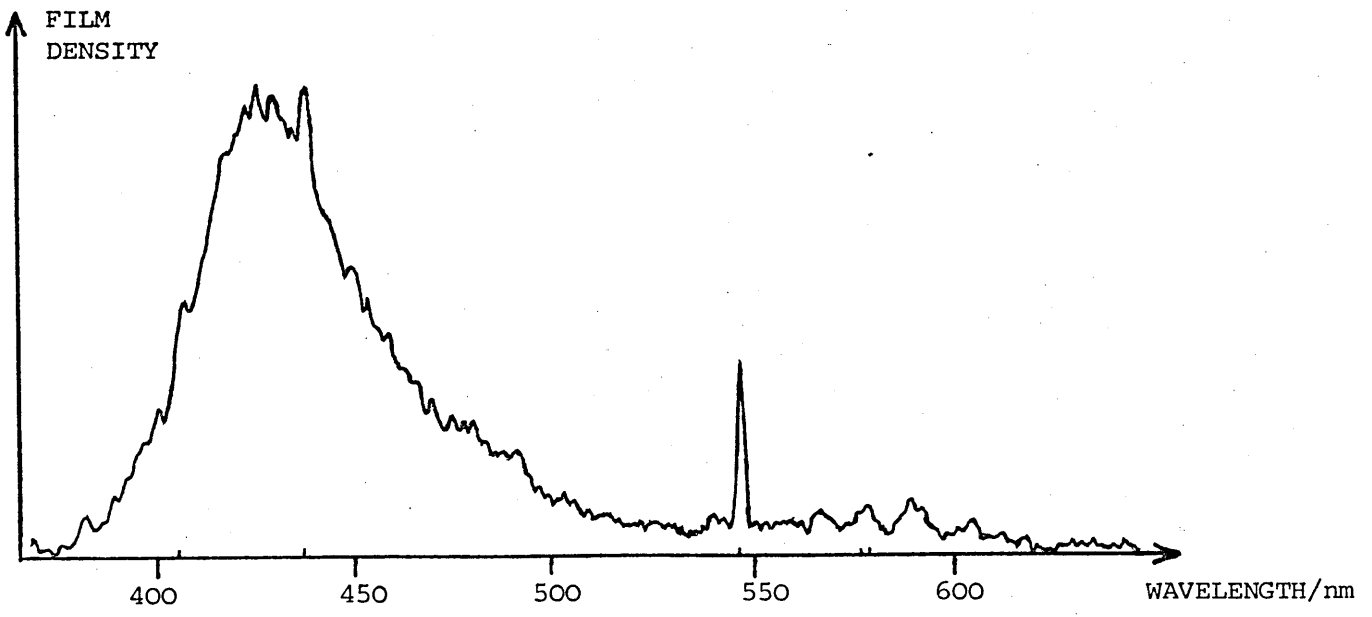

FIGURE 3.34 TL OF GREEN FLUORITE, HEIGHTS QUARRY, CUMBRIA; (IRRADIATED SAMPLE).

Mercury calibration lines can be seen at 404.7, 435.8, 546.1, 577.0 and 579.1 nm. Before TL the sample was heated to 500°C to exhaust all THL, and was then irradiated (see section 3.3.4).

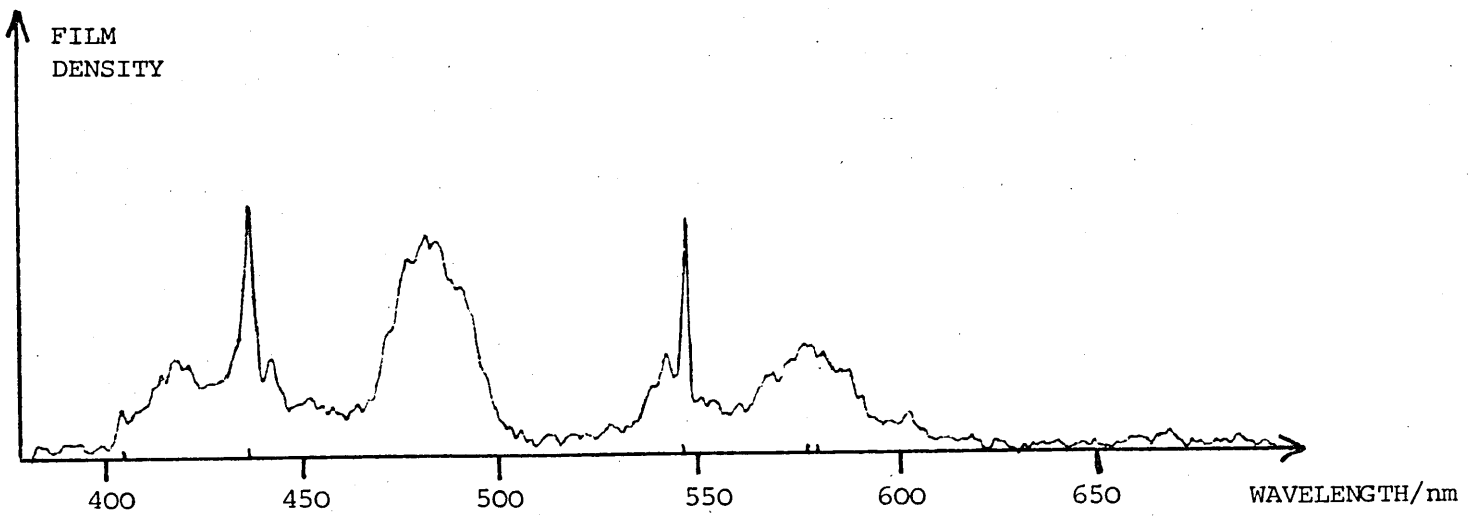

content was changed. After irradiation the relative TL intensities were different and dysprosium bands at ≃ 480 and ≃ 573 nm were visible with much greater relative intensity than the terbium lines of figure 3.31.

The low temperature THL spectrum (of a natural sample, unheated and unirradiated) is a bright continuum. While from 180°C to 350°C (above room temperature) the THL contains a number of bands. These are recorded in figure 3.35. Evidence of terbium, dysprosium and europium emission can be seen. The spectra obtained from this sample emphasize the different information that can be obtained from luminescence of a material (THL or TL) when the previous treatment (heat or irradiation) of the sample changes. This sample appears to contain traces of a number of rare earth ions. The relative intensity of their emission during TL or THL depending on the previous treatment of the sample.

Faint-purple fluorite from Weardale, Cumbria shows from its TL spectrum (figure 3.36) that terbium and dysprosium are present, and some Eu^{2+} emission also occurs.

Blue fluorite from Cumbria was cut on the diamond saw. The TL spectrum was recorded (figure 3.37) and evidence of traces of terbium and dysprosium was noticed. There appears to be a less intense (Eu^{2+}) peak around 420 nm than was recorded with fluorite 4.

3.4 Discussion

The nitrogen gas discharge emission recorded from cut or crushed sugar was expected and has been reported many times in the literature. The TL of yellow calcite and the fluorites however, has not been recorded before with high resolution. I have found that the TL recorded from

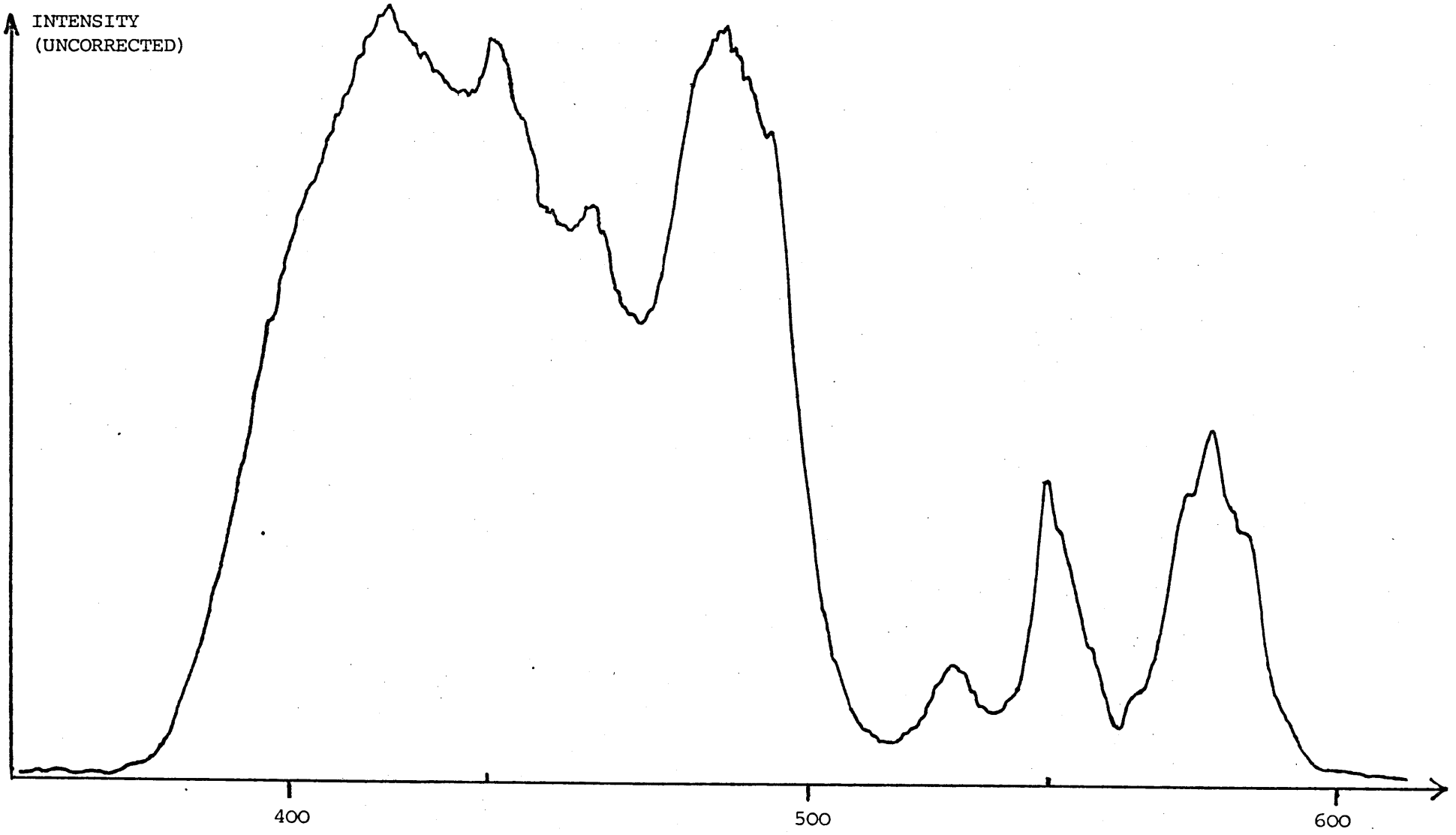

FIGURE 3.35 THL OF GREEN FLUORITE, HEIGHTS QUARRY, CUMBRIA

180 to 350° C above room temperature. Mercury calibration lines can be seen at 435.8 and 546.1 nm.

FIGURE 3.36 TL OF FAINT PURPLE FLUORITE, WEARDALE, CUMBRIA

Mercury calibration lines can be seen at 404.7, 435.8, 546.1, 577.0 and 579.1 nm.

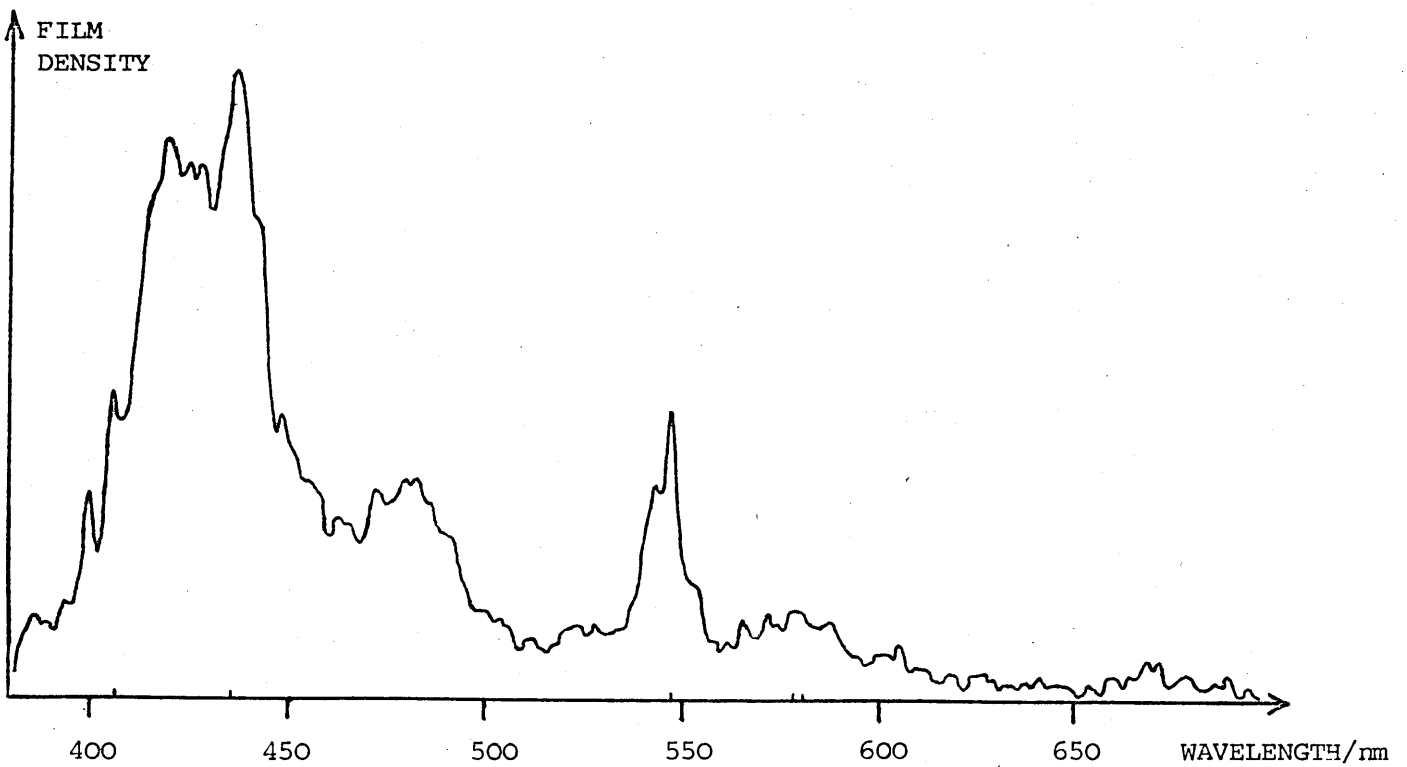

FIGURE 3.37 TL OF BLUE FLUORITE, CUMBRIA

Mercury calibration lines can be seen at 404.7, 435.8, 546.1, 577.0 and 579.1 nm.

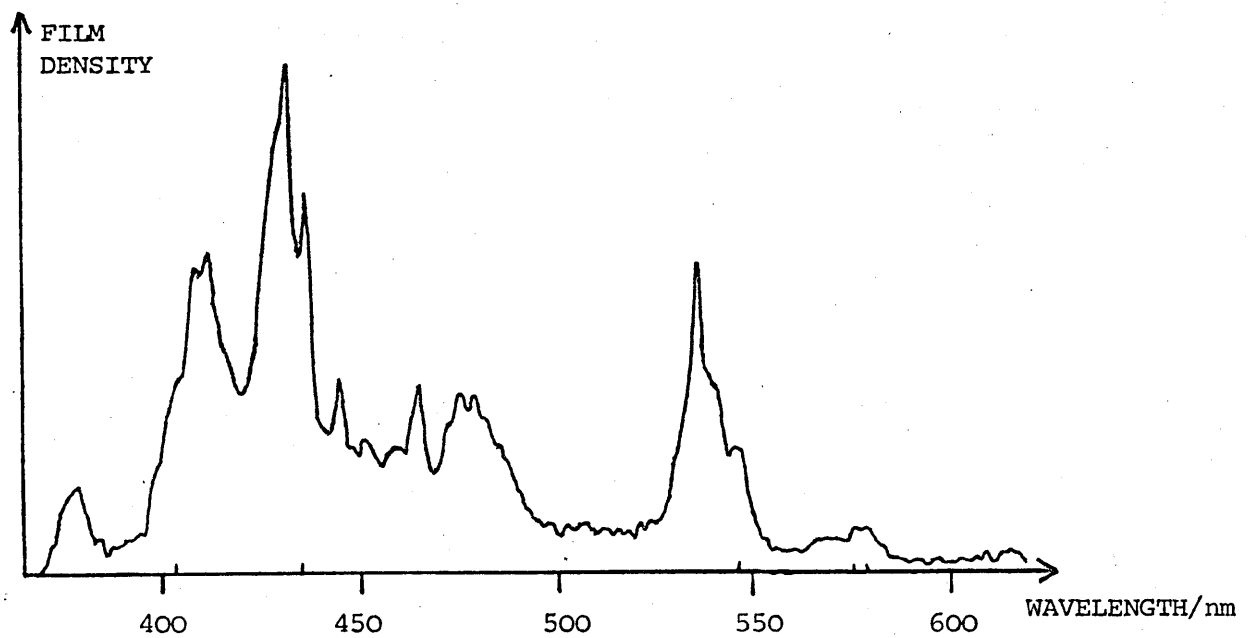

samples of fluorites can be fitted to the energy level diagrams for the triply ionized rare earths (figure 2.3). I have also observed emission from doubly ionized europium. The TL of yellow calcite appears to arise from traces of the rare earth samarium. Differences between energies calculated from energy level diagrams and those energies observed experimentally may occur due to a) crystal field splittings of energy terms and different splittings for atoms in different sites, see appendix 1, b) superposition of a vibrational structure onto the emission spectrum.

The width of the spectral lines makes it unlikely that they originate from atoms or ions in the gaseous state. Thus the TL cannot originate from atoms evaporated into the gas phase in the region of a growing crack.

The TL emission for some of my samples has been measured after they have been heated and I have compared TL with THL and PL. Differences in the spectra indicate that the condition of the emitting centres is not the same in all cases. My comparison of THL with TL suggests that the release of electrons from traps in the material as a result of applying mechanical energy to the material and generating heat (THL) may account for *some* but not all of the TL emission. Wick (1937) observed the THL and TL of fluorites. Unlike the results reported here Wick saw no differences between the THL and TL spectra.

Fluorites doped with samarium, europium, gadolinium, terbium and dysprosium are noted for their bright PL (El'yashevich, 1953) and are the only triply ionized rare earth dopants that I have observed to give a bright TL in fluorite (with the exception of gadolinium whose fundamental emission is outside the spectral range of my apparatus). I have also observed the TL of doubly ionized europium. A nitrogen gas discharge was observed in a number of cases. One suggested mechanism

for the TL excitation is that of PL excitation by the ultra-violet radiation present in the nitrogen gas discharge. But in some cases reported above no nitrogen gas discharge was seen with the rare earth emission. This result suggests that PL excitation by a nitrogen discharge can only be partially responsible for the excitation of fluorite fluorescence. A radiationless population mechanism has been proposed by Lin and Wutz *et al.* (1980), whereby excited state population occurs as a result of high temperatures or pressures at the fracture surface.

CHAPTER 3

APPENDIX 1

Crystal Field Effects

Rare earth dopants in fluorite normally exist in the RE^{3+} configuration with the RE^{3+} ion substituting for a Ca^{2+} ion (An exception is europium which is usually found as Eu^{2+}). The dopant ion is thus normally surrounded by eight equivalent nearest neighbout F^- ions forming the corners of a cube as described in chapter 2, appendix 2. These ions have an electrostatic interaction with the 4f electrons of the RE^{3+} ion. To a good approximation the 4f electrons can be regarded as moving in an electric field set up by the neighbouring ions, known as the crystalline electric field. The energy of interaction with this field is smaller, for ions of the 4f group, than coulomb, exchange, and spin-orbit interactions within the ions. It gives rise to a "Stark" splitting of the $2J + 1$ levels of the ion. For example the term ^3H (for a $4f^2$ configuration) splits into levels ($^3H_6$, $^3H_5$ and $^3H_4$) due to spin-orbit interaction. Then splitting of the levels by the weak crystal field occurs determined by the quantum number J (which is written as a suffix e.g. $J = 6$ for $^3H_6$ etc.). This is similar to the effect of an external electric field on the spectrum of an atom but is more complex because the electrostatic potential set up by the neighbouring F^- ions varies over the space occupied by the 4f electrons. The overall splittings of each level of a 4f ion are generally of order 100 cm^{-1}. The basic reason for the splitting is that the wave-functions corresponding to different values of the orbital magnetic quantum number M_L have different angular dependences and hence the distribution of electronic charge in the crystalline electric field varies. The interaction is zero (in first order) for ions such as Gd^{3+}

with a half filled shell carrying no orbital angular momentum (L = 0).

Ions with an odd number of electrons have half integral values of S and hence also of J. In this case the states occur in pairs which have the same charge distribution, and thus retain the same energy in an electric field. Typical examples are Ce^{3+} ($4f^1$) and Er^{3+} ($4f^{11}$).

The changing symmetry of the crystal field in different compounds and at different atomic sites (some RE ions may not be in cubic sites) is a factor which determines the number and position of observed spectral lines. However as already stated transitions in the RE^{3+} spectra only differ by around $\simeq$ 100 cm^{-1} from one another in different crystals with different symmetry.

The magnitude of the crystal field splitting can, in principle, be calculated. The electrostatic potential near a RE atomic site can always be expressed as a series of spherical harmonics†. This

---

†Take for example, the very simple case of a RE ion at the centre of a regular octahedron, side 2a. The positive RE ion is surrounded by six ions of charge (-e). The potential (V) at the RE ion site is

$$V = \frac{-6e}{4\pi\varepsilon_o a} - \frac{e}{4\pi\varepsilon_o} \cdot \frac{r^4}{a^5} \cdot \frac{7}{2} \left\{ C_{4,0} + \left(\frac{5}{14}\right)^{\frac{1}{2}} (C_{4,4} + C_{4,-4}) \right\}$$

where $r^2 = x^2 + y^2 + z^2$; and $C_{4,0}$, $C_{4,4}$ and $C_{4,-4}$ are spherical harmonics.

This reduces to

$$V = \frac{-6e}{4\pi\varepsilon_o a} - \frac{e}{4\pi\varepsilon_o} \cdot \left(\frac{35}{a^5}\right) \cdot (x^4 + y^4 + z^4 - \frac{3}{5} r^4)$$

with a cartesian coordinate system originating at the RE ion site.

electrostatic potential (V) will change the energy of an electron by ΔE where

$$\Delta E = \int \psi^* \, (-eV) \, \psi \, d\tau$$

ψ is the electronic wavefunction. Such calculations are described in detail by Dieke (1968) and Hayes (1974). The crystal field splittings of the levels of some rare earth ions are shown in figure 3.38. As explained in chapter 3, diagrams such as this would be necessary for a detailed interpretation of the TL of fluorite samples, doped with rare earths at specified atomic sites.

The crystal field model has considered the ion to be in a static electric field produced by the neighbouring ions. Other interactions may represent a coupling of the ion to the crystal lattice so that there can be some transfer of energy between the RE ion and lattice vibrations.

FIGURE 3.38 CRYSTAL FIELD PERTURBATIONS

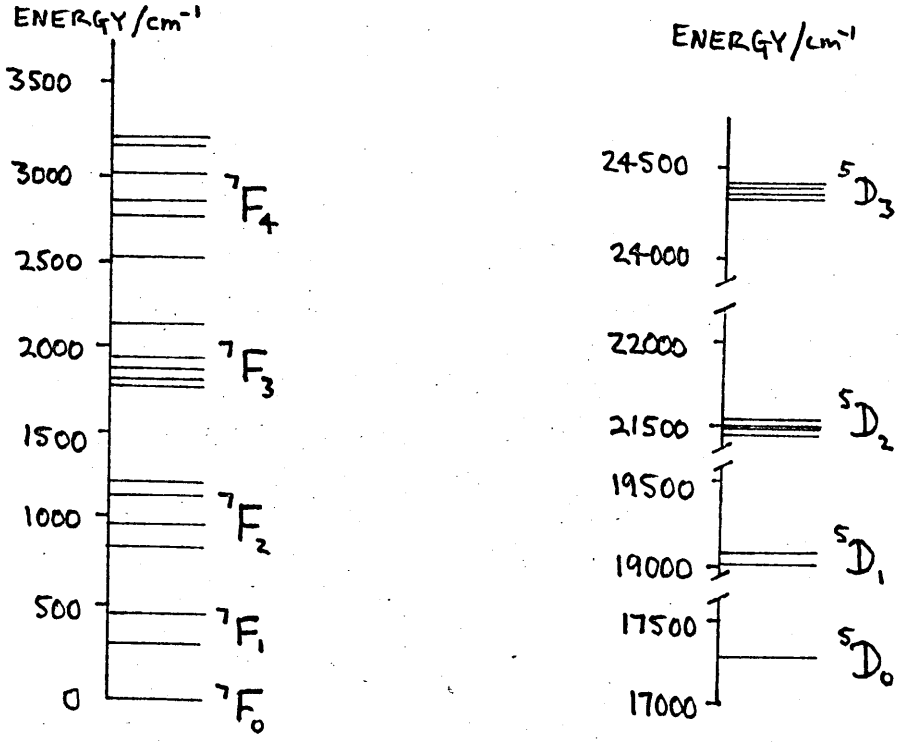

Crystal field splitting of levels of the terms ^7F and ^5D of Eu^{3+} in tetragonal sites in CaF_2.
After Hayes (1974).

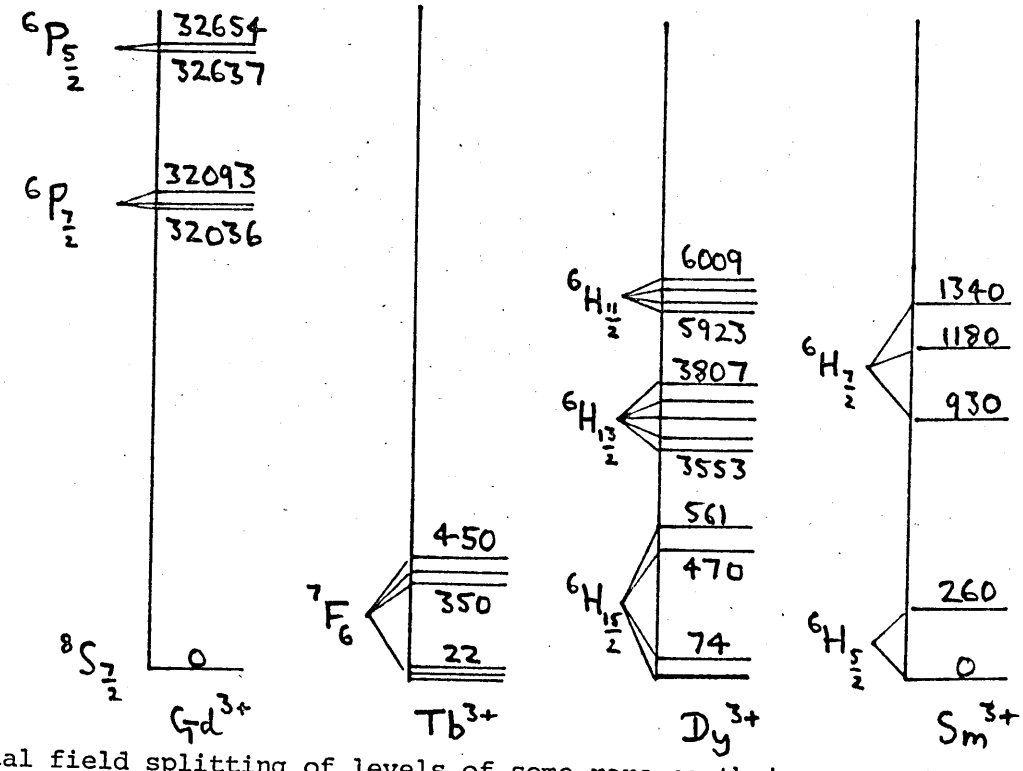

Crystal field splitting of levels of some rare earth ions at cubic sites in CaF_2. The energy of each state relative to the ground state is given in cm^{-1}. The spacings of the terms are at 0.1 of the scale of the crystal field components, except for Gd^{3+}.
After Hayes (1974).

CHAPTER 4

TRIBOLUMINESCENCE CONTINUOUS SPECTRA

4.1.1 Introduction

Some materials were found to give a continuous spectral emission throughout the sensitivity range of the IIT spectrograph when samples were cut against the rotating diamond saw blade. In this chapter I shall describe the measurement of this emission and suggest a number of possible explanations for the presence of a continuum. The line spectra obtained by cutting certain materials on the diamond saw were discussed in chapter 3.

One aim of the experiments was to ascertain the origin of the continuous emissions. Possible origins to be discussed in detail later are:

a) Crystal photoluminescence induced by gas discharge excitation or crystal luminescence induced by another mechanism e.g. radiationless repopulation or electron bombardment (electroluminescence).

b) Chemical reaction or oxidation at the newly created surfaces.

c) Frictional heating of a small volume of sample by the saw blade.

d) Black body like emission from high temperature regions at the tips of growing cracks in the material. Much of the energy used in plastic deformation of the material, as new surfaces are created, is released as heat which could lead to these high temperature regions.

The broad shape of the continua obtained, for example figure 4.1, provided an *a priori* case for fitting these continua to black body radiation curves, to investigate whether the emission was from high

FIGURE 4.1 TL OF SODA-LIME GLASS

Mercury calibration lines can be seen at 404.7, 435.8, and 546.1 nm.

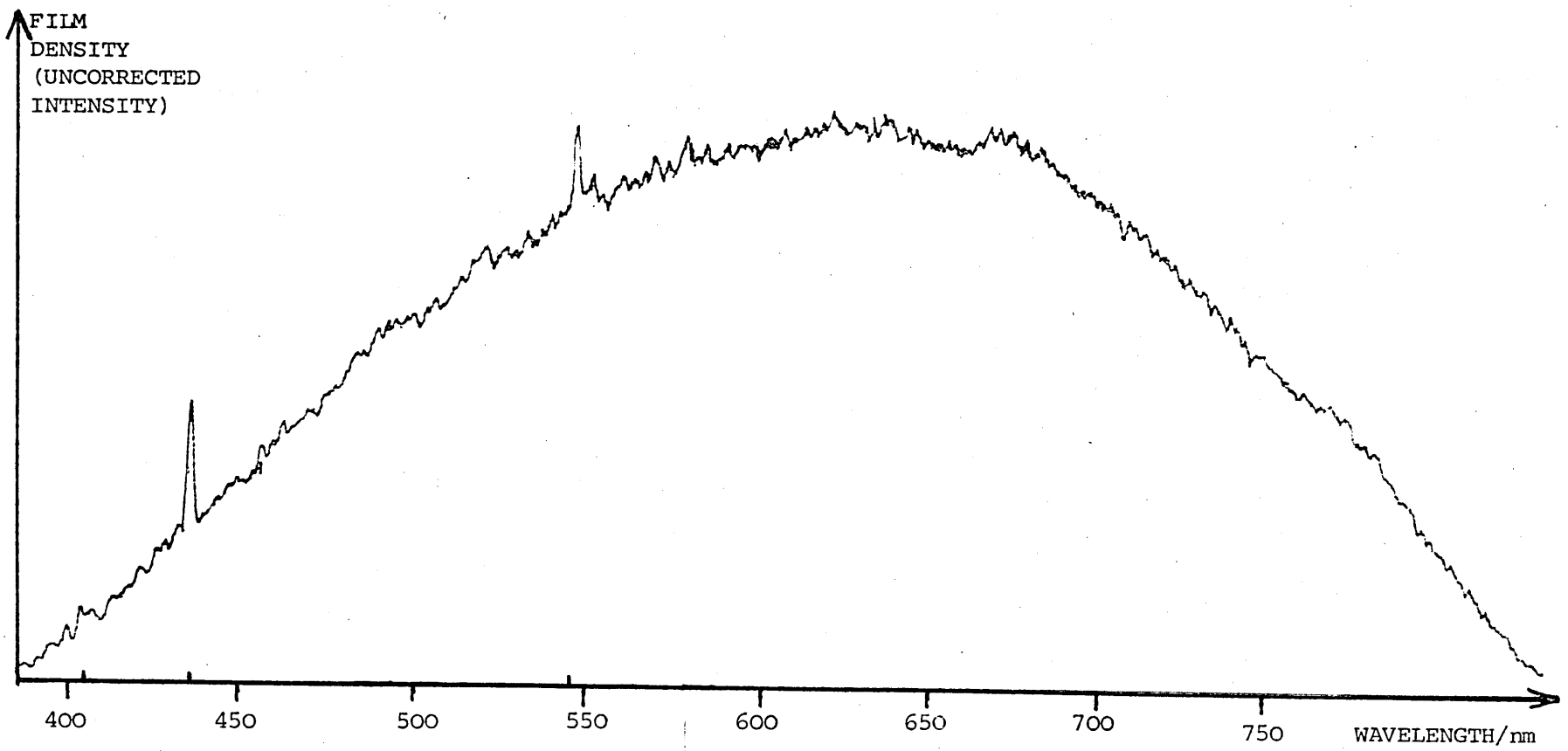

temperature regions in the material. This would enable me 1) to establish which, if any, single temperature could characterize the emission and 2) to compare temperatures from different materials.

I will discuss the fitting of a black body radiation emission to continuous TL spectra. It is, of course, important to exclude nitrogen gas discharge lines from this curve fitting procedure. Hence it is important to record the emission with sufficient resolution. If the light observed when polycarbonate or polysulphone were cut (chapter 3) had been recorded with only low spectral resolution a spurious black body fit to the nitrogen emission lines could have resulted. Weichert and Schonert (1978) measured the intensity of light emission from quartz and glass spheres that were fired at 170 ms^{-1} into a target. The intensity was measured with four photomultipliers and filters (at 420, 560, 800 and 1100 nm) but they failed to state whether they took account of any nitrogen gas discharge emission lines in their blue intensity ($\simeq$ 420 nm) measurement so their values for the intensity of the continua in the blue *may* be spurious.

The spectral emission obtained from cutting quartz and steel, and a number of different glasses[†], on the rotating diamond saw blade, was recorded as explained in chapter 2. Black body temperature fits were made in two spectral ranges 460-550 nm and 550 - 700 nm. Due to IIT noise and fall off in spectral sensitivity near 400 nm and near 750 nm the fit was not extended below 460 nm or above 700 nm. The fit was made in two ranges as a precautionary measure, because, if the resulting two temperatures differed it would suggest that more

---

[†]The TL of fractured glass was noted by Wick (1937), but she did not record any spectra.

than one emission mechanism could be operating. The black body radiation curve fitting procedure is described in appendix 1.

Typical *uncorrected* densitometer traces of the TL recorded during the cutting of soda-lime glass and quartz are shown in figures 4.1 and 4.2 respectively. The corresponding *corrected* spectra are shown in figure 4.3. The corrected TL emission spectrum of cut quartz is shown, with temperature fits in the two spectral ranges 460-550 nm and 550-700 nm, in figure 4.4.

4.1.2 Effect of Cutting Speed and Force on the Emission of Soda-Lime Glass and Quartz

Experiments were made with a quartz sample to determine the effect of cutting speed and cutting force (along a radius of the saw blade) on the observed spectrum. The results are presented in the table below.

Cutting speed† in surface metres per second	Cutting force in grams weight	Temperature of best fit in range 460-550 nm	Temperature of best fit in range 550-700 nm
ms^{-1}	g	K	K
11.5	30	3150	2550
11.5	60	3250	2400
11.5	90	3225	2400
3.8	30	3000	2250
3.8	60	2950	2300
3.8	90	3100	2250

Every temperature is the result of at least three separate experiments giving a maximum standard deviation of ≃ 200 K in each temperature

†1440 rpm (high speed) is equivalent to 11.5 surface ms^{-1} and 480 rpm (low speed) is equivalent to 3.8 surface ms^{-1}.

FIGURE 4.2 TL OF QUARTZ (CUT)

Mercury calibration lines can be seen at 404.7, 435.8, and 546.1 nm.

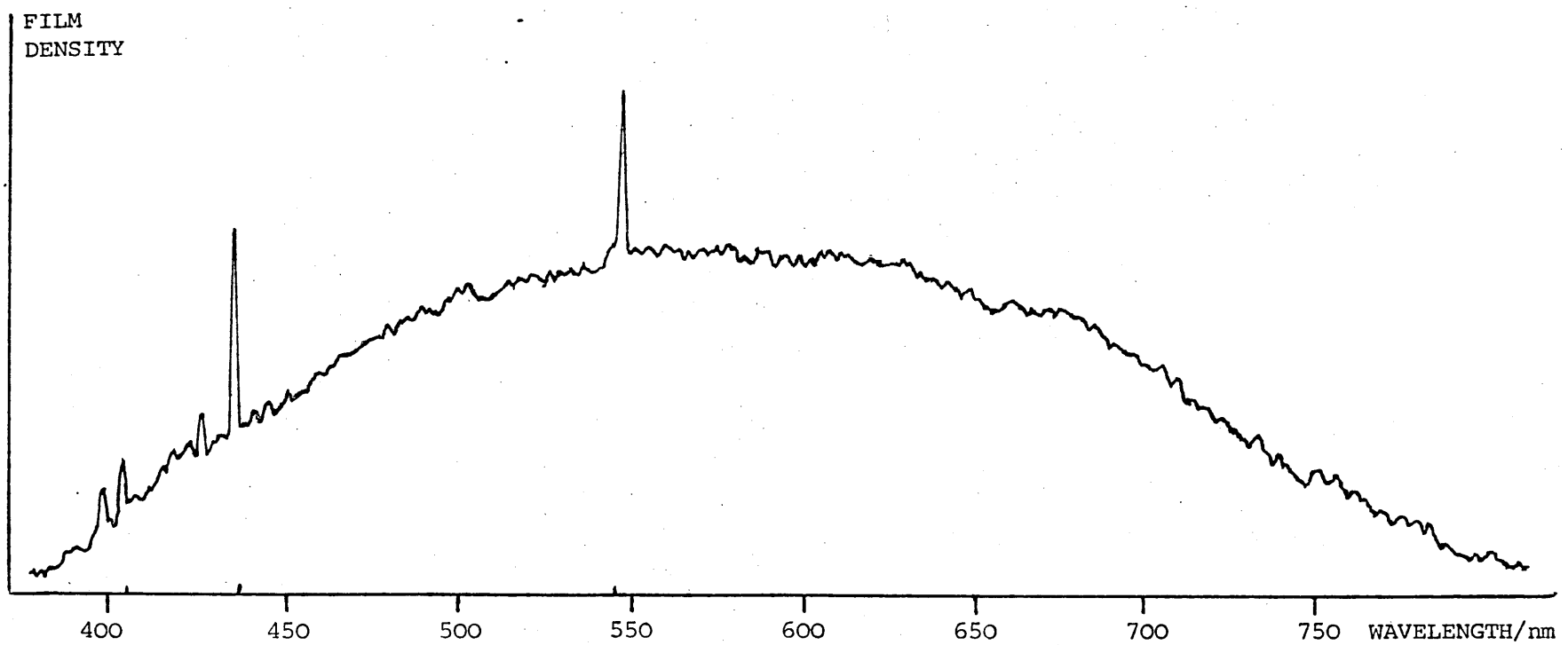

FIGURE 4.3 TL OF CUT QUARTZ AND SODA-LIME GLASS, INTENSITY CORRECTED.

Arbitrarily normalised
at 675 nm.

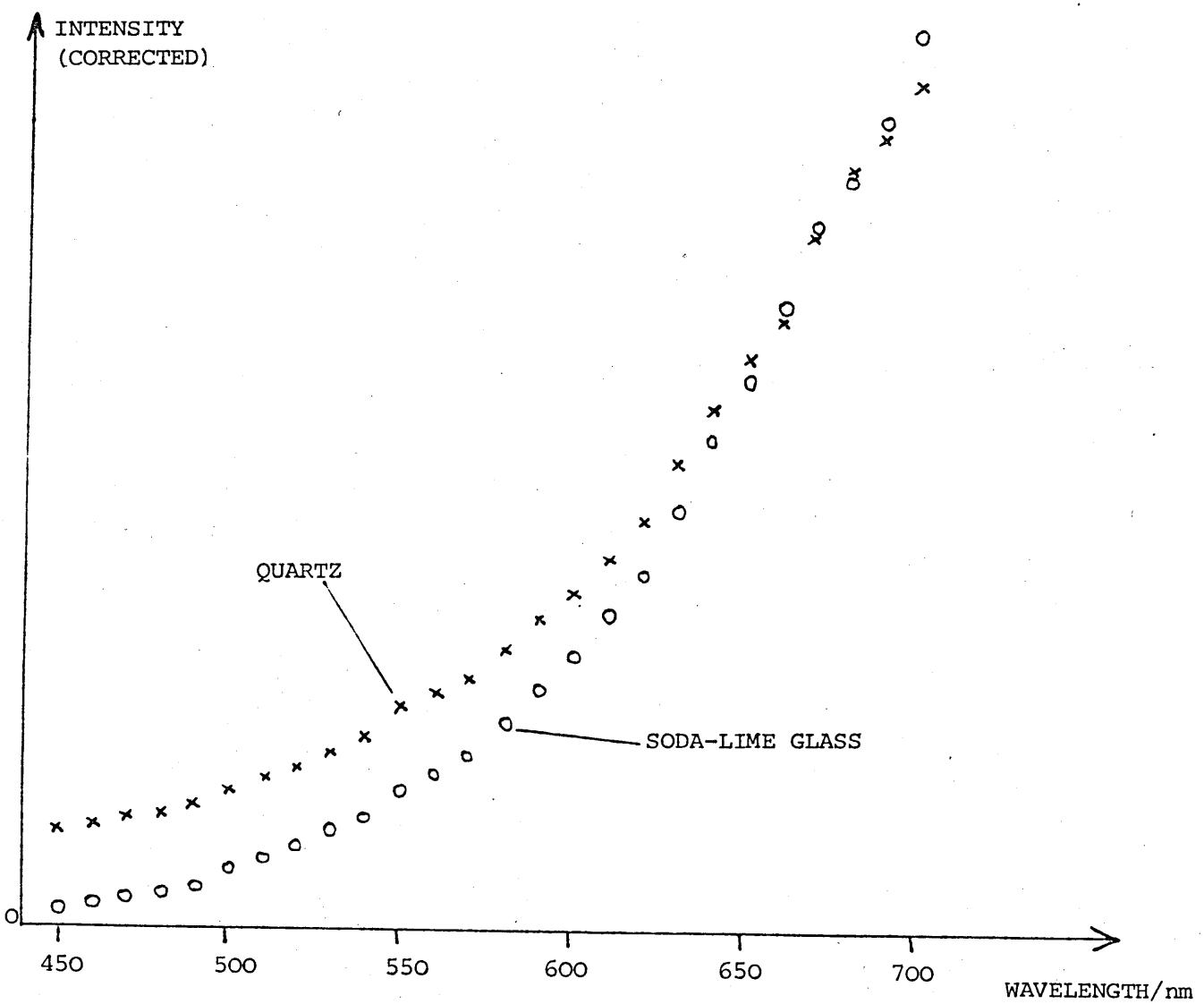

FIGURE 4.4 TYPICAL CORRECTED TL INTENSITY OF CUT QUARTZ, WITH THREE BLACK BODY EMISSION CURVES.

Normalised at 570 nm.

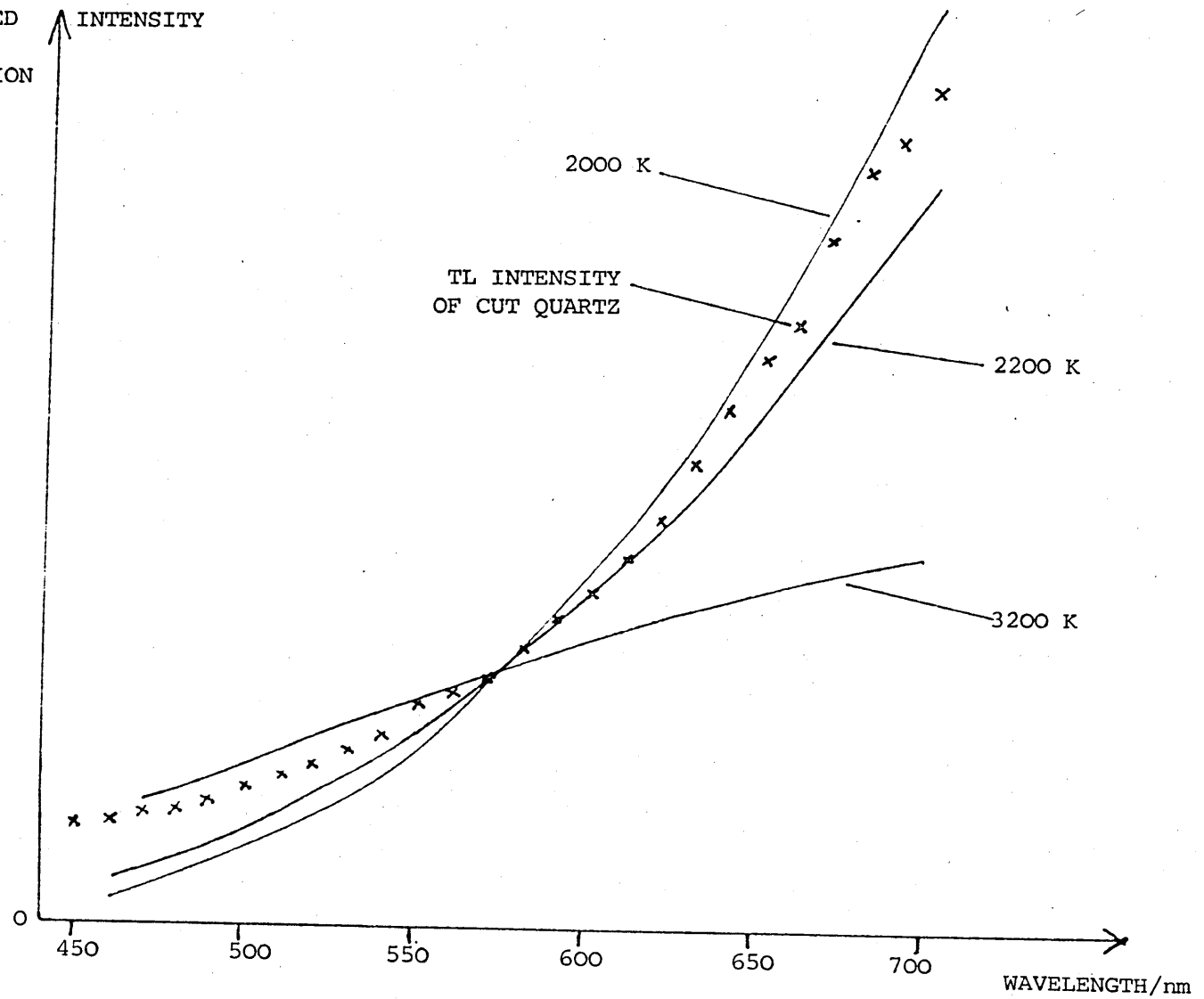

recorded in the table. A number of conclusions can be drawn:

a) In general the lower the cutting speed the lower the recorded temperature, although temperatures of both low and high speed cutting are within the 200 K error bar.

b) A higher temperature fit is obtained in the range 460-550 nm than in the range 550-700 nm. This can be explained as the result of fitting a temperature to a combination of both quartz PL and thermal emission. Quartz PL (figure 4.5) is mostly confined to the region of less than 550 nm in wavelength.

c) Within the range 30 to 90 grams weight, cutting force has no effect on measured temperature, and all fluctuations are within the error bar of 200 K.

Similar results were obtained for soda-lime glass, and are presented in the table below.

Cutting speed in surface metres per second	Cutting force in grams weight	Temperature of best fit in range 460 - 550 nm	Temperature of best fit in range 550-700 nm
ms^{-1}	g	K	K
11.5	30	2850	1900
11.5	60	2800	1975
11.5	90	2850	2000
3.8	30	1900	1850
3.8	60	2000	1825
3.8	90	2050	1900

Conclusions a), b) and c) above apply to these results. The PL of this sample of soda-lime glass was confined to a region of less than about 500 nm in wavelength. Temperatures for low speed and high speed cutting are each within the experimental error of ≃ 200 K, as are temperatures for cutting forces of 30 to 90 grams weight. Only high

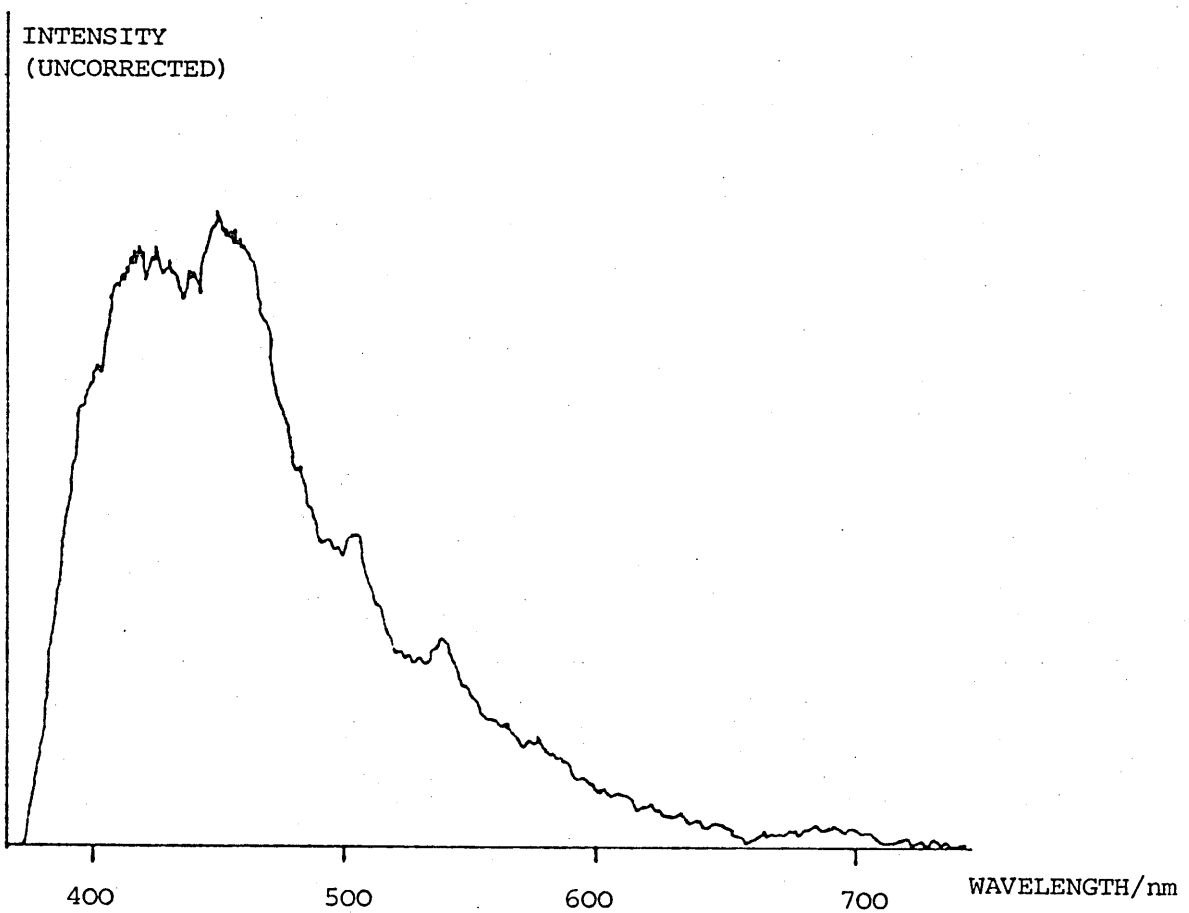

FIGURE 4.5 PL OF QUARTZ

350 nm excitation. Recorded on S20 photocathode photomultiplier.

speed cutting spectra were measured (section 4.1.4) for the remainder of the materials studied and a cutting force of 60 grams weight was used.

4.1.3 Comparison of Quartz TL obtained by Cutting and by Crushing

Spectra obtained by diamond saw cutting of a material could not always be compared with the spectra obtained by crushing the same material; the latter was frequently too weak to be recorded. However in those cases where the spectra obtained by both methods could be compared (yellow calcite, sugar, quartz and terbium doped fluorite) they were found to be identical, except in the case of quartz. Nitrogen gas discharge lines were recorded when quartz was fractured (figure 4.6) and when it was cut; and in addition a strong background continuum (figure 4.2) was visible when the samples were cut. Only a weak background continuum was present in the TL of the fractured sample (figure 4.6). A possible explanation is that there is more than one mechanism responsible for light emission resulting from the application of mechanical energy to quartz, and that one mechanism is dominant when quartz is cut (possibly radiationless population, Lin and Wutz et al., 1980) and another (possibly nitrogen gas discharge induced PL) when it is fractured. The fractured quartz TL continuum cannot reasonably be associated with emission from a hot region near the cutting surface since a black body radiation fit to the corrected spectrum gives a temperature of about 22000 K; but the fractured quartz TL does resemble the PL spectrum of the quartz sample(figure 4.5).

The TL of quartz was first reported by Beals (1923), see chapter 2. He rubbed pieces of quartz tube together and saw a continuous spectrum extending throughout the visible and into the ultra-violet with no sign of any spectral lines. Longchambon (1925) studied TL due to fracturing (not rubbing) quartz, and noted a continuum, intense from

FIGURE 4.6 TL OF QUARTZ (FRACTURED)

Mercury calibration lines can be seen at 404.7, 435.8, 546.1, 577.0 and 579.1 nm.

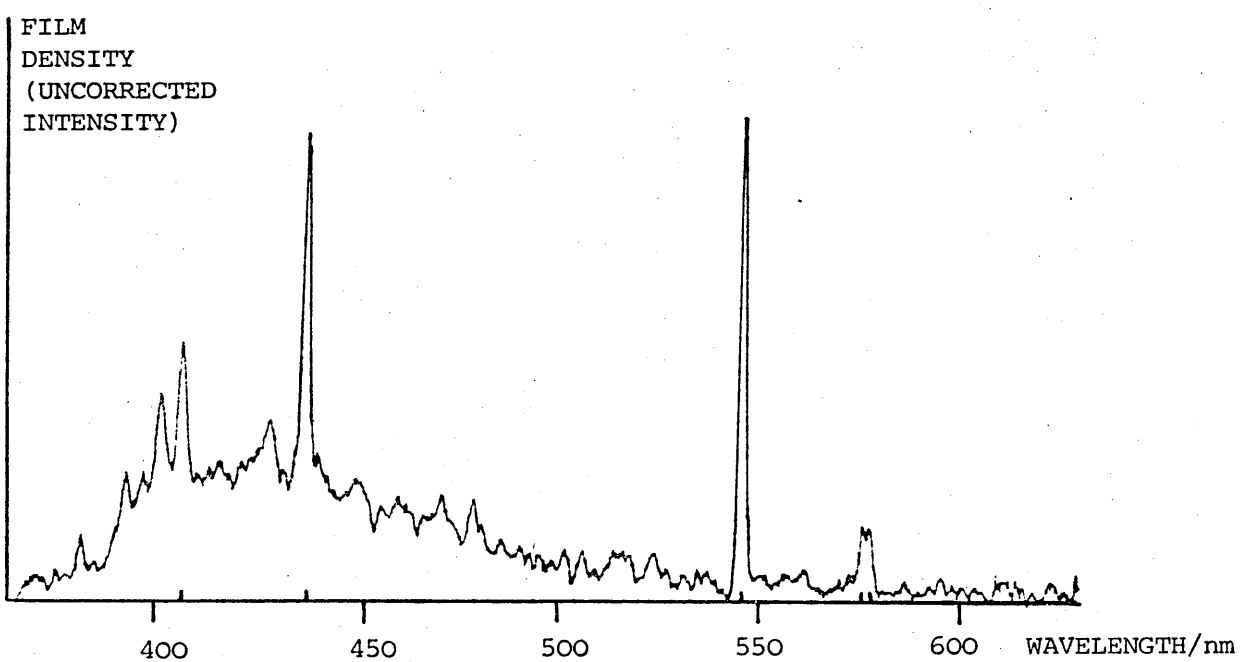

480 to 430 nm, weak below 430 nm, and with nitrogen lines at 436 and 424 nm. This is similar to my recorded TL spectrum of fractured quartz.

4.1.4 Other Materials

Typical uncorrected spectra of armourplate glass, lead glass, pyrex and steel are shown in figures 4.7, 4.8, 4.9 and 4.10. These spectra were intensity corrected and black body temperature fits were made as explained above. The results for each material were averaged and are shown with melting point data in table 4.1.

I suggested above, a) to d) in section 4.1.1, possible origins for the continuous spectral emission. The temperature to be expected near the cutting surface in each material may be calculated on the basis of two of these models:

1) Frictional Heating

2) Release of plastic deformation energy near the tips of growing cracks in the material.

A comparison of temperatures calculated using each model, with the experimental results obtained by diamond saw cutting, will test the applicability of the models to these experiments.

4.2 Frictional Heating Model

When one solid slides over another the local points of contact on the surface are raised to a high temperature. This temperature can be high enough to cause emission of significant radiation in the visible region of the spectrum (Bowden and Thomas, 1954). Bowden, Stone and Tudor (1947) showed that the hot spots of some non-conducting

FIGURE 4.7 TL OF ARMOURPLATE GLASS

Mercury calibration lines can be seen at 404.7, 435.8, 546.1, 577.0 and 579.1 nm.

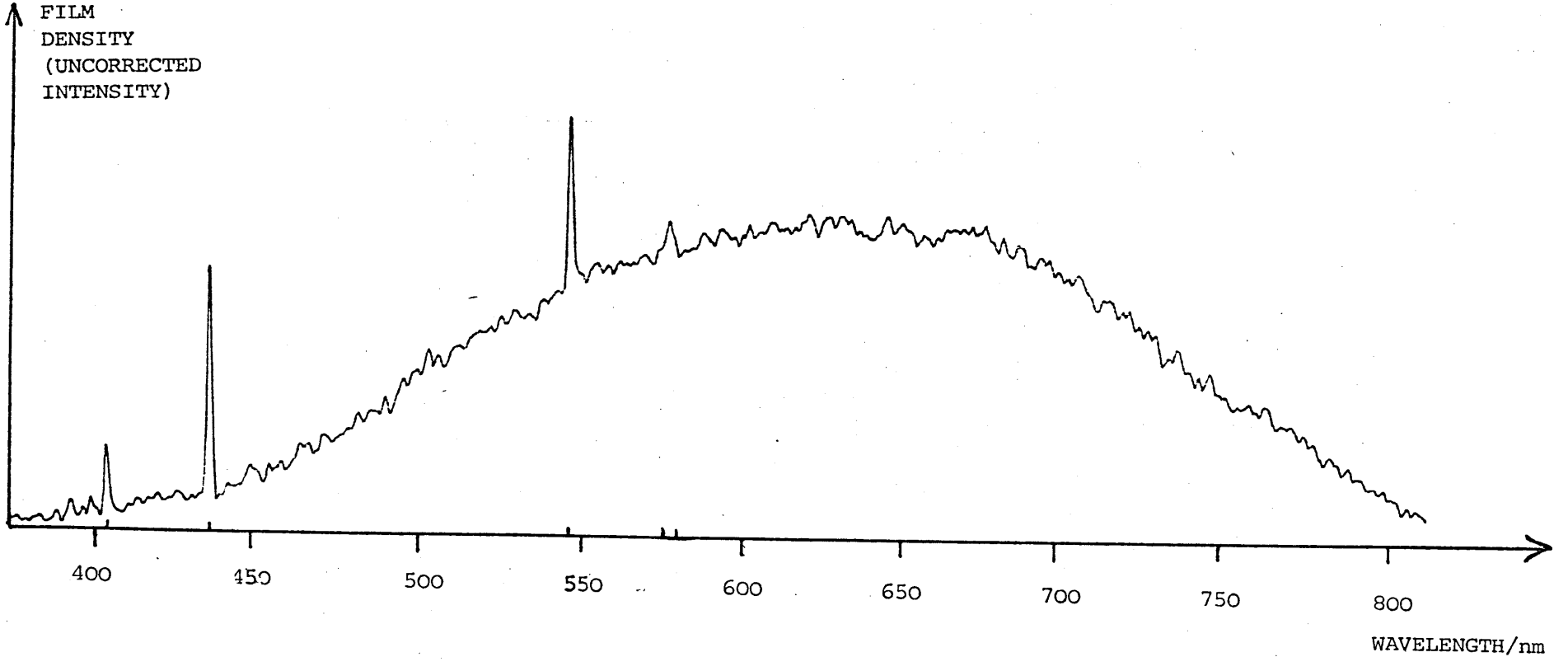

FIGURE 4.8 TL OF LEAD GLASS

Mercury calibration lines can be seen at 404.7, 435.8, 546.1, 577.0 and 579.1 nm.

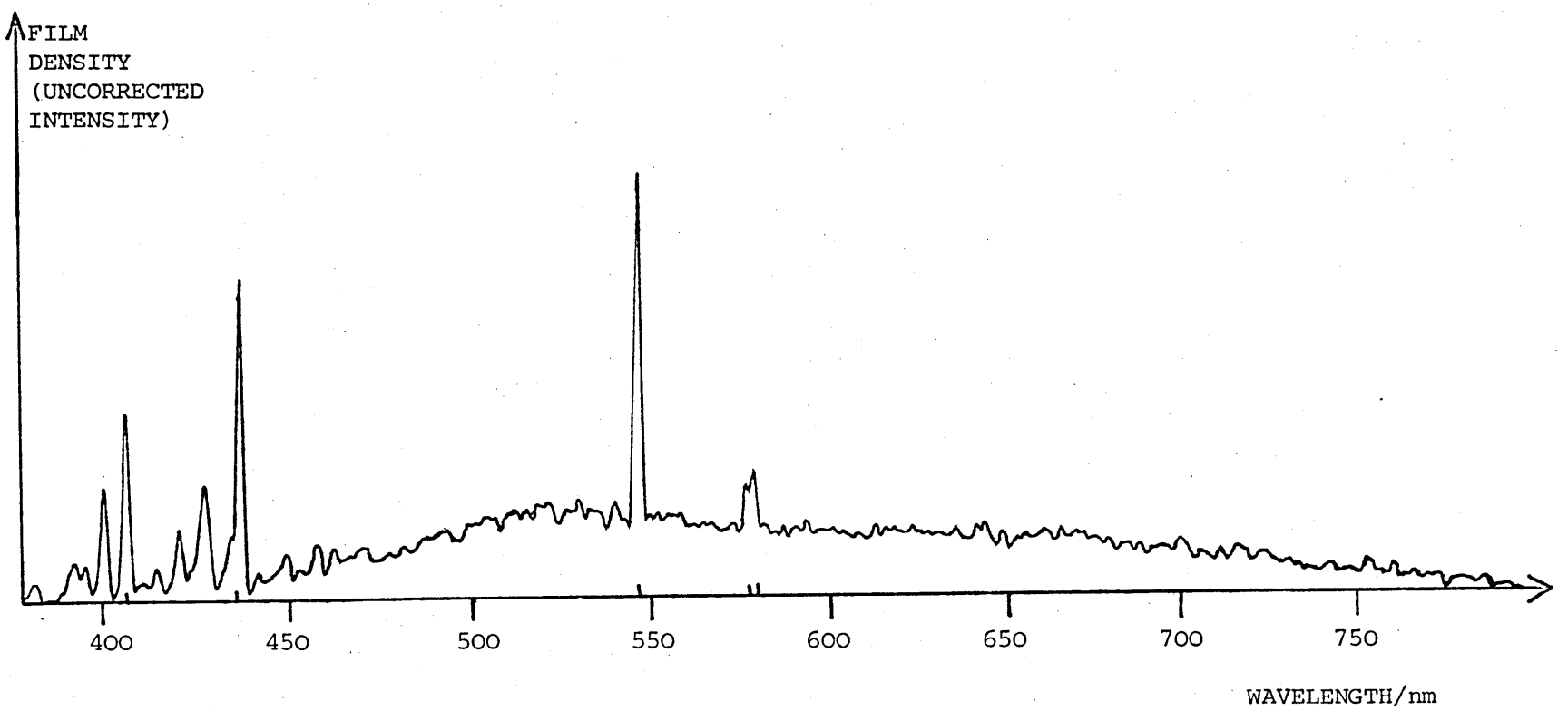

FIGURE 4.9 TL OF PYREX

Mercury calibration lines can be seen at 404.7, 435.8, 546.1, 577.0 and 579.1 nm.

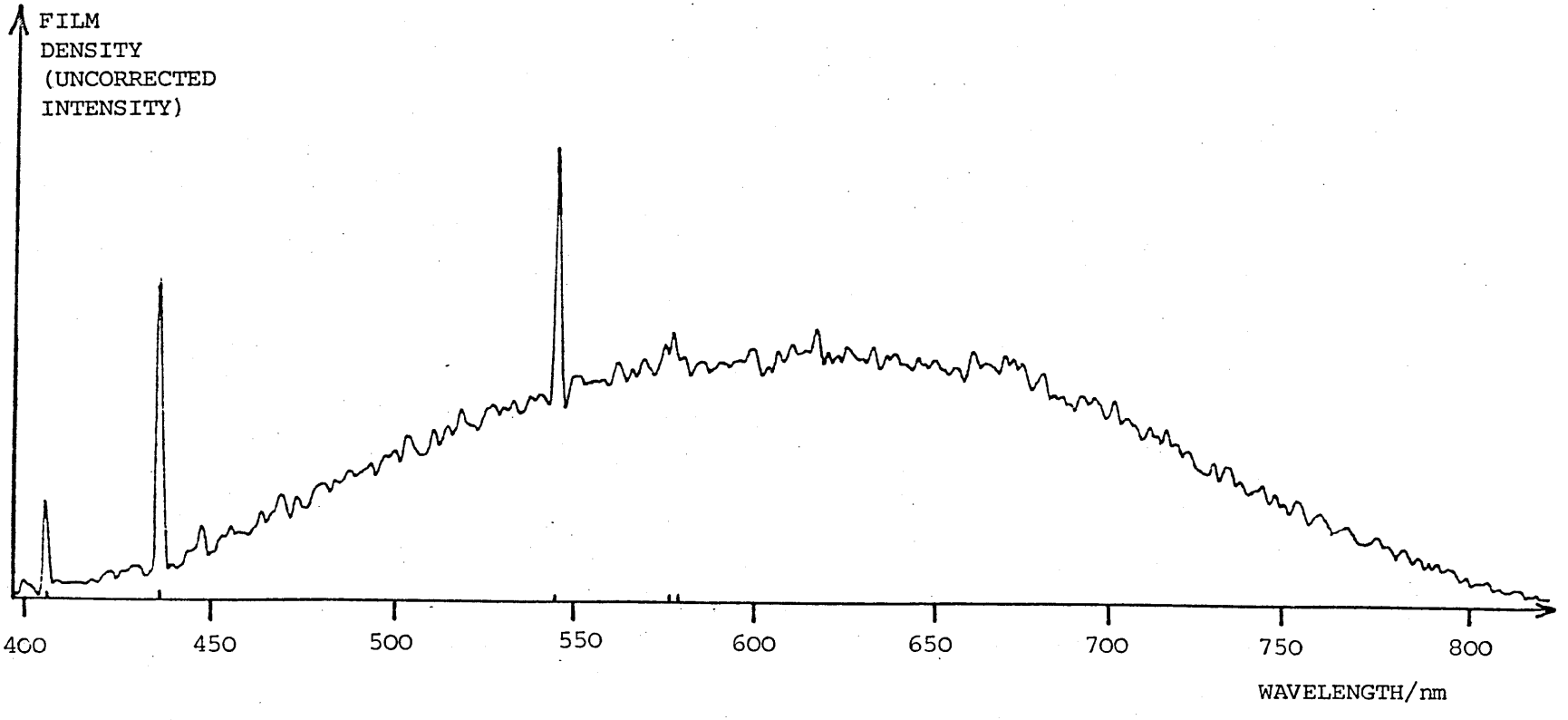

FIGURE 4.10 TL OF STEEL

Mercury calibration lines can be seen at 404.7, 435.8, 546.1, 577.0 and 579.1 nm.

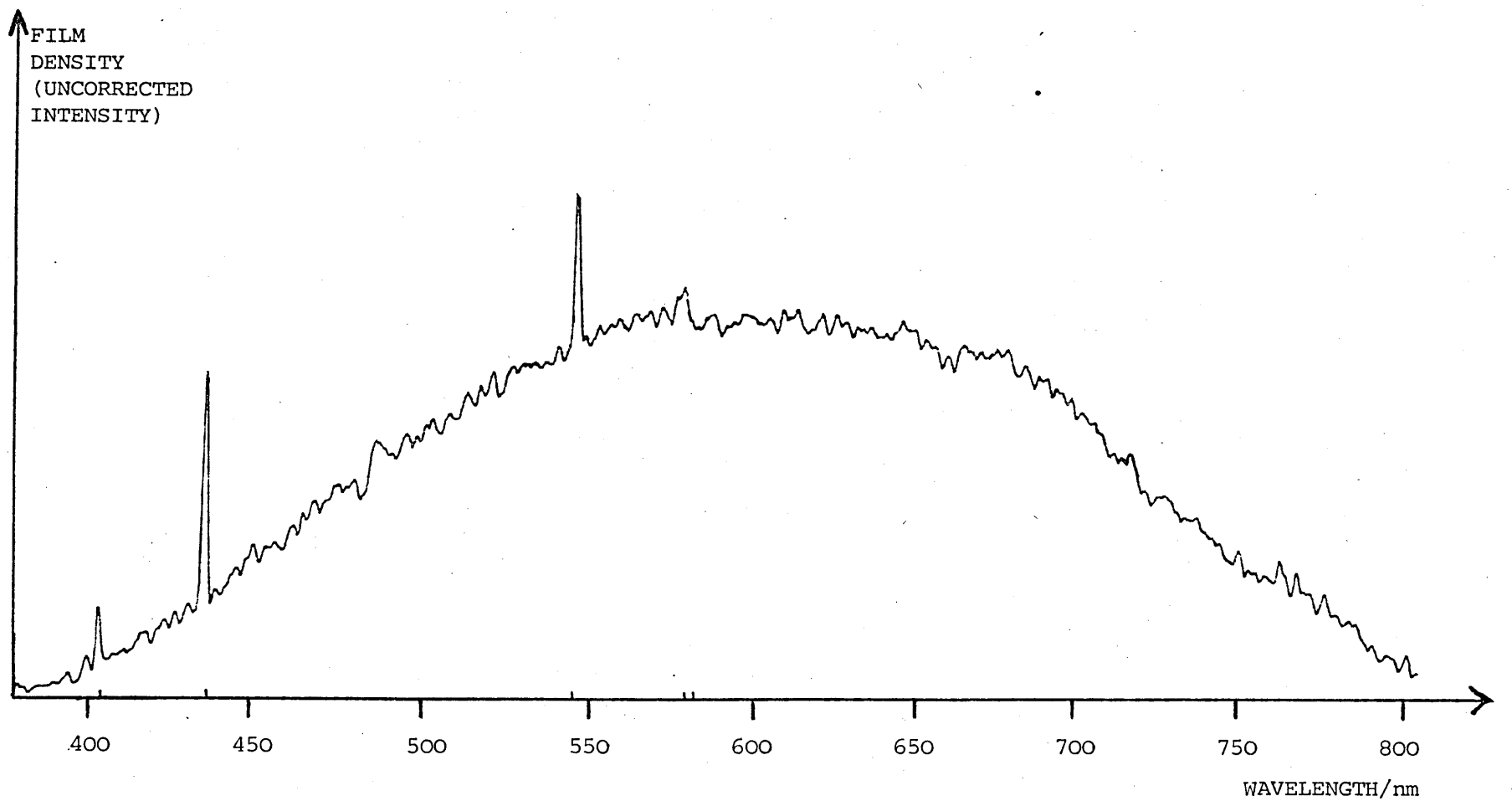

Material	Temperature in kelvins for spectral range 460-550 nm	Temperature in kelvins for spectral range 550-700 nm	Melting Point in kelvins
Quartz	3150 (SD 200)	2400 (SD 100)	1880
High Density Lead Glass	2700 (SD 100)	2050 (SD 150)	650-710[a] Softens 730-830 Flows
Pyrex	2200 (SD 100)	2000 (SD 50)	1090 Softens 1520 Flows
Soda-lime Glass	2800 (SD 200)	1975 (SD 200)	968 Softens 1280 Flows
Armourplate Glass	1900 (SD 150)	1800 (SD 50)	950[a] Softens 1260 Flows
Steel	2400 (SD 200)	2000 (SD 200)	≃ 1810

Black body spectral distributions were fitted to the light emitted from the above materials when they were cut, with 60 grams force on the diamond saw. Each temperature is an average of at least three results; from which the standard deviation (SD) was obtained. "Softens" and "Flows" are defined in terms of viscosity see a).

a) Bolz and Tuve (1973).

TABLE 4.1 BLACK BODY RADIATION TEMPERATURES

transparent solids could be observed directly by eye and recorded photographically. High surface temperatures occur readily but there is usually a maximum temperature for given materials. By using materials of known melting point Bowden and Thomas were able to show experimentally that the temperature rise is limited to the melting point of the lower melting point material.

With aluminium rubbing against glass they noted some very hot spots (temperature greater than the melting point of either material) and concluded that these were due to chemical oxidation or "burning" of the metal.

All the temperatures that I measured were lower than the melting point of diamond (3800 K), and greater than the samples' melting points. Thus, for example, the melting point of quartz is 1880 K while the continuum emission in the range 550 to 700 nm fitted a black body temperature of $\simeq$ 2400 K. On this basis the frictional heating model appears to be inapplicable to my results.

4.3 Crack Tip Temperature Model

During the fracture of a material, elastic energy is consumed at the crack tip. In a perfectly brittle failure no energy is lost in permanent deformation of the material i.e. in plastic flow. Energy is used only in the elastic energy changes involved in creating the fracture surfaces and in the kinetic energy of the fragments. In an ideal brittle material the energy consumed (fracture surface energy) would be expected to be 0.1 to 2 Jm^{-2} (Field, 1971). Experiments however show that even solids which are normally thought of as perfectly brittle (e.g. glass) have fracture surface energies of about

5 Jm^{-2}. The extra energy is used in plastic deformation at the crack tip, even in so called brittle materials. Most of this energy is converted to heat and normally 60% to 90% (Weichert and Schonert, 1978) of the energy required to propagate the crack is released as heat. A high temperature region is expected to move with the crack and the temperature of this region can be calculated by considering the crack tip as a moving heat source. The classical linear heat conduction equation is transformed into a frame of reference moving with the source and the equation is solved under the assumptions that thermal conductivity (k) and †thermal diffusivity (λ) are independent of temperature. An inspection of data tables (Touloukian, 1967) shows that this is justified because the temperature dependence of k and λ is weak. The use of the classical heat conduction equation is legitimate because the mean free phonon path length is much less than the smallest dimension of any region which is assumed to be in thermal equilibrium. Loss of heat by radiation is negligible compared with conduction into the sample.

The method of solution proposed by Weichert and Schonert (1978) assumes a rectangular heat source moving through the material with the speed of a crack tip. The heat source is shown in figure 4.11. The assumption of uniform heat evolution (Q) leads (Weichert and Schonert, 1978) to

$$T(x,y) = T_o + \frac{Q}{2\delta hw}\ \theta\left(\frac{x}{\delta}, \frac{y}{\delta}, \frac{d}{\delta}, \frac{u\delta}{2\lambda}\right) \qquad 1$$

where T_o is the ambient temperature, Q the crack heat ($\simeq$ 75% of fracture surface energy), u the crack velocity, h the specific heat

---

†Thermal diffusivity equals thermal conductivity divided by specific heat per unit volume. It has SI units of m^2s^{-1}.

per unit mass†, 2δ the width of the heat source in a direction perpendicular to its motion, d is the heat source length and θ is a normalised temperature function, which depends on $\frac{u\delta}{2\lambda}$ and the position coordinates x and y from the centre of the moving source. The dependence of θ on $\frac{u\delta}{2\lambda}$ for four positions in the moving source (with $d = 2\delta$) is shown in figure 4.12. The maximum temperature occurs at the back of the source when $\theta \simeq 1$; that is at high crack velocities when $\frac{u\delta}{2\lambda} > 10$. The highest temperature near the crack tip, on this model, is thus approximately given by

$$T = T_o + \frac{Q}{2\delta h w} \qquad 2$$

provided that

$$\frac{u\delta}{2\lambda} > 10 \qquad 3$$

Data from a number of references is collected in table 4.2 and is used to calculate, with equations 2 and 3 above, an approximate crack tip temperature for some of the samples that I have studied. The calculated temperatures are shown in table 4.2. If the crack velocity is less than $20\lambda/\delta$ (shown in table 4.2) then the calculated temperature will be less than the value given in table 4.2.

The calculated temperatures are dependent on Q and 2δ, which are not known with great precision. Errors in Q and 2δ could vary the calculated temperature by a factor of 2 or more.

A comparison of my diamond saw cutting temperatures (table 4.1) with the calculated temperatures of table 4.2 shows no agreement between the figures. Also different experimental temperature fits occur in the two spectral ranges 460 to 550 and 550 to 700 nm. This suggests

† w is sample density

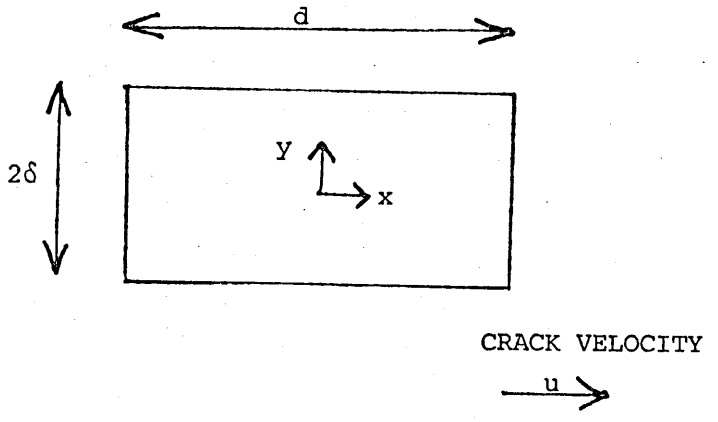

FIGURE 4.11 THE MOVING HEAT SOURCE USED TO MODEL CRACK TIP HEAT EMISSION. The source is one unit long in the 'z' direction.

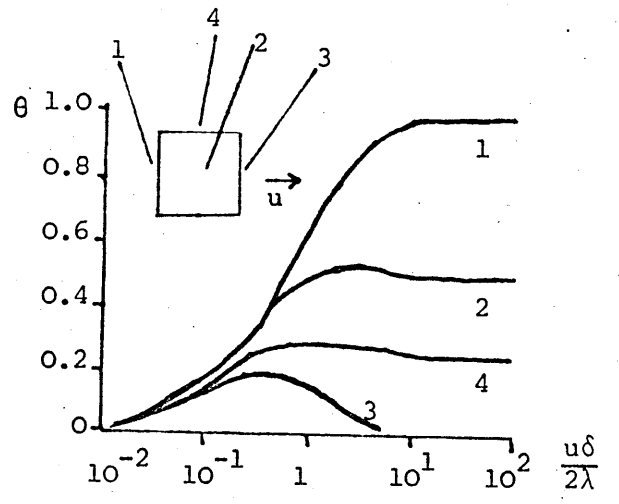

FIGURE 4.12 THE DEPENDENCE OF θ ON $\frac{u\delta}{2\lambda}$ FOR FOUR POSITIONS IN THE MOVING SOURCE.

See section 4.3, where θ, the normalised temperature function, is discussed.

After Weichert and Schonert (1978).

	Pyrex	Soda-lime Glass	High Density Lead Glass	Quartz	Steel
Q Jm^{-2}	7.5 a	4.2 a	3 a	10 c	10^{5} b
2δ m	$3x10^{-9}$ b	$3x10^{-9}$ b	$3x10^{-9}$ b	$\simeq 3x10^{-9}$ b	$2x10^{-4}$ b
h $J\,kg^{-1}\,K^{-1}$ Specific Heat	975 a	890 b	500 e	750 e	635 d
w $kg\,m^{-3}$ density	2230 a	2470 a	5100 a	2650 d	7870 d
k $J\,m^{-1}\,s^{-1}\,K^{-1}$ thermal cond.	1.67 (550°C) 1.13 (20°C) b	1.03 b	.54 e	1.36 e	50 e
$\lambda = k/hw$ m^2s^{-1} Thermal Diffusivity	$.076x10^{-5}$ d	$.05x10^{-5}$ b	$.02x10^{-5}$ e	$.068x10^{-5}$ e	10^{-5} b
u ms^{-1} typical crack velocity	2100 a,f	1500 a	1000 a	2600 d	2500 d
$20\lambda/\delta$ m s^{-1}	10000	6700	2700	9000	2
Calculated Temperature from Equation 2, Section 4.3 with T_o=273 K	1400 K	900 K	670 K	1950 K	370 K

a) Swallowe 1980

b) Weichert and Schonert 1978

c) Estimate from b)

d) Bolz and Tuve 1973

e) Baumeister 1978

f) Approximately equals half the longitudinal stress wave velocity (Fox and Ruiz 1970)

The calculated temperature will be less than the value shown, for crack velocities less than $20\lambda/\delta$.

TABLE 4.2 CRACK TIP TEMPERATURE CALCULATION DATA

either that the model used for calculation is inapplicable to my experiments, or that some other luminescence emission is present in addition to any black body radiation. Experiments with the spectrofluorimeter showed that quartz and the glasses were photoluminescent in the blue and so any PL induced during cutting by, for example, a nitrogen gas discharge, could affect the 460-550 nm region black body fit.

The TL of amethyst (quartz with manganese as an impurity) produced when samples are cut on a diamond saw, is probably of a PL origin. The TL emission (figure 4.13) is typical of the PL emission from a manganese doped sample (Hardy and Zink, 1976). An attempted black body fit to the emission gave temperatures of 3400 K in the range 460-550 nm and 2400 K in the range 550-700 nm. The difference between these temperatures suggests that a single temperature source is definitely not the origin of the emission in this case.

Absorption by the sample may also occur. Zircon, $ZrSiO_4$ (Ceylon) when cut on the diamond saw, exhibits a strong continuum, but with some of the strongest absorption bands of the mineral (Webster, 1964) superimposed, in particular the 653 and 683 nm bands (figure 4.14).

4.4 Conclusions and Comparison with other Work

This is the first time that the emission of light obtained by cutting various glasses and minerals on a diamond saw has been studied. Light emission from the glasses was too faint to record when limited quantities of small samples were fractured, but was much brighter when the samples were cut on the diamond saw. The light was recorded on the IIT spectrograph and a black body radiation temperature fit was made. No single temperature could describe the emission, and I

FIGURE 4.13 TL OF AMETHYST

Mercury calibration lines can be seen at 404.7, 435.8, 546.1, 577.0 and 579.1 nm.

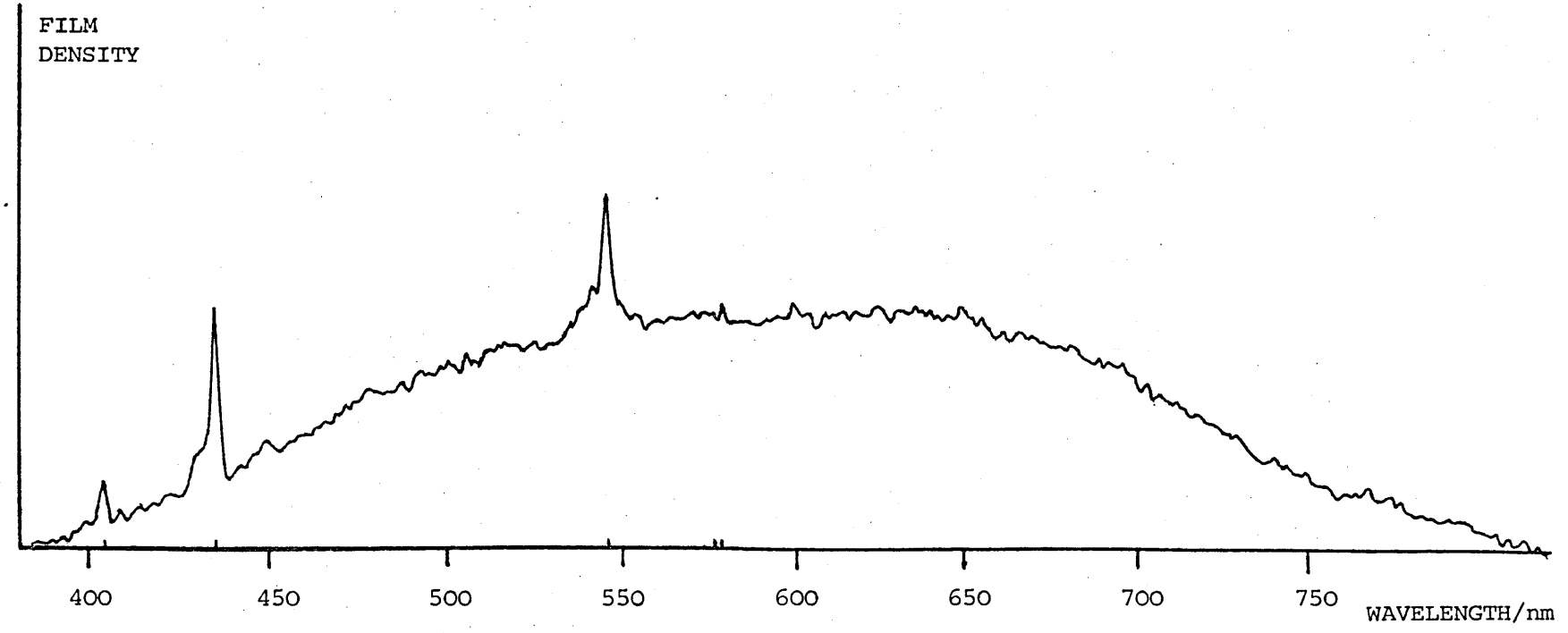

FIGURE 4.14 TL OF ZIRCON

Mercury calibration lines can be seen at 404.7, 435.8, 546.1, 577.0 and 579.1 nm.

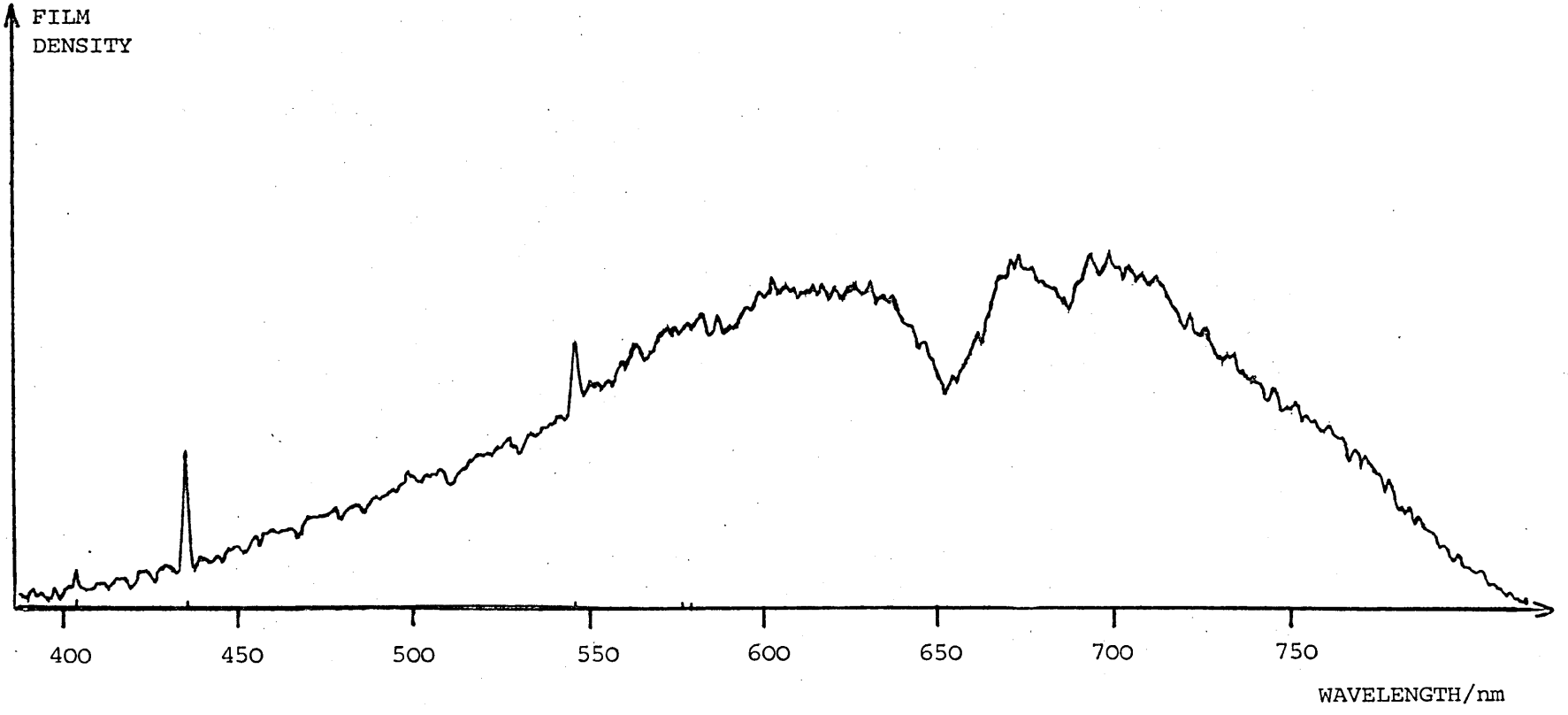

conclude that the emission arises from a combination of impurity states excited either radiatively (in the cases where a nitrogen gas discharge is present) or non-radiatively (Lin and Wutz et al., 1980), and possibly indirectly from frictional heating which could excite THL. Boron has been suggested as a possible glass impurity by Roberts (1980). Impurity emission from sodium in glasses is unlikely since I would expect to see the sodium 'D' lines, and have not done so. They are observed when soda-lime glass is heated (in a flame) and in the TL of crushed sodium chloride (Krutyakova and Smirnov, 1979).

The TL of fractured quartz was found to be a nitrogen gas discharge with a blue continuum superimposed. This continuum resembles the PL of the same sample. When quartz was cut on the diamond saw a bright continuum was observed, and with some samples the nitrogen gas discharge lines were faintly recorded. I suggest that a number of mechanisms are responsible for light emission from quartz. When quartz is fractured a nitrogen gas discharge is present, with its origin in high electric fields across air filled cracks. This results in faint quartz PL. When quartz is cut the material is continually removed with the diamond teeth and new surfaces are constantly being formed. The observed light emission during cutting could be a combination of thermal emission from the release of plastic deformation energy, combined with impurity luminescence (possibly by radiationless population, Lin and Wutz et al., 1980). That impurity emission does occur during cutting of amethyst is evidence for this. Perhaps the nitrogen discharge is faint and sometimes not observed during cutting because the new surfaces are formed rapidly and in quick succession. See section 2.4.3 where Chandra's work on the kinetics of nitrogen gas discharge TL is discussed. He found that the TL did not appear at the instant of

application of stress to a sample.

The temperatures which I obtained, by fitting the TL spectra of diamond saw cut quartz and glasses to black body radiation curves, in the range 460 to 550 nm, are of the same order of magnitude as the temperatures found by Weichert and Schonert (1978) of 3200 K for glass (unspecified type) and 4700 K for quartz. However as mentioned earlier in this chapter, the authors failed to state whether any nitrogen gas discharge emission was present, so a comparison of my results with theirs may be unjustified.

The high temperatures observed when steel is cut (see table 4.1) are much greater than those calculated on a crack tip temperature, or a frictional heating model; and are probably due to chemical oxidation (burning) of steel particles (they may be initially heated by friction) which raises them to the melting point of steel, but no higher due to the large latent heat. Light emission from burning iron and steel flakes has been investigated by Ohman (1978 and 1979), who suggested that the emission may in part be a tribo-induced discharge luminescence. He has suggested that effects of a similar kind may contribute to the light emission of meteors, comets and other celestial objects. He reported identifying lines of CH, Fe, C_2 and CN in the emission. An examination of one of his densitometer traces (e.g. figure 1 in Ohman, 1979) shows that these lines are largely obscured by film grain noise. He used a spectrograph and camera system without any image intensification. I could not positively identify any such lines in the emission that I recorded from cut steel, with the IIT spectrograph.

In summary, I have shown that the IIT spectrograph apparatus can be usefully applied to a study of TL. I have obtained a number of new TL spectra and suggested possible explanations for the emission.

Further work on the elucidation of TL mechanisms could be usefully undertaken by preparing pure samples of many of the materials that I have studied, and then doping them with trace elements like manganese or the rare earths to see the effect this has on their TL emission.

CHAPTER 4

APPENDIX 1

Black Body Radiation

Energy radiated from a black body is distributed between the different wavelengths according to Planck's Radiation Law; thus

$$\Delta E \propto \frac{1}{\lambda^5 \left(\exp\left(\frac{hc}{kT\lambda}\right) - 1\right)} \Delta\lambda$$

which reduces to

$$\Delta E \propto \frac{1}{\lambda^5 \left(\exp\left(\frac{1.44 \times 10^7}{\lambda T}\right) - 1\right)} \Delta\lambda$$

if λ is expressed in nanometres and T in kelvins. With these units the peak wavelength is given by $\lambda T = 2.9 \times 10^6$.

The procedure for assigning a temperature to a measured spectrum was as follows:

The unknown radiation, and black body radiation of temperature T, were normalized in intensity at one wavelength (usually in the middle of the spectral range). The sum of the squares of the differences, at each 10 nm wavelength increment, between the intensity of the unknown radiation and that of the black body radiation, was calculated as the "error". T was varied to minimize this error. The procedure was repeated to see if other normalization wavelengths resulted in a smaller error. The temperature of the unknown radiation was then equated to the temperature of the best fit. This procedure was, of course,

always carried out on intensity corrected spectra.

The spectral emissivity of the materials which I studied may vary with wavelength, but I could find no data† (with appropriate sample temperatures) in the range 400-750 nm and so no correction factors were added to my black body fits. It is however thought that changes in emissivity in the range 400-750 nm will be small (Roberts, 1980).

---

†Dialog Information Retrieval Service, Palo Alto, California, U.S.A. December 1980.

CHAPTER 5

Spatial Studies of Semiconductors

5.1.1 Introduction, and Purpose of the Study

One object of this research was to show that a spatial study of the electroluminescence (EL) and photoluminescence (PL) of semiconductor specimens can be usefully undertaken with an image intensifier tube (IIT) coupled to a microscope. Information about spatial inhomogeneities in the samples is obtained. I shall illustrate my description of the method with typical experimental results.

Spatial inhomogeneities in supposedly uniform materials have been noted by a number of workers. For example some cyclotron resonance experiments to determine carrier effective mass have resulted in a double resonance peak because the active area of the sample was spatially inhomogeneous. In alloys such as $Ga_{1-x}Al_xAs$ (an alloy of GaAs and AlAs) any spatial variation in the composition (i.e. in x) over the area of a specimen will lead to changes in band gap and emission frequency and also to changes in radiative recombination efficiency. Properties usually vary smoothly with x and data for GaAs (x = 0) and AlAs(x = 1) are given in table 5.1.

Spatial variations in the physical properties of semiconductors can have important consequences in electronic devices. For example in integrated circuit fabrication, and when a slab of material is cut into a number of small pieces all requiring similar characteristics.

I made a comparison for $Ga_{1-x}Al_xAs$ between spatial information provided by a) EL observed with my high gain IIT microscope

	Gallium Arsenide	Aluminium Arsenide	Gallium Phosphide	Crystalline Silicon
Band Gap at 300 K in eV	1.435	2.16	2.25	1.11
Band Type	Direct	Indirect	Indirect	Indirect
Lattice Constant in nm	.565	.566	.545	.543
Electron Mobility at 300 K, in $m^2 V^{-1} s^{-1}$	.88	.12	.012	.135
Hole Mobility at 300 K, in $m^2 V^{-1} s^{-1}$	.040	.042	.012	.048
Electron Effective Mass m_e^*	.07	.5	.13	Longitudinal .98 Transverse .19
Hole Effective Mass m_h^*	.5	Longitudinal 1.06 Transverse .49	.67	.52

Data from Williams and Hall (1978)

TABLE 5.1 SEMICONDUCTOR PROPERTIES

b) Scanning electron microscope secondary electron contrast (SEC) and c) Scanning electron microscope cathodoluminescence (CL). These last two facilities were provided by The Department of Metallurgy and Science of Materials, University of Oxford. I also studied the EL of GaP and the PL of amorphous silicon (a-Si).

5.1.2 Summary of Experimental Technique

My spatial study used an IIT coupled to a microscope. The apparatus is shown schematically in figure 5.1. The specimen of typical size $5mm^2$ was either a) made to electroluminesce by passage of an electric current or b) induced to PL by He - Ne laser excitation light of 632.8nm or c) for the purposes of focusing on the sample surface, illuminated obliquely with ambient light from a variable brightness microscope lamp. See figure 5.2.

An image of the specimen was formed by the microscope objective and projection eyepiece on the first photocathode of the IIT. At greater than 100 x linear magnification the system resolution at high light levels is in principle limited only by optical microscope resolution (about 1 μm). At very low light levels the resolution can be limited by photon statistics. Filters could be inserted into the light path (figure 5.1) to select a particular wavelength region from the specimen or, in the case of PL, to block excitation light scattered by the sample and prevent it reaching the IIT. The Nikon F2 camera was used (as described in Chapter 2) to record the IIT phospher output.

The apparatus enables low light level emission from an area of the specimen to be imaged and recorded, quickly and easily. The use of IIT microscope combinations is further discussed by Charman (1966).

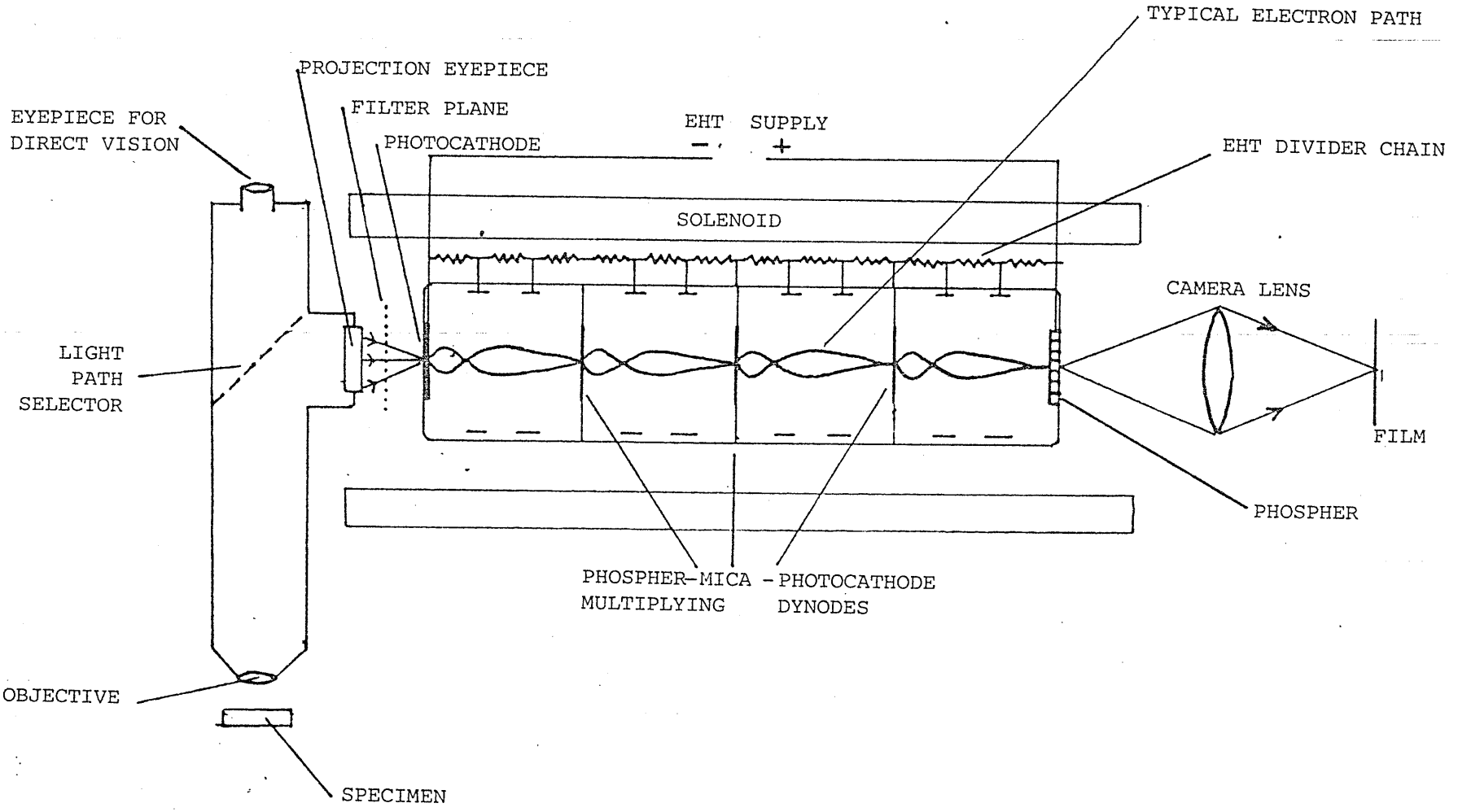

FIGURE 5.1 SCHEMATIC DIAGRAM OF IIT MICROSCOPE

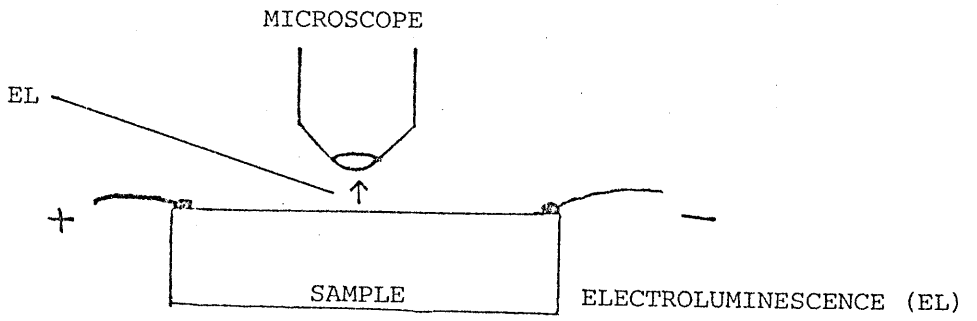

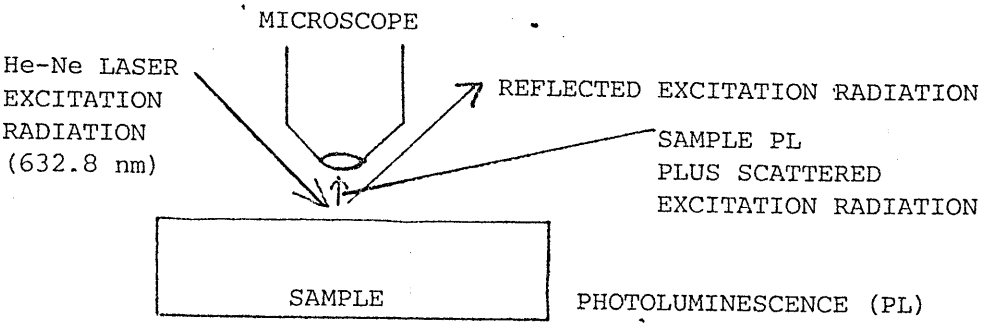

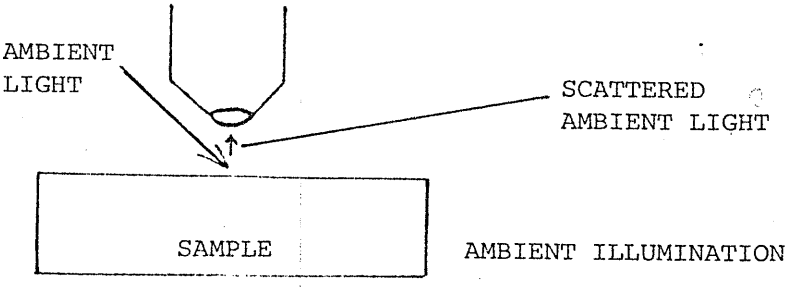

FIGURE 5.2 LUMINESCENCE REGIMES

5.2 Physical Properties of Specimens

This section describes the structural and electrical properties of the materials that were studied. These materials were $Ga_{1-x}Al_xAs$, GaP, amorphous silicon and amorphous red phosphorus.

5.2.1 Structural Properties

The semiconductors $Ga_{1-x}Al_xAs$ and GaP crystallize in the zinc blende structure, which has a tetrahedron as the basic structural unit. The lattice can be considered as two interpenetrating face centred cubic sub-lattices displaced by one quarter of a body diagonal. In the case of GaP one of these lattices would be Ga atoms the other P atoms. In the case of $Ga_{1-x}Al_xAs$ one lattice contains only As atoms the other either a Ga or an Al atom at each lattice site so as to give the correct proportion of Ga to Al atoms (the value of x) overall. Lattice constants are quoted in table 5.1.

GaP, GaAs, AlAs and $Ga_{1-x}Al_xAs$ are called III-V compounds since they contain equal numbers of atoms from group III and group V of the periodic table. GaP is a typical III-V binary alloy while $Ga_{1-x}Al_xAs$ which is an alloy of GaAs and AlAs is a III-V ternary alloy.

Crystalline silicon is made of tetrahedra of silicon atoms. The lattice has a diamond structure. The structure is closely related to the zinc blende structure. The only difference is that in the diamond structure each atom is identical, (figure 5.3). In crystalline silicon the tetrahedral angle is always $\cos^{-1}(-\frac{1}{3}) = 109.47^{\circ}$ and the dihedral angle is always 60°. In amorphous silicon the tetrahedron is slightly distorted, the tetrahedral angle varies by $\pm 10^{\circ}$ and dihedral angle varies from 0° to 60°. The structure of an amorphous solid is the same as that

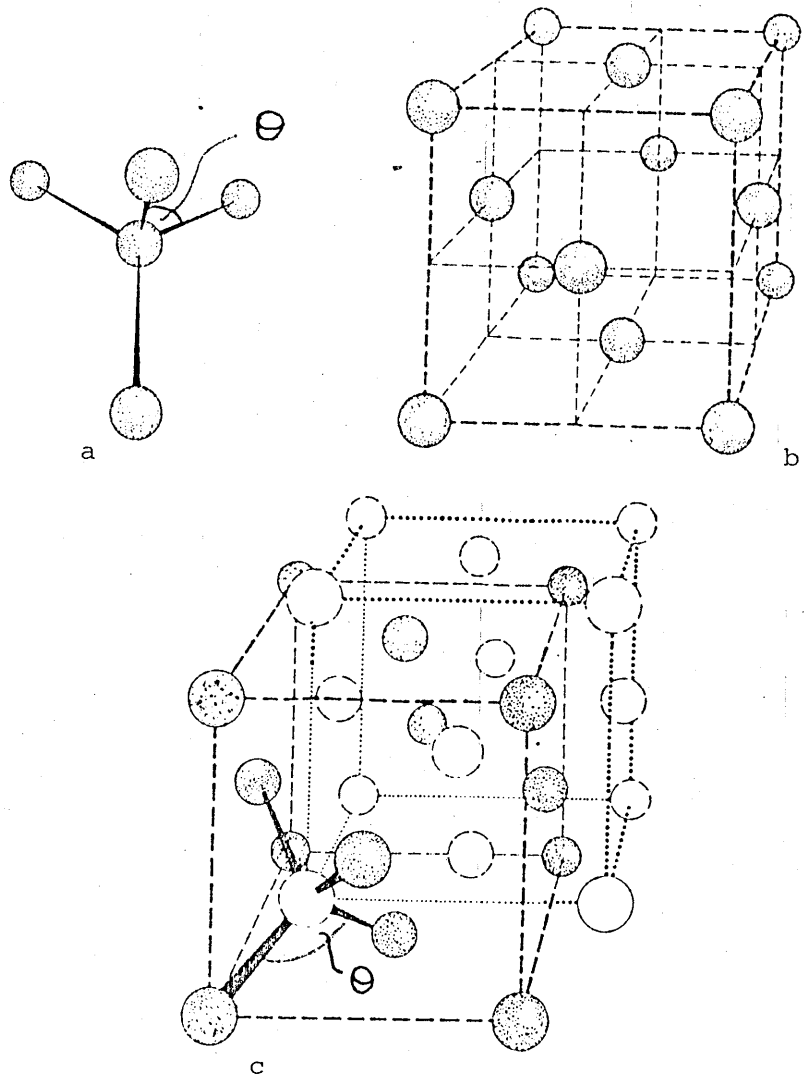

a) The tetrahedral bond, θ is the tetrahedral angle.

b) The face-centred cubic structure.

c) Interwoven face-centred cubic structure. When shaded and unshaded atoms are the same the structure is called diamond, when they are different the structure is called zinc blende. The tetrahedral bond shows how the atoms of shaded and unshaded sites are linked. Cube edges define <100> axes; the tetrahedral bond defines <111> axes.

FIGURE 5.3 THE FACE-CENTRED CUBIC STRUCTURE

of a supercooled liquid. There is good short range order and the positions of nearest neighbours are essentially the same as in the crystalline state, but there is no long range order so that at a distance far from a particular atom other atoms appear to be randomly distributed. Due to the lack of translational invariance the wave vector (k) is not a constant of motion and there is no sharp density of states gap. Figure 5.4 shows the density of states versus energy plotted for a crystalline semiconductor and figure 5.5 shows the same plot for an amorphous semiconductor with the disorder induced band tails shaded. In the extended states of the amorphous semiconductor ($\varepsilon>\varepsilon_c$ and $\varepsilon<\varepsilon_v$) the drift mobility is about 10^{-3} to 10^{-5} m^2 $v^{-1}s^{-1}$. In the disorder induced band tails ($\varepsilon<\varepsilon_c$ and $\varepsilon>\varepsilon_v$) localization sets in and the mobility drops by two to three orders of magnitude. The band gap is defined as this mobility gap where conduction changes from being by delocalized electrons (which can move readily through the solid) to localized electrons (which are strongly bound with almost zero mobility).

5.2.2 Electrical Properties

GaAs has a number of properties that would be useful in many devices, namely a high mobility and a direct energy gap. However this gap is 1.4 eV wide and GaAs luminescence is not visible to the human eye. AlAs has an indirect band gap of 2.16 eV. $Ga_{1-x}Al_xAs$ is a useful alloy because x can be chosen to produce a high mobility, direct energy gap semiconductor, with visible luminescence suitable for light emitting diode applications. I investigated samples with x = 0, .115, .35, .52 and 0.7. As an example of how properties change with x, see figure 5.6 which shows how the band gap changes with x, and figure 5.7 which shows how CL spectra change with x.

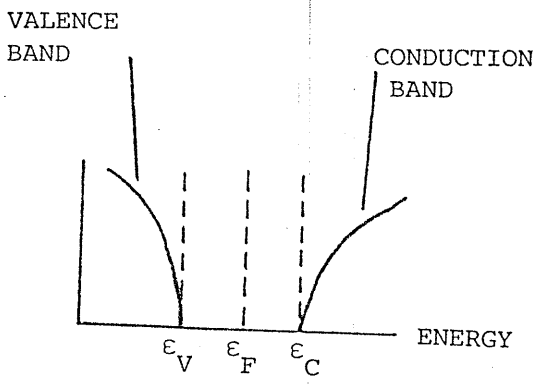

SCHEMATIC DIAGRAM OF THE DENSITY OF STATES OF A CRYSTALLINE SEMICONDUCTOR (After Omar 1975)

FIGURE 5.4

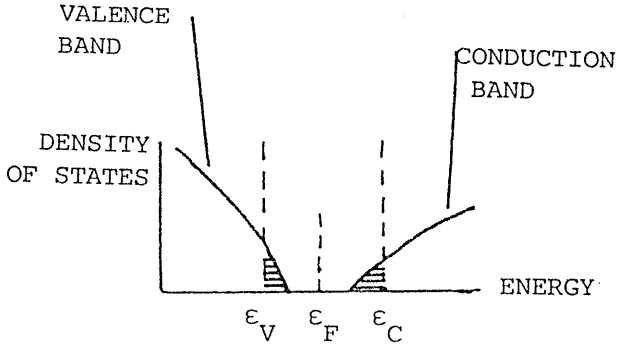

SCHEMATIC DIAGRAM OF THE DENSITY OF STATES OF AN AMORPHOUS SEMICONDUCTOR. (After Omar 1975)
Shaded regions represent disorder induced band tails.

FIGURE 5.5

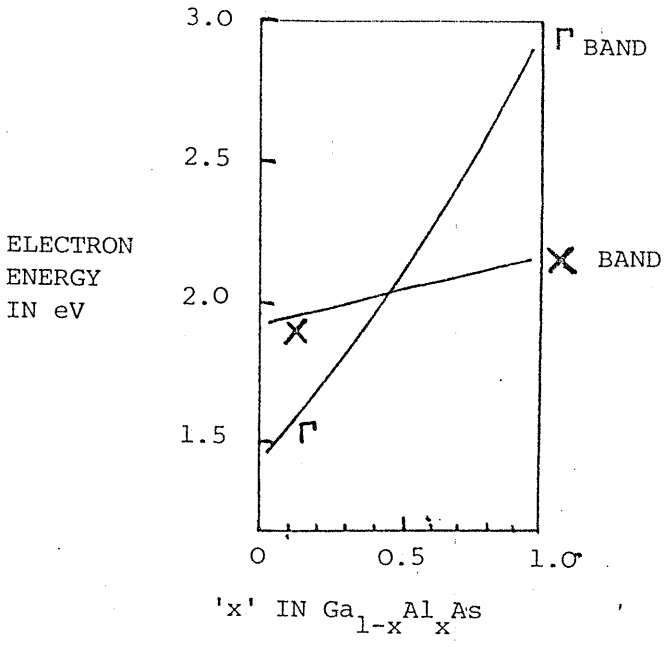

THE BAND STRUCTURE OF $Ga_{1-x}Al_xAs$ AT 300 K (after Onton et al., 1974)

FIGURE 5.6

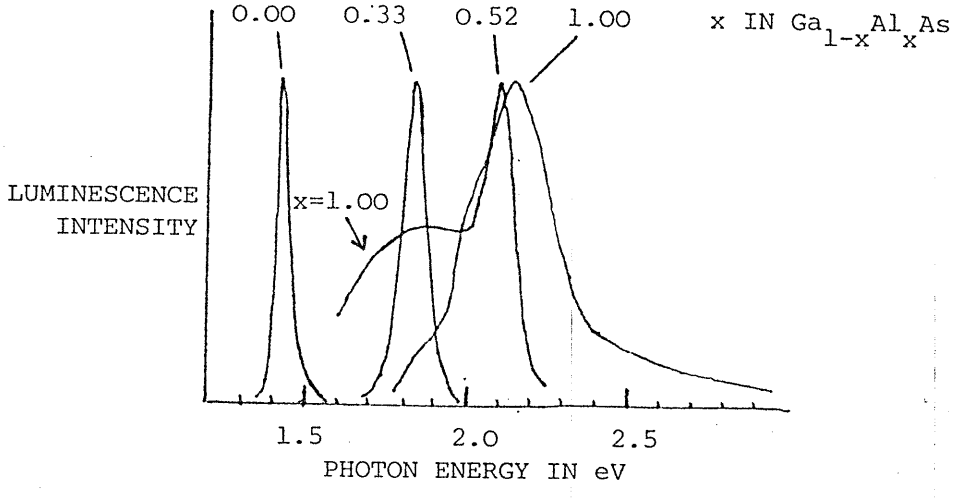

CATHODOLUMINESCENCE SPECTRA OF $Ga_{1-x}Al_xAs$ AT 300 K (after Onton et al., 1974)

FIGURE 5.7

GaP is an indirect band gap semiconductor. The calculated radiative recombination probability for band to band recombination is four orders of magnitude lower than in a direct gap semiconductor. Impurity centres are used to overcome this inherent disadvantage in producing luminescence from GaP. Radiative recombination can occur via impurity levels, usually by doping with nitrogen or, zinc and oxygen. For example the substitution of nitrogen for a group V atom establishes a short range potential which captures an electron which can then bind to a hole to form a bound exciton (Williams and Hall 1978). This results in an increased electron hole recombination probability compared with pure GaP and means that despite its indirect gap it is a useful material for luminescent displays (Williams and Hall, 1978).

Amorphous materials can exhibit significant electrical conduction and they can be substitutionally doped (Spear 1977). They are of interest because, a) some amorphous materials show unusual switching properties (the ovonic diode) and b) devices made from amorphous materials are potentially cheaper to manufacture than their crystalline counterparts, particularly if large areas are required. The application of amorphous silicon to solar cell technology is discussed by Elliott (1979). My samples of a-Si were prepared by deposition in a glow discharge and were kindly lent for this experiment by Dr. I. Austin, University of Sheffield. This and other methods of thin film preparation are reviewed by Vossen and Fern (1980).

I also made a brief study of amorphous red phosphorus. The material is 3- fold co-ordinated and thought to consist of orthorhombic and rhombohedral double layers (Beyeler and Veprek 1980). Its PL is discussed by Kirby and Davis (1980), but was found to be too weak for detection in the present IIT microscope system.

5.3 Introduction to Electroluminescence (EL), Cathodoluminescence (CL) and Photoluminescence (PL)

Luminescence is the spontaneous emission of electromagnetic radiation (in excess of thermal equilibrium black body radiation) after excitation of a system to a state of non-equilibrium by an external source.

In semiconductors, whether the excitation is by EL, CL or PL, luminescence results from the radiative recombination of excess carriers. The intensity of radiation (I) is given by $I \propto R n_e n_h$ where R is the radiative recombination efficiency (this may vary spatially particularly near dislocations, defects and impurities), n_e is the electron concentration and n_h is the hole concentration. I used the IIT microscope system to study the luminescence of semiconductors with a variety of sources.

5.3.1 Photoluminescence (PL)

This term is used when the excitation is by absorption of electromagnetic radiation and when the emitted radiation is of a lower energy than the excitation radiation. (With my apparatus I observed emitted radiation in or near the visible region of the spectrum). Three basic stages are involved in the PL process in semiconductors: a) Creation of electron-hole pairs by the absorption of light. b) Diffusion of these pairs through the material. c) Recombination often, but not always, emitting light. Followed by escape of the emitted radiation.

Excitation is produced by irradiating the sample with light of photon energy greater than the semiconductor band gap. This excitation takes

place within an absorption length of the surface. This distance is small for a direct gap semiconductor (Absorption coefficient typically 10^6 to 10^7 m^{-1}). The excess carriers diffuse away from the surface (due to the concentration gradient), at the same time recombining to re-establish equilibrium, figure 5.8. Non radiative recombination can occur in which the energy is transferred to the lattice by phonon production. When recombination is radiative the photon has an equal chance of being emitted in any direction. This recombination occurs (with average intensity given by $I \propto Rn_e n_h$) after an average recombination time τ_r from the creation of the electron hole pair. This is not to be confused with the scattering time τ_s which occurs in $\mu = \frac{e\tau_s}{m^*}$ where μ is carrier mobility and m* is the effective mass. (τ_s is the time between those collisions which reduce the momentum of the charge carrier to zero, note that $\tau_r >> \tau_s$).

Those photons emitted towards the sample surface will escape providing they are not reabsorbed or reflected at the sample-space interface. Due to the high refractive index (n) of many semiconducting compounds (n = 3.37 for GaP) only a small part of the light will escape from the surface. With direct gap semiconductors this internally reflected light is reabsorbed while in indirect gap semiconductors light can suffer multiple internal reflections before escaping from the specimen at special positions such as scratches on the sample surface, or the edges of the sample. This multiple internal reflection in indirect gap material was clearly seen in my study of GaP (figure 7.22c).

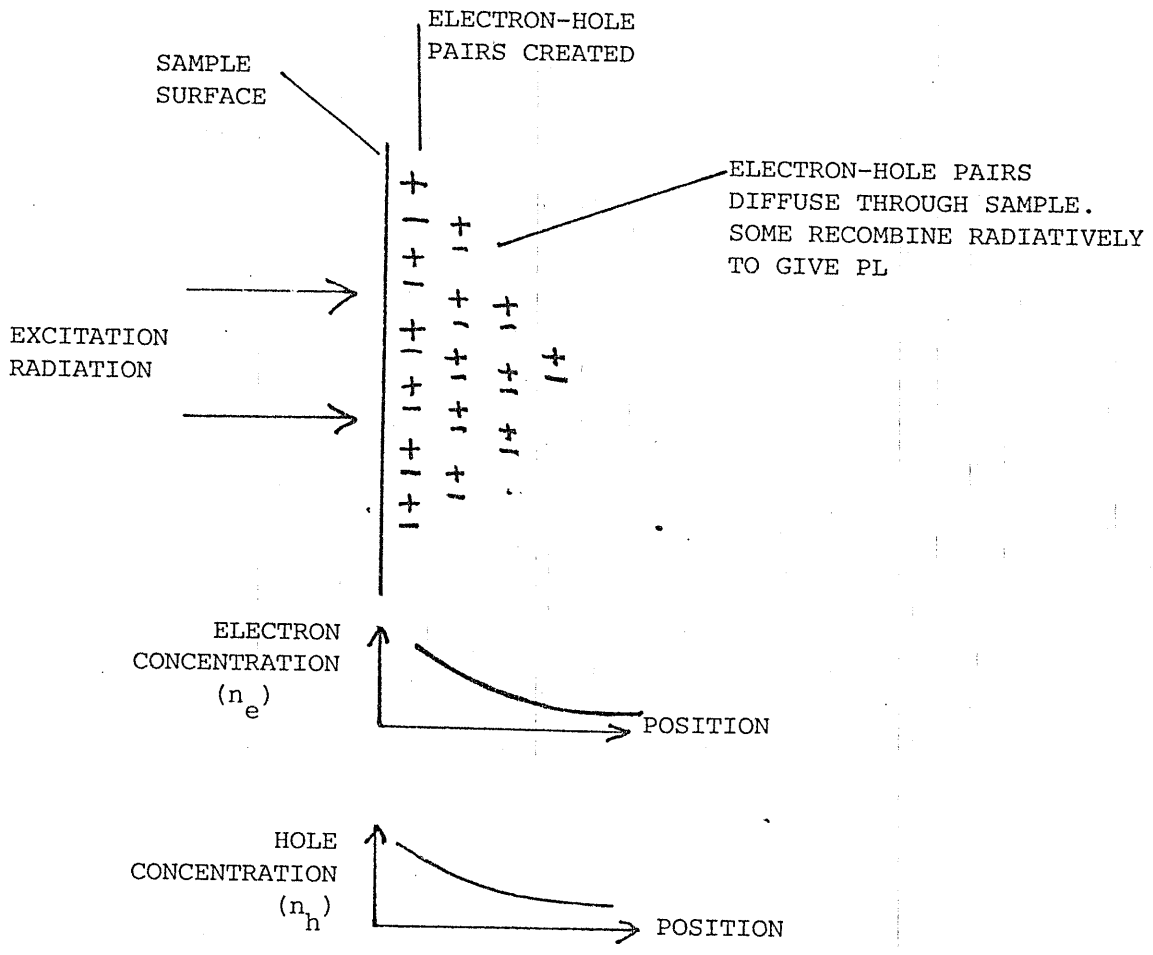

DIAGRAMMATIC REPRESENTATION OF PHOTOLUMINESCENCE (PL)

FIGURE 5.8

5.3.2 Electroluminescence (EL)

This term is used when excitation of luminescence is by the passage of an electric current through the material. The current can produce an excess of minority carriers and radiative recombination of these excess carriers results in EL. The intensity of radiation (I) is again given by

$$I \propto R n_e n_h$$

When a current passes through a forward biased pn junction electrons are injected into the p type material and holes into the n type material. The electrons in the p type material are minority carriers, as are the holes in the n type material. The injected minority carriers make a large percentage difference to the minority carrier concentration, while the same number of injected majority carriers will have a negligible effect (because of the large number of majority carriers) on the majority carrier concentration. The injected minority carriers recombine with the majority carriers (holes recombining with electron majority carriers in the n- type material and visa versa) and when the recombination is radiative light is produced. This is the basis of light generation in the light emitting diode. Similarly an injection of minority carriers may occur at a metal-semiconductor contact. An injection of majority carriers will not however result in a significant increase in recombination because there will be no extra minority carriers with which these majority carriers can recombine.

To study EL electrical contact must be made with the specimen. Two types of electrical contact may be made to a semiconductor (either to a sample of uniform material or to a sample containing a pn junction). One is an ohmic contact, the other is a Schottky barrier

contact. Figure 5.9 gives band diagrams for a metal and n- type semiconductor and shows the relationship of the vacuum level to the fermi level. In the metal, the vacuum level is at an energy $e\phi$ above the fermi level and ϕ is the work function (units eV). Only those electrons which can surmount such a potential barrier can escape from the metal into the vacuum. In the semiconductor the electron affinity A is measured from the bottom of the conduction band. Depending on the differences between ϕ and A different current voltage relationships apply when contact is made between the metal and the semiconductor. On contact, the band potential must change in the semiconductor so that the fermi level in the bulk of the semiconductor can be aligned with that in the metal. The potential changes in the semiconductor are brought about by a redistribution of the charge between the semiconductor and the metal. There are no changes of potential in the metal because of its high conductivity.

When $\phi > A$ electrons will diffuse out of the semiconductor leaving behind a depletion region which will make the semiconductor positive with respect to the metal and so prevent further diffusion, figure 5.9. There is always a potential barrier (ϕ - A) to the electron flow from the metal into the semiconductor and this is not altered by any applied potential. However, the barrier to electron flow from the semiconductor into the metal can be reduced by applying a positive potential to the metal. This type of contact is called a Schottky barrier contact and acts as a rectifier.

If $\phi < A$ electrons can flow freely from the metal to the semiconductor or visa versa, figure 5.9.

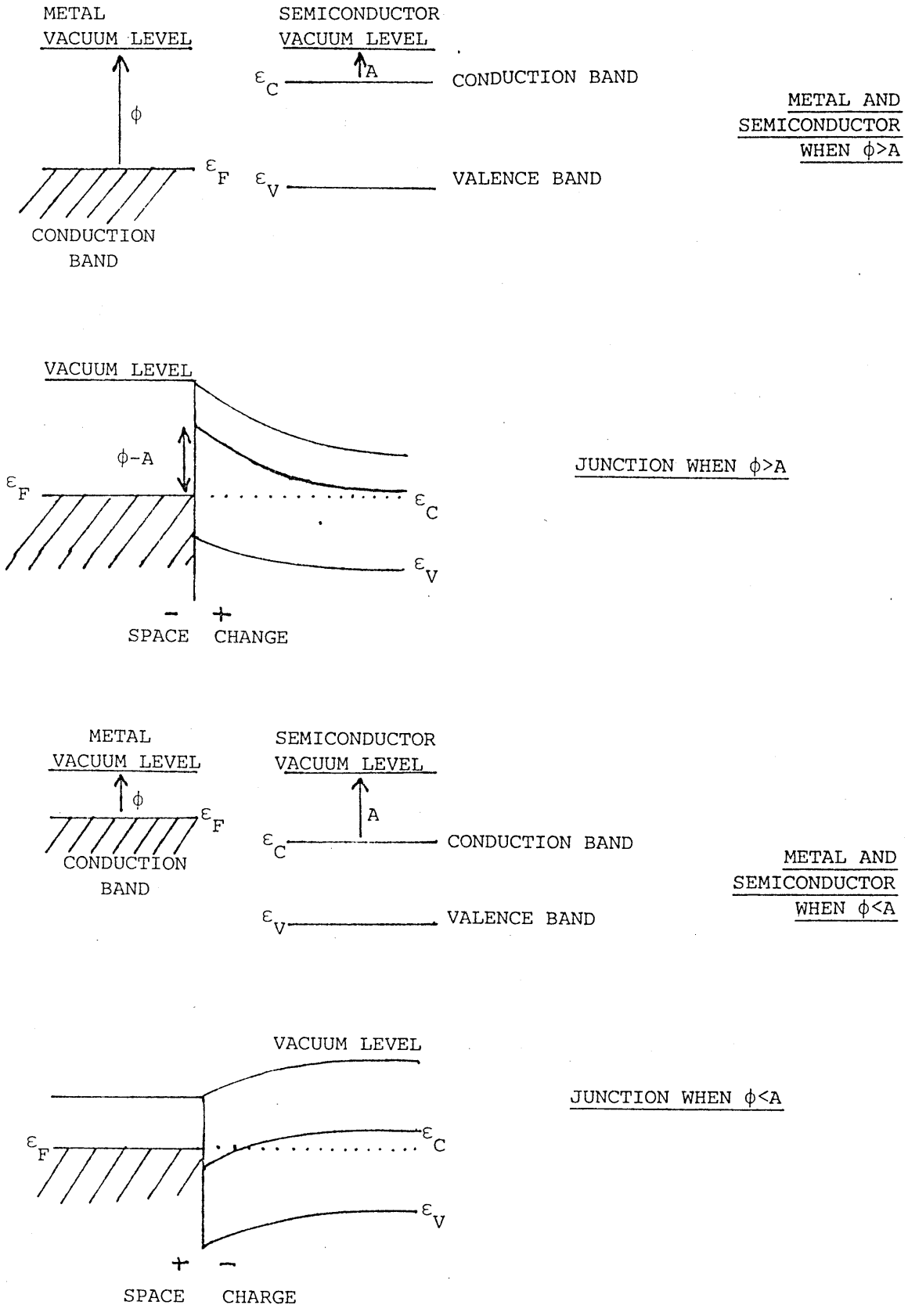

FIGURE 5.9 BAND DIAGRAMS FOR METAL AND N-TYPE SEMICONDUCTOR WHEN ϕ>A AND WHEN ϕ<A

Similar diagrams can be drawn for a metal to p type semiconductor contact, where the rectifying contact occurs for $\phi > A$ and the ohmic contact for $\phi < A$ (Rhoderick, 1978). An ohmic contact will not inject excess carriers, there is negligible voltage drop across it compared with the voltage drop across a device, and it does not affect the V : I characteristic. In practice ohmic contacts are often made by forming a transition region of semiconductor and metal alloy (Keramidas, 1979) at the semiconductor surface so that the depletion layer is so thin that carriers can readily tunnel through it. Ohmic contacts to the $Ga_{1-x}Al_xAs$ † samples were made by alloying metallic indium onto a very thin film of n^+ GaAs which had been deposited on the sample surface. The excess GaAs layer was then etched away using an ammonium and hydrogen peroxide solution.

5.3.3 Cathodoluminescence (CL)

This term is used when the excitation of luminescence is by bombarding the sample (under vacuum) with an electron beam (typically 10 keV in energy). The excess carriers diffuse away from their point of origin and recombine. Light is emitted if the recombination is radiative. The sample may be imaged using a scanning electron microscope CL attachment (to direct light from the specimen to a photomultiplier tube) and my CL pictures were obtained in this way.

5.4 Comparison of PL, EL and CL

Changes in recombination efficiency and the ratio of radiative to non radiative recombination provide information about defects which occur in the material (Petroff, Logan and Savage, 1980, and references therein). The luminescence spectrum of PL, EL and CL

† Except sample B with x = 0.35.

can give information on the band gap and impurities in the material. There are however differences between the techniques. In this section I shall discuss the differences and explain the advantages of my IIT microscope equipment for observing PL and EL.

PL enables uniformly doped samples (without pn junctions or electrical contacts) as well as contacted specimens and pn junctions, to be studied. The spectrum of PL can be studied and also the decay of PL after removal of the excitation (time resolved PL). PL is often studied at low temperatures where PL efficiency is greater and where line widths are narrower. Spatial studies of PL normally involve scanning the sample surface with a laser (Williams and Hall, 1978 and Heinke, 1975). The IIT microscope enables the sample to be studied quickly without the need for expensive scanning equipment. If necessary the PL spectrum of an area of the specimen can be measured by replacing the IIT with a monochromator and photomultiplier.

EL can only be observed when carriers recombine radiatively. The light energy produced by radiative recombination in any small volume of the specimen is proportional to $Rn_e n_h$ (see above) which can be large a) near the electrical contacts to the specimen where minority carriers are injected and both n_e and n_h are large, even though R may be small and b) away from the contacts in the bulk of the material, near defects or impurities where R is large, although the minority carrier concentration (either n_e or n_h) may be small. The light produced by radiative recombination must also be able to escape from the specimen before it can be observed.

Measurement of the EL distribution around each contact can give information about the uniformity and area of the contact. I have studied samples (fabricated with the intention of being uniform)

which have ohmic contacts. The IIT and microscope enable low light intensity (and hence low current) EL to be studied. This work represents the first application of a high gain IIT microscope to low current EL studies. Samples cannot always be successfully studied at low temperature because the sample's resistance increases sharply with falling temperature (carrier freeze out) and very large voltages may be required. However with the IIT microscope I was able to record EL at ~ 80 K from some $Ga_{1-x}Al_xAs$ samples, even though it was fainter than at room temperature. One advantage of EL over PL is that no filtering out of scattered excitation radiation is needed. This advantage is particularly important when the recombination radiation is imaged (as in my IIT microscope equipment) since optical resolution and contrast are slightly degraded when filters are inserted in the optical path.

With CL the inherent electron beam energy (typically 10 keV) is greater than the energy of PL excitation sources or of the carriers injected during EL (~ 1eV), so that CL can be used to study at room temperature the luminescence of materials that normally show no PL unless they are cooled. However this beam power has distinct disadvantages a) The sample temperature can be raised by tens of degrees at high beam currents causing large spectral shifts in emission lines b) The penetration depth is so large that epitaxial materials with micron thick layers cannot be studied at high beam voltages c) The large penetration depth means that absorption of the emitted light on its passage through the material is appreciable and can cause distortion of the CL spectrum d) The penetration depth depends on beam energy e) High beam energies produce radiation damage f) Radiative recombination efficiency is reduced by the production of carriers whose average thermal energy is greater than if they were in equilibrium with the lattice (so

called "hot" carriers) g) The experimental arrangement is more complex than PL or EL h) The mechanism of carrier injection bears no relation to injection in real electrical devices, EL is superior in this respect.

PL and EL when observed with an optical microscope will have a resolution limited by the microscope (~ 1 μm in the visible, 400 to 700 nm); although sometimes a microscope is used for scanning and the intensity of the whole field of view is integrated to give a resolution of about 20 μm (depending on the particular microscope objective). In CL the resolution is limited by a combination of electron beam size and carrier diffusion. If the diffusion length is much greater than the beam diameter detailed variations in CL efficiency will not be recorded since the CL intensity recorded for every point on the specimen will in fact be an average over a much larger area. CL spatial resolution can be as good as 1 μm (Booker, Ourmazd and Darby, 1979).

Above I have listed the relative merits of PL, EL and CL studies of luminescence. The IIT microscope system that I have used, with its very high optical gain enables spatial studies of a) low current EL, b) PL and c) low temperature PL (about 80 K with a purpose built cryostat to be described in chapter 6); without the need for a scanning system. The equipment will be described in detail in chapter 6 and typical results, illustrating the value of the technique, will be presented in chapter 7.

CHAPTER 6

Apparatus for the Spatial Study of Semiconductors

6.1 Purpose and Objectives of the IIT microscope design

The purpose of the IIT microscope apparatus was to allow a spatial study of low light level electroluminescence (EL) and photoluminescence (PL), at room temperature and at ~80K from a number of semiconductor specimens. The specimens were in the form of thin layers deposited on substrates. The surface area of each specimen was about $5mm^2$ or less. A microscope was necessary for observation of the light emission from small areas of the samples. Provision needed to be made for cooling the samples to liquid nitrogen temperature and mounting the samples in such a way that EL and PL could be excited and then observed with the microscope. It was also necessary to be able to move the sample relative to the microscope so that the whole area of the sample could be studied. The microscope was fitted with a projection eyepiece so that the image of a part of each specimen could be focused onto the first photocathode of the IIT. Other requirements for the microscope were that it should be possible to view the specimen through an eyepiece as an alternative to projecting the image onto the IIT and that provision should be made for the insertion of filters into the optical path. A microscope (without an IIT) for the study of photoluminescence is described by Stringfellow and Greene (1969).

To cool the sample an evacuated optical cryostat was constructed to be positioned on the microscope stage. The geometry of the cryostat window was chosen so that PL excitation of the sample would be possible. A long working distance objective was fitted to the

microscope so that the sample could be focused through the cryostat window. Electrical leads were provided so that EL of contacted samples could be observed in the cryostat. The long working distance objective and projection eyepiece were chosen so that at highest magnification the system resolution was limited by optical microscope magnification, (about 1 μm). Lower magnifications were possible with other objectives and eyepieces so that a larger area of the sample could be observed with lower spatial resolution. The IIT output could be photographed with the Nikon F2 camera as described in Chapter 2. The cryostat is shown in figure 6.1, and it is shown mounted on the microscope, which is connected to the IIT in figures 6.2 and 6.3. The latter arrangement, which is the IIT microscope used in these studies, is shown diagrammatically in figure 5.1. The following sections will describe the apparatus in more detail.

6.1.1 The Microscope

A microscope was needed to project the specimen image onto the front photocathode of the IIT. A "University Lynx" (Gillett and Sibert) microscope was selected. The microscope is diagrammatically represented in figure 5.1. The microscope was fitted with a three-way head so that the specimen could be seen in the viewing eyepiece or projected via the projection eyepiece, or could be optically isolated.

To enable the system to focus on specimens through the cryostat window a long working distance objective was needed, in addition other objectives were purchased for low magnification investigations and for use with specimens that were observed at room temperature and not mounted in the cryostat. Objectives are characterized by their magnification and numerical aperture (NA). NA is given by

$$NA = n \sin \alpha$$

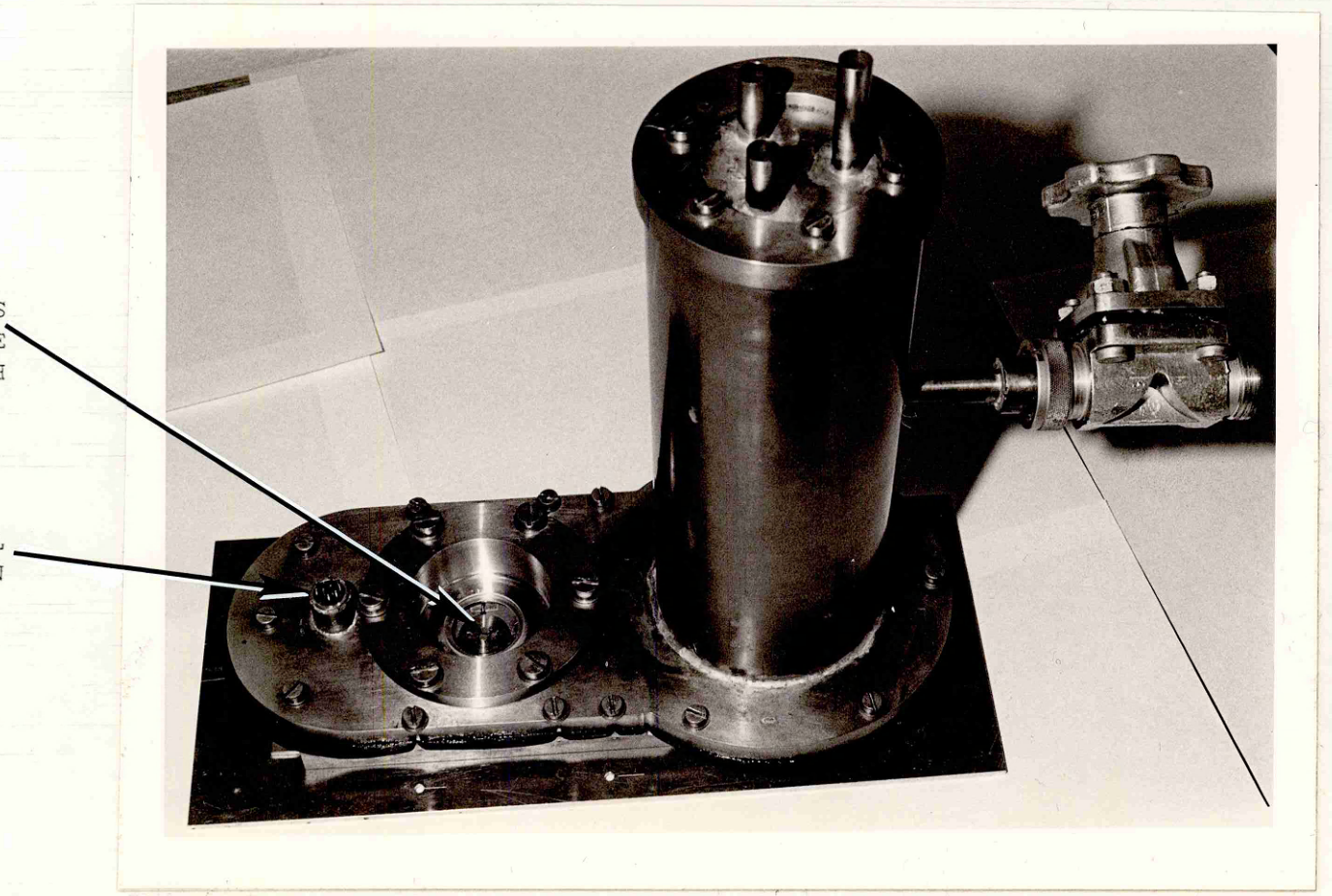

FIGURE 6.1 THE CRYOSTAT

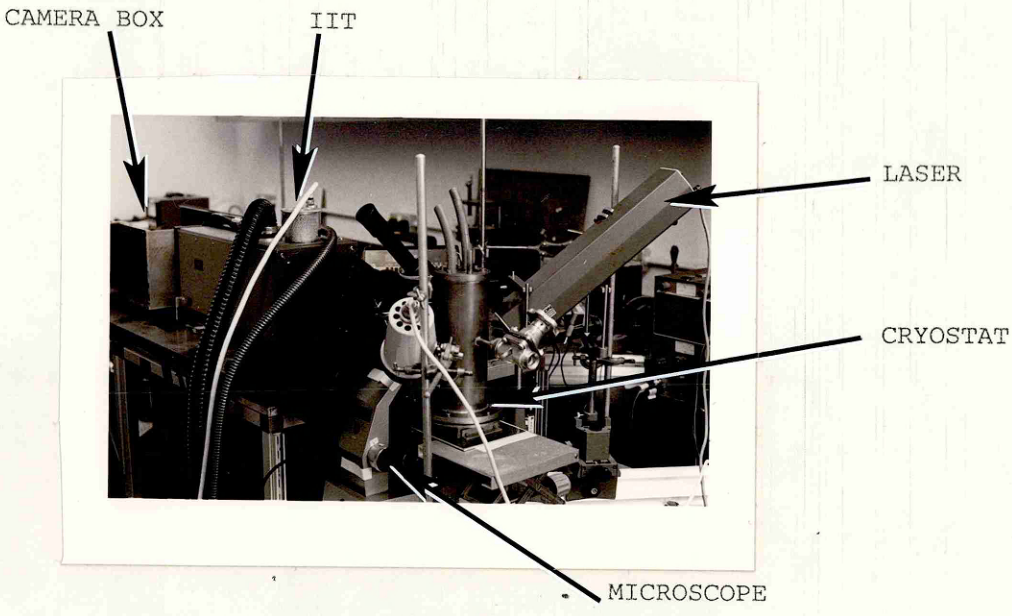

FIGURE 6.2 THE CRYOSTAT AND MICROSCOPE CONNECTED TO THE IIT

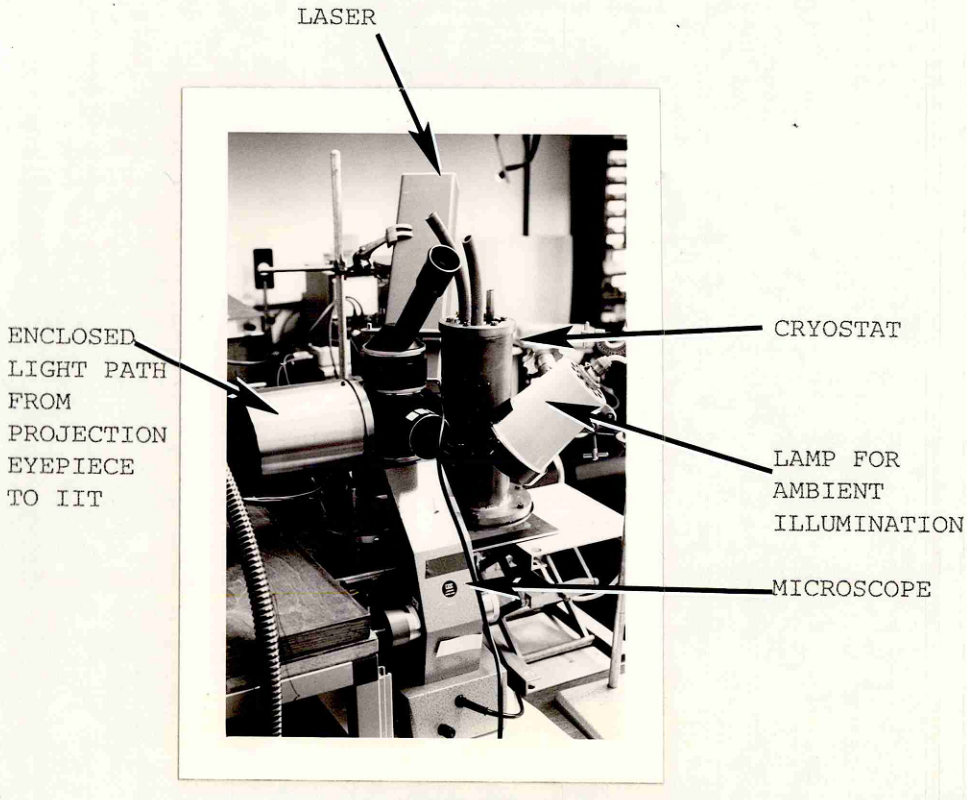

FIGURE 6.3 THE CRYOSTAT AND MICROSCOPE

where n is the refractive index of the medium between object and objective and α is the half angle of the cone of light entering the objective. Unfortunately low magnification high NA objectives (which would have been useful in this study for low magnification low light intensity observations) are not generally available because a high NA is normally associated with high resolution (rather than a high light collection ability) and so is not necessary for low magnification work. Resolution as a function of NA is shown in figure 6.4. The following objectives were used in this work, x 6.3 NA .16, x 10 NA .25, x 20 NA .54, x 40 NA .70, x 60 NA .85, x 100 NA 1.25 (oil immersion), and x 32 NA .40 (long working distance Leitz, with about a 6mm air gap between the front lens element and the specimen).

The following eyepieces were available although normally the lowest magnification eyepiece was used because it resulted in the brightest projected image: x 4 projection (Gillett and Sibert), x 5 projection (Olympus), x 10 projection (Beck), x 20 projection (Beck) and a x 8 viewing eyepiece fitted with cross hairs used only for direct visual observation.

In many cases I used the x 32 long working distance objective and the x 4 projection eyepiece. This resulted in ~300 μm diameter of specimen being visible on the IIT with a microscope objective limited resolution of about 1 μm (when the system was exactly focused) and with an IIT limited resolution (300 μm of specimen projected across 40 mm of ~0.1 mm resolution photocathode) of less than 1 μm. A photograph taken through the IIT microscope with this magnification, of a back lit test graticule with 10 μm divisions, is shown in figure 6.5, the same graticule is shown with higher magnification in figure 6.6.

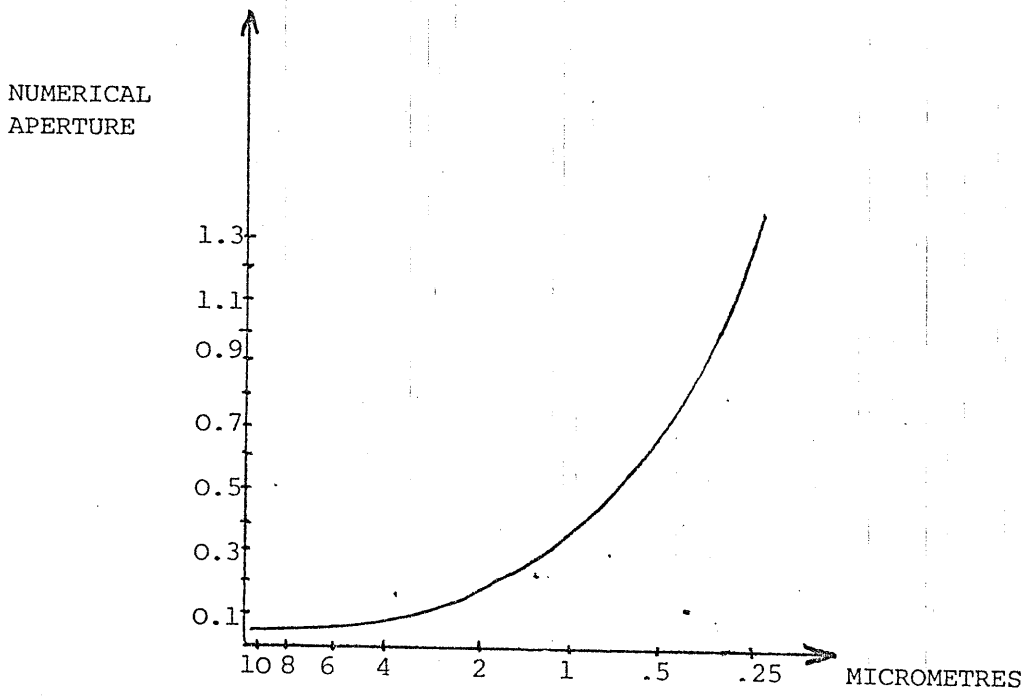

MICROSCOPE OBJECTIVE RESOLVING POWER
AS A FUNCTION OF NUMERICAL APERTURE
FOR LIGHT OF 550 nm WAVELENGTH

FIGURE 6.4

FIGURE 6.5 PHOTOGRAPH OF TEST GRATICULE TAKEN WITH THE IIT MICROSCOPE

One small division equals 10 μm

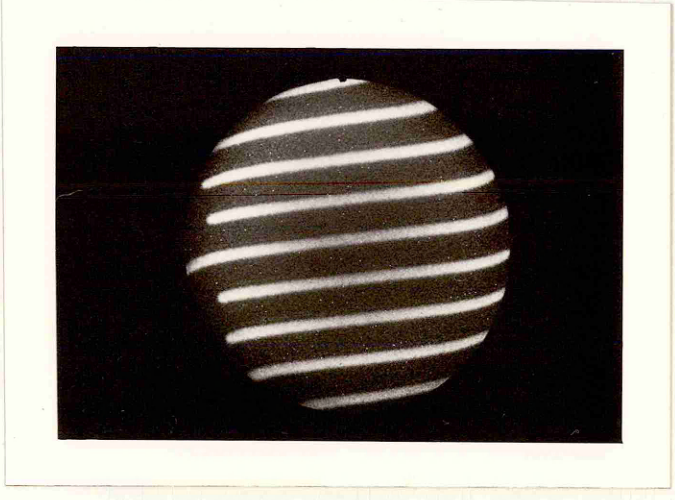

FIGURE 6.6 HIGH MAGNIFICATION PHOTOGRAPH OF TEST GRATICULE TAKEN WITH THE IIT MICROSCOPE

One division equals 10 μm

One difficulty was in accurately focusing the microscope onto the IIT. Focusing the microscope had to be performed by observing the IIT output. Photographic focusing (that is making a series of photographs of the IIT phospher, each with a slightly differing focus setting) was possible with low magnification (> 2 mm of sample filling the IIT photocathode), but with high magnification (such as figure 6.6) this was not possible due to slight mechanical shifts in the system (particularly if the cryostat was used) during the 20 minute film development period. This meant that the actual resolution in some cases was between 2 and 3 μm. For very bright specimens the objective iris could be closed, reducing the NA (and hence resolution), but increasing the depth of field (which is proportional to $(NA)^{-2}$) resulting in an overall improvement in resolution due to better focus.

The microscope had a translating stage (uncalibrated) to which the cryostat was secured. Thin polytetrafluoroethylene (PTFE) washers were placed between the stage and the cryostat to tilt the specimen slightly with respect to the objective. This was sometimes necessary at low magnification (>2 mm of specimen filling photocathode) when parts of the specimen could be in focus and parts out of focus due to the specimen surfaces not being exactly parallel.

A remote control focusing device was made from a commercial drill-bit extender with a hand grip at one end and a fixture for connecting to the microscope focusing knob at the other. The device was one metre long and was used for focusing the microscope while observing the IIT output directly or while looking into the camera viewfinder.

6.1.2 The Cryostat

A cryostat was designed to fix to the microscope stage and to enable PL and EL of semiconductor specimens to be studied at about liquid nitrogen temperature. The cryostat was designed for use with the long working distance objective, and the geometry of the window and its mount were carefully chosen to allow PL excitation from a suitably placed laser to reach the sample. The cryostat was provided with a means for measuring the sample temperature (discussed later) and easy access for sample changing, and was also designed so that it would not need refilling with liquid nitrogen at intervals of less than 20 minutes. The main features of the cryostat are shown in figure 6.7. The sample is mounted on a high conductivity (HC) copper disc which screws firmly into a HC copper plate. The end of this plate is soft soldered to the base of a brass can containing liquid nitrogen. This HC copper sample plate is baffled, to reduce the room temperature thermal radiation, by two other HC copper plates both soldered to the nitrogen can, one above and one below the sample plate. The lower baffle was supported at its further end from the nitrogen can by a PTFE rod. The nitrogen can was supported by three 0.3 mm thick and 10 mm diameter stainless steel tubes, which also allowed access for filling the can with nitrogen. Stainless steel was used to minimize heat conduction. Care was taken during construction to avoid overheating the tubes while soldering because overheating can lead to the tubes becoming porous. The cryostat outer case was made of brass.

The sample disc is mounted directly below the cryostat window. A series of differing height threaded copper discs enabled the distance between sample and window to be kept constant despite varying sample thicknesses. Originally the glass window was 6 mm thick. This was later replaced with 3 mm thick spectrosil to reduce scattered light.

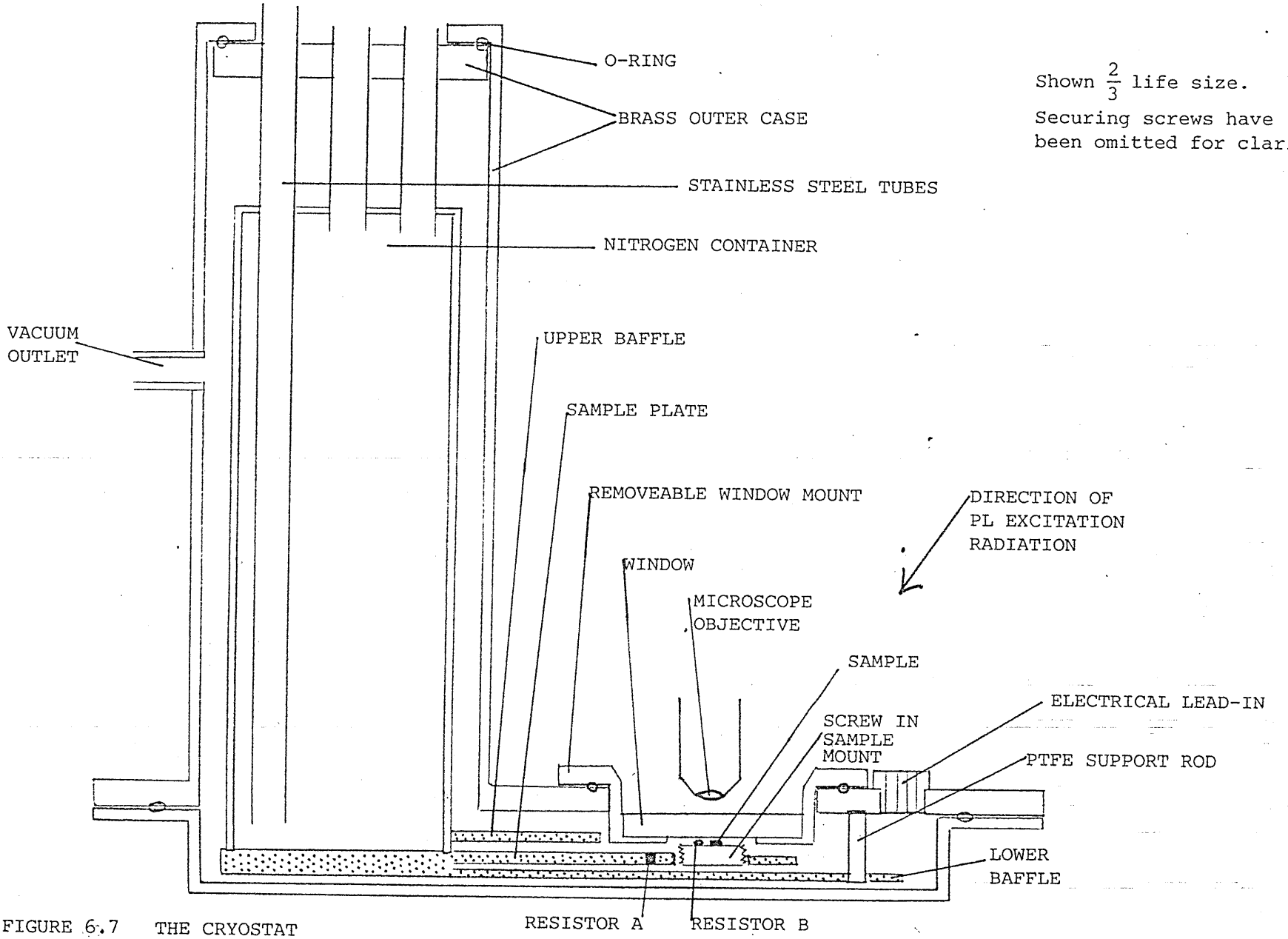

Shown $\frac{2}{3}$ life size.

Securing screws have been omitted for clarity

FIGURE 6.7 THE CRYOSTAT

The glass discs were fixed in position with "Oxford Instruments M5/M6 epoxy resin". Electrical connections to the interior of the cryostat were made via an "Oxford Instruments Ltd. type G1" pin connector. Wires from the pin connector were heat sunk to a connecting block on the lower copper baffle before being taken to the sample. This pin connector also provided contact with two "Allen-Bradley" resistors that were used to measure the cryostat temperature. These temperature sensing resistors were 470 Ω and ⅛W rating. Before mounting in the cryostat a number of these resistors were tested (they were first coated with a thin layer of varnish to avoid electrolysis) by measuring their resistance at room temperature, in a melting ice/water solution at 0°C, and in liquid nitrogen. The resistors obey the empirical relationship (Rose-Innes, 1973 and S. Swithenby, 1979)

$$\log_{10}R = a + b\,\frac{1}{T^{\frac{1}{2}}}\,(\log_{10}R)^{\frac{1}{2}}$$

where R is in ohms, T in kelvins and a and b are constants. Sometimes due to thermal cycling the room temperature resistance may change by a few percent but the difference between room temperature and liquid nitrogen temperature resistance was found to be constant for each resistor. Resistor A was 472 Ω at 19°C, 639 Ω at 77 K, and 477 Ω at 0°C leading to a = 2.54 and b = 1.38. Resistor B was 499 Ω at 19°C, 688 Ω at 77 K and 504 Ω at 0°C leading to a = 2.57 and b = 1.33. Resistor A was mounted through the sample plate in position A of figure 6.7. Resistor B was mounted on the sample disc next to the sample and was fixed to the disc with low temperature varnish (GE type 7031).

The cryostat was leak tested using an Edwards LT 112 pump. After sealing and outgassing, the pressure in the cryostat remained below 10^{-4} torr for more than 24 hours. After the evacuated cryostat was

filled with liquid nitrogen refilling was required about once an hour. The cryostat window did not mist up. When low temperature equilibrium had been reached (about 10 minutes after commencing cooling) resistor A measured 630 Ω corresponding by the equation given above to 80 K, and resistor B measured 651 Ω corresponding to 84 K. The sample temperature was taken as 84 K (sometimes written as ~80 K). All resistances were measured on the 10 K Ω scale of a Data Precision model 2480 calibrated digital multimeter. The maximum test current on this scale is 330 μA which leads to a maximum heat dissipation in each temperature sensing resistor at ~80 K of I^2R ~ .07 mW. This is negligible compared to the 14.mW cm^{-2} which is radiated (according to Stefan's Law) from a 300 K surface to a 77 K surface. The finished cryostat is shown in figure 6.1.

6.1.3 The Image Intensifier and Camera

The IIT microscope made use of the same IIT (with S20 photocathode) as the triboluminescence (TL) work. The IIT output was photographed with the Nikon F2 camera. The main difference in photographically recording the IIT output between this study and that of TL spectra was the stationary nature of the spatial images which meant that long time exposures could be made to improve the signal to noise ratio on the photographic negative.

6.1.4 The Laser

Photoluminescence (PL) in the cryostat was excited using a 0.5 mW (Spectra-Physics model 155) helium-neon (He-Ne) laser with 632.8 nm emission. The laser was supported on an "Ealing" optical bench with adjustable mounts so that it could be accurately aligned. The laser beam was incident at ~45° to the sample surface so that directly

reflected light from the sample surface did not enter the microscope objective. The beam diameter was 0.88 mm to the e^{-2} points.

In addition to spatial observations of PL with the IIT microscope, PL spectra were recorded with the laser as an excitation source using a scanning monochromator and photomultiplier to measure the microscope output. The sample was positioned under the microscope in the same way as for PL studies. Since such measurements were taken over a period of several minutes it was important to use a laser with little amplitude drift over this period. After a warm up interval (~1 hour) there was found to be little drift (<5%) in the long term laser output intensity. As a precaution laser drift was measured before and after each PL spectrum measurement. In all cases the laser was filtered through an "Ealing 31-6703" interference filter to remove faint infra red emission that was generated in the laser tube. The laser is shown mounted beside the cryostat in figure 6.2.

6.1.5 Filters

When photoluminescence (PL) was to be studied the scattered excitation light that entered the microscope objective needed to be filtered out from the accompanying PL. A number of filters were tested for their ability to block the 632.8 nm laser light but to pass the longer wavelength PL. The selected filter had to be of good optical quality as it would be placed in the microscope imaging path (figure 5.1). The filters were tested with the laser as source and an S20 photomultiplier (behind neutral density filters to prevent overload) as detector. The following were tested: Oriel LP 700, Oriel LP 780, Barr and Stroud RG 715, Ealing 26-4432 (665 nm cut on), Ealing 26-4499 (IR black glass), Ealing 4473 (790 nm cut on) and Schott BG18 (790 nm cut on). The strongest blocking of 632.8 nm light occurred with a

combination of Ealing 26-4499 and Oriel LP 780 filters. A standard lamp spectrum was plotted on the monochromator (with a photomultiplier detector) both with and without these filters present and the resulting transmission curve is plotted in figure 6.8.

6.1.6 Electroluminescence Apparatus

The study of electroluminescence (EL) required a power supply and a means of controlling its output so that the electrically excited specimen would not overheat. A pulsing system was used. The output of a stabilized power supply (Kingshill model 15A01C with a maximum output of 150v at 125 mA) was pulsed with a reed switch. The controlling pulses to the switch were provided by a "Farnell" pulse generating system which could provide a counted number of positive or negative pulses, with a duration of 0.1 μs to 1.5 s and with a spacing of 0.1 μs to 1.5 s. With the aid of a double beam oscilloscope the reed switch response was measured, table 6.1. Its output pulse length was found to correspond to its input pulse length for durations greater than about 5 ms. The sample was pulsed in the circuit of figure 6.9. Both the potential difference across, and current through, the sample were observed and measured during each pulse on a double beam oscilloscope (Y_1 and Y_2 plates).

6.2 Spectral Measurement of PL and EL

It was found necessary to measure the spectrum of the area of a sample that was observed with the IIT microscope. To achieve this the microscope, cryostat (if used), specimen, and laser or EL pulsing equipment, were left untouched but the IIT was replaced with a monochromator (Czerny-Turner type, "Spex Minimate") such that the required part of the specimen image entered the monochromator slits. The slits were interchangeable giving a band pass of 1 to 20 nm.

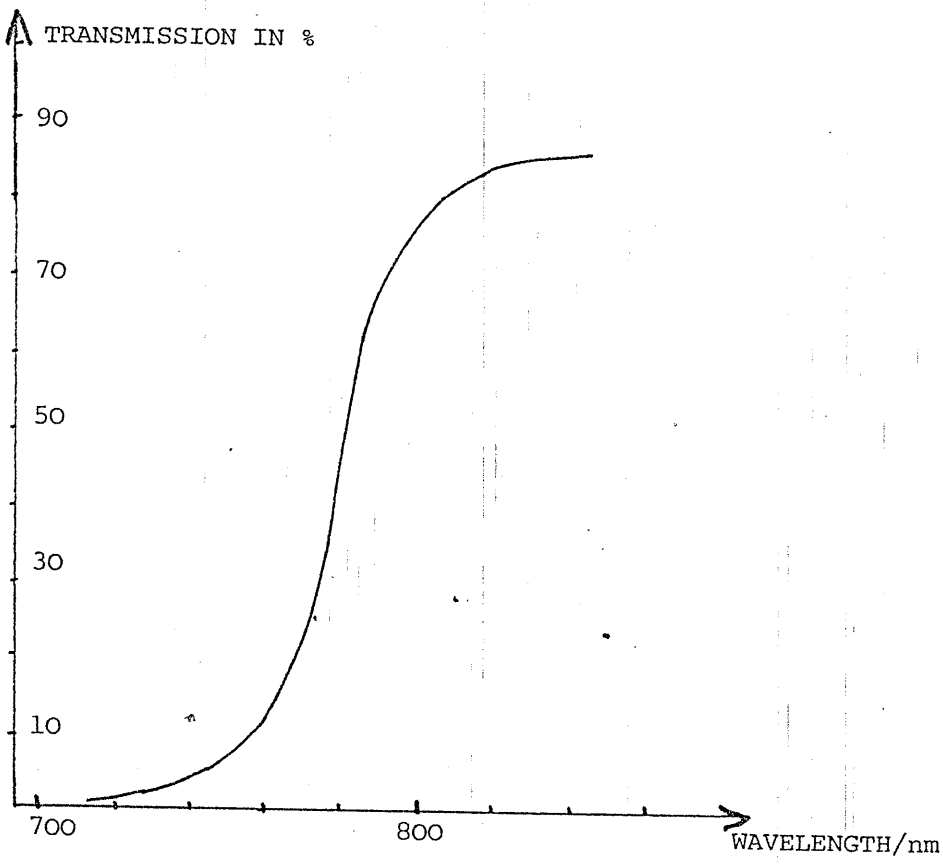

TRANSMISSION CHARACTERISTIC OF EALING 26-4499 AND ORIEL LP780 FILTER SANDWICH

FIGURE 6.8

LENGTH OF CONTROLLING PULSE APPLIED TO REED SWITCH/ms	LENGTH OF OUTPUT PULSE/ms
10	10
5	5
4	3½
3	2
2	1
1	0

REED SWITCH RESPONSE

TABLE 6.1

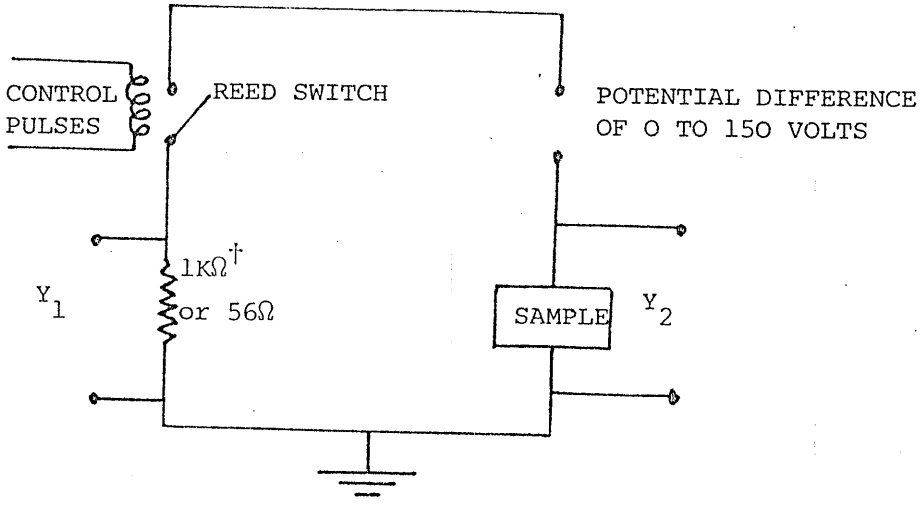

† Depends on sample resistance.

FIGURE 6.9 ELECTROLUMINESCENCE PULSING CIRCUIT

With high microscope magnification (x 32 objective and x 20 eyepiece) areas as small as 10 μm diameter could have their spectrum measured. The monochromator was scanned at speeds between 200 nm min^{-1} and 12.5 nm min^{-1}. The monochromator output was measured with one of two photomultiplier tubes.

Either a) an EMI type 9659B with an S20 spectral response (figure 6.10a) similar to the response of the IIT. Its sensitivity was 220 μA per lumen.
or b) an EMI type 9684B with an S1 type spectral response (figure 6.10b) and sensitivity of 18 μA per lumen.

Both photomultipliers could be used in a cooled housing to reduce the dark current (thermoelectric cooling to $-20^{o}C$ was available). The dark current could be further reduced where necessary with a focusing magnet assembly (EMI type C122 or C121) which reduced the effective photocathode area by 80% or 95% respectively.

The photomultiplier output current was measured on a "Keighley" electrometer capable of detecting 10^{-12}A. The electrometer provided a 0 to 1 volt dc output corresponding to its meter's full scale deflection. This output was used to drive a chart recorder.

6.3 Cathodoluminescence Apparatus

The cathodoluminescence (CL) and secondary electron (SEC) pictures were made with the kind help of Dr. D.B. Darby of the Department of Metallurgy and Science of Materials, University of Oxford. They were made at a beam energy of 30 keV on a scanning electron microscope. The CL was collected by a light guide and recorded without wavelength selection on an extended S20 photomultiplier.

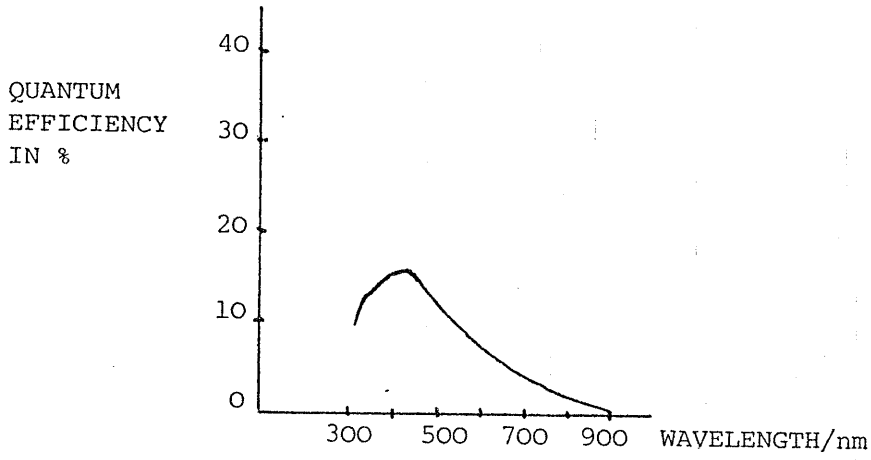

QUANTUM EFFICIENCY OF 9659B PHOTOMULTIPLIER
(S20 PHOTOCATHODE)

FIGURE 6.10a

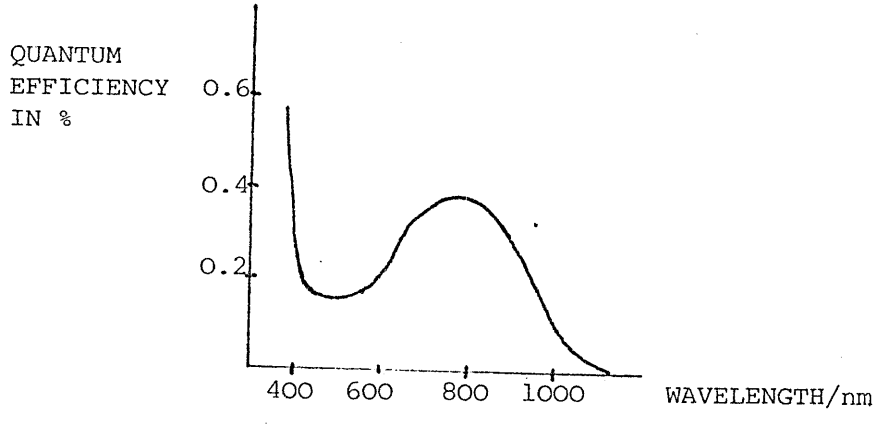

QUANTUM EFFICIENCY OF 9684B PHOTOMULTIPLIER
(S1 PHOTOCATHODE)

FIGURE 6.10b

(after data supplied by EMI, Hayes, Middlesex)

CHAPTER 7

Results and Conclusions from the Spatial Study of Semiconductors

In this chapter I describe the main results obtained in my spatial study of semiconductors. I will discuss the significance of the results, and the conclusions to be drawn both about the samples and about the usefulness of the IIT microscope for spatial studies. I will describe the results for each material separately and will also discuss why certain materials gave no results.

7.1.1 Gallium Aluminium Arsenide ($Ga_{1-x}Al_xAs$)

I studied samples of this material with x = 0., 0.115, 0.35, 0.52 and 0.7. The band gap is direct when $x < 0.37$ (Williams and Hall, 1978) and indirect when x is greater than this. Each sample was mounted on the microscope stage at room temperature and pulsed with up to 150 V across all combinations of its electrical contacts. For example, a sample with four electrical contacts would be tested twelve times. The microscope image was projected, as explained in chapter 6, onto the IIT photocathode. The IIT output was inspected for electroluminescence (EL) as different parts of the sample surface were observed, by moving the microscope stage. Some, but not all, of the samples with x = 0.35 and x = 0.52 were found to exhibit EL.

7.1.2.1 $Ga_{1-x}Al_xAs$ with x = 0.52

Description of the Sample

This sample was alkyl vapour grown onto a semi-insulating GaAs substrate. Onto this substrate a high resistance layer of GaAs was deposited followed by the active layer. This was a 7μm thick layer

of x = 0.52 $Ga_{1-x}Al_xAs$, doped to have an n type carrier concentration of 9 x 10^{23} m^{-3}. The electron mobility at room temperature in this layer was 10^{-1} m^2 V^{-1} s^{-1}. Contacts to the sample were made by a) depositing a thin (1.8 μm) layer of heavily n type doped GaAs onto the sample surface b) alloying (at ≃ 200°C for 1 hour) dots of metallic indium onto the surface c) etching away the heavily n-type doped GaAs layer d) carefully soldering fine wires to the indium dots. Figure 7.1 is a photograph of the sample surface with ambient illumination taken through the IIT microscope at low magnification. The sample is illuminated by a tungsten bulb positioned about 0.1 m from its surface and controlled by a "variac". The contacts are numbered for reference and contacts 3 and 4 are about 4 mm apart. The small spots of light visible on the photographic prints are IIT noise arising mainly from thermal emission of electrons at the IIT photocathode.

Initial Location of EL sites

All combinations of the five contacts were tested to see if they induced EL anywhere in the material. EL was observed near contacts 3 and 4 only. The brightest EL was observed near contact 4 when that contact was positive, and near contact 3 when that contact was positive, with respect to the other contacts on the sample.

Measurement of Light Intensity from Each EL Site

I measured the total light intensity from near contact 3 and also from near contact 4. The measurements were made by directing the microscope output onto a photomultiplier tube (with an S20 photocathode and hence the same nominal spectral response as the IIT). The applied potential difference to the sample was pulsed (to avoid Joule heating) and was observed on one trace of a double beam oscilloscope. The other beam displayed the photomultiplier output.

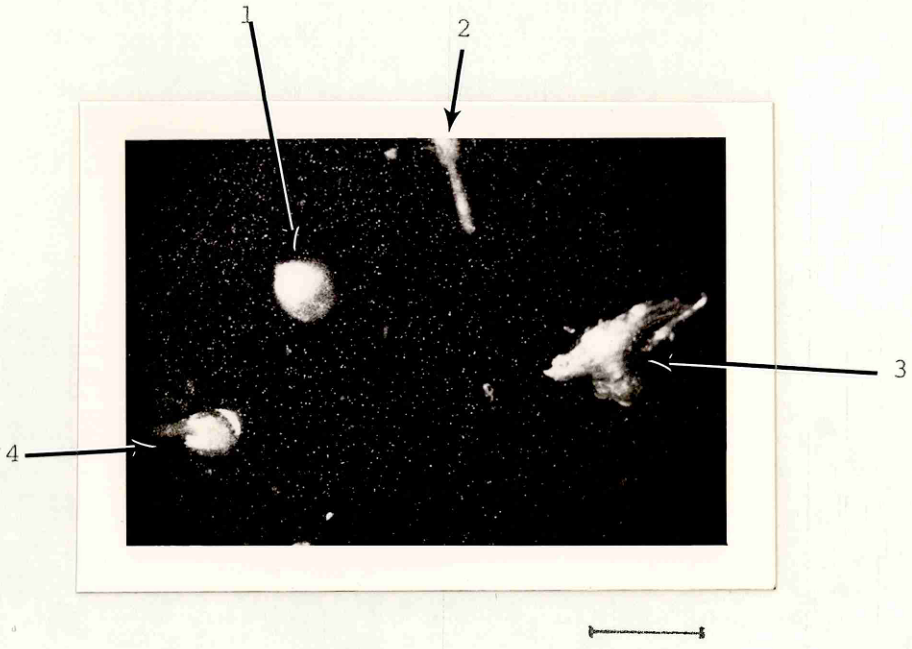

FIGURE 7.1 SURFACE OF $Ga_{1-x}Al_x As$ (x = 0.52)

SAMPLE WITH AMBIENT ILLUMINATION, RECORDED THROUGH THE IIT MICROSCOPE

Scale bar equals 1 mm

Light intensity was plotted against voltage for contact 3 and for contact 4. For each contact the plot is made with both polarities (contact 4 positive, contact 3 negative is described as $4^{+}\ 3^{-}$ etc.) see figures 7.2 and 7.3. The plots were only made where a voltage pulse (of minimum duration 5 ms) applied to the sample produced a constant value current pulse. If there was evidence of thermal runaway such as a steady increase in current during a pulse then either the pulse length was reduced, or the plot was discontinued. The values of light intensity against voltage at $\simeq$ 80 K were measured in the same way but with the sample mounted in the cryostat.

Interpretation of EL Site Intensity Measurements

Later in this chapter I will show that spatial examination of the sample suggests that a p-n junction could have formed by indium diffusion into the material near to each contact. The variation of the EL intensity, at each contact, with voltage, is consistent with the EL being produced by carrier injection across such p-n junctions, one situated near each contact. Bright EL is observed near contact 4 when that contact is positive, or near contact 3 when it is positive. This is consistent with the p-n junction model if the p side of the junction is nearest to the contact. Thus the EL near contact 4 is brighter when contact 4 is positive with respect to contact 3 because then the p-n junction near contact 4 is forward biased. When such a junction is forward biased, I would expect the light intensity to increase linearly with current (Williams and Hall, 1978). This is close to the behaviour of the EL near contact 4 when that contact is positive (figure 7.2), and near contact 3 when that contact is positive (figure 7.3). When such a junction is reverse biased I would expect to observe *no* EL at low applied voltages because no minority carrier injection occurs. Faint EL at large applied voltages is observed near contact 4 when that contact is

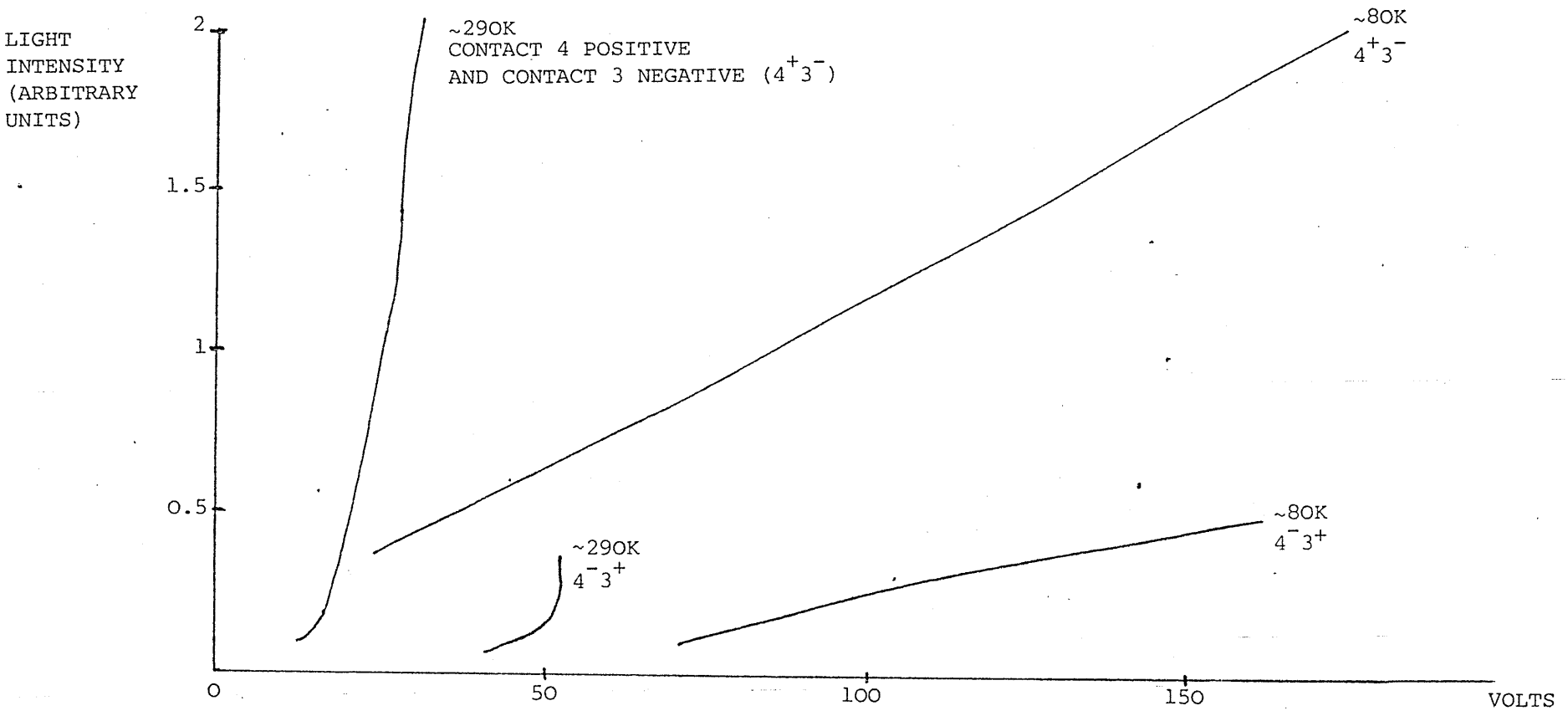

TOTAL LIGHT INTENSITY FROM NEAR CONTACT 4 ON x = 0.52 $Ga_{1-x}Al_xAs$ AT BOTH ~290K AND ~80K, WITH CONTACT 4 BOTH POSITIVE AND NEGATIVE. THE CIRCUIT WAS COMPLETED VIA CONTACT 3.

FIGURE 7.2

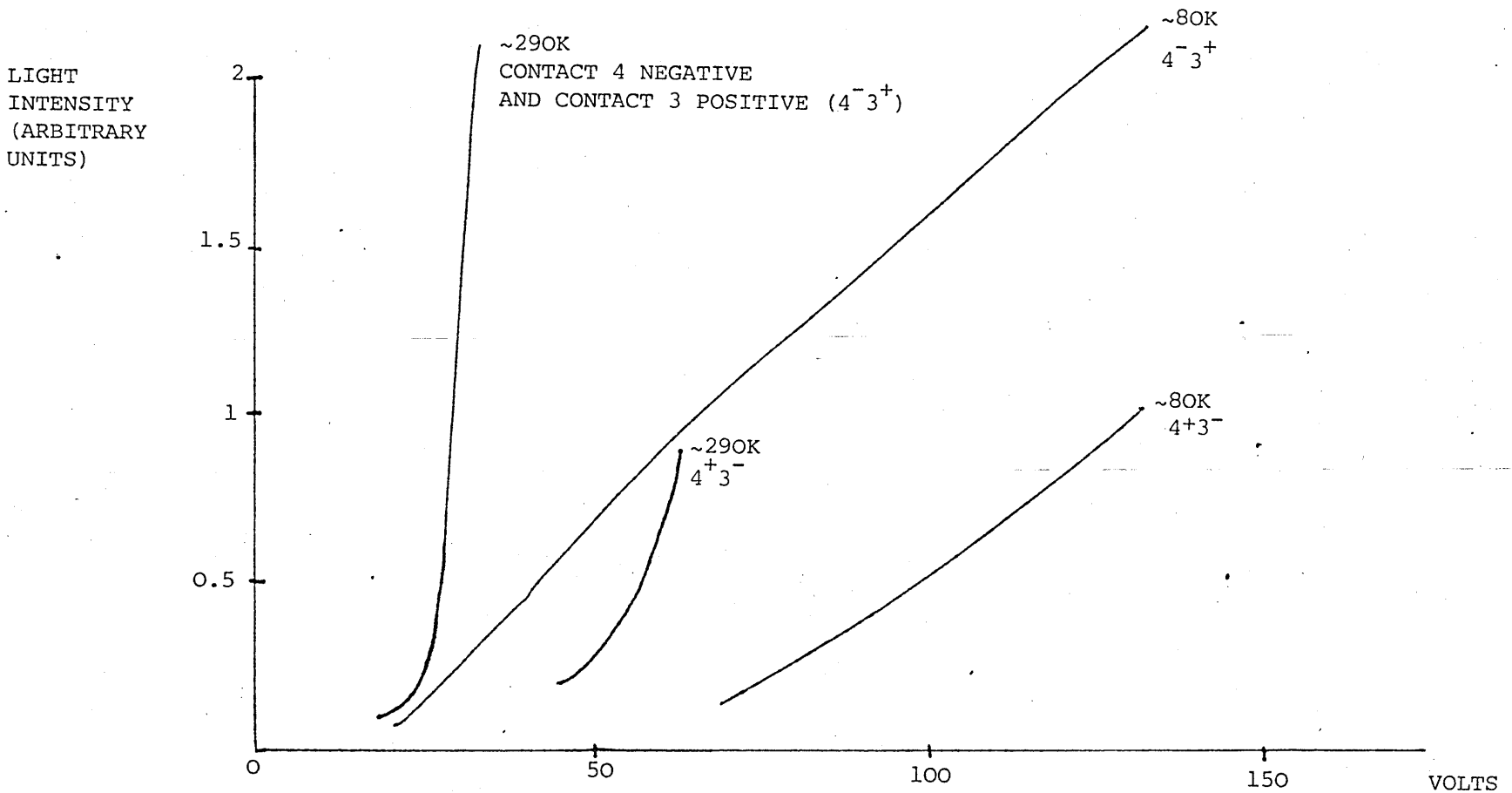

TOTAL LIGHT INTENSITY FROM NEAR CONTACT 3 ON x=0.52 $Ga_{1-x}Al_xAs$ AT BOTH ~290K AND ~80K, WITH CONTACT 3 BOTH POSITIVE AND NEGATIVE. THE CIRCUIT WAS COMPLETED VIA CONTACT 4.

FIGURE 7.3

negative (figure 7.2), and near contact 3 when it is negative (figure 7.3). This behaviour can be explained with the p-n junction model. At large voltages some EL is expected from a reverse biased p-n junction (Dean, 1969) due to minority carrier injection by tunnelling and to minority carrier production by impact ionization. The latter occurs when a high energy conduction band electron collides with a valence band electron knocking it into the conduction band and leaving a hole in the valence band.

The current against voltage characteristic of the sample was also plotted, with pulsing, at room temperature and ≃ 80 K, (figure 7.4). Carrier freeze out, as described in chapter 6, is clearly evident in the difference between the room temperature and ≃ 80 K resistance values. In the model that proposes a p-n junction at each contact, current flow through the junction at one contact to the sample is in the opposite direction to current flow through the junction at the other contact. Thus I would not expect the sample to act as a diode.

Spectral Measurement of EL

Bright EL was visible from around contact 3 when it was positive with respect to contact 4. Also bright EL was visible from around contact 4 when it was positive with respect to contact 3. The EL spectra of these contacts were measured with the monochromator as explained in chapter 6. Three areas of EL around contact 3 (see figure 7.6c) were each found to have the same spectrum. Contact 4 had a different EL spectrum. These spectra are shown in figure 7.5a and figure 7.5b. The spectra at a given position did not depend on the current path in the specimen. The spectrum of contact 3 appears to be a substrate GaAs spectrum (Onton et al., 1974) that of contact 4 exhibits three peaks, one of which is a GaAs substrate spectrum.

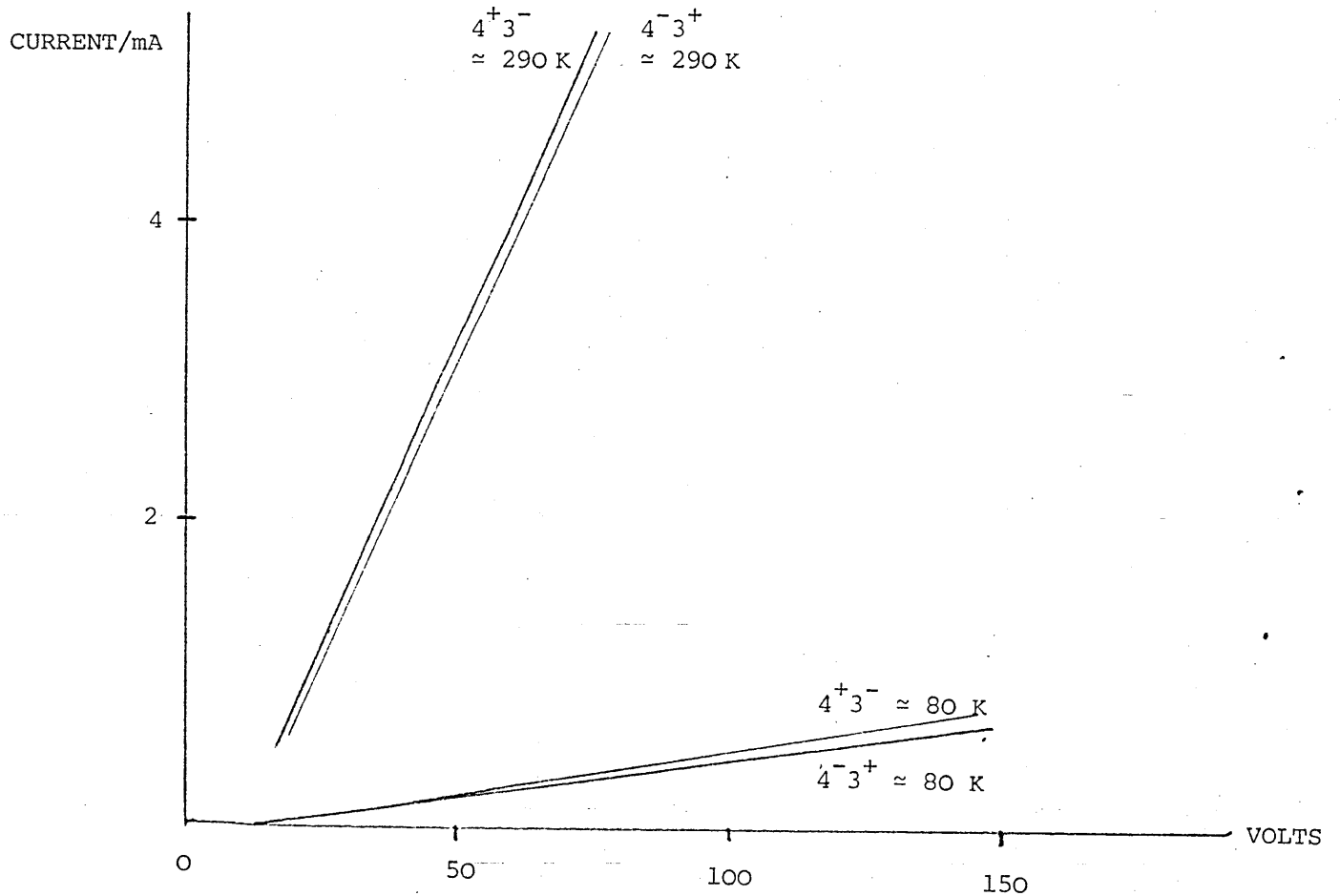

CURRENT PLOTTED AGAINST VOLTAGE, FOR THE CURRENT FLOW BETWEEN CONTACTS 3 AND 4 OF THE x = 0.52 $Ga_{1-x}Al_xAs$ SAMPLE. PLOTTED FOR BOTH POLARITIES AT ≃ 290 K AND ≃ 80 K. PULSING WAS USED TO AVOID OVERHEATING THE SAMPLE. CARRIER "FREEZE-OUT" IS EVIDENT.

FIGURE 7.4

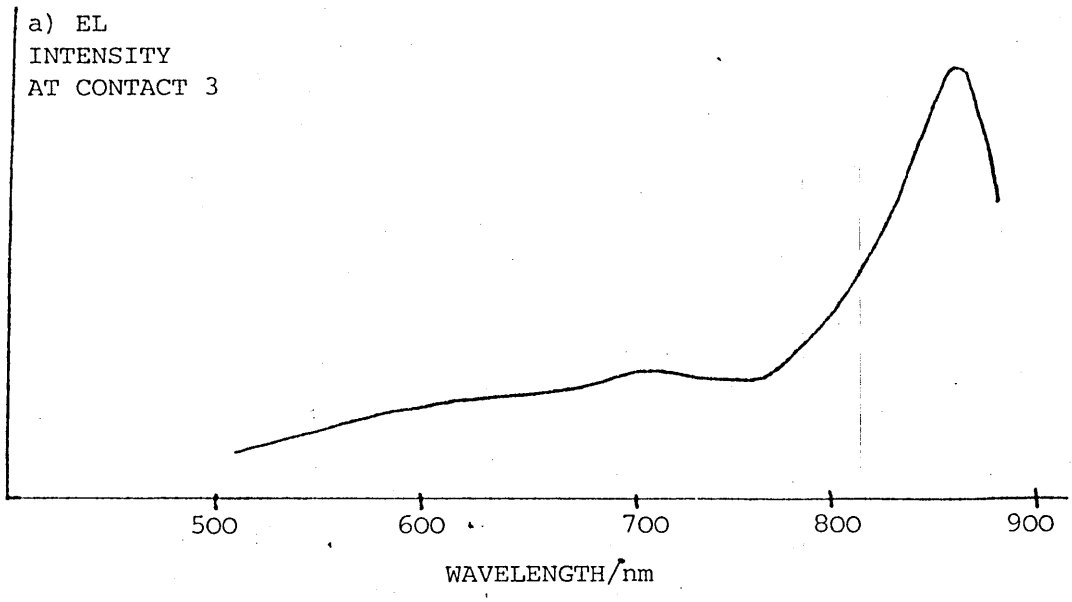

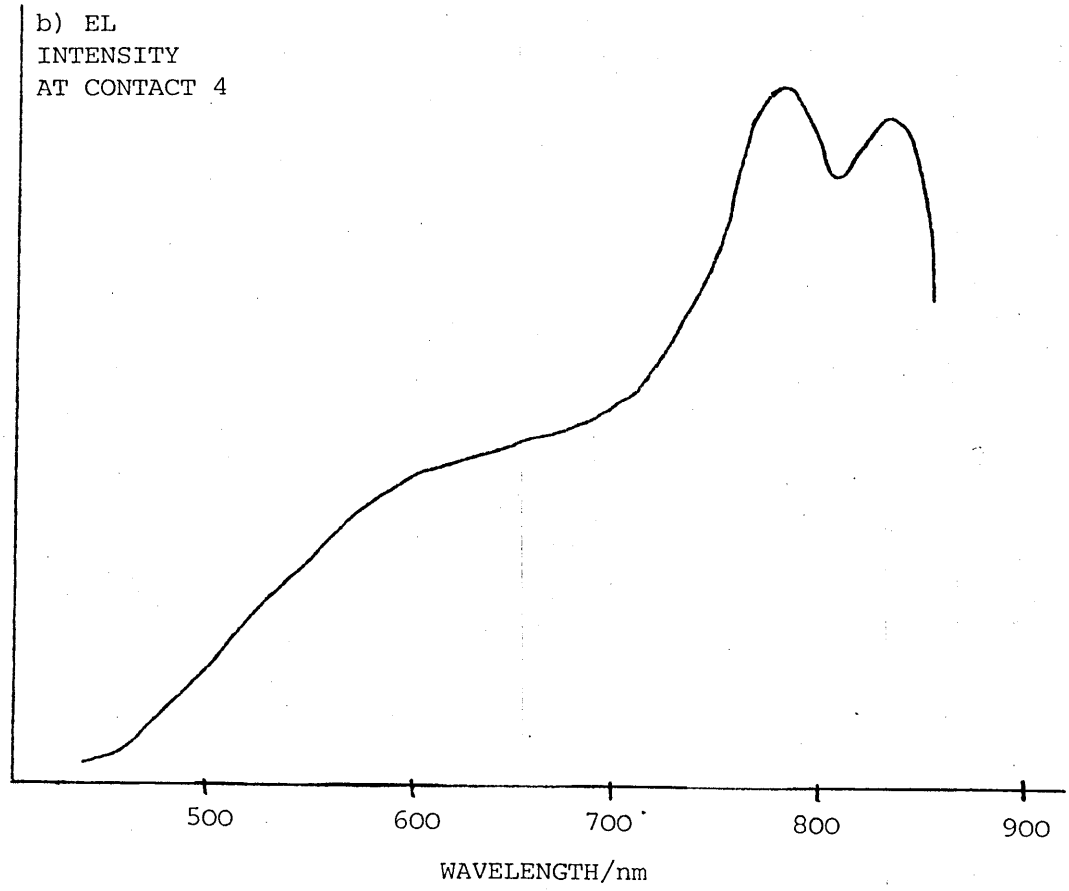

INTENSITY CORRECTED ELECTROLUMINESCENCE (EL) SPECTRA AT CONTACTS 3 AND 4 OF $x = 0.52$ $Ga_{1-x}Al_xAs$ SAMPLE.

FIGURES 7.5a AND 7.5b

The short wavelength peak is consistent with a nominal aluminium concentration of $x \simeq 0.52$ by comparison with Onton, Lorenz and Woodall (1974). The middle peak corresponds to $x \simeq 0.15$ and it is suggested that there is a small area near contact 4 with this reduced aluminium concentration.

So far I have discussed the total light intensity and its spectral distribution for each of the contacts that exhibit EL on this sample. Below I shall describe the results of a spatial examination of this light with the IIT microscope.

Figure 7.6a is a record of the EL near contact 4 when one hundred 0.5 second pulses of 3 mA and polarity $3^- 4^+$ are used. The mark to space ratio of the pulsing was one to one, and the IIT gain was set to about 10^6, (an EHT value of 33 kV). The same mark to space ratio and IIT gain are used in all the following except where stated. Figure 7.6b is a record of the EL of contact 3 when one hundred 0.5 second pulses of 3 mA and polarity $3^+ 4^-$ are used. The same bright EL was seen from contact 3 with $1^- 3^+$, $2^- 3^+$ and $4^- 3^+$. Figure 7.6c shows the relationship of the EL from contacts 3 and 4, it is a superposition of a picture of the bright EL from near contact 4 when that contact is positive, and of the bright EL from near contact 3 when that contact has positive polarity. The conclusion to be drawn from figures 7.6a and 7.6b is that the bands of EL have a width of less than 50 μm. No EL was seen further away from the contacts than this. The band of EL around contact 4, and the three bands around contact 3 were studied in greater detail at higher magnification, at both room temperature and at $\simeq$ 80 K in the cryostat. The EL from contact 3 (at room temperature with $4^- 3^+$) is shown along with faint ambient illumination in figure 7.7a. Part of figure 7.7a is marked and this part is shown with higher magnification in

FIGURE 7.6a EL NEAR CONTACT 4 OF $Ga_{1-x}Al_xAs$ (x = 0.52)
No ambient light

FIGURE 7.6b EL NEAR CONTACT 3 OF $Ga_{1-x}Al_xAs$ (x = 0.52)
No ambient light

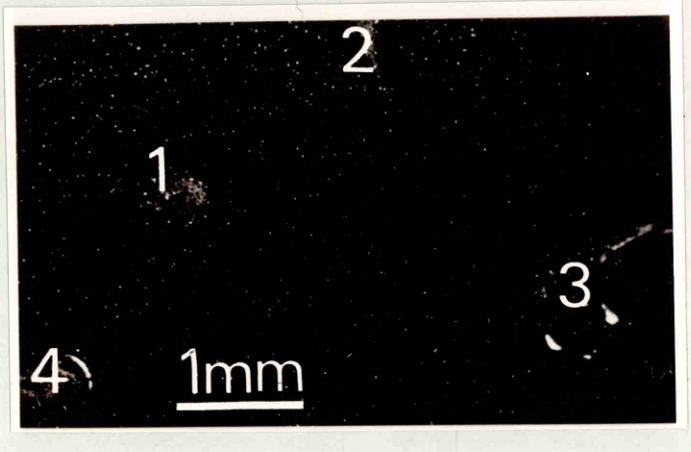

FIGURE 7.6c EL NEAR CONTACT 3 AND NEAR CONTACT 4 OF $Ga_{1-x}Al_xAs$ (x = 0.52), WITH FAINT AMBIENT ILLUMINATION

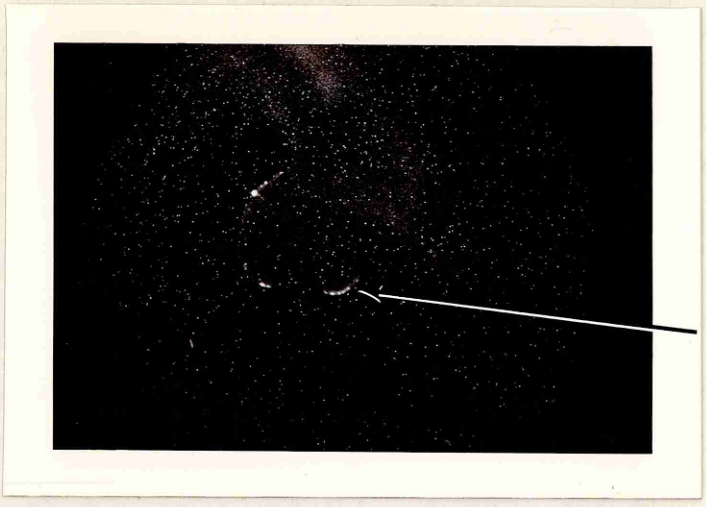

FIGURE 7.7a EL NEAR CONTACT 3 OF $Ga_{1-x}Al_xAs$ (x = 0.52)
SAMPLE WITH FAINT AMBIENT ILLUMINATION

Sample at room temperature

FIGURE 7.7b EL NEAR CONTACT 3 OF $Ga_{1-x}Al_xAs$ (x = 0.52) SAMPLE

One hundred x 0.1 second 72 volt pulses were used in this photograph.

Sample at room temperature. Scale bar equals 50 μm.

figure 7.7b (with 72 V pulses) and in figure 7.8a (with 150 V pulses). The highest useful magnification was obtained with the x 20 eyepiece and x 32 long working distance objective, which projected 70 μm across the 40 mm IIT phospher. A graticule with divisions of 10 μm was photographed at this magnification figure 7.8b. At this highest magnification the bright spot of figure 7.8a was studied a) at ≃ 80 K with sample voltages of 90 to 150 V, equivalent to electric fields of 23600 to 39500 Vm^{-1} and b) at ≃ 290 K with sample voltages of 10 to 75 V, equivalent to electric fields of 2600 to 19700 Vm^{-1}. No structure could be found in this spot, or any of the other points of EL around contact 3. All the EL appeared to originate from points whose size was limited by the resolution of the IIT microscope system. Their size was <2 μm. Typical is figure 7.9 which shows the bright spot of figure 7.8a.

The EL from near contact 4 was also studied at high magnification and low temperature. Unlike contact 3, I was able to resolve some structure in the EL at contact 4. Figure 7.10a shows the contact EL (fifty 150 V pulses of 0.1 s at ≃ 80 K with 4^+ 3^- polarity and no ambient light). The EL is repeated in figure 7.10b with the addition of ambient light to show the relation between the EL position and the contact edge. There was a slight deliberate shift of focus between figure 7.10a and figure 7.10b to bring the contact edge into better focus. It is clear that the EL occurs about 50 μm away from the edge of the indium dot. Two of these regions of EL (arrowed in figure 7.10a) were examined with greater magnification a) in figure 7.11 at room temperature with 75 V pulses (200 pulses of 0.01 s duration with 4^+ 3^-) b) in figure 7.12a and figure 7.12b at ≃ 80 K with 90 V pulses, and in figure 7.13a and figure 7.13b at ≃ 80 K with 150 V pulses. From these and other similar photographs and also by direct observation of the IIT a range

FIGURE 7.8a EL NEAR CONTACT 3 OF $Ga_{1-x}Al_xAs$ (x = 0.52) SAMPLE.
Four hundred x 0.01 second 150 volt pulses were used in this photograph. Sample at ≃ 80 K.
Scale bar equals 50 μm.

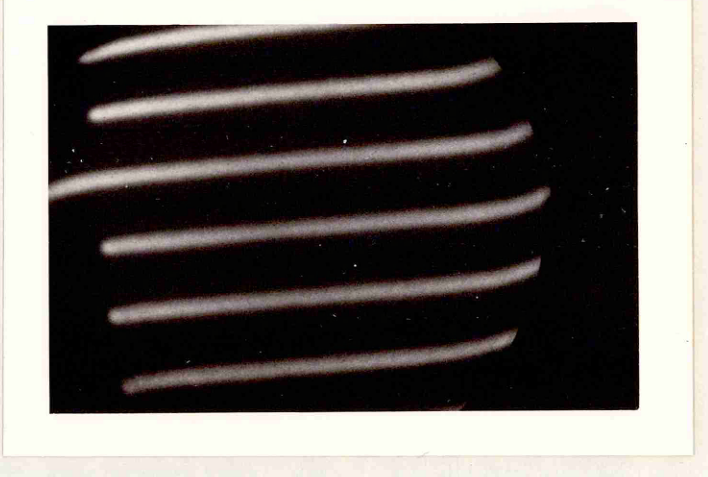

FIGURE 7.8b GRATICULE AT MAGNIFICATION OF FIGURE 7.9
One division equals 10 μm.

FIGURE 7.9 EL NEAR CONTACT 3 OF $Ga_{1-x}Al_xAs$ (x = 0.52) SAMPLE.

The bright spot seen here is marked in figure 7.8a.

Scale bar equals 10 μm

Examined in figure 7.11

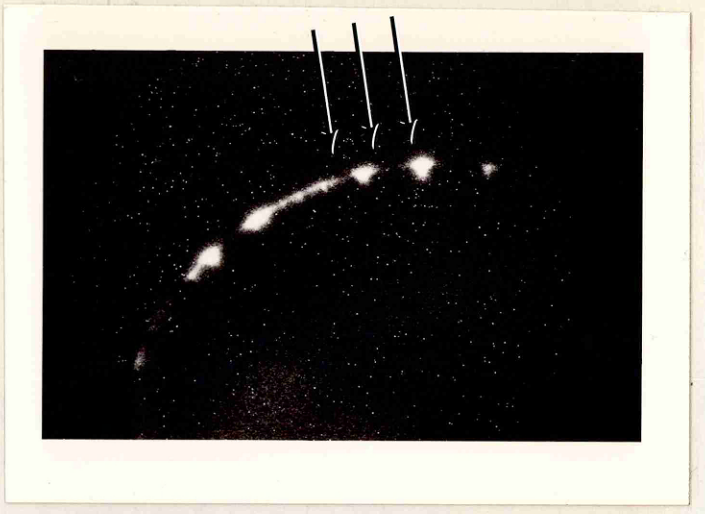

FIGURE 7.10a EL NEAR CONTACT 4 OF $Ga_{1-x}Al_xAs$ ($x = 0.52$) SAMPLE.

150 V pulses. Sample at ≃ 80 K. No ambient illumination.

Scale bar equals 50 μm.

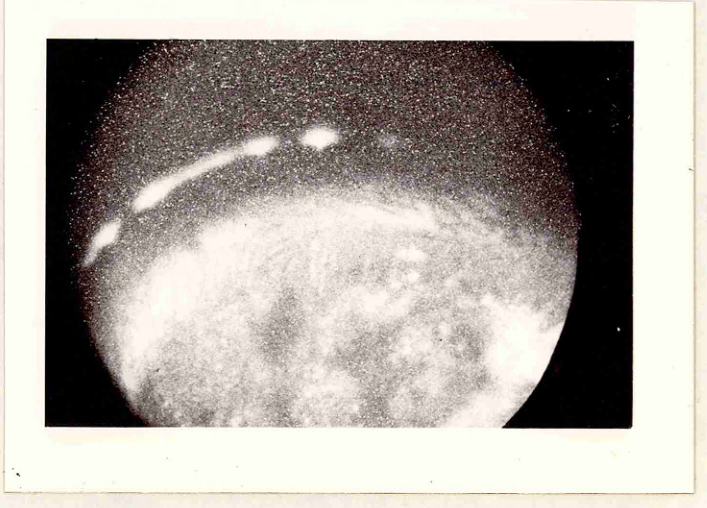

FIGURE 7.10b THE EL OF FIGURE 7.10a WITH AMBIENT ILLUMINATION TO SHOW CONTACT EDGE.

There was a deliberate shift of focus between figures 7.10a and 7.10b to bring the contact edge into better focus.

Scale bar equals 50 μm

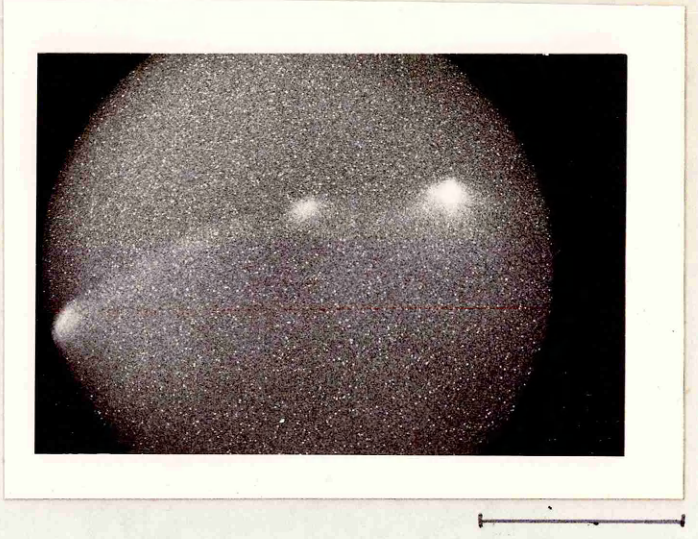

FIGURE 7.11 EL REGION INDICATED IN FIGURE 7.10a AT ROOM TEMPERATURE WITH 75 V PULSES.
Scale bar equals 50 μm.

FIGURE 7.12a EL NEAR CONTACT 4 OF $Ga_{1-x}Al_xAs$ (x = 0.52) SAMPLE, AT ≃ 80 K WITH 90 V PULSES.
Scale bar equals 10 μm.

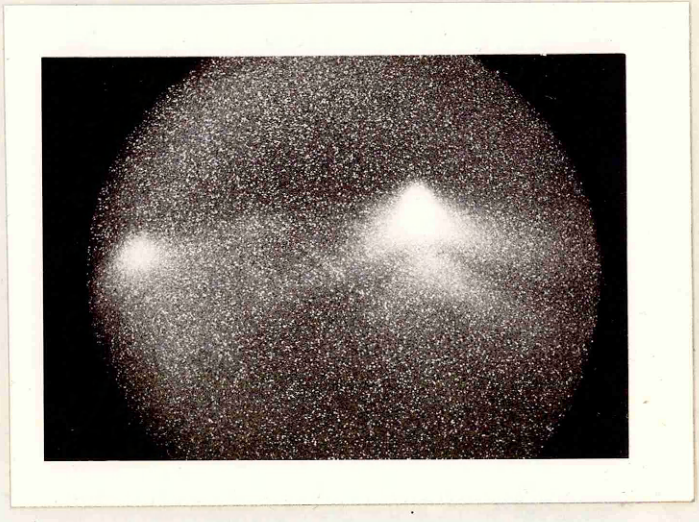

FIGURE 7.12b EL NEAR CONTACT 4 OF $Ga_{1-x}Al_xAs$ (x = 0.52) SAMPLE, AT ≃ 80 K WITH 90 V PULSES.
Scale bar equals 10 μm.

FIGURE 7.13a EL NEAR CONTACT 4 OF $Ga_{1-x}Al_xAs$ (x = 0.52) SAMPLE, AT ≃ 80 K WITH 150 V PULSES.
Scale bar equals 10 μm

FIGURE 7.13b EL NEAR CONTACT 4 OF $Ga_{1-x}Al_xAs$ (x = 0.52) SAMPLE, AT ≃ 80 K WITH 150 V PULSES.
Scale bar equals 10 μm

for the EL was estimated at both room temperature and ≃ 80 K. Observations were made for any variations of the range with electric field. Estimates of range were complicated a) when varying the electric field because this also varied the current through the specimen and hence the brightness of EL and, b) because of focusing difficulties (see section 6.1.1); a blurred image will have an apparent "range". "a)" was overcome by estimating range as the approximate distance over which the density recorded on the photographic negative varied by a factor of e^{-1}. It was possible to measure the range with the sample at ≃ 80 K with between 90 V and 150 V across the sample; and at room temperature with between 10 V and 75 V across the sample. Measurements outside this region were not made either because of the possibility of thermal runaway or because the EL was too faint. The effect of "b)" was minimized by recording a series of pictures of the sample with varying focus and using the one with minimum "range" and hence minimum blur. The estimated experimental ranges are given in table 7.1. The EL near contact 4 originated from a band about 50μm from the contact and appeared to decay both towards and away from the contact. Ranges were estimated for the decay in both directions. To ensure that the trails of EL were not artifacts of the optics (e.g. internal reflections) the experiments were repeated with the sample rotated by 90^{o} and the same results were obtained.

7.1.2.2 Discussion of Results from $Ga_{1-x}Al_xAs$ with x = 0.52

In the previous section I presented the results of my spatial EL study of x = 0.52 $Ga_{1-x}Al_xAs$. The brightest EL was observed near contact 4 when that contact was positive and near contact 3 when that contact was positive. This behaviour is expected from n type samples with positive contacts.

CONTACT	TEMPERATURE	SAMPLE VOLTAGE REGION OVER WHICH EL WAS OBSERVED, IN VOLTS	AVERAGE ELECTRIC FIELD ACROSS SAMPLE IN VOLTS PER METRE	OBSERVED ELECTROLUMINESCENCE RANGE
3	≃ 80 K	90 to 150	23700 to 39500	< 2 μm
3	≃ 290 K	10 to 75	2600 to 19700	< 2 μm
4 Towards Contact	≃ 80 K	90 to 150	23700 to 39500	≃ 20 μm
4 Towards Contact	≃ 290 K	10 to 75	2600 to 19700	< 2 μm
4 Away from Contact	≃ 80 K	90 to 150	23700 to 39500	< 2 μm
4 Away from Contact	≃ 290 K	10 to 75	2600 to 19700	< 2 μm

TABLE 7.1 EXPERIMENTALLY MEASURED RANGES IN $x = 0.52$ $Ga_{1-x}Al_xAs$

The EL near contact 4 appears to originate from a line spaced about 50μm from the edge of the physical contact. The EL appears to decrease in brightness towards the contact and a range has been assigned to this decay (table 7.1). The EL also decays, on the side of the band away from the contact, but this decay occurs in a distance less than the IIT microscope system resolution and has a range <2μm. This is not the behaviour that was expected. Initially I expected each contact to behave like an ohmic metal to semiconductor contact as described in chapter 5. With appropriate polarity so that such a contact injects minority carriers (for this n type sample this corresponds to a positive contact) I expected to see a decay in EL intensity away from the contact as the minority carrier concentration was reduced by recombination (on the assumption of a uniform distribution of radiative recombination centres). EL intensity is proportional to $Rn_e n_h$ where R is the radiative recombination efficiency n_e the electron concentration and n_h the hole concentration. EL is seen a) in regions of the sample such as near the contacts when minority carriers are injected and both n_e and n_h are large even though R may be small, and b) at radiative recombination centres throughout the material away from the contacts where R is enhanced even though either n_e or n_h may be small because of carrier recombination near to the contacts. However, as explained above, I did not observe a uniform decay in EL intensity away from the contact.

A possible explanation of my experimental result is obtained by studying the fabrication of the contact. The contacts were made by alloying indium (In) dots onto the surface of the material for one hour at 200° C. During this process indium could have either a) evaporated from the contact and been deposited, and then diffused through the material or b) diffused directly through the $Ga_{1-x}Al_xAs$.

The diffusion coefficients of indium in GaAs and in AlAs are not known with any precision (Nat. Bur. Standards, U.S.A., 1980) but using reasonable estimates (Willardson and Beer, 1968) a calculation can be made of the diffusion distance (L^{IN}) of indium in GaAs, for the heat treatment undergone by this sample (200°C for one hour).

$$d^{IN} = d_o^{IN} \exp(-\Delta E/kT)$$

$$L^{IN} = \sqrt{(2\, d^{IN}\, t)}$$

The diffusion occurs during a time interval t at a temperature of T kelvins, ΔE is the diffusion activation energy, d^{IN} the diffusion coefficient and d_o^{IN} the diffusion constant. "d^{IN}" and "d_o^{IN}" are used to avoid confusion with "D" and "D_o" which occur later in this chapter. If $d_o^{IN} = 1.50 \times 10^{-2}\ m^2\ s^{-1}$ and ΔE = 1eV (both reasonable estimates, see Nat. Bur. Standards, U.S.A., 1980, and Barnard, 1973) then $L^{IN} \simeq 50\mu m$. Such estimates of d_o and ΔE show that diffusion of indium through 50μm of GaAs, during the contact alloying process, is possible. The bulk of the sample is n-type $Ga_{1-x}Al_xAs$. Indium is an acceptor dopant and the diffusion of indium into the material near the contact has created a p type region close to the contact. A p-n junction has thus been formed in the material by indium diffusion close to the contact. There must be more than one p-n junction in the sample since overall the sample does not act as a diode (figure 7.4). I would expect such a junction to have formed near every contact since all the contacts were fabricated in the same way. Possibly the EL from the junction near contact 3 is partially obscured from view, (hidden beneath the indium dot) so that its EL does not look the same as that at contact 4.

The EL behaviour near contact 4 can be explained by such a junction. The p side of the junction (the indium doped side near the contact),

into which electrons are injected as minority carriers when contact 4 is positive, exhibits the observed decay in EL towards the contact because of electrons radiatively recombining with holes, see figure 7.14. Holes are injected into the n type bulk of the sample and they also recombine but their perceived range is less because the hole mobility (μ_h) is less than electron mobility (μ_e) in GaAs (μ_e = 0.88 $m^2 V^{-1} s^{-1}$, μ_h = .04 $m^2 V^{-1} s^{-1}$), AlAs (μ_e = .12 $m^2 V^{-1} s^{-1}$, μ_h = .042 $m^2 V^{-1} s^{-1}$), and their alloys at room temperature.

It is thought that a number of recombination centres and defects give the bright spots near the junction and that the bright 'tails' to these spots are low resistance paths in the material.

An estimate can be made of the range that would be expected of carriers injected across such a p-n junction and can be compared with the experimental observations. How the range should vary with changing electric field and temperature will also be considered.

Two regimes can be identified a) at very low electric fields where the injected minority carrier range as a result of diffusion is much greater than the range which results from drift in the electric field. If τ_r is the recombination time (not to be confused with the scattering collision time (τ_s) that appears in $\mu = e\,\tau_s (m^*)^{-1}$) and D is the diffusion coefficient then the average distance travelled by a minority carrier before recombination, is called the diffusion length L_D and is given by

$$L_D = \sqrt{(2D\tau_r)}$$

b) at larger electric fields where diffusion is negligible compared with drift in the electric field (E), then the minority carrier range (R) is greater than the diffusion length (L_D) by a factor y^{-1}

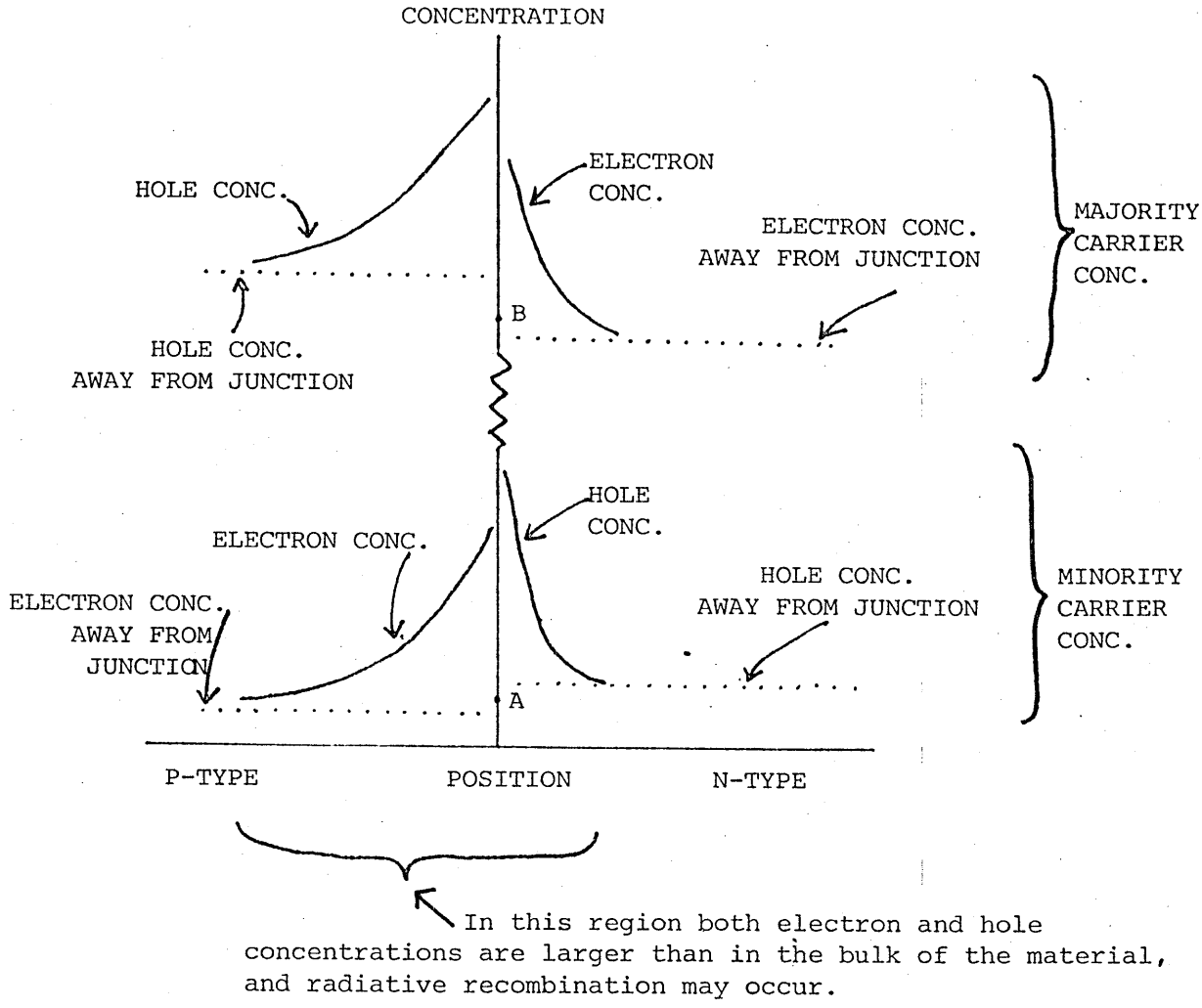

The difference between the minority carrier concentration (A above) and the majority carrier concentration (B above) is typically three or more orders of magnitude but depends on the material and doping.

FIGURE 7.14 SCHEMATIC DIAGRAM OF A FORWARD BIASED P-N JUNCTION

$$R = \frac{L_D}{y}$$

$$\text{Where } y = \sqrt{1 + \left(\frac{\mu E L_D}{2D}\right)^2} - \frac{\mu E L_D}{2D}$$

R can be approximated by $\mu E \tau_r$.

The electron mobility in the bulk of the material is 0.1 $m^2 V^{-1} s^{-1}$ at room temperature. Assuming that $\mu \alpha T^{-3/2}$ (which assumes that mobility is limited by phonon scattering) then the mobility is approximately 0.74 $m^2 V^{-1} s^{-1}$ at 80 K. The diffusion coefficient is found from the Einstein relation

$$D = \frac{\mu k T}{e}$$

which gives $D = 2.5 \times 10^{-3} m^2 s^{-1}$ at room temperature and $D = 4.9 \times 10^{-3} m^2 s^{-1}$ at 80 K.

The results of these calculations for three different estimates of recombination time τ_r (10^{-7}, 10^{-8} and 10^{-9} s) and for the upper and lower observed pulsing voltages at room temperature (10V to 75V) and at 80 K (90V to 150V) are given in table 7.2.

A comparison of my experimental results for the decay towards contact 4 (where electrons are minority carriers), with the calculated ranges, suggests a recombination time for electrons in p type material of about 6×10^{-10} s. With this recombination time the calculated range with 120 V (midway between 90V and 150V) pulses at 80 K is ≃20 μm while the calculated range at room temperature with 30V pulses is about 2 μm. Similar calculations for hole range (assuming $\tau_r \simeq 10^{-10}$ s) on the other side of the p-n junction give <2 μm due to the small hole mobility (table 5.1). For example at ≃ 80 K with 39500 Vm^{-1}

≃ 293 K	With $\tau = 10^{-7}$ s	With $\tau = 10^{-8}$ s	With $\tau = 10^{-9}$ s
Diffusion Distance (L_D)	22	7	2
Range with 2600 Vm^{-1}	60	10	2.2
Range with 19700 Vm^{-1}	380	40	4
≃ 80 K			
Diffusion Distance (L_D)	31	10	3
Range with 23700 Vm^{-1}	3400	358	32
Range with 39500 Vm^{-1}	5700	600	54

ALL RANGES AND DIFFUSION DISTANCES ARE QUOTED IN MICROMETRES

TABLE 7.2 CALCULATED RANGES AND DIFFUSION DISTANCES

field and $\tau_r \simeq 10^{-10}$ s, R is found to be $\simeq 2\mu m$.

The experimental observations at contact 4 can thus be explained by p-n junction formation, coupled with some material inhomogeneities giving rise to regions of higher radiative recombination efficiency. That the material is inhomogeneous is confirmed by the presence of several bright radiative recombination centres. The EL observed from contact 3 could also be associated with a p-n junction formation although only one side of this junction is visible, the rest is possibly hidden under the indium dot. No EL was observed from any other contacts on this sample. Perhaps at those contacts the electrical contact is visually obscured underneath the indium dot so that no light can escape.

The EL spatial study of this specimen with the IIT microscope has shown the usefulness of the technique. I have obtained information on the material homogeneity (from the position of light emission centres and from their spectra) and on the uniformity and area of electrical contacts. A perfectly uniform flat contact would be expected to produce a ring of light around its edge of constant width, while an inhomogeneous contact will produce an inhomogeneous distribution of light e.g. discrete spots. No illumination will be observed if the region of light emission is hidden under the indium dot.

Without the IIT microscope, photographs of the EL, if possible at all, would have required very long time exposures (of the order of hours), and a quick visual inspection of the sample surface would have been impossible.

7.1.3 $Ga_{1-x}Al_xAs$ with $x = 0.35$ sample A

This sample was grown by liquid-phase epitaxy on a GaAs substrate. The sample was doped n type. With the IIT microscope EL was observed from points in the bulk of the material. Figure 7.15a is of the sample under faint ambient illumination as seen through the IIT microscope. The sample is about $4mm^2$ and the contacts are numbered 1 to 4. The EL visible from this specimen is shown in figure 7.15b. It occurs near contact 4. Faint ambient illumination makes contact 4 visible while the EL appears as some dots to the bottom right of the contact. Figure 7.15b was taken with 4^+ 1^- and 20 x 0.1 second pulses of 26 mA and 40 volts. This area of the sample was examined with increased magnification and it was found that different parts of the EL pattern were illuminated depending on the current flow pattern in the material. Figures 7.16a to 7.16f are pictures of the EL area shown in figure 7.15b but with increased magnification. The orientation of figures 7.16a to 7.16f is the same as that of figures 7.15a and 7.15b. Figures 7.16a to 7.16f were all made with 10 x 0.01 second pulses of 60 mA and $\simeq$ 30 V with the sample at room temperature. Figures 7.16a to 7.16f differ in the pairs of contacts that were used to produce the current flow in the material. The current flow in the sample may be compared to that in a plane with two point contacts (figure 7.17). The EL is observed between contacts 1 and 4 (figure 7.15a) and I would expect the current in this region to be greatest when contacts 1 and 4 are connected, less when 2 and 4 are connected and least of all when 3 and 4 are connected. Figures 7.16a, 7.16b and 7.16c of EL with 1^- 4^+, 2^- 4^+ and 3^- 4^+ respectively connected, show that the decrease in EL brightness is what would be expected from the current flow pattern in a uniform specimen. When the polarity is reversed so that contact 4 is negative (figures 7.16d, 7.16e and 7.16f) different parts of the

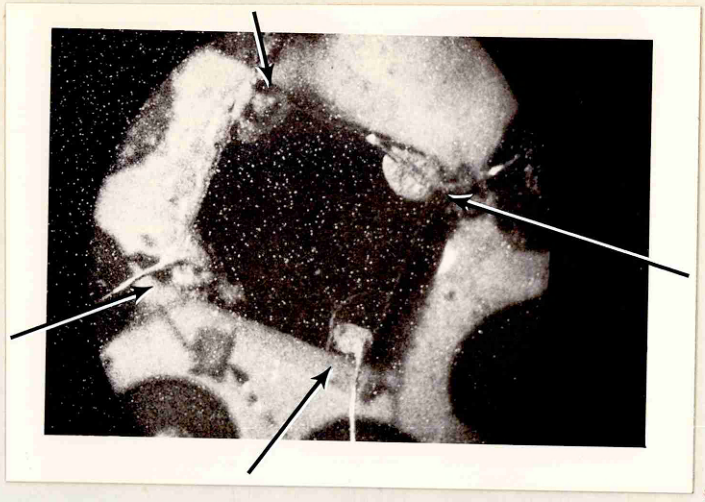

FIGURE 7.15a $Ga_{1-x}Al_xAs$ (x = 0.35) WITH AMBIENT ILLUMINATION.
Contacts are numbered 1 to 4.
Scale bar equals 2 mm.

FIGURE 7.15b EL NEAR CONTACT 4 OF $Ga_{1-x}Al_xAs$ (x = 0.35), WITH FAINT AMBIENT ILLUMINATION.
Scale bar equals 1 mm.

FIGURE
7.16a

$1^{-}\ 4^{+}$

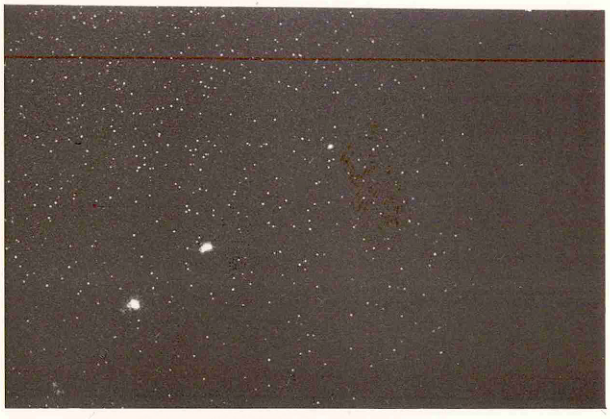

FIGURE
7.16b

$2^{-}\ 4^{+}$

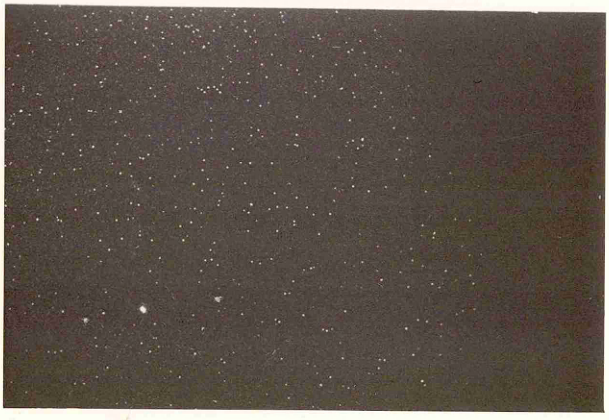

FIGURE
7.16c

$3^{-}\ 4^{+}$

FIGURES 7.16a, 7.16b AND 7.16c. EL NEAR CONTACT 4 OF $Ga_{1-x}Al_xAs$ ($x = 0.35$) USING DIFFERENT PAIRS OF ELECTRICAL CONTACTS TO THE SAMPLE.

Scale bar equals 100 μm.

FIGURE
7.16d

$1^{+}\ 4^{-}$

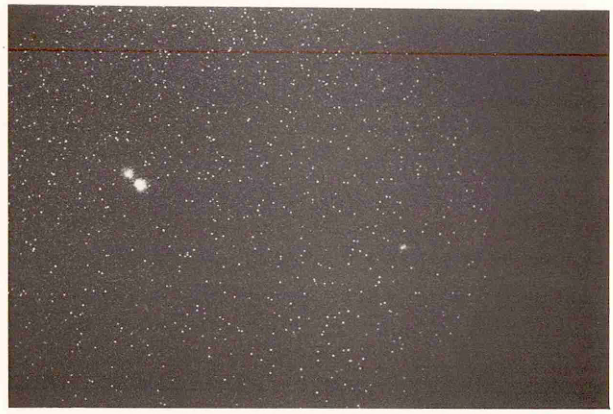

FIGURE
7.16e

$2^{+}\ 4^{-}$

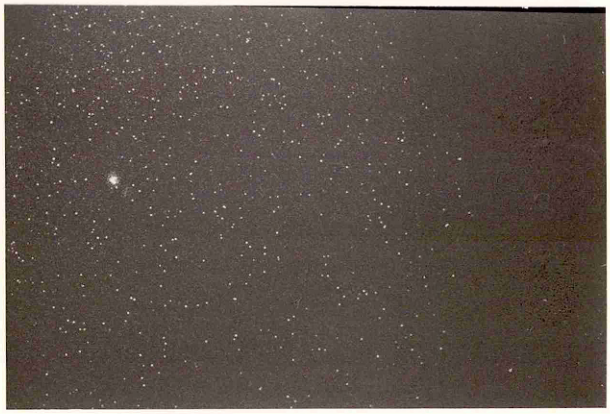

FIGURE
7.16f

$3^{+}\ 4^{-}$

FIGURES 7.16d, 7.16e AND 7.16f. EL NEAR CONTACT 4 OF $Ga_{1-x}Al_xAs$ ($x = 0.35$) USING DIFFERENT PAIRS OF ELECTRICAL CONTACTS TO THE SAMPLE.

Scale bar equals 100 μm.

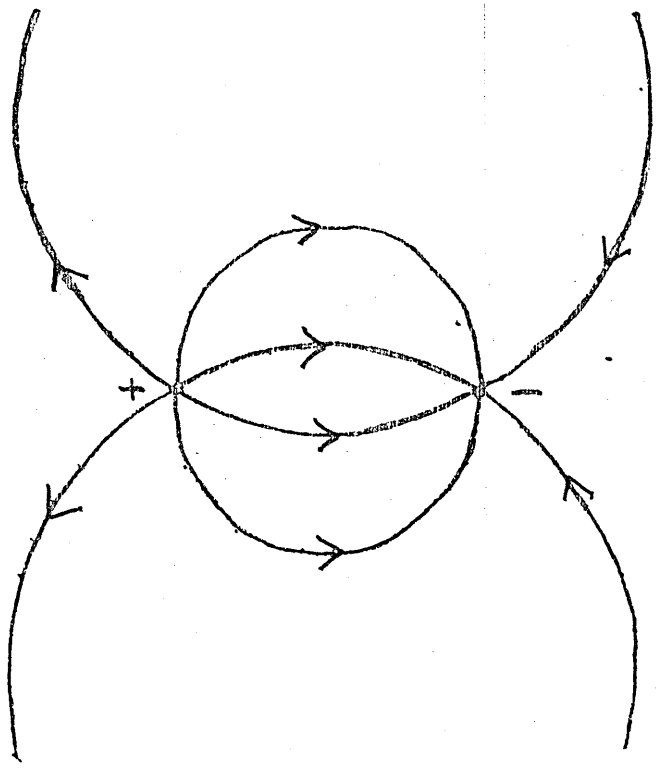

SOME LINES OF CONVENTIONAL CURRENT FLOW ON A CONDUCTING PLANE WITH TWO POINT CONTACTS.

FIGURE 7.17

sample emit EL but again there is a decrease in brightness (and one EL centre becomes invisible) in going from $1^+ 4^-$ to $2^+ 4^-$ to $3^+ 4^-$. Another factor in the intensity observed at a radiative recombination centre must be its closeness to the minority carrier source because this affects the number of carriers that reach a particular recombination centre.

The above results again show the usefulness of an IIT microscope study of EL. I believe that no decay of light is observed from the contacts in this material because of a long radiative recombination time. (The resistivity of the x = 0.35 sample is about two orders of magnitude less than the resistivity of the x = 0.52 sample). EL is only seen from a small number of radiative recombination centres within the bulk of the material (this is also shown in the study of sample B of x = 0.35 $Ga_{1-x}Al_xAs$, see below). The importance of an EL study, which is demonstrated by this sample, is that the radiative recombination centres important to a particular current flow in the specimen are highlighted, while those in a part of the specimen where no current flows are not shown up. No such emphasis is given by photoluminescence (PL) or cathodoluminescence (CL) spatial studies.

To obtain further information for comparison with that provided by EL I a) studied the area of figures 7.16a to 7.16f under ambient light, b) measured the EL spectra of the points of EL and c) studied the contact with a scanning electron microscope.

The EL "line" is shown, recorded by the IIT microscope, in figure 7.18a. This picture of the EL line is repeated in figure 7.18b where in addition there is superimposed on it a picture of the contact taken through the IIT microscope with ambient illumination. From a comparison of figures 7.18a and 7.18b it is clear that there is a

FIGURE 7.18a EL NEAR CONTACT 4 OF $Ga_{1-x}Al_xAs$ (x = 0.35) WITH POLARITY 4^+ 1^-.
Scale bar equals 100 μm.

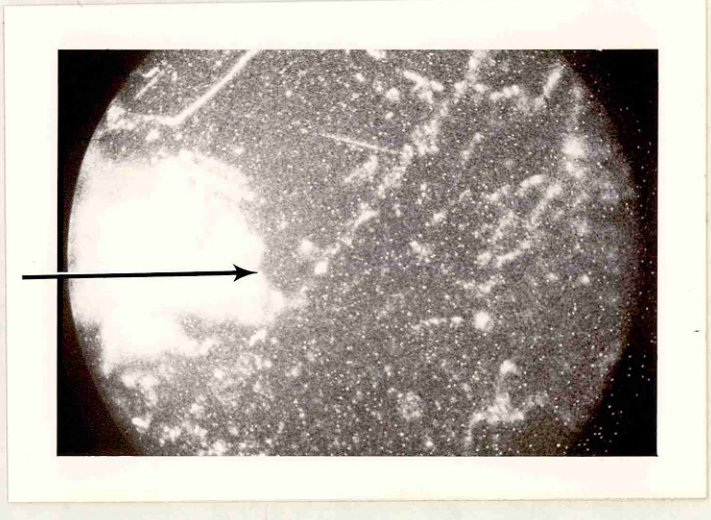

FIGURE 7.18b EL OF FIGURE 7.18a SUPERIMPOSED ON A PHOTOGRAPH OF THE SAMPLE, TAKEN WITH AMBIENT ILLUMINATION AND SHOWING CONTACT 4.
Scale bar equals 100 μm.

visible feature, possibly a growth step, along the line from which the EL originates.

Figure 7.19 is a superposition of figures 7.16a to 7.16f and shows all the points of EL visible on this sample. With the microscope and a photomultiplier tube, as explained in chapter 6, the EL spectra of all the points were measured. The spectra were found to be the same within 10nm. A typical corrected spectra is shown in figure 7.20 peaking at 650 (± 10)nm. This peak position corresponds to $x = 0.35$ (± .05) (Onton, Lorenz and Woodall, 1974). The direct to indirect band gap crossover occurs at $x \simeq 0.37$ ($\simeq$ 647 nm) so a sample with a composition of $x = 0.35$ has a direct, or near direct, band gap.

No large material inhomogeneities were revealed by the EL spectra, as they were in the case of the $x = 0.52$ sample.

The line along which all but two of the points of EL occur (the two which do not occur along this line are marked in figure 7.19) in addition to being visible under ambient illumination is also clearly seen when the sample is studied with a scanning electron microscope. On the scale of figure 7.19 the same area of the sample is shown with secondary electron contrast (SEC) figure 7.21a, and cathodoluminescence (CL) contrast (without wavelength selection and using an extended S20 photomultiplier) in figure 7.21b. There is no evidence on either the SEC or CL pictures to suggest where on the line the points of EL may occur. It is thought that this line is a growth step and that dislocations, impurities or precipitates of aluminium are acting as radiative recombination centres at points along the line. The CL picture shows a small change in brightness across the line, which could be due to many things, one of which is a small

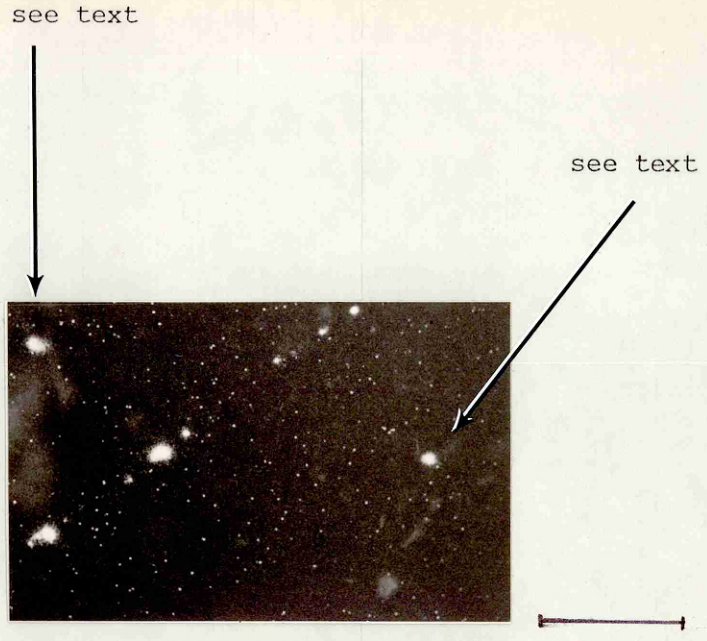

FIGURE 7.19 A SUPERPOSITION SHOWING ALL THE POINTS OF EL FROM NEAR CONTACT 4 OF $Ga_{1-x}Al_xAs$ (x = 0.35). Scale bar equals 100 µm.

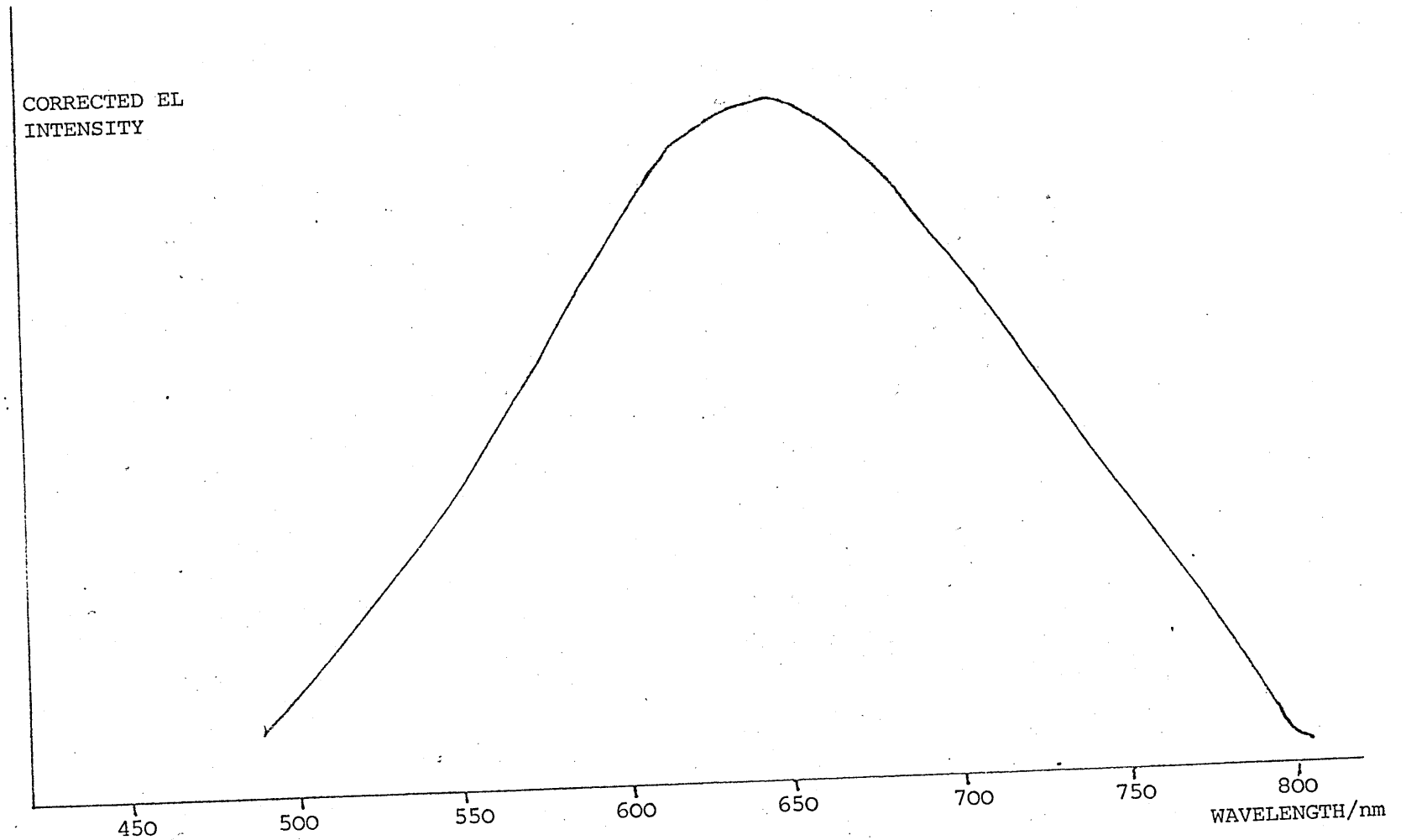

Recorded with sample polarity of 1^{+} 4^{-}. Bandwidth 2½ nm.

FIGURE 7.20 ELECTROLUMINESCENCE SPECTRA OF x = 0.35 $Ga_{1-x}Al_xAs$ SAMPLE, CONTACT 4.

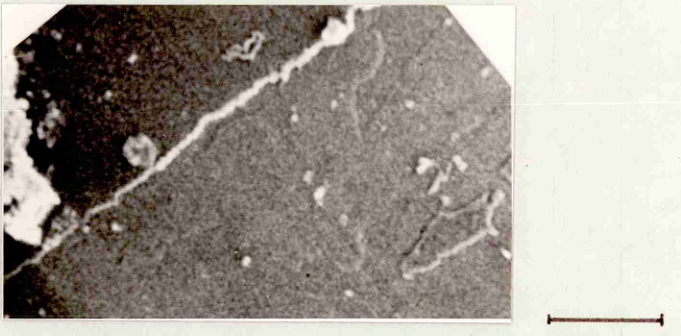

FIGURE 7.21a SECONDARY ELECTRON CONTRAST PHOTOGRAPH OF THE AREA OF $Ga_{1-x}Al_xAs$ (x = 0.35) SHOWN IN FIGURE 7.19. Scale bar equals 100 μm.

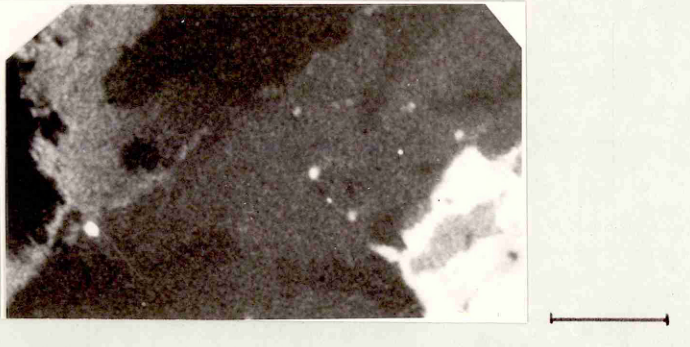

FIGURE 7.21b CATHODOLUMINESCENCE CONTRAST PHOTOGRAPH OF THE AREA OF $Ga_{1-x}Al_xAs$ (x = 0.35) SHOWN IN FIGURE 7.19. Scale bar equals 100 μm.

change in x across the line. The change in the EL spectra between points of EL on either side of the line (arrowed in figure 7.19) suggests $\Delta x < \cdot 05$.

In summary my study of this sample of $Ga_{1-x}Al_xAs$ with $x = 0.35$ has shown that useful information can be obtained in a spatial study of EL which is not provided by CL or SEC contrast studies. I have shown that CL and SEC scans, although they do provide spatial information do not give evidence of the exact position of radiative recombination centres. The EL picture provides definite information on the position of radiative recombination centres, the data is also influenced by the current paths in the specimen whereas CL and SEC are not influenced in this way. The EL information is perhaps more applicable to samples under device conditions because the mechanism of carrier injection is similar to that in many real devices ($\simeq$ 1eV electrons injected via electrical contacts rather than $\simeq$ 10 keV electrons bombarding the surface). The IIT microscope apparatus was particularly useful for these EL studies because of its optical high gain which firstly enabled the EL to be located easily and secondly reduced the time required to photograph the EL. In the weaker cases the EL could not have been photographically recorded at all without the IIT.

I attempted a spatial study of the PL of this specimen using a 0.5 mW He-Ne laser with the IIT and microscope, but the PL was hardly detectable above the IIT noise even at liquid nitrogen temperature.

7.1.4 $Ga_{1-x}Al_xAs$ with $x = 0.35$ sample B

Another sample of the same material as $Ga_{1-x}Al_xAs$ sample A with $x = 0.35$ was briefly studied in EL with the IIT microscope. It had

four electrical contacts which were made by evaporating gold onto the sample surface and then alloying it to the surface by heating. It contained a number of radiative recombination centres which are visible in figure 7.22a. The centres could be clearly seen through the IIT microscope with a potential difference of 30 V applied to the sample. This result implies that the minority carrier range in the bulk of the material is at least of the same order of magnitude as the sample size. With the approximation $R = \mu E \tau_r$, where $\mu \simeq 0.1\ m^2V^{-1}s^{-1}$, $E \simeq 15000\ Vm^{-1}$ and $R > 2mm$; it follows that $\tau_r > 10^{-7}$ s. In this case τ_r is the average (radiative and non radiative) recombination time for a minority carrier. Only at certain points in the material is the radiative recombination time enhanced, and then light emission may be seen from these points.

7.1.5 $Ga_{1-x}Al_xAs$ samples with $x = 0$, 0.115 and 0.7

I could detect no EL from samples with these values of x. There are a number of possible reasons for this, a) the $x = 0$ and $x = 0.115$ samples are direct gap materials. If they radiate they will do so at longer wavelengths than 800nm. This is near the edge of the IIT sensitivity range (figure 6.10a). The IIT gain for the emission from these samples is at least five times less than the gain for emission from the $x = 0.35$ and 0.52 samples. b) The $x = 0.7$ sample has an indirect band gap so that radiative recombination from this material is expected to be at least two orders of magnitude less intense (Williams and Hall, 1978) than from the direct gap samples. So any EL produced by these samples may be too weak to detect above IIT noise. c) The materials may contain few radiative recombination centres so that no detectable light is produced. d) The materials may contain many non-radiative recombination centres so that no light is produced. Study of a

FIGURE 7.22a
EL OF $Ga_{1-x}Al_xAs$
(x = 0.35)
SAMPLE B

Scale bar
equals 0.5 mm.

ELECTRICAL CONTACT

ELECTRICAL CONTACT

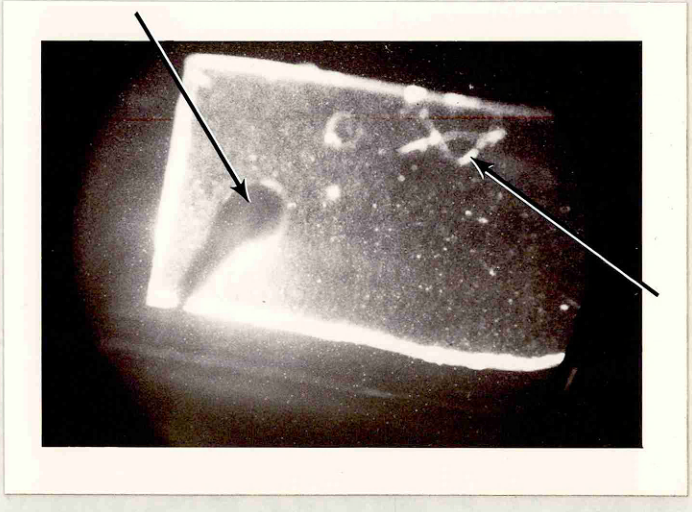

FIGURE 7.22b
EL OF GALLIUM
PHOSPHIDE

Scale bar
equals 0.5 mm.

SURFACE SCRATCH

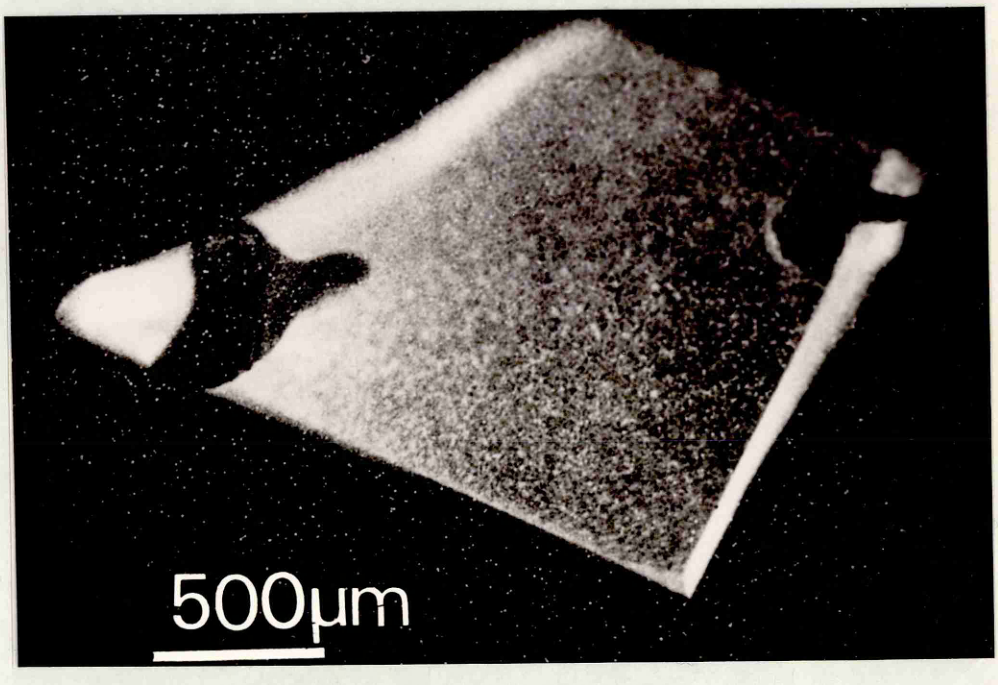

FIGURE 7.22c EL OF GALLIUM PHOSPHIDE
Sample pulsed with 50 mA.

wider range of samples should enable the reasons why some do not exhibit EL to be more closely examined.

7.2 Gallium Phosphide

A number of GaP samples were studied. They were all in the form of thin films on glass substrates and were typically 2 mm in length and breadth. Electrical contacts were made to these samples by alloying indium dots onto the surface for 10 minutes at about 200°C. The EL of these samples was studied, and they were all found to behave similarly. The samples exhibited a decay in EL away from one contact (this was the contact of minority carrier injection and so depended on sample doping and polarity). Light was also seen from scratches on the specimen surface and from the edges of the sample. Typical examples are shown in figure 7.22b and figure 7.22c.

It is important to note that the range observed in GaP (about 1 mm) is not the range associated with a single injected minority carrier before recombination occurs. GaP is an indirect band gap semiconductor. Its EL emission is much greater than would be expected of an indirect gap material because of the presence of impurities, as explained in chapter 5, but its absorption is typical of an indirect gap material. The small absorption typical of an indirect gap semiconductor means that light which is generated within the sample will be internally reflected (figure 7.23) and will suffer multiple reflection before finally being absorbed, or escaping from the specimen. The light will escape from the specimen where it reaches the surface at less than the critical angle, and this often happens at the sample edge or at scratches on the surface. This was tested by deliberately scratching the surface of the sample.

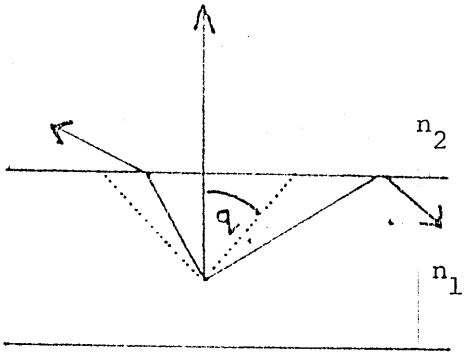

The critical angle is q where

$$\sin q = \frac{n_2}{n_1}$$

For Gallium phosphide $n_1 = 3.37$ and $q \simeq 17^{\circ}$.

FIGURE 7.23 THE CRITICAL ANGLE FOR TOTAL INTERNAL REFLECTION.

In direct or near direct gap materials (depending on sample thickness and surface preparation) most of the internally reflected light is lost by self absorption (Bergh and Dean, 1972). This appears to be the case with all my $Ga_{1-x}Al_xAs$ samples where no light could be found originating from purposely scratched samples or from the sample edges. The light from such samples of $Ga_{1-x}Al_xAs$ is always produced by recombination close to the point of observation.

To summarize, care is needed in interpreting the results of the observation of EL from thin films of indirect gap semiconductor because of the occurrence of multiple internal reflections.

7.3 Amorphous Silicon

The potential technological importance of amorphous silicon (a-Si) for large area devices such as solar cells means that a quick and inexpensive way of measuring the uniformity of deposited a-Si films could have a number of applications. I proposed to study, with the IIT microscope, the uniformity of a thin layer of a-Si (kindly lent by Dr. I. Austin, University of Sheffield).

The thin layer ($\simeq$ 1 μm) of a-Si was nitrogen doped and deposited by glow discharge (Vossen and Kern, 1980) onto a glass substrate. The sample was uncontacted so I studied it with PL excitation. The PL efficiency of a-Si is a good indicator of its quality. The efficiency depends on doping and drops by orders of magnitude in doped samples (Nashashibi, 1977; Austin, 1979 and Priv. Comm.).

Before studying the material spatially with the IIT, I measured its PL spectrum to check that the emission was within the sensitivity range of the IIT. The PL intensity of a-Si is much greater at liquid nitrogen temperature than at room

temperature so the sample was always studied while mounted in the cryostat; with the microscope, monochromator and photomultipliers as explained in chapter 6. The PL was excited with a 632.8 nm He-Ne laser producing 0.5 mW. I measured the PL spectrum of the a-Si on both S1 and S20 photocathodes figure 7.24. The spectrum of the standard lamp through the system (including the cryostat window) was also measured on both photocathodes leading to the corrected PL spectrum of a-Si as shown in figure 7.25. The spectrum is discussed by Street (1978).

I concluded from the PL spectra that an S20 photocathode (similar to that in the IIT) was sensitive to the a-Si PL although an S1 photocathode would give an improvement of signal by a factor of about three.

A check was made on the sensitivity to a-Si PL of the IIT's photocathode in case it differed markedly from the photomultiplier's S20 photocathode. With the apparatus used above to measure the a-Si PL spectra the photomultiplier was replaced by the IIT so that the IIT was used as a non-imaging detector. The total IIT light output was proportional to the PL signal within the monochromator bandpass.

As the monochromator pass band was scanned from 400 nm to 900 nm two peaks were seen. The faint laser line excitation peak at 632 nm (greatly reduced in intensity by blocking filters) and the PL peak at about 854 nm (not 860 nm as measured on the S20 photomultiplier because the S20 photocathodes of IIT and photomultiplier were not identical). The intensity corrected a-Si PL peak occurs at $\simeq$ 960 nm. This established that the IIT photocathode was sensitive to a-Si PL. As a final check to ensure that the IIT was responding to a-Si PL

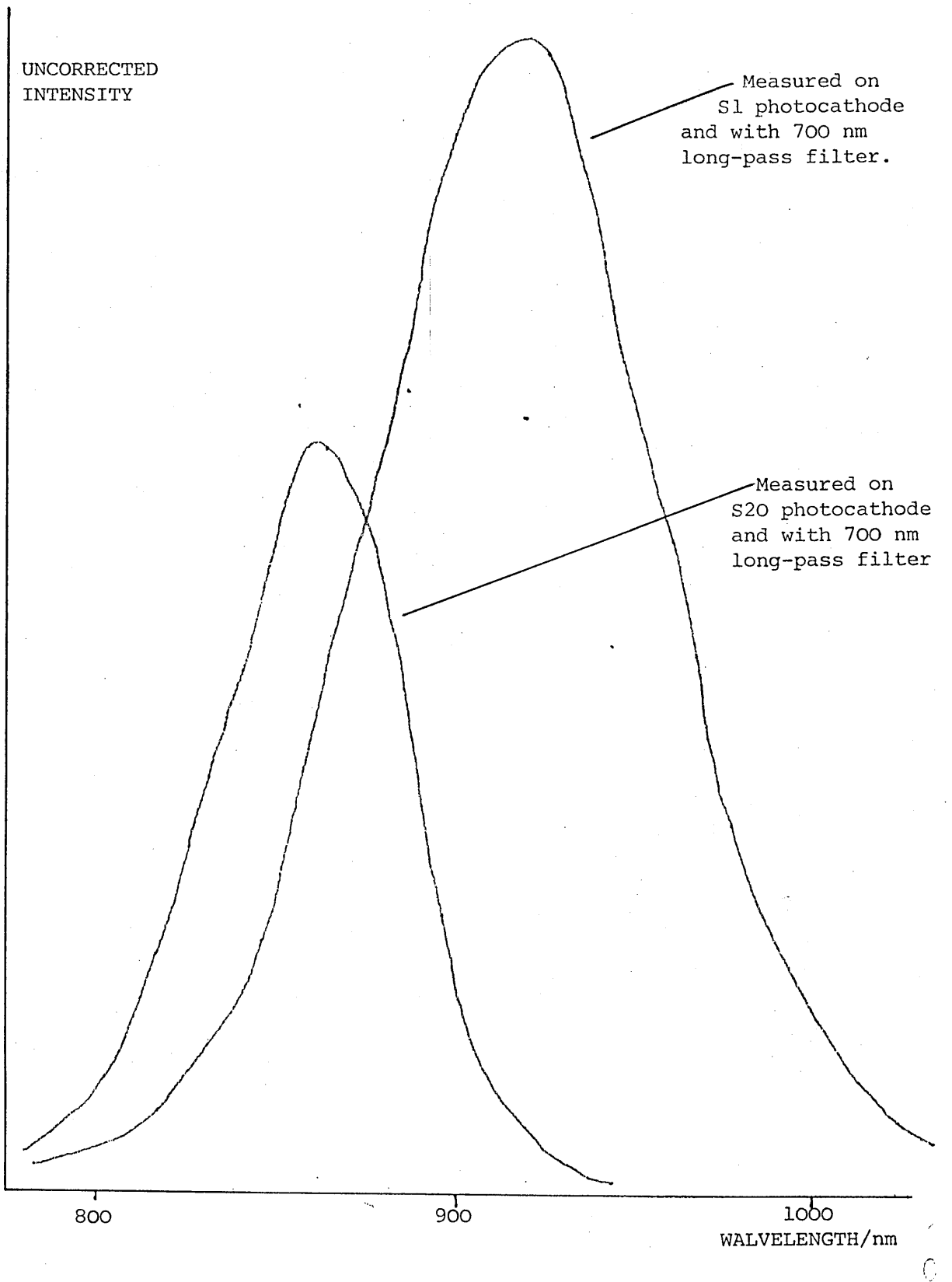

FIGURE 7.24 AMORPHOUS SILICON PHOTOLUMINESCENCE AT ≃ 80 K (UNCORRECTED).

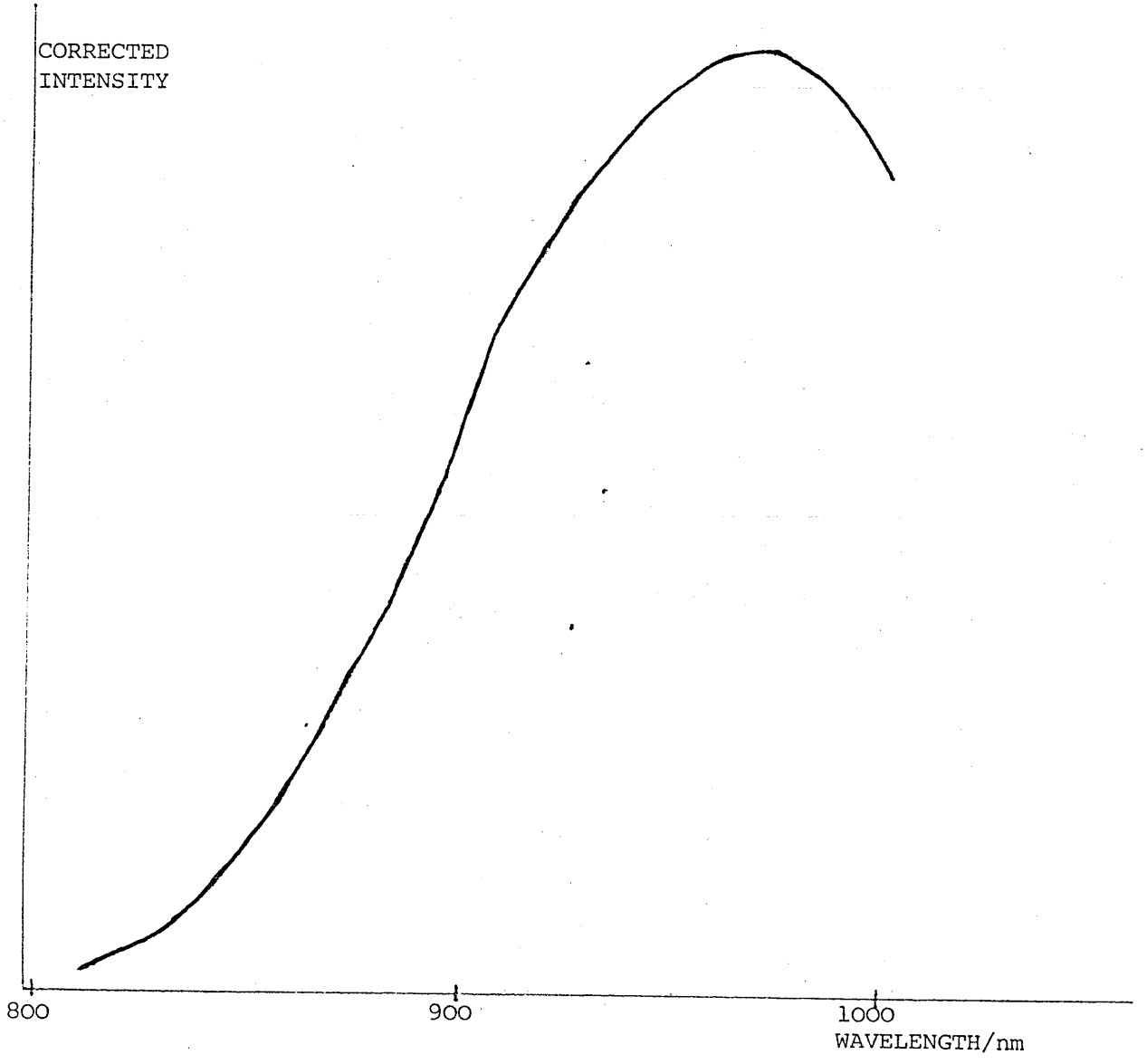

FIGURE 7.25 AMORPHOUS SILICON PHOTOLUMINESCENCE AT ≃ 80 K (CORRECTED).

and not to scattered laser light breaking through the blocking filters the sample of a-Si was aligned and focused by surface reflected ambient light while in the cryostat at room temperature. The sample was excited with the laser and observed to see if any signal which would be either room temperature PL or filter break through, could be detected on the IIT. With the best cut off filter (chapter 6) only a very faint IIT output was seen at this stage. The sample was then cooled to ≃ 80 K and an image was seen on the IIT phospher. Since scattered light and filter breakthrough will not change with sample temperature but a-Si PL is much brighter at low temperatures (Nashashibi et al., 1977) it follows that the IIT output recorded with the sample at ≃ 80 K is a-Si PL.

After the sample had cooled it had to be periodically refocused. It was found easiest to focus on the sample edge. Figures 7.26a, 7.26b and 7.26c, (all recorded and printed with the same exposure) show the results of a series of experiments as described in the previous paragraph. Figure 7.26a is just IIT phospher noise, figure 7.26b is a-Si PL at room temperature combined with excitation light breakthrough and figure 7.26c is a-Si PL with the sample at ≃ 80 K. In figure 7.26c about 80 μm of sample fills the IIT phospher. At this high magnification focusing the sample was found to be difficult due to the lack of surface features. At lower magnification one edge of the sample is shown in figure 7.27a and another in figure 7.27b. Both figures 7.27a and 7.27b have a dark diffuse circle in the centre. This is due to the IIT gain varying slightly spatially, and is not a property of the sample. Searches were made for spatial variations in the PL of the sample while the sample was slowly moved by translating the microscope stage to which the cryostat was attached. The sample surface was studied in detail but no surface features were found. Any crystalline regions within the

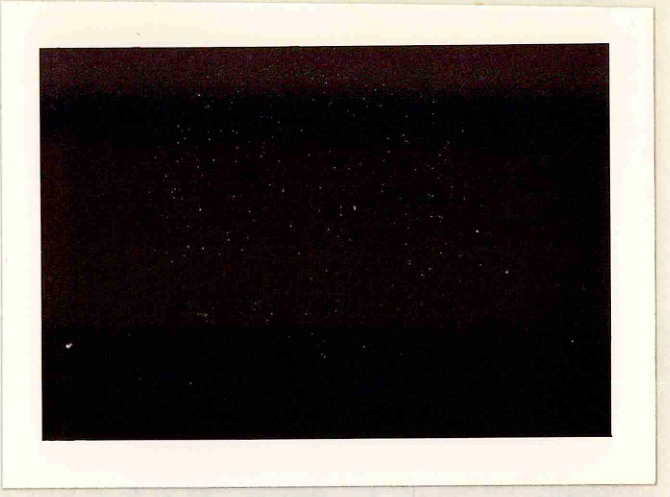

FIGURE 7.26a
IIT PHOSPHER NOISE

Same exposure as figures 7.26b and 7.26c.

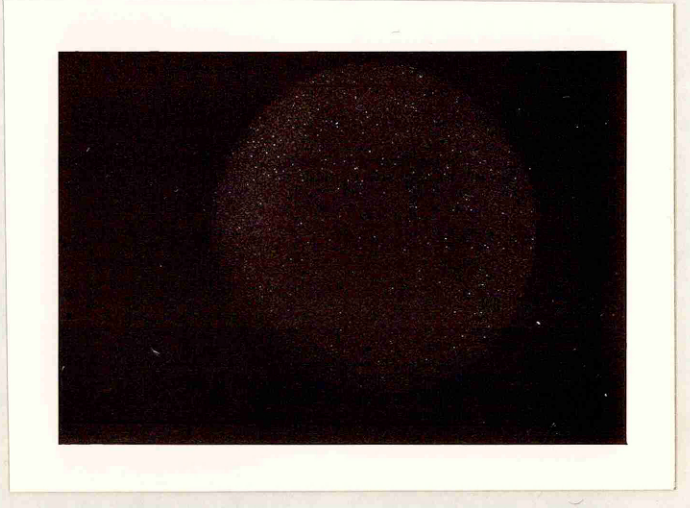

FIGURE 7.26b
a-Si PL AT ROOM TEMPERATURE.

Combined with excitation radiation breaking through the filters.

Scale as figure 7.26c.

FIGURE 7.26c
a-Si PL AT ≃ 80 K.

Only difference from figure 7.26b is the sample temperature.

Scale bar equals 25 μm.

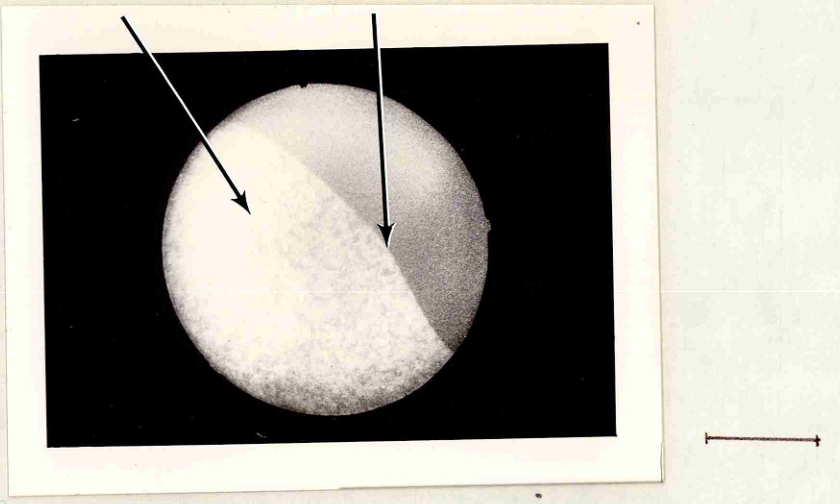

FIGURE 7.27a a-Si PL AT ≃ 80 K.
Sample edge is visible. Scale bar equals 100 μm.

FIGURE 7.27b a-Si PL AT ≃ 80 K.
Sample edge is visible. Scale bar equals 100 μm.

amorphous material would have been seen as dark patches because the PL of crystalline silicon (peak at 1100 nm) is outside the spectral response of the IIT.

Within the limits of my experiment I can conclude that the sample is uniform with regard to luminescence efficiency on a scale greater than about 2 μm.

7.4 Amorphous Phosphorus

With the apparatus that was used (see above) to observe the sensitivity of the IIT photocathode to a-Si PL, I tested a sample of amorphous phosphorus (a-P) to see if a spatial study of it would be possible. However there was too little PL signal within the spectral sensitivity range of the IIT, both from a thin film and from bulk red amorphous† phosphorus samples. (Kirby and Davis, 1980).

7.5 Conclusions and Comparison with other work

I have used a four stage high gain IIT coupled to a microscope to observe the low direct current (of order 10 mA) EL (at room temperature and ≃ 80 K) in bulk semiconductors in the visible and near infra red with a spatial resolution almost as high as optical microscope resolution (1 to 2 μm). I have established the usefulness, and shown some of the limitations, of this technique. For direct gap semiconductors that luminesce within the sensitivity range of the IIT my experiments have shown that an IIT microscope study can provide useful information on the contacts and the material. A

---

† Obtained from Mining and Chemical Products Ltd. of London.

comparison of my EL pictures with scanning electron microscope SEC and CL contrast pictures showed that the EL result is more closely related to the current flow pattern in a sample than are the SEC or CL results. To my knowledge this is the first comparison of CL with EL data. I have shown the limitations of the technique when indirect gap material is studied particularly with regard to estimating minority carrier range. I have also shown that the spatial uniformity of amorphous silicon can, in principle, be studied with the IIT microscope and a nitrogen cryostat.

The only other applications of high gain IIT techniques to the study of semiconductors appear to have been by, a) Panyutin and Chashnikov (1975) who studied recombination radiation from silicon p-n junctions. They used an image intensifier (USSR type UMI-95) and a microscope to give them an ultimate specimen resolution of 20 μm. They were able to record recombination radiation from a silicon p-n junction with a base thickness of 200 μm and a current density of greater than 20 A cm^{-2}, b) Ivanov et al. (1975) who studied GaAs under acoustoelectric instability conditions; and, c) Yamasaki (1975) and Voss (1971) who studied the plasma spread in high current carrying (typically 100A) thyristors. Other investigators (Ueda et al. (1979) and Arro et al. (1972) have used lower gain image converter systems, or silicon vidicon television cameras, but these have a high background noise which makes single photon and very low light level detection difficult.

The spatial variation of PL in a sample of GaAs was studied by Heinke (1975) who used a specially adapted helium cryostat to observe specimens to a spatial resolution of 5 μm. He excited the sample with an 8 mW He-Ne laser and detected the PL by scanning with an S1 photocathode photomultiplier. He did not use an IIT.

7.6 Suggestions for further work

Further heating of the $x = 0.52$ $Ga_{1-x}Al_xAs$ sample (in a hydrogen reducing atmosphere) to see if further diffusion of indium takes place would give extra information on the nature of the contacts. A spatial study of the light emission from an a-Si EL junction (Pankove and Carlson, 1976) could enable radiative recombination centres to be isolated. A possible extension of the work would be to use an S1 photocathode IIT (or to use an image converter with an S1 photocathode and an output in the visible positioned in front of the S20 IIT to effectively increase its spectral range) to increase the gain of the system in the near infra red. This should enable the luminescence of crystalline silicon to be observed with a very high optical power gain.

Further studies could be made of all the materials mentioned above. The main problem is availability of samples. Samples containing known defects or impurities are hard to prepare but would be particularly useful.

REFERENCES

ANGELOS R., ZINK J.I. and HARDY G.E. (1979); J. of Chemical Education; 56; 6; pp 413-414.

ARRO I. et al. (1972); Toim Eesti Nsv Tead Akad (USSR); 21; pp 169-173.

AUSTIN I., RICHARDS K. and SEARLE T.M. (1979); Inst. Phys. Conf. Ser. No. 43, Chapter 30, pp 1155-1158.

BACON F. (1605); The Advancement of Learning. Book IV. Chapter 3.

BAILIFF I.K., MORRIS D.A. and AITKEN M.J. (1977); J. Phys. E; 10; pp 1156-1160.

BARNARD R.W. (1973); "Plating in the Electronics Industry"; American Electroplaters Society; pp 38-51.

BAUMEISTER T. (1978); Marks Standard Handbook for Mechanical Engineers, Eighth Edition, Mc Graw-Hill.

BEALS C.S. (1923); Trans. R. Soc. Can.; Section III; 125.

BECKER J. (1972); Rontgenblatter; 25; 7; pp 311-313.

BERGH A.A. and DEAN P.J. (1972); Proc. IEEE; 60.

BEYELER H.U. and VEPREK S. (1980); Phil. Mag. B; 41; 3; pp 327-340.

BIRD G.R., JONES R.C. and AMES A.E. (1969); Appl. Opt.; 8; pp 2389-2405.

BOLZ R.E. and TUVE G.L. (1973); Applied Engineering Science Data Book, 2nd Edition, C.R.C.

BOOKER G.R., OURMAZD A. and DARBY D.B. (1979); J. De Physique; 40; Supp. 6; pp 19-21.

BOWDEN F.P., STONE M.A. and TUDOR G.K. (1947); Proc. Roy. Soc. A; 188; 329.

BOWDEN F.P. and THOMAS P.H. (1954); Proc. Roy. Soc. A; 223; pp 29-39.

BURKE J. (1898); Nature, London; 78; 156.

CHANDRA B.P. (1976); Indian J. Pure and Appl. Phys.; 14; pp 874-876.

CHANDRA B.P. and ELYAS M. (1977); Indian J. Pure and Appl. Phys.; 15; pp 744-745.

CHANDRA B.P. (1978); Czech J. Phys. B 28; pp 84-87.

CHANDRA B.P. and ELYAS M. (1979); J. Phys. C; 12; L695-L698.

CHANDRA B.P. and SHRIVASTAVA K.K. (1979); Pramana; 13; 6; pp 611-615.

CHANDRA B.P. and VERMA R.D. (1980); Indian J. Pure and Appl. Phys.; 18; 8; pp 608-609.

CHANDRA B.P. and ZINK J.I. (1980); Phys. Rev B; 21; 2; pp 816-826.

CHARMAN W.H. (1966); J.R. Micros. Soc.; 86; 33.

CHUDACEK I. (1966); Czech J. Phys.; B 16; 520.

COLEMAN C.I. and BOKSENBERG A. (1976); Contemp. Phys.; 17; 3; pp 209-236.

COTTON F.A., GOODGAME D.M.L. and GOODGAME M. (1962); J. Am. Chem. Soc.; 84; 167.

CURIE D. (1963); Luminescence in Crystals, Methuen, London.

DAINTY J.C. and SHAW R. (1974); Image Science, Academic Press, London.

DEAN P.J. (1969); Applied Solid State Science; 1; Academic Press.

DIEKE G. (1968); Spectra and Energy Levels of Rare Earth Ions in Crystals, Interscience Publishers, New York.

ELLIOTT S.R. (1979); Nature; 277; 85.

EL'YASHEVICH M.A. (1953); Spectra of The Rare Earths, United States Atomic Energy Commission Report AEC-tr-4403.

EMI LTD. (1975); "Image Intensifier Tubes", Published by EMI Electronics Ltd., Blyth Road, Hayes, Middlesex.

FIELD J.E. (1971); Contemp. Phys.; 12; pp 1-31.

FOX P.G. and SORIA-RUIZ J. (1970); Proc. R. Soc. A; 317; pp 79-90.

FOX P.G. and FULLER K.N.G. (1971); Nature Phys. Sci.; 234; pp 13-14.

GERNEZ D. (1908); Ann. Chim. Phys.; 15; 516.

GLAZUNOV E. (1963); Instrum. Exper. Tech. (USSR); 1; pp 110-111.

GRIEGLEB G. (1961); "Electron-Donator-Acceptor-Komplexe",Springer-Verlag, West Berlin.

GRUNER S. (1973); Princeton University Technical Report No. 16, Contract AT(11-1)-3120.

HALLER, LIPPMANN and BOUTY (initials not quoted) (1909); Annales de Chimie et de Physique; 8th Series; 18.

HARDY G. and ZINK J. (1976); Inorg. Chem.; 15; 12; pp 3061-3065.

HARDY G., BALDWIN J.C. et al. (1977); J. Am. Chem. Soc.; 99; 11; pp 3552-3558.

HARNWELL G. (1949); "Principles of Electricity and Magnetism", McGraw-Hill, pp 276.

HARVEY E. (1957); "A History of Luminescence from the Earliest Times until 1900", The American Philosophical Society, Philadelphia.

HAYES W. (1974); "Crystals with the Fluorite Structure", Clarendon Press, Oxford.

HEINKE W. (1975); Inst. Phys. Conf. Ser. No. 23; pp. 380-386.

HEINRICH P. (1820); Die Phosphorescenz der Korper (Nurnberg); 4; 425.

HERZBERG G. (1950); "Molecular Spectra and Molecular Structure, 1, Spectra of Diatomic Molecules"; Van Nostrand, Princeton.

HERZBERG G. (1971); "The Spectra and Structures of Simple Free Radicals"; Cornell Univ. Press.

HIKATA A. and ELBAUM C. et al. (1963); J. Appl. Phys.; 34; 2154.

HURT C.R., McAVOY N., BJORKLUND S., and FILIPESCA N. (1966); Nature Lond.; 212; 179.

IKEDA T. (1962); Japan J. Appl. Phys.; 1; 13.

IMHOF A. (1917); Phys. Z; 18; 78 and 374.

IREDALE P. and RYDEN D.J. (1967); AERE Harwell Report No. R-5112.

IVANOV L.P. et al. (1975); Sov. Phys. Semicond.; 9; pp 916-918.

JONES O.C. (1970); "Tables of Spectral Power Distribution, Dept. of Trade and Industry"; Nat. Phys. Lab. Publ. Q.14.

JENNY D.A. (1957); J. Appl. Phys.; 28; 1515.

KAFALAS P. (1968); Proc. 8th Int. Congress on High Speed Photography, Stockholm; John Wiley and Sons, London.

KERAMIDAS V.G. (1979); Inst. Phys. Conf. Ser. No. 45. Chapter 5, pp 396-410.

KIRBY P.B. and DAVIS E.A. (1980); J. Non. Crys. Sol.; 35; pp 945-950.

KODAK Ltd. (1973); "Plates and Films for Scientific Photography"; ISBN 0879850833; pp 18.

KRANYA U., KNEBS I., and LAIZAU V. (1977); Polym. Mech. (USA); 13; 10; pp 638-641.

KRUTYAKOVA V.P. and SMIRNOV V.N. (1979); J. Appl. Spectrosc. (USA); 30; 603-5.

LANGEVIN M. (1913); Rapports et discussions du Conseil de Physique; published in Paris (1921) by Gaunthier-Villars. pp 251.

LENARD P., SCHMIDT F. and TOMASCHEK T. (1928); Handb. Exp. Phys.; 24; 976.

LIN S.H., WUTZ D., HO Z.Z. and EYRING H. (1980); Proc. Natl. Acad. Sci. USA; 77; 3; pp 1245-1247.

LONGCHAMBON H. (1922); C. r. Hebd. Seanc. Acad. Sci. Paris; 174; 118.

LONGCHAMBON H. (1925); Bull. Soc. Trans. Min. (France); 48; pp 130-193.

MARFUNIN A. (1979); Spectroscopy of Luminescence and Radiation Centres in Minerals", Springer-Verlag, Berlin.

MASCARENHAS Y.P., de ALMEIDA V.N. and LECHAT J.R. (1980); Acta. Cryst.; B36; pp 502-504.

MAUDE N. (1980); Brit. J. of Photography; 127; 6271; 983.

MEYER K. and GRAGERT E. (1963); Phys. Stat. Sol.; 3; 2005.

MEYER K. and POLLY F. (1965a); Phys. Stat. Sol.; 8; 441.

MEYER K. and POLLY F. (1965b) Ber. Bunsenges; 69; 244.

MEYER K. and OBRIKAT D. (1969); Z. Phys. Chem.; 240; 309.

MEYER K., OBRIKAT D. and ROSSBERG M. (1970a); Kristall Tech.; 5; 181.

MEYER K. OBRIKAT D. and ROSSBERG M. (1970b); Kristall Tech.; 5, 5.

NASHASHIBI T.S., AUSTIN I.G. and SEARLE T.M. (1977); Proc. 7th Int. Conf. on Amorphous and Liquid Semiconductors; pp 392-396.

NATIONAL BUREAU OF STANDARDS USA, (1980); United States Dept. of Commerce, Diffusion in Metals Data Center, Building 223. AL53, Washington D.C. 20234; Contact Michael E. Read.

NELSON D.M. (1926); J. Opt. Soc. Am.; 12, 207.

NIELSEN J. (1930); J. Opt. Soc. Am.; 20; pp 701-718.

NIELSEN J. (1947); J. Opt. Soc. Am.; 37; 6; pp 494-499.

NYSWANDER R.E. and COHN B.E. (1930); Phys. Rev.; 36; pp 1257-1260.

OHMAN Y. (1978); Astrophysics and Space Sci.; 55; pp 39-47.

OHMAN Y. (1979); Physica Scripta; 20; pp 620-627.

OMAR M. (1975); "Elementary Solid State Physics", Addison-Wesley.

ONTON A., LORENZ M.R. and WOODALL J.M. (1974); J. Cryst. Growth; 27; pp 166-176.

PANKOVE J.I., and CARLSON D.E. (1976); Appl. Phys. Lett.; 29; 9; pp 620-622.

PANYUTIN E.A., and CHASHNIKOV I.G. (1975); Instrum. Exp. Tech. (USA); 18: pp 941-943.

PEARSE R. and GAYDON A. (1963); "The Identification of Molecular Spectra"; Third Edition, Chapman and Hall, London.

PETROFF P.M., LOGAN R.A., and SAVAGE A. (1980); Phys. Rev. Lett.; 44; pp 287-291.

RANDALL R.P. (1966); Adv. in Elect. and Elect. Phys.; 22A; 87.

REYNOLDS G.T. (1966); Appl. Optics; 5; 4; pp 577-583.

REYNOLDS G.T. (1980); Microscopica Acta; 83; 1; pp 55-62.

RHODERICK E.H. (1978); "Metal-Semiconductor Contacts"; Oxford University Press.

ROBERTS D. (1980); Private Communication.

ROSE A. (1973); "Vision: Human and Electronic"; Plenum Press.

ROSE-INNES A.C. (1973); "Low Temperature Laboratory Techniques"; The English Universities Press Ltd.; pp 138.

SCARMOZZINO R. (1971); Solid St. Commun.; 9; 1159.

SPEAR W.E. (1977); Adv. Phys.; 26; pp 811-845.

STRINGFELLOW G.B. and GREENE P.E. (1969); J. Appl. Phys.; 40; 1; pp 502-507.

STREET R.A. (1978); Phil. Mag. B.; 37; pp 35-42.

SWALLOWE G. (1980); Private Communication.

SWITHENBY S. (1979); Private Communication.

TAKADA S. (1977); Photog. Sci. and Eng.; 21; 3; pp 139-141.

THIESSEN P.A. and MEYER K. (1970); Naturwissenschaften; 57; 423.

TOULOUKIAN Y.S.(editor) (1967); "Thermo-physical Properties of High Temperature Solid Materials, Volume 4"; Macmillan, New York.

TRAUTZ M. (1905); Z. Phys. Chem.; 53; 1.

TRAUTZ M. (1910); Ion; 2; 77.

TSCHUGAEFF L. (1901); Ber. dt. Chem. Ges.; 34; 1820.

UEDA O. et al. (1979); J. Appl. Phys.; 50; pp 765-772.

VERNADSKY W.J. (1910); Bull Acad. Sci. St. Petersbourg; 4; 1037.

VOIGT M. (1913); Rapports et discussions du Conseil de Physique; published in Paris (1921) by Gaunthier-Villars, 241.

VOSS V.P. (1971); Proc. VDE Meeting, Dynamiche Probleme der Thyristortechnik; Munich; pp 251-262.

VOSSEN J.L. and KERN W. (1980); Physics Today (USA); 33; 5; pp 26-33.

WALTON A.J. (1977); Adv. Phys.; 26; 6; pp 887-948.

WALTON A.J. and BOTOS P. (1978); J. Phys. E.; 11; pp 513-514.

WALTON A.J. (1980); Private Communication.

WALTON A.J. and DEBENHAM N. (1980); Nature; 284; pp 42-44.

WATERS J.R., REYNOLDS G.T., SCARL D.B., and ZDANIS R.A. (1962); IRE Trans. Nucl. Sci.; N8; 9; pp 239-242.

WAWNER K. and KRUKONIS V. (1976); J. Comp. Mat.; 10; 382.

WEBSTER R. (1964); "The Gemmologist's Compendium"; Third Edition; NAG Press Ltd., London.

WEDGWOOD T. (1792); Phil. Trans. R. Soc.; 82; 28.

WEICHERT R., and SCHONERT K. (1978); J. Mech. Phys. Solids; 26; pp 151-161.

WEISER H.B. (1918a); J. Phys. Chem.; 22; 480.

WEISER H.B. (1918b); J. Phys. Chem.; 22; 576.

WICK F. (1937); J. Opt. Soc. Am.; 27; 275.

WICK F. (1940); J. Opt. Soc. Am.; 30; 302.

WILLARDSON R.K. and BEER A.C. (1968); "Semiconductors and Semimetals, volume 4, Physics of III-V Compounds" Academic Press.

WILLIAMS E.W. and HALL R. (1978); "Luminescence and the Light Emitting Diode"; Pergamon Press, pp 112-3.

YAMASAKI H. (1975); IEEE Trans. Electron Devices; ED-22; pp 65-68.

ZINK J.I. (1974); J. Am. Chem. Soc.; 96; 6775.

ZINK J.I. (1978); Accts. of Chemical Research; 11; 8; pp 289-295.

ZINK J.I., HARDY G.E., and GLIEMANN G. (1980); Inorg Chem.; 19; 2; pp 488-492.

Recent Publications

Chandra B.P. (1980) Indian Journal of Pure and Applied Physics, Vol. 18, pp 743-746.

Pye M. (1981) The Sunday Times, 29th March, article entitled "Mother Earth's Flying Saucers".

Dundon G.P. (1980) Semiconductor International 1980, Brighton, England, paper entitled "A cheap way to detect failure sites on LSI devices using fluorocarbon" sponsored by Analog Devices BV, Limerick, Ireland.